

**FEEDBACK COOLING THE MECHANICAL
MOTION OF A DIAMAGNETIC PARTICLE IN A
MAGNETO-GRAVITATIONAL TRAP**

by

Bradley R Slezak

B.S. Computer Engineering, University of Pittsburgh, 2008

M.S. Physics, University of Pittsburgh, 2014

Submitted to the Graduate Faculty of
the Dietrich School of Arts and Sciences in partial fulfillment
of the requirements for the degree of

Doctor of Philosophy

University of Pittsburgh

2018

UNIVERSITY OF PITTSBURGH
DIETRICH SCHOOL OF ARTS AND SCIENCES

This dissertation was presented

by

Bradley R Slezak

It was defended on

April 13th 2018

and approved by

Brian D’Urso, Department of Physics, Montana State University

Wolfgang Choyke, Department of Physics and Astronomy

Randall Feenstra, Department of Physics, Carnegie Mellon University

David Pekker, Department of Physics and Astronomy

Hanna Salman, Department of Physics and Astronomy

Vladimir Savinov, Department of Physics and Astronomy

Dissertation Advisors: Brian D’Urso, Department of Physics, Montana State University,

Wolfgang Choyke, Department of Physics and Astronomy

FEEDBACK COOLING THE MECHANICAL MOTION OF A DIAMAGNETIC PARTICLE IN A MAGNETO-GRAVITATIONAL TRAP

Bradley R Slezak, PhD

University of Pittsburgh, 2018

We set out to create a mechanical system with a size scale generally considered to reside in the classical regime and make it behave quantum mechanically. Our system consists of a silica microsphere diamagnetically levitated in an ultra-high vacuum environment. The combination of a strong magnetic field gradient, generated by ferromagnetic pole pieces and permanent magnets, and the gravitational interaction create a 3-dimensional trap for the particle. We measure the particle's motion in the trap by scattering laser light off of the particle, and use that measurement to provide negative feedback to the particle, removing mechanical energy via a radiation pressure damping force from a second laser. In the ideal case, the energy of the particle will near that of its quantum mechanical ground state. It is in this regime that we aim to create non-classical states of the particle's mechanical motion. By measuring the decoherence rate or the evolution of quantum uncertainty of non-classical states of the trapped particle, we may be able to observe deviations from quantum mechanical predictions that can be attributed to the gravitational interaction.

TABLE OF CONTENTS

PREFACE	xvi
1.0 INTRODUCTION	1
1.1 Dissertation Outline	1
1.2 Background of Mechanical Oscillators	1
1.2.1 Motivation	1
1.2.2 Cold Damping	2
1.2.3 Clamped Systems	2
1.2.4 Optically Trapped Particles in Vacuum	3
1.3 Our System - Magnetically Trapped Particles in Ultra-High Vacuum	4
1.3.1 A Magneto-Gravitational Trap	4
1.3.2 Experiment Overview - Feedback Cooling of Mechanical Motion	9
1.3.3 Long Term Goals	12
1.3.3.1 Quantum Mechanics	12
1.3.3.2 Classical Mechanics - Measurement of G	13
1.3.4 Reported Progress	13
1.4 Mathematical Description	14
1.4.1 Damped, Thermally Driven Harmonic Oscillator	14
1.4.1.1 $\langle x^2 \rangle$, Effective Temperature, and Power Spectral Density	15
1.4.1.2 Discrete Fourier Transform	19
1.4.1.3 Natural Damping and Feedback Damping	20
1.4.1.4 Pressure Damping (Damping From Air Molecule Collisions)	21
1.4.2 Quantum Harmonic Oscillator	23

1.5	Comparison with Optical Trapping	25
2.0	EXPERIMENTAL DESIGN AND PROCEDURES	27
2.1	Chapter Outline	27
2.2	Experimental Process	27
2.3	Optical and Feedback Design	29
2.3.1	High Level Summary	29
2.3.2	Description of Optical Components	29
2.3.2.1	Diode Lasers	31
2.3.2.2	Illumination and Collection	31
2.3.2.3	Support Optics	34
2.3.2.4	Quadrant Photodiode Detector (QPD)	35
2.3.2.5	High Speed Camera	37
2.3.2.6	Galvo	37
2.3.3	Electronics and Feedback System	37
2.4	Mechanical Support, Vacuum Chamber, and Vacuum System Design . . .	39
2.4.1	Vacuum Chamber Design Considerations	40
2.4.2	Vacuum Chamber	41
2.4.3	PEEK Gaskets	42
2.4.4	Re-entrant UHV Flange	44
2.4.5	Mechanical Support	46
2.4.6	Vacuum System Design	49
2.4.7	Previous Setups	53
2.5	Mass Determination	56
2.5.1	Angular Oscillation Frequency	57
2.5.2	Position Sampling	60
2.5.3	Discussion	62
2.5.4	Mass Results	67
2.6	Particle Neutralization	68
2.6.1	Loading and Verification of Charge	70
2.6.2	Rough Neutralization	72

2.6.3	Complete Neutralization	73
2.7	Detector Calibration	79
2.7.1	Camera Calibration	81
2.7.2	Quadrant Photodiode Calibration	87
2.7.2.1	Linear Range Test	88
2.7.2.2	Example Particle Calibration	91
3.0	FEEDBACK COOLING RESULTS AND DISCUSSION	95
3.1	Chapter Outline	95
3.2	Target Results	95
3.3	Example Results	98
3.3.1	Experimental Parameters	98
3.3.2	Results	100
3.4	Summarized Results	106
3.5	Discussion	109
3.5.1	Cooling Efficiency	109
3.5.2	Pressure	111
3.5.2.1	Large Particle, Large Amplitude Damping	113
3.5.2.2	Other Considerations	118
3.5.3	Vibration Sources	121
3.5.4	Particle Rotation	124
3.5.5	Detection Noise Floor and Detector Sensitivity	127
3.5.5.1	Expected Noise Floor	128
3.5.5.2	Detector Sensitivity (Volts per Meter of Movement)	131
3.6	Summary and Outlook	132
3.6.1	Possible Reasons for Vertical Limitation	133
3.6.1.1	Energy Transfer and Signal Coupling Between DOF	133
3.6.1.2	Signal to Noise	133
3.6.1.3	Filtering Limitations	134
3.6.1.4	Laser Noise	135
3.6.1.5	Vibration Sources	135

3.6.1.6	Rotational Energy Transfer	135
3.6.1.7	Damping from Magnetic and Electric Field Effects	136
3.6.2	Moving Forward	136
4.0	OTHER EXPLORED APPROACHES	138
4.1	Chapter Outline	138
4.2	A Micro-molecule	138
4.2.1	Description of Motion	139
4.2.2	Experimental Procedure	140
4.2.3	Micro-Molecule Results	141
4.3	An Over-damped Harmonic Oscillator as Pseudo-free Particle	145
4.3.1	Rationale	145
4.3.2	RC Feedback Filter Attempt	146
4.3.2.1	Results	147
4.3.3	Parameter Estimates	148
4.3.4	RLC Feedback Filter Attempt	150
4.3.4.1	Results	151
4.3.5	Challenges	152
4.3.6	Outlook	153
4.4	Moving the Table Vertically to Damp Particle Motion	154
APPENDIX A.	SHOT NOISE LIMITED DETECTION	156
A.1	Radiation Pressure Shot Noise	156
A.2	Detection - Overcoming Johnson Noise in the Detector	159
A.3	Detection Signal to Shot Noise for a Split Detector	160
A.3.1	Radiation Shot Noise Power and Signal Shot Noise Comparison	163
APPENDIX B.	FEEDBACK SYSTEM	165
B.1	Quadrant Photodiode Amplifier	165
B.2	Low Pass Filters	166
B.3	Galvo Control Circuit	167
B.4	Programmable Gain Amplifier, High-Pass Filter, and Sallen-Key Filter	168
B.5	Feedback Driving Circuit	169

B.6	Balanced and Cooled Detector	170
B.6.1	Front and Back Flanges	171
B.6.2	Electronics Mounting Plate	172
B.6.3	Mounting Plate Mechanical and Cooling Supports	172
B.6.4	Vacuum Chamber and Table Mount	173
B.6.5	Circuit Diagram	175
B.6.6	Expected Noise Floor	175
B.6.7	Effect of Cooling	177
B.6.8	Cooling Notes	178
B.7	Modifications for Over-damping	178
B.7.1	Dual Cooling Laser Modification	178
B.7.2	Feedback Circuit Modification	179
APPENDIX C. ALIGNMENT PROCEDURE		182
C.1	Optical Components List	182
C.2	Laser Coupling	183
C.3	Beam Collimation and Alignment	183
C.4	Setting Focal Lengths	184
C.5	Initial Alignment	185
C.6	Objective Resolution and Magnification	186
C.7	Placing the Chamber	189
C.8	Quadrant Photodiode Focus and Alignment	191
APPENDIX D. HARDWARE		193
D.1	Table Enclosure	193
D.2	Pole Pieces	195
D.2.1	Materials	195
D.2.2	Design	195
D.2.3	Lapping Procedure	196
D.2.4	Trap Assembly	199
D.2.5	Assembly and Trap Frequencies	201
D.2.6	Hiperco 50A and Magnet Data Sheets	203

APPENDIX E. SUPPORT SOFTWARE	205
E.1 PEEK Diamond Turning Program	205
APPENDIX F. PROCEDURES	206
F.1 Loading	206
F.1.1 Loading Setup	206
F.1.1.1 Horn Setup	206
F.1.1.2 Particle Preparation	206
F.1.1.3 Chamber and Vacuum Preparation	206
F.1.1.4 Optics Preparation	207
F.1.2 Loading Procedure	207
F.1.3 Chamber Baking	210
F.1.3.1 Baking Setup	210
F.1.3.2 Chamber Baking Procedure	211
F.1.4 Ion Pump Baking	212
F.1.5 PEEK Gasket Tightening	213
F.1.6 Baking Tables	213
APPENDIX G. ALL COOLING RESULTS	217
BIBLIOGRAPHY	231

LIST OF TABLES

1	Comparison of optical and magneto-gravitational trapping parameters.	25
2	Table of particles used for mass calculations.	67
3	Table of average of mass results.	67
4	Table of all mass measurements	68
5	Table of temperature results and fit parameters for 10-15-2017 particle. . . .	101
6	Summary of T_{eff} for example cooling results for different calculation schemes.	105
7	Cooling results - Bozeman - ‘Top Hat’ Mount	107
8	Cooling results - Pittsburgh - ‘Top Hat’ Mount	107
9	Cooling results - Pittsburgh - Translation Mount	108
10	Table of temperatures and resistance values for thermistor NTCASCWE3 . . .	178
11	Table of optical component part numbers	182
12	Pressure Table from October 2017 - Bozeman	214
13	Pressure Table from November 2017 - Bozeman	215
14	Pressure Table from December 2017 - Bozeman	216

LIST OF FIGURES

1	Illustration of the magnetic trap and pole piece configuration	5
2	Illustrations of x - y and y - z planes of the magnetic trap	6
3	Plots of the magnetic field strength $ B $ for slices in the x - y and y - z planes . .	8
4	Plots of the potential energy with and without the gravitational interaction .	9
5	A simplified diagram of the feedback cooling experiment	10
6	Illustration of the shift in particle equilibrium position due to the control laser	10
7	Illustration of the damping mechanism created by the control laser	11
8	System diagram showing the main optical components and feedback path . .	30
9	Images of the illumination and collection laser beams.	32
10	Photograph of the transmitted illumination beam blocker.	34
11	Dark-field and bright-field images of a silica microsphere	35
12	Illustration of quadrant photodiode imaging and signal generation	36
13	A system diagram displaying the feedback loop in its entirety.	38
14	The main vacuum chamber and the adapter chamber.	41
15	Hexagonal PEEK UHV gasket design	43
16	The design of the window flange, incorporating the PEEK glass-metal seal. .	45
17	The model of the objective mount and an image of the mount in use.	46
18	The model of the “top hat” chamber mount and an image of the mount in use.	47
19	Full assembly of trap plate support structures.	48
20	Schematic of the entire vacuum system, including rough, HV, and UHV divisions.	49
21	The rough vacuum section of the vacuum system	50
22	The High Vacuum (HV) section of the vacuum system	51

23	The Ultra-High Vacuum (UHV) section of the vacuum system	53
24	Previous mounting designs for the trap chamber	54
25	The original vacuum system, which supported 4 large pumps.	55
26	Thermal and cooled power spectra from the Quadrant Photodiode Detector .	58
27	Fits for determining the oscillation frequencies from uncooled particle motion	60
28	Histograms of the thermalized amplitudes of a 1.54 μm silica microsphere . .	61
29	Histograms of thermalized amplitude squared on a semi-log plot.	62
30	A histogram of a particle that is not in thermal equilibrium	63
31	Power spectra generated from camera data	65
32	Fits for determining the resonant frequencies from camera data	65
33	A camera spectrum showing strong transverse coupling into the vertical signal	66
34	Change in particle location in the trap after rough neutralization.	69
35	View of typical electrical connections to the trap pole pieces.	70
36	View of the ultrasonic horn and electrical connection.	71
37	View of the radiation source during rough neutralization	73
38	An illustration of the UV light neutralization process	74
39	View of the mounting design to accommodate UV light illumination	74
40	UV lamp holder design and placement on the chamber	76
41	Demonstration of particle neutralization and a charge sign change	77
42	Two demonstrations of charge control indicating complete neutralization . . .	79
43	Analysis of amplitude calibration for high speed camera in the axial direction	83
44	Analysis of amplitude calibration for high speed camera in the vertical direction	85
45	Fits for determining the camera calibration	86
46	Plots to determine the axial linear range of the QPD	89
47	Plots to determine the vertical linear range of the QPD	90
48	Axial and Vertical QPD particle calibration spectra	92
49	Axial and Vertical QPD particle calibration spectra	93
50	Fits for determining the QPD calibration for a particle	94
51	Power spectral density plots of maximally cooled 1.54 μm SiO_2 sphere	101
52	Broad frequency plots of maximally cooled 1.54 μm SiO_2 sphere	102

53	Comparison of Power Spectra for Thermal Motion and Cooled Motion	104
54	Graphical summary of cooling results obtained	106
55	Plots examining cooling vs damping width provided by the feedback	110
56	Extracted natural damping Γ_A for all cooling results	112
57	Summary of large particle, large amplitude damping	114
58	Plots of axial large particle, large amplitude damping	115
59	Plots of vertical large particle, large amplitude damping	116
60	Comparison of measured rates with rates extracted from cooling	118
61	Comparison of cooling results at several pressures for silica 1.54	119
62	Comparison of cooling results at several pressures for silica 7.75	120
63	Comparison of cooling data and vibration data	122
64	Normalized cross-correlation plots of particle motion with vibration data . . .	124
65	Images of non-uniform polystyrene particle	126
66	Spectra showing likely rotational motion of polystyrene particle	127
67	Comparison of QPD noise floor and cooling results.	128
68	Time sequences of the two-particle ‘micro-molecule’ motion	142
69	Micro-molecule power spectral densities, normal and transformed coordinates	143
70	Demonstration of COM and vibrational mode micro-molecule cooling	144
71	Theoretical amplitude and phase response of V_R in an RC circuit	147
72	Power spectra showing over-damping of a particle	148
73	Theoretical amplitude and phase response of V_R in an RLC circuit	151
74	Power spectra of overdamped spectra using the RLC filter	152
75	Equilibrium position shift as a result of axial cooling laser	153
76	Image of the surface transducers utilized for shaking the optical table	154
77	Comparison of laser feedback results and table shaking feedback results . . .	155
78	Simulated ground state signal from split detector	164
79	Quadrant photodiode sum, difference, and amplification circuit diagram. . . .	166
80	Diagram of low pass filters for DC offset control.	167
81	Schematic of the galvo drive circuit	168
82	Schematic of the PGA and bandpass filter.	169

83	Schematic of the laser drive circuit and high current drive circuit.	170
84	Front and back flanges for balanced, cooled detector	171
85	Plate for mounting balanced detector electronics	172
86	Mechanical support for balanced detector mounting plate	173
87	The main vacuum chamber and mounting structure for the balanced detector	174
88	The fully assembled balanced and cooled photodiode detector	174
89	Schematic for a low noise, balanced detector	175
90	Comparison of noise for the balanced detector when cooled and uncooled . . .	177
91	A second 660 nm laser for axial feedback in the over-damping experiment . .	179
92	Additional axial feedback path for RC over-damping experiment	180
93	Analog RC circuit setup for axial feedback in over-damping experiment . . .	180
94	Additional axial detector path for RLC over-damping experiment	181
95	Analog RLC circuit setup for axial feedback in over-damping experiment . . .	181
96	Example setup of the ‘two iris’ alignment method	184
97	Setup for testing the resolution and magnification of an objective.	187
98	Transmission images of the USAF 1951 resolution target.	188
99	Alternate setup for illumination with an LED (reflection illumination)	188
100	Image of 660 nm trap shadow detection to align the chamber	190
101	Image of the trap shadow at the first image plane	190
102	Plots for determining optimal location of QPD focusing lens.	192
103	Images of the table top enclosure.	194
104	Dimensions of top and bottom pole pieces, machined from Hiperco 50A . . .	196
105	Nominal dimensions (in μm) for lapping of pole piece tips and trap alignment.	197
106	Comparison of top and bottom pole pieces as machined and after lapping. . .	198
107	Pole piece assembly of the trap used for example cooling results	199
108	Images of trap assembly	200
109	A side view of a finished trap assembly	202
110	Hiperco 50A data sheet (provided by Ed Fagan, Inc)	203
111	SmCo magnet data sheet	204
112	Example of loading horn proximity to trap.	210

113 Comparison of trap location when chamber is cool and when baked.	212
--	-----

PREFACE

LIST OF ABBREVIATIONS, ACRONYMS, AND OTHER DEFINITIONS

ADC: Analog to Digital Converter

COM: Center of Mass

DOF: Degree of Freedom (corresponding to 3-dimensions of particle motion)

EOM: Electro-optic Modulator

FFT: Fast Fourier Transform - Computer implementation of discrete Fourier Transform

FWHM: Full Width at Half Maximum

galvo: A mirror mounted on a current-controlled positioning stage

g.u.: Galvo Unit - An arbitrary unit corresponding to a discrete voltage change

HV: High Vacuum - Corresponds to pressures P , $10^{-9} \leq P \leq 10^{-6}$ Torr

lp/mm: Line Pair per millimeter - Refers to the size scale of a microscope resolution target

OBJ: Objective

OL: Objective Lens

PGA: Programmable Gain Amplifier

PSD: Power Spectral Density - See Section [1.4.1.1](#)

PX: Pixel - Refers to the physical sensing unit on a camera

QF: Quickflange

QPD: Quadrant Photodiode Detector - Main detector utilized for real-time monitoring

SNR: Signal to Noise Ratio

SQL: Standard Quantum Limit - Refers to the limitation of measurement and momentum uncertainties, given by the uncertainty principle

TEC: Thermoelectric Cooler

UHV: Ultra-High Vacuum - Corresponds to pressures $\leq 10^{-9}$ Torr

numpy: Open source computer package for Python language containing numerical methods

trackpy: Open source computer package containing methods for feature finding in images

Arduino: Open source microcontroller with on-board analog inputs and outputs

MATHEMATICAL SYMBOL DEFINITIONS

Many definitions come from two often referenced equations, Eq. 1.13:

$$\ddot{x}_i + \Gamma \dot{x}_i + \omega_i^2 x_i = F'_i(t)$$

and Eq. 1.29:

$$PSD_{x_i}(f) = \frac{A}{(f_i^2 - f^2)^2 + \gamma^2 f^2}$$

For the entire document, any subscript $i = x, y, z$ corresponds to the specified axes only.

The following definitions are consistent throughout the document:

m : Mass

ω_i : Natural angular frequency

f_i : $\omega_i/2\pi$

Γ_i : Damping coefficient, defined as a rate

γ_i : $\Gamma_i/2\pi$ - This is the FWHM of the curve in Eq. 1.29

T_{eff} : Effective temperature, defined in Eq. 1.19.

T_i : The effective temperature in a specified degree of freedom

$\hat{N}_i = \hat{a}_i^\dagger \hat{a}_i$: The number operator for a quantum harmonic oscillator in the number basis

\bar{n} : Average number of energy quanta, defined in Eq. 1.56

x_i : The displacement from equilibrium

ρ : Mass density

ACKNOWLEDGMENT

I would like to say a special thank you to my advisors, Dr. Brian D’Urso and Professor Choyke, for their guidance and support.

I especially thank Dr. Brian D’Urso, Dr. Hanna Salman, Dr. Vladimir Savinov, and Leyla Hirschfield, whose support and advice in making difficult decisions was crucial to my success.

Finally, a heartfelt thank you to my wife and best friend Maureen for being incredibly supportive and understanding throughout my time as a graduate student.

1.0 INTRODUCTION

1.1 DISSERTATION OUTLINE

This dissertation is organized into four chapters.

Chapters 1 through 3 represent the main topics and work related to this dissertation. Chapter 1 is intended to introduce the studied system and provide a background and motivation for the work contained herein. A description of the magneto-gravitational trap is provided, and the important mathematical definitions for analyzing the system and results are outlined. Chapter 2 provides the justification and explanation of the experimental system's design, including detailed procedures of all techniques that were developed for this dissertation. Chapter 3 provides the main results of this dissertation, along with discussion.

Chapter 4 provides several interesting techniques that were developed during the course of study. While they lay somewhat outside the main goal of this dissertation, the information provided may be useful for future progress.

Finally, the appendices provide more detail into system design parameters and the full set of result plots corresponding to the results listed in Section [3.4](#).

1.2 BACKGROUND OF MECHANICAL OSCILLATORS

1.2.1 Motivation

Nano-mechanical oscillators, or more generally mechanical oscillators, belong to a subset of Physics generally considered as nano-mechanics. The prefix *nano* is perhaps a bit too

specific, as the systems range from the nanometer to micrometer scale. The goal of these systems is to create a mechanical system of considerable size, one that would typically be considered classical, and control it well enough to probe its quantum mechanical properties. The research aims to explore the fundamental nature of quantum mechanics, for instance answering the question of how large an object can be while still behaving quantum mechanically.

1.2.2 Cold Damping

According to the correspondence principle, the behavior of a quantum mechanical system must lend itself to a classical description in the limit of large energies [1]. As such, in order to observe quantum mechanical effects on an oscillator system, the energy of the oscillator should be on the order of its ground state energy. For any mechanical oscillator system, the thermal environment of the system will play a role in its dynamics. Any system in contact with a thermal environment and left to evolve will eventually come into thermal equilibrium with the environment, which will likely be at an energy much larger than the ground state energy (of course, this depends on the environmental temperature and the magnitude of the ground state energy itself).

In order to reach energy scales near the ground state energy, the mechanical motion of the system is removed via a cold damping mechanism. In our case, we remove energy by a process known as feedback cooling. Essentially, a particle’s motion is monitored, and that information is fed back to the particle in order to remove energy from its mechanical motion.

1.2.3 Clamped Systems

The field of studying mechanical oscillators as probes into mesoscale quantum mechanics began with systems of “clamped” mechanical oscillators, meaning mechanical systems that were physically attached to their environment (for example, a micron-scale capacitive drum fabricated on a sapphire substrate [2]). By various mechanisms, several of these types of mechanical systems were cooled to their quantum mechanical ground state ([2, 3, 4]). Systems such as that in [2] can actually be cooled near their ground state simply by physically

cooling the substrate to which they are attached.

Since these systems are in physical contact with their environment, complications arise because of the undesirable traits of that physical connection: namely, the physical contact introduces inescapable decoherence and damping mechanisms to the motions. But, to be clear, the clamped systems were not a failure - in addition to reaching the ground state, they also enabled interesting experiments, including observation of forces from interactions with squeezed light [5], which is a strictly quantum mechanical phenomenon.

1.2.4 Optically Trapped Particles in Vacuum

Systems consisting of an optically trapped dielectric particle in a vacuum environment [6, 7, 8, 9, 10] emerged to combat the limitations of these clamped systems. These systems place a dielectric nano-sphere or microsphere at the focus of a high intensity laser beam, which levitates the particle and generates a 3-dimensional restoring force; the surrounding air molecules are then removed to limit interaction with the environment. Since there is no physical contact with any substrates, these particles can theoretically achieve extreme isolation from their physical surroundings, limited only by the background pressure of the air molecules with which the particle collides.

While great progress has been achieved in cooling these systems [10], some complications are created by the nature of the trapping mechanism. In order to optically trap a particle, a large optical intensity must be used to create a trapping force that is larger than that of the scattering force created by the same laser. It has been suggested that these high intensities can result in stability problems when reaching intermediate or high vacuum [11, 12, 13, 14]. Some groups have begun utilizing charged particles with hybrid electro-optical traps or Paul traps [15, 16, 17], but these require the use of oscillating electric fields which introduce additional challenges. In addition, due to small particle sizes and other experimental choices, the collection efficiency of these systems can be quite small, which ultimately limits their ability to reach the ground state.

Because of the excellent isolation and control of these ‘levitated particle in a vacuum’ systems, they make excellent candidates for ultra-weak force sensors [11, 12, 18, 19] and

similarly searches for new Physics [20, 21, 22].

1.3 OUR SYSTEM - MAGNETICALLY TRAPPED PARTICLES IN ULTRA-HIGH VACUUM

In order to address some of the complications of the optically trapped particle systems, we elected to create a different type of trap relying on gravity and the weak diamagnetism exhibited by many materials.

1.3.1 A Magneto-Gravitational Trap

For our system, we utilize an entirely passive trapping mechanism created by the combination of diamagnetism and gravity. An in depth analysis of the design and operating principles of the trap were previously completed [23, 24]. Since this work is not completed as part of this dissertation, a summary of the key concepts of the trapping are discussed.

Consider the potential energy of a particle with some magnetic moment $\vec{\mu}$ in an external magnetic field \vec{B} :

$$U = -\vec{\mu} \cdot \vec{B} \quad (1.1)$$

Following from Eq. 1.1 we consider a sphere of homogeneous magnetic material, without a permanent moment but with a moment induced by the field \vec{B} , in the gravitational field near the Earth's surface [25]:

$$U = -\frac{\chi B^2 V}{2\mu_0} + mgy \quad (1.2)$$

$$\frac{U}{V} = -\frac{\chi B^2}{2\mu_0} + \rho gy \quad (1.3)$$

where χ is the (volume) magnetic susceptibility of the material, V is the sphere's volume, m is the sphere's mass, μ_0 is the vacuum permeability, ρ is the material density, g is the acceleration due to gravity near the Earth's surface, and y is the vertical height. For diamagnetic

particles $\chi < 0$, meaning the magnetic potential energy term is minimized at a magnetic field minimum.

In order to use the potential in Eq. 1.2 to trap and levitate a particle, the magnetic force $\vec{F}_B = -\vec{\nabla}U$ must be strong enough to balance gravity. Since most common diamagnetic materials have very small values of $|\chi|$ ($\sim 1 \times 10^{-5}$), either the magnetic field or its gradient must be quite large to generate an adequate interaction strength. We choose to create a strong magnetic field gradient by making the size scale of the magnetic trap small ($\sim 100 \mu\text{m}$). To create the trap, we sandwich SmCo permanent magnets between ferromagnetic pole pieces machined from highly magnetic material (Hiperco 50A), orient the poles in a quadrupole configuration to create a field minimum, and shape the tip of each piece into sharp point.

An illustration of our magnetic trap is shown in Fig 1. In Fig. 1 (a), we show the SmCo magnets (grey) sandwiched between ferromagnetic pole pieces. The magnet orientations are chosen to create a quadrupole configuration, with the alternating north and south poles indicated by the red and blue pieces, respectively. In Fig. 1 (b) we show a closeup of the trapping region and a definition of our coordinate axes. For the remainder of this dissertation, we will refer to the axial direction as z , which is along the long axis of the trap; the vertical direction is y ; and the transverse direction x is perpendicular to each.

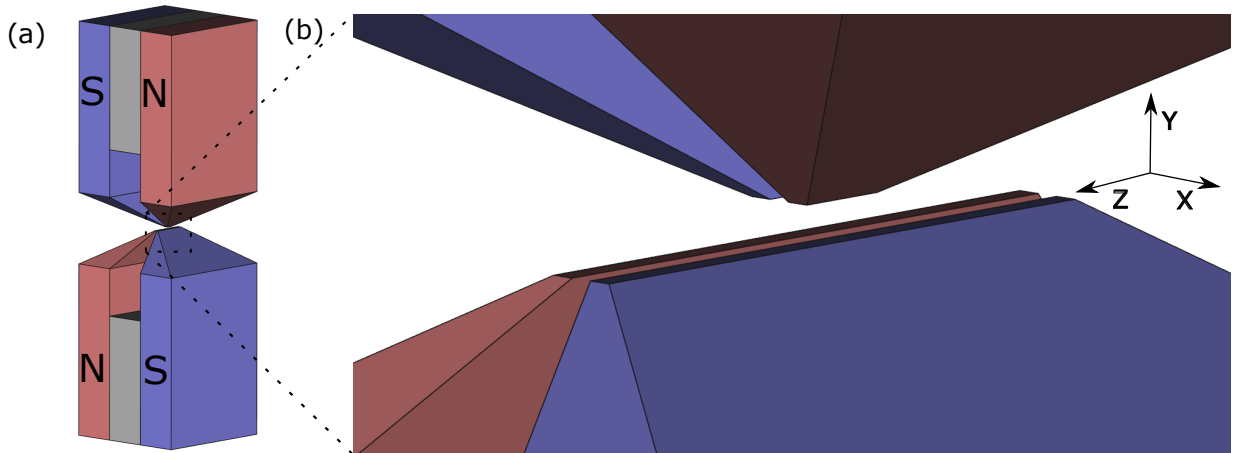


Figure 1: Illustration of (a) the quadrupole configuration of the pole pieces and (b) the trapping region of the magneto-gravitational trap with defined axes.

When viewing from the side (looking straight down the z axis), it is easy to see that a magnetic quadrupole field in the $x - y$ plane will be generated at the trap center along the axis of symmetry (z). As $|B| = 0$ at the center of the quadrupole, we have created a field minimum and thus a trapping force in these two directions. This quadrupole design can be seen graphically in Fig. 2 (a).

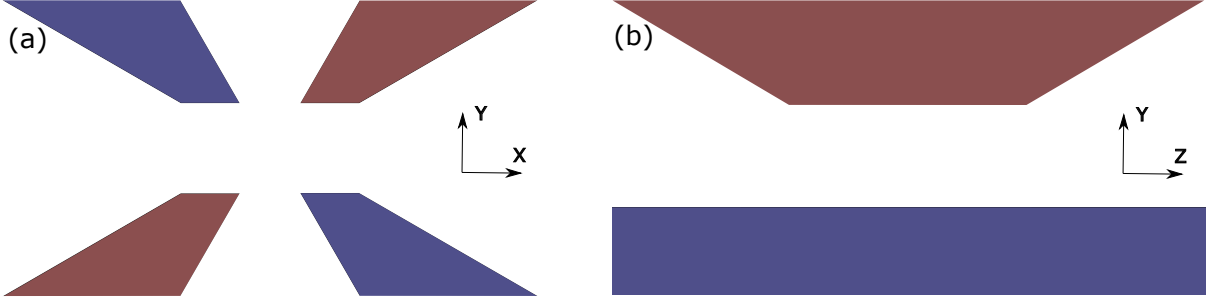


Figure 2: Illustrations of the trap when viewing down the axis of symmetry z (a) and a view from the front (along x axis) in (b), which shows the sharper cut of the top pole pieces.

To break the quadrupole symmetry along the z -axis, the top pole pieces are machined to a sharp point. This creates a gradual increase in the height of the vertical midpoint between the top and bottom as we move axially (along z) outward from the center of the trap, with the zero-field region of the magnetic field following. As such, we effectively curve the quadrupole field upwards in the $y - z$ plane. The asymmetry in the top and bottom pole piece lengths along the symmetry axis is shown graphically in Fig. 2 (b).

To provide a quantitative description of the magnetic field, we note that, in a region free from magnetic sources, we can solve Laplace's equation for the magnetic scalar potential [26]:

$$\nabla^2 \Phi_M = 0 \quad (1.4)$$

with the magnetic field then:

$$\vec{B} = -\nabla \Phi_M \quad (1.5)$$

As such, a natural choice for an expansion of the magnetic potential is the spherical harmonics:

$$\Phi_M(r, \theta, \phi) = \sum_{l=0}^{\infty} \sum_{m=-l}^l [A_{lm} r^l + B_{lm} r^{-(l+1)}] Y_l^m(\theta, \phi) \quad (1.6)$$

Based on symmetry arguments [23, 27], we choose to utilize three non-zero, real spherical harmonics (instead of the complex basis in Eq. 1.6) for the expansion:

$$Y_{2,-2}(\theta, \phi) = i\sqrt{\frac{1}{2}} (Y_2^{-2}(\theta, \phi) - Y_2^2(\theta, \phi)) \quad (1.7)$$

$$Y_{3,1}(\theta, \phi) = \sqrt{\frac{1}{2}} (Y_3^{-1}(\theta, \phi) - Y_3^1(\theta, \phi)) \quad (1.8)$$

$$Y_{4,-4}(\theta, \phi) = i\sqrt{\frac{1}{2}} (Y_4^{-4}(\theta, \phi) - Y_4^4(\theta, \phi)) \quad (1.9)$$

We solve for the constants A_{lm} (with $B_{lm} = 0$ to keep the field finite at $r = 0$) by numerically fitting experimental data on the trapping strength in each direction [27]. Plots of the magnetic field strength, generated for the specific trap data obtained in Section 3.2, are displayed in Fig. 3. The quadrupole nature of the field is visibly evident in Fig. 3 (a), where the strength of the magnetic field increases linearly in each direction. The gentle vertical curvature of the zero field region as $|z|$ increases is evident in Fig. 3 (b).

Considering the magnetic field alone, we still have only created confinement in two degrees of freedom: the curvature of the zero field region simply confines the particle in a curved cylindrical shape (like a macaroni noodle), with the particle completely free along the symmetry axis of the noodle (z). However, when we orient the curvature in the vertical

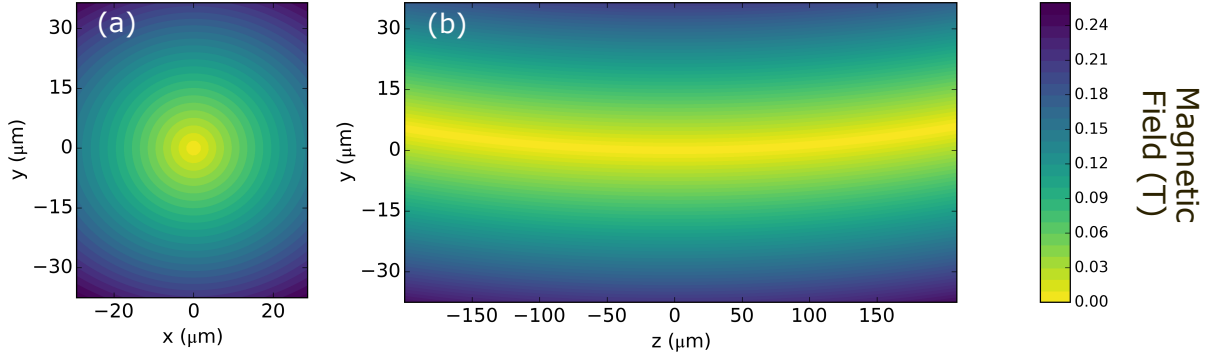


Figure 3: Plot of the magnetic field strength $|B|$ for (a) a slice in the $x - y$ plane at $z = 0$ and (b) a slice in the $y - z$ plane at $x = 0$.

direction, the gravitational effect plays a key role in creating a trapping force in the final direction (z).

This important aspect of the trapping mechanism is demonstrated by plotting the potential given by Eq. 1.2. In Fig. 4 (a) and (b), we plot slices of the potential corresponding to the same slices shown in Fig. 3. In the case of the full potential U/m , the plots in Fig. 4 (a) and (b) display a potential minimum and gradient in all three directions. In addition, we see that the symmetry of the quadrupole in (a) has been broken, as gravity has biased the equilibrium position to $y < 0$.

In contrast, if we plot Eq. 1.2 *without* the gravitational potential energy term ($U/m - gy$) as shown in Fig. 4 (c) and (d), we find a minimum and gradient only in the transverse (x) and vertical (y) directions. Fig. 4 (d) then shows equipotential lines along the axis of the curved quadrupole, with no gradient to keep the particle trapped in the z direction. This illustrates the critical role that gravity plays, making this a true magneto-gravitational trap.

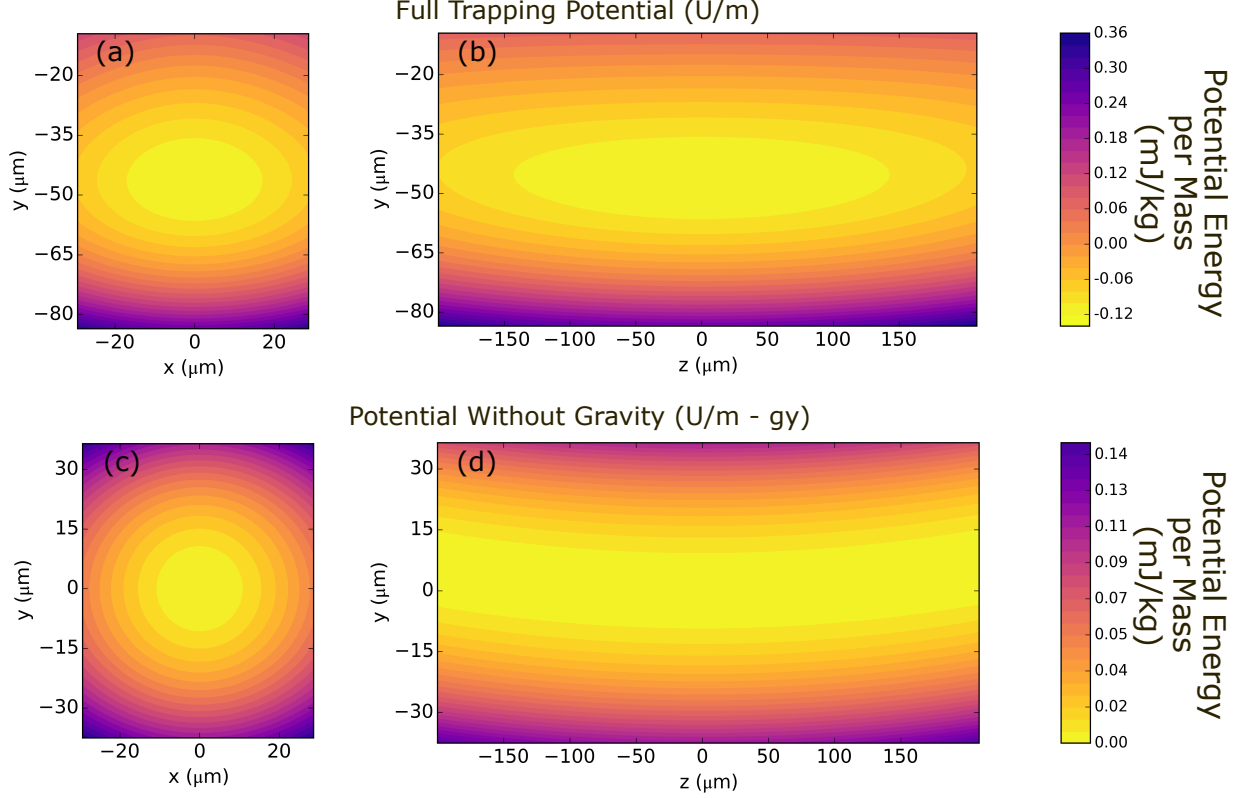


Figure 4: Plots of the full potential in (a),(b) showing 3-dimensional confinement. Plots of the magnetic potential only in (c),(d) showing confinement only in two degrees of freedom.

1.3.2 Experiment Overview - Feedback Cooling of Mechanical Motion

We now provide a high level overview of the experimental machinery as a reference point for the remainder of the discussion.

As discussed, we place a diamagnetic particle in the magneto-gravitational trap outlined in Section 1.3.1. Due to unavoidable thermal excitation, the particle has a non-zero average amplitude of motion. In the simplest of terms, our goal is to monitor the motion of the trapped particle and use that information to slow the particle down, until the laws of quantum mechanics prevent us from doing so further. This process of damping the particle's motion is referred to as ‘feedback cooling’ of its mechanical motion, which is not to be confused with

cooling the internal temperature of the particle.

A simplified version of the experiment is provided in Fig. 5. We illuminate a trapped particle with diode laser light (blue) and collect the scattered light with an objective. We image the particle onto a quadrant photodiode detector (QPD) which generates an electrical signal proportional to the particle's displacement (see Section 2.3.2.4). We then generate a velocity signal from the displacement voltage and use it to amplitude modulate a second diode laser (red), which provides a damping force to the particle via radiation pressure.

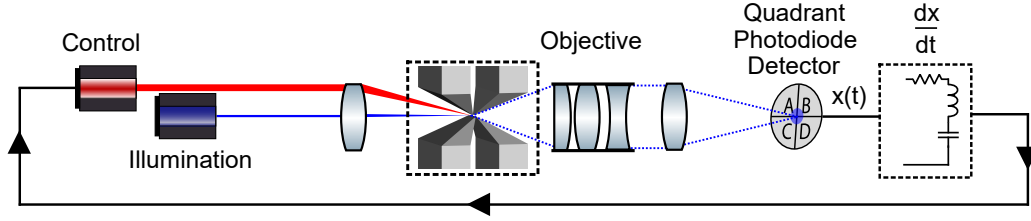


Figure 5: A simplified diagram of the feedback cooling experiment. A trapped particle is illuminated with laser light (830 nm, blue in the figure) and its motion monitored by a photodiode detector. Its motion is used to generate a damping force (via radiation pressure modulation) with a second control laser (660 nm, red).

Fig. 6 and Fig. 7 provide an illustrative description of the feedback damping mechanism in a single direction. As shown in Fig. 6, the radiation pressure force generated by the control laser shifts the particle's equilibrium position in the trap in the direction of the light's propagation.

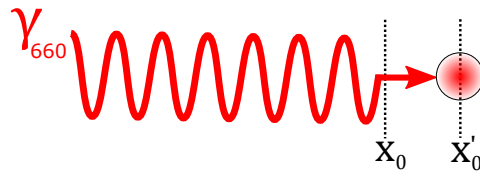


Figure 6: The radiation pressure force generated by the non-zero average intensity of the control laser light shifts the particle's equilibrium position x_0 to a new position x'_0 .

The damping mechanism is described graphically in Fig. 7 by considering two cases when

the particle's position is displaced to one side of the equilibrium position, x'_0 . The damping force is intuitive in the case of the particle's velocity being anti-parallel with the control laser light's propagation direction, as shown in Fig. 7 (a). The intensity of the light is increased proportionally from its average value, increasing the radiation pressure force on the particle and thus slowing it down (damping its motion). Although a bit more subtle, a similar mechanism is at work when the particle's velocity is parallel with the control laser light's propagation, as shown in Fig. 7 (b), where the intensity of the light is decreased proportionally to the velocity. In this case, it is easiest to describe the damping force by an increase in the restoring force caused by the change in the equilibrium position, x'_0 to x''_0 .

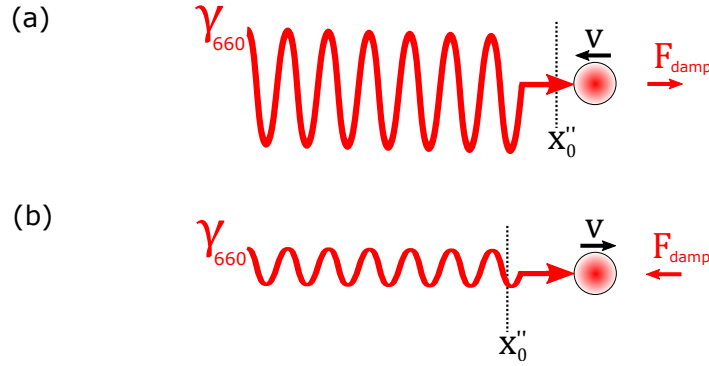


Figure 7: (a) The control laser intensity is increased as the particle moves against its direction of propagation, slowing the particle down. (b) The control laser intensity is decreased as the particle moves in the same direction as its propagation, slowing the particle down via an increase in the restoring force.

This single-sided approach to control is utilized for all experiments in this dissertation. As discussed in Section 3.6.1.1 and again in Section 4.3, it may be better to utilize a symmetric (double-sided) approach for better control in the future and to reduce complications arising from excess laser noise.

Ideally, we experimentally control all physical interactions with the particle. However, since collisions with air molecules disrupt the cooling (by adding kinetic energy to the particle), we place the entire trap and particle into a vacuum chamber capable of reaching Ultra-High Vacuum (UHV) pressures ($P \sim 10^{-10}$ Torr or better). In the ideal case, only

the magneto-gravitational trapping interaction and the fully controlled radiation interaction with the laser light remain.

A mathematical description of the system follows in Section 1.4, in which we treat the trapped particle as a three-dimensional harmonic oscillator.

1.3.3 Long Term Goals

We can segment the goals of the project into two distinct areas - experiments in the quantum mechanical realm (which is the intent of this dissertation), and classical gravitational measurements.

1.3.3.1 Quantum Mechanics The first goal, which is the goal that this dissertation is working towards, is to demonstrate feedback cooling at or near the ground state energy level of the trapped particle (a harmonic oscillator). In addition to representing a significant achievement in its own right, a ground state cooling demonstration would indicate that we have sufficient control over the system to perform more complex quantum mechanical experiments.

Once we reach energy levels near the quantum regime, we aim to generate non-classical states of the harmonic oscillator. Again, this would represent a significant achievement in its own right. The non-classical state we have in mind is a squeezed state of the harmonic oscillator; measurement of a squeezed quadrature (Δx in our case) would provide incontrovertible evidence that we can manipulate the system with quantum mechanical precision. We can generate said squeezed state by non-adiabatic shifts to the particle's trapping strength via our control laser, as suggested in [9], or by a parametric drive to the particle at twice the oscillator natural frequency [28].

Finally, the long term goal of the system is to utilize the non-classical states of extended objects to test and place limits on theories of the effects of gravitational interactions on quantum states. For instance, it has been suggested that tests on Gaussian states of the harmonic oscillator (like a squeezed state) yield different results based on a quantum mechanical formulation of gravitational interaction [29] (interestingly, in another publication

[30] it is suggested that the same formulation could also be tested without the use of squeezing or state tomography). Other suggested experiments concern measuring the decoherence of spatially-separated quantum superposition states [31, 32, 33]. With the precise control over external interactions allowed by our system, we may be able to place limits on theories of gravitational decoherence.

1.3.3.2 Classical Mechanics - Measurement of G As mentioned, levitated oscillators in vacuum are excellent candidates for weak-force sensing. Our system is particularly well suited for a classical measurement of the Newtonian gravitational constant, G . In short, because our system has the unique ability to achieve very low oscillation frequencies (~ 10 mHz) with very little damping, we can utilize a large trapped particle to make a precision measurement of G . A precision measurement of G would be of great significance, as current measurements of the constant disagree well beyond their quoted experimental uncertainties [34].

1.3.4 Reported Progress

Our goal is to cool the motion of our mechanical oscillator near its quantum ground state. In terms of energy, this is a factor of $k_B T_{295} / \hbar \omega_i \approx 10^{11}$ below the ambient ($T \sim 295$ K) thermal equilibrium energy. Previous results achieved for effective temperatures of a diamond nanocrystal in a magneto-gravitational trap quoted cooling factors of $\sim (5 \times 10^2, 1 \times 10^2)$ below ambient for two degrees of freedom [24]. Results reported in this dissertation achieve cooling factors of $\sim (1 \times 10^6, 3 \times 10^5)$ below ambient for the same degrees of freedom (with a silica microsphere), which is a factor of at least 10^3 improvement.

This leaves a remaining factor of $\sim 10^6$ cooling to reach the ground state.

1.4 MATHEMATICAL DESCRIPTION

1.4.1 Damped, Thermally Driven Harmonic Oscillator

For most of the analysis in this document, the trapped particle will be treated as a mass in a 3-dimensional harmonic potential. The classical Hamiltonian for a particle in a harmonic potential and isolated from an external environment is given as:

$$H = \sum_i \frac{p_i^2}{2m} + \frac{1}{2} k x_i^2 \quad (1.10)$$

where the subscript i denotes the degree of freedom, p the particle's momentum, m the particle's mass, k the spring constant of the potential, and x the particle's displacement from equilibrium.

We can also write the differential equation governing the motion of a particle in the three dimensional well by way of Newton's 2nd law of motion, $\sum_i F_i = m \sum_i a_i$. Assuming a drag force that is proportional to the particle's velocity ($F_{drag} = -c\dot{x}_i$), and accounting for the possibility of an external driving force F , we write the equation:

$$\sum_i m\ddot{x}_i = \sum_i -c\dot{x}_i - k_i x_i + F_i(t) \quad (1.11)$$

By defining the natural angular frequency:

$$\omega_i^2 \equiv k_i/m \quad (1.12)$$

and rearranging, and focusing on only one degree of freedom, we arrive at:

$$\ddot{x}_i + \Gamma \dot{x}_i + \omega_i^2 x_i = F'_i(t) \quad (1.13)$$

where we have introduced the damping constant Γ and F'_i .

The homogeneous solution ($F'_i(t) = 0$) in the under-damped regime ($\Gamma^2 - 4\omega_i^2 < 0$) is easily solvable, and is given by the function:

$$x_i(t) = X e^{-\frac{\Gamma}{2}t} \cos(\omega' t + \phi) \quad (1.14)$$

with $\omega' = \sqrt{4\omega_i^2 - \Gamma^2}/2$, and X and ϕ given by initial conditions.

It can also be useful to solve this equation in the frequency domain, where the differential equation transforms to an algebraic equation. Recall the symmetric definition of the Fourier Transform and its inverse:

$$\tilde{f}(\omega) = \frac{1}{\sqrt{2\pi}} \int_{-\infty}^{\infty} f(t) e^{-i\omega t} dt \quad (1.15a)$$

$$f(t) = \frac{1}{\sqrt{2\pi}} \int_{-\infty}^{\infty} \tilde{f}(\omega) e^{i\omega t} d\omega \quad (1.15b)$$

and note that the Fourier Transform (denoted as \mathcal{F}) of the time derivative of a function is given by the convenient equation[35]:

$$\mathcal{F}[f^{(n)}(t)] = (i\omega)^n \tilde{f}(\omega) \quad (1.16)$$

Fourier transforming Eq. 1.13 yields an algebraic expression for $\tilde{x}_i(\omega)$:

$$\tilde{x}_i(\omega) = \frac{\tilde{F}'_i(\omega)}{(\omega_i^2 - \omega^2) + i\Gamma\omega} \quad (1.17)$$

As a result, if the driving force $F_i(t)$ is known, the motion of the particle can be found by taking the inverse Fourier Transform \mathcal{F}^{-1} (Eq. 1.15(b)) of $\tilde{x}_i(\omega)$, as given by Eq. 1.17.

As we continue, it is important to discuss the reasons behind solving the system analytically by introducing the measurement metric $\langle x_i^2 \rangle$, the concept of effective temperature (T_{eff}), and the Power Spectral Density (PSD).

1.4.1.1 $\langle x^2 \rangle$, Effective Temperature, and Power Spectral Density As the particle motion is cooled via feedback damping, we need a way to report the amount of cooling that we have achieved. The most obvious way of doing this is by measuring the average magnitude of the particle's displacement from equilibrium, $\langle |x_i| \rangle$. Specifically, we choose to measure the average value of its displacement squared, $\langle x_i^2 \rangle$. But, simply reporting $\langle x_i^2 \rangle$ provides no information as to how well the particle has been cooled; alternatively stated, comparing the average displacement-squared measurements of systems with different mass and/or natural

frequencies becomes meaningless without this extra information. To account for this, it is common to introduce the concept of effective temperature, T_{eff} .

By the equipartition theorem, we know that, for a particle in thermal equilibrium with its environment, the average amount of energy in each quadratic degree of freedom in the Hamiltonian is $\langle E \rangle = \frac{1}{2}k_B T$, where T is the temperature of the environment. For the harmonic oscillator Hamiltonian Eq. 1.10, this leads us to a simple expression for the average potential energy of a single degree of freedom (DOF):

$$\langle V \rangle = \frac{1}{2}k_B T = \frac{1}{2}m\omega_i^2 \langle x_i^2 \rangle \quad (1.18)$$

where k_B is Boltzmann's constant, and we have replaced the spring constant k_i with $m\omega_i^2$ via Eq. 1.12.

Solving for T in Eq. 1.18 allows us to assign an effective temperature to an $\langle x_i^2 \rangle$ measurement, via the proportionality constant of $m\omega_i^2/k_B$:

$$T_{eff} = \frac{m\omega_i^2}{k_B} \langle x_i^2 \rangle \quad (1.19)$$

Calculating $\langle x_i^2 \rangle$ is trivial, given any sampling of position data over time. However, it is also convenient to calculate $\langle x_i^2 \rangle$ in the frequency domain, which provides several advantages over utilizing the time domain data.

We make use of Parseval's Theorem to relate the frequency representation to the time representation[35]:

$$\int_{-\infty}^{\infty} |f(t)|^2 dt = \int_{-\infty}^{\infty} |\tilde{f}(\omega)|^2 d\omega \quad (1.20)$$

Following from Eq. 1.17, we have:

$$|\tilde{x}_i(\omega)|^2 = \frac{|\tilde{F}'_i(\omega)|^2}{(\omega_i^2 - \omega^2)^2 + \Gamma^2 \omega^2} \quad (1.21)$$

Next, we analyze the random driving force per unit mass, $F'_i(t)$, in Eq. 1.13. In this case, the random force arises from any of the fluctuation-dissipation mechanisms in the system (for example, in the ideal case of our magnetically trapped particle in vacuum, the only uncontrolled interaction of the particle with its environment would be that of collisions with

residual air molecules in the chamber or thermal radiation). We assert that such a force is a wide-sense stationary process [36], defined by:

1. The mean value of the force is independent of time, i.e. $\langle F'_i(t) \rangle = \mu$.
2. The autocorrelation function is a function in the delay time τ ,
i.e. $\langle F'_i(t)F'_i(t + \tau) \rangle = F''(\tau)$.

Specifically, thermal noise is a zero-mean process whose autocorrelation function is a delta function in τ [37]:

$$\langle F'_i(t) \rangle = 0 \quad (1.22)$$

$$\langle F'_i(t)F'_i(t + \tau) \rangle = \xi\delta(\tau) \quad (1.23)$$

Since the drive force is a random process, we consider the ensemble average $E[F'_i(t)]$ over some measurement period, T_s . We define $F'_{i,s}(t)$ as a single sampling of $F'_i(t)$:

$$F'_{i,s}(t) = \begin{cases} F'_{i,s}(t) & -T_s/2 \leq t \leq T_s/2 \\ 0 & \text{else} \end{cases} \quad (1.24)$$

Then

$$\begin{aligned} E[|\tilde{F}'_i(\omega)|^2]_s &= \frac{1}{2\pi} \int_{-T_s/2}^{T_s/2} \int_{-T_s/2}^{T_s/2} \langle F'_i(t')F'_i(t) \rangle e^{-i\omega t'} e^{i\omega t} dt' dt \\ &= \frac{1}{2\pi} \int_{-T_s/2}^{T_s/2} \int_{-T_s/2-t'}^{T_s/2-t'} \langle F'_i(t')F'_i(t' + \tau) \rangle e^{i\omega\tau} dt' d\tau \\ &= \frac{1}{2\pi} \int_{-T_s/2}^{T_s/2} \int_{-T_s/2-t'}^{T_s/2-t'} \xi\delta(\tau) e^{i\omega\tau} dt' d\tau \\ &= \frac{1}{2\pi} \xi \int_{-T_s/2}^{T_s/2} dt' \\ &= \frac{1}{2\pi} \xi T_s \end{aligned} \quad (1.25)$$

Thus, following from Eq. 1.21:

$$|\tilde{x}_i(\omega)|^2_s = \frac{1}{2\pi} \frac{\xi T_s}{(\omega_i^2 - \omega^2)^2 + \Gamma^2 \omega^2} \quad (1.26)$$

Finally, we calculate $\langle x_i^2(t) \rangle$, utilizing Eq. 1.20 and Eq. 1.26:

$$\begin{aligned}\langle x_i^2(t) \rangle_s &= \frac{1}{T_s} \int_{-T_s/2}^{T_s/2} x_i(t)^2 dt \\ &= \frac{1}{T_s} \int_{-\infty}^{\infty} |\tilde{x}_i(\omega)|_s^2 d\omega \\ &= \int_{-\infty}^{\infty} \frac{1}{2\pi} \frac{\xi}{(\omega_i^2 - \omega^2)^2 + \Gamma^2 \omega^2} d\omega\end{aligned}\tag{1.27}$$

The result of Eq. 1.27 is typically referred to as the Power Spectral Density (PSD) of the signal. (Here, in the terminology used in the literature, my definition refers to the two-sided PSD.) We note that this analysis arrives at the same result as invoking the Wiener-Khinchine theorem [37], which states that the PSD and autocorrelation function are Fourier Transform pairs.

Alternatively, we can write the function in terms of f instead of ω , noting that $d\omega = 2\pi df$:

$$\langle x_i^2(t) \rangle_s = \int_{-\infty}^{\infty} \frac{1}{(2\pi)^4} \frac{\xi}{(f_i^2 - f^2)^2 + \gamma^2 f^2} df\tag{1.28}$$

Or, in the case where we fit the parameters, we can absorb the factors of 2π into the constant A :

$$PSD_{x_i}(f) = \frac{A}{(f_i^2 - f^2)^2 + \gamma^2 f^2}\tag{1.29}$$

Eq. 1.29 is provided in an incredibly useful form, as a fit to the function makes it easy to determine both the center frequency, $f_i = \omega_i/2\pi$ and width (FWHM) of the curve $\gamma = \Gamma/2\pi$, making it easy to retrieve ω_i and Γ of Eq. 1.13. In any case, the integral of the PSD has a closed form, as derived in [38]:

$$\int_{-\infty}^{\infty} \frac{1}{(a^2 - x^2)^2 + b^2 x^2} dx = \frac{\pi}{ba^2}\tag{1.30}$$

and in the case of Eq. 1.29:

$$\int_{-\infty}^{\infty} \frac{A}{(f_i^2 - f^2)^2 + \gamma^2 f^2} = A \frac{\pi}{\gamma f_i^2}\tag{1.31}$$

In the case of thermal equilibrium, the result of Eq. 1.31 can be combined with the average thermal energy presented in Eq. 1.18 to place a normalization constraint on the strength constant A :

$$A = \frac{k_B T \Gamma_A}{8\pi^4 m} \quad (1.32)$$

where we have labeled Γ as Γ_A to denote the relation of the two at thermal equilibrium.

1.4.1.2 Discrete Fourier Transform Since all real signals are both finite in time and sampled with discrete time steps, the discrete version of the Fourier Transform is used when analyzing data. Instead of a continuous function of time $x_i(t)$ over a sample period of T_s , we now have a discrete sampling:

$$x_i[n] = x_i(t = n\Delta t), \quad n = 0..N - 1 \quad (1.33)$$

where N is the number of samples, n represents the index of each sample spaced evenly by Δt in time, and with the relationship to the sampling period $T_s = N\Delta t$.

For this document, we utilize the Fast Fourier Transform (FFT) as defined by the numpy package ([39],[40]) in the Python programming language:

$$X[k] = \sum_{n=0}^{N-1} x_i[n] \exp(-2\pi i \frac{nk}{m}) \quad (1.34)$$

In the discrete analog of Parseval's Theorem, we have the relation:

$$\sum_{n=0}^{N-1} |x[n]|^2 = \frac{1}{N} \sum_{k=0}^{N-1} |X[k]|^2 \quad (1.35)$$

By definition:

$$\langle x_i^2 \rangle = \frac{1}{N} \sum_{n=0}^{N-1} |x_i[n]|^2 \quad (1.36)$$

Utilizing Eq. 1.35, we have:

$$\langle x_i^2 \rangle = \frac{1}{N^2} \sum_{k=0}^{N-1} |X_i[k]|^2 \quad (1.37)$$

Now, we utilize the power spectrum that we have computed ($|X_i[k]|^2$) to estimate the Power Spectral Density that we computed earlier in Eq. 1.29. To do so, we need to normalize the power spectrum to the correct units, such that integration over frequency yields the $\langle x_i^2 \rangle$ measurement we seek.

Following from Eq. 1.37, and noting that the frequency spacing $\Delta f = 1/(N\Delta t)$:

$$\begin{aligned}
\langle x_i^2 \rangle &= \frac{1}{N^2 \Delta f} \sum_{k=0}^{N-1} |X_i[k]|^2 \Delta f \\
&= \frac{\Delta t}{N} \sum_{k=0}^{N-1} |X_i[k]|^2 \Delta f \\
&= \sum_{k=0}^{N-1} \left(\frac{\Delta t}{N} |X_i[k]|^2 \right) \Delta f \\
&\approx \int_{-\infty}^{\infty} PSD_{x_i}(f) df
\end{aligned} \tag{1.38}$$

Explicitly stated, this means we estimate the power spectral density function in Eq. 1.29 via a normalized version of the discrete Fourier Transform:

$$PSD_{x_i}(f) \equiv \left(\frac{\Delta t}{N} |X_i(f)|^2 \right) \tag{1.39}$$

where f in the right hand side corresponds to the discrete points $f = k\Delta f$.

Eq. 1.38 allows us to fit the parameters $\{A, f_i, \gamma\}$ of Eq. 1.29, which in turn (utilizing Eq. 1.30) gives us an analytical form for $\langle x_i^2 \rangle$:

$$\langle x_i^2 \rangle = A \frac{\pi}{\gamma f_i^2} \tag{1.40}$$

For all cases where the FFT of the time data can be calculated, this is the method that is used to compute $\langle x_i^2 \rangle$, and subsequently T_{eff} .

1.4.1.3 Natural Damping and Feedback Damping We now follow the analysis of Section 1.4.1 to describe the mathematical consequence of providing feedback damping to the particle. As discussed, result Eq. 1.32 stresses the intimate relationship between the natural damping Γ_A , environmental temperature T , and the ‘strength’ of random fluctuations (A), which is essentially a statement of the fluctuation-dissipation theorem.

In the language of the PSD curve in Eq. 1.29, the thermal environment of the particle sets the amplitude (A) and width ($\gamma_A = \Gamma_A/2\pi$) of the resonance peak. By assuming a perfect feedback mechanism (one that adds no noise or driving, leaving A unchanged), the mathematical consequence of the feedback is to modify $\Gamma = \Gamma_A \rightarrow \Gamma = \Gamma_A + \Gamma_{fb}$. In the regime of any significant cooling, $\Gamma_{fb} \gg \Gamma_A$ and the natural damping is overwhelmed by the feedback damping, stated by modifying Eq. 1.13:

$$\ddot{x}_i + (\cancel{\Gamma_A} + \Gamma_{fb})\dot{x}_i + \omega_i^2 x_i = F'_i(t) \quad (1.41)$$

We copy the PSD result Eq. 1.40 for convenience:

$$\langle x_i^2 \rangle = A \frac{\pi}{\gamma f_i^2}$$

With the assumptions discussed, we use this result to relate temperatures to the damping rates:

$$\frac{T_A}{T_{fb}} = \frac{\langle x_i^2 \rangle_A}{\langle x_i^2 \rangle_{fb}} \leq \frac{\Gamma_{fb}}{\Gamma_A} \quad (1.42)$$

Solving for Γ_A , we can place an upper limit on the natural damping of the system:

$$\Gamma_A \leq \frac{T_{fb}}{T_A} \Gamma_{fb} \quad (1.43)$$

or, solving for T_{fb} and knowing the thermal (ambient) temperature and damping rates, we can express the cooled temperature as a ratio of damping rates:

$$T_{fb} = T_A \frac{\Gamma_A}{\Gamma_{fb}} \quad (1.44)$$

1.4.1.4 Pressure Damping (Damping From Air Molecule Collisions) The most obvious source of natural damping in the system is damping due to collisions with residual air molecules in the chamber. As the pressure in the chamber is reduced, the number of molecules and thus the number of collisions with the particle is reduced. In the regime in which the mean free path of gas molecules is larger than the particle size, the natural damping of the particle is linearly proportional to the pressure in the chamber [41]. There

is some confusion in the literature about the usage and derivation of Eq. 1.45. To avoid any possible ambiguity or confusion, the definitions that follow are specifically defined in [41] unless otherwise noted.

In [41], the drag force on a particle moving through a fluid medium is:

$$\vec{F}_{drag} = -\frac{4}{3}\pi r^2 n_g m_g \bar{c}_g \vec{v} \quad (1.45)$$

where r is the particle radius, n_g is the number density (number per unit volume) of gas molecules, m_g is the mass of a gas molecule, \bar{c}_g is the thermal speed of the gas molecules, and \vec{v} is the speed of the particle.

To avoid any mistakes in the interpretation of ‘mean speed’, we note that \bar{c}_g is defined in [41] as the mean of the magnitude of the velocity of the particles:

$$\bar{c}_g = \sqrt{\frac{8k_B T}{\pi m_g}} \quad (1.46)$$

This is explicitly defined in [41] as $\bar{c} = 2/\sqrt{\pi h}$, with h defined as $h = m/2k_B T$, where m is the sphere’s mass and T is the temperature of the gas.

Performing substitution and algebra, writing $m = (4/3)\pi r^3 \rho$ and $n_g = P/k_B T$ (which is also explicitly defined in [41]), and noting that $F_{drag}/m = \Gamma \dot{x}_i$ is the damping term in Eq. 1.13, we arrive at:

$$\Gamma(P) = \frac{P}{\rho r} \sqrt{\frac{8}{\pi} \frac{m_g}{k_B T}} \quad (1.47)$$

where we have introduced the particle’s mass density, ρ . We also note that the pressure P in this relation is in units of Pa. As an example, we calculate $\Gamma(P)$ for a common set of parameters:

- $P = 2.0 \times 10^{-10}$ Torr (with 1 Torr = 133.3 Pa).
- $m_g = 4.79 \times 10^{-26}$ kg (This is the weighted average of 78.5 % N₂ and remainder O₂).
- $m_{N_2} = 28$ AMU, $m_{O_2} = 32$ AMU, 1 AMU = 1.66×10^{-27} kg.
- $T = 295$ K.
- $\rho = 1800$ kg/m³.

- $r = 1.54 \text{ } \mu\text{m}$.

For these parameters, we estimate $\Gamma = 1.05 \times 10^{-7} \text{ s}^{-1}$.

The product of the mean free path (\bar{l}) of air molecules and pressure at room temperature (T=293 K) is [42]:

$$\begin{aligned}\bar{l}P &= 6.6 \times 10^{-3} \text{ m} \cdot \text{Pa} \\ &\approx 5 \times 10^{-5} \text{ m} \cdot \text{Torr}\end{aligned}\tag{1.48}$$

Using the radius of the largest particle trapped ($r \approx 4.0 \text{ } \mu\text{m}$) suggests the use of Eq. 1.47 is applicable at pressures $P \ll 10 \text{ Torr}$.

There are some other versions of the drag equation given in Eq. 1.45. The most common other version is provided in [43, 44] as a function of the Knudsen number K_n (which is the ratio of the mean free path of molecules to the particle radius). We note that it is explicitly stated in [43, 44] that the formula given by Eq. 1.45 follows from that given in [43, 44]. We choose to refer only to Eq. 1.45 as the parameters are more intuitive.

1.4.2 Quantum Harmonic Oscillator

In a regime where the particle's total energy in a DOF is on the order of $\hbar\omega_i$, a quantum mechanical description of the system is required. We then treat the Hamiltonian in Eq. 1.10 quantum mechanically by introducing the position and momentum operators, \hat{x}_i and \hat{p}_i , respectively:

$$\hat{H} = \sum_i \frac{\hat{p}_i^2}{2m} + \frac{1}{2}m\omega_i^2\hat{x}_i^2\tag{1.49}$$

It is common to reformulate the problem algebraically by introducing the raising and lowering operators, \hat{a}_i^\dagger and \hat{a}_i , respectively:

$$\hat{a}_i^\dagger = \sqrt{\frac{mw}{2\hbar}} \left(\hat{x}_i - \frac{i}{mw}\hat{p}_i \right)\tag{1.50}$$

$$\hat{a}_i = \sqrt{\frac{mw}{2\hbar}} \left(\hat{x}_i + \frac{i}{mw}\hat{p}_i \right)\tag{1.51}$$

Substitution into Eq. 1.49 yields the Hamiltonian:

$$H = \sum_i \hbar\omega_i \left(\hat{a}_i^\dagger \hat{a}_i + \frac{1}{2} \right) \quad (1.52)$$

The combination of operators $\hat{a}^\dagger \hat{a}$ is frequently called the number operator:

$$\hat{N}_i = \hat{a}_i^\dagger \hat{a}_i \quad (1.53)$$

By choosing to work in the so-called number state basis, we can label each eigenstate of the Hamiltonian with an integer, based on the action of \hat{N} on these states:

$$\hat{N}_i |n_i\rangle = n |n_i\rangle \quad (1.54)$$

As such, the energy spectrum of the Hamiltonian in this basis is:

$$E_{n_i} = \hbar\omega_i \left(\frac{1}{2} + n_i \right) \text{ for } n_i = \{0, 1, 2 \dots \infty\} \quad (1.55)$$

In the literature, the combination $\hbar\omega_i$ is identified as one quantum of energy. It is then common to characterize any generic state $|\Psi_i\rangle = \sum_{j=0}^{\infty} c_j |j_i\rangle$ by its average number of energy quanta \bar{n} , or:

$$\langle \Psi_i | \hat{H} | \Psi_i \rangle = \hbar\omega_i \left(\bar{n} + \frac{1}{2} \right) \quad (1.56)$$

This is introduced because, like T_{eff} in Eq. 1.19, it is a common metric for describing how well a particle has been cooled. Compared to using T_{eff} , which provides a common basis for comparing systems of different oscillators, using the metric \bar{n} gives a better idea of how close to the ground state energy level a measurement is (since all harmonic oscillators have a ground state of $\bar{n} = 0$).

Quantum mechanically, and depending on the type of state being measured, it does not strictly make sense to define an equality based on invoking the equipartition theorem of Eq. 1.18 and relating it to Eq. 1.56. However, it is still useful to define these as equivalent metrics, purely as a way of reporting results, especially in the regime of $\bar{n} \gg 1$:

$$\langle V \rangle = \frac{1}{2} k_B T = \frac{1}{2} m \omega_i^2 \langle x_i^2 \rangle = \frac{1}{2} \hbar\omega_i \left(\bar{n} + \frac{1}{2} \right) \quad (1.57)$$

From Eq. 1.57, we can assign an effective temperature for the ground state ($n_i = 0$):

$$T_{n=0} \equiv \frac{1}{2} \frac{\hbar \omega_i}{k_B} \quad (1.58)$$

Using the machinery introduced in Eq. 1.51 through Eq. 1.56, we can rigorously compute the fluctuations in x_i of the ground state:

$$\langle 0_i | \hat{x}_i^2 | 0_i \rangle = \frac{1}{2} \frac{\hbar}{m \omega_i} \quad (1.59)$$

1.5 COMPARISON WITH OPTICAL TRAPPING

Now that we have explained the experiment, math, and language of levitated oscillator systems, we make an overall comparison between our magneto-gravitational trap system and of an optical trap. While fundamentally similar, there are many experimental differences between the two. These are summarized in Table 1, with the values for optical trapping extracted from [10].

	Optical[10]	Magneto-Gravitational
Wavelength	1064 nm	830 nm & 660 nm
Incident Power	70 mW	$\sim 10 \mu\text{W}$
Scattered Power	$\sim 4 \mu\text{W}$	$\sim 10 \text{ nW}$
Collection Efficiency	.0005	~ 0.1
Cooling Method	Parametric cooling with trap laser	Feedback cooling with second laser
Particle Mass (diameter)	$1 \times 10^{-18} \text{ kg}$ (100 nm)	$3 \times 10^{-15} \text{ kg}$ (1.54 μm)
Oscillation Frequencies	100 kHz	10-100 Hz
Coldest T_{eff} Achieved	450 μK	140 μK
Corresponding \bar{n}	63	3×10^5

Table 1: Comparison of optical and magneto-gravitational trapping parameters.

This table highlights parameters in the system that are orders of magnitude different from each other. Notably, optical trapping requires the use of very large optical powers and intensities in order to levitate the particle and overcome the scattering force. The mass of the particles in these two cases is also in stark contrast. It is suggested in [45] that particles smaller than the wavelength are utilized to increase the trapping force to scattering force

ratio, but we see in [46] that micron sized particles can be trapped as well. Because of the small particle size (light scattered from small particles scatters roughly isotropically, compared to mostly forward scattering for larger particles), the collection efficiency quoted in the optical case is quite poor. Finally, and perhaps most importantly, the trapping frequencies are much higher in the optical trapping case.

The frequencies are quite important, as there are several advantages to having higher frequencies:

- The trapping frequencies would then be away from frequencies from other noise sources (like seismic vibration [46]).
- Higher trapping frequencies lead to a larger maximum cooling rate (see discussion of α in Section 3.5.1).
- Higher trapping frequencies have higher ground state energies.

However, we note that, according to the theory of the standard quantum limit presented in [23], there is no hope of reaching the ground state with the collection efficiency as quoted in [10].

We believe that the unique attributes of our system, namely the high collection efficiency coupled with very low incident illumination powers, make our system a viable approach to reaching energy levels near the quantum ground state. In addition, the low oscillation frequencies and stable, passive trapping mechanism open up experimental possibilities (such as a measurement of G) that are unique to our system, and make studying this system a promising and worthwhile investment.

2.0 EXPERIMENTAL DESIGN AND PROCEDURES

2.1 CHAPTER OUTLINE

Here, we outline the design of the experiment, and then provide the experimental procedures that are important to and new for this dissertation work. Section 2.2 provides a high level overview of the process, whilst the rest of the chapter goes into significant detail regarding all experimental setup and procedures.

2.2 EXPERIMENTAL PROCESS

Typically, the particles utilized for experiments are $1.54\text{ }\mu\text{m}$ SiO_2 particles. Particles are loaded into the trap at atmospheric pressure by vibrating them off of the tip of an ultrasonic horn (see Section F.1).

Particles are essentially always loaded with non-zero net charge. At the very least, the majority of the charge is removed by bringing a radiation source close to the particle in atmospheric pressure, as outlined in Section 2.6.2. This is important as charge can cause unwanted effects in the particle motion, such as (but not limited to) unwanted drives from electrical sources and the potential for energy loss (damping) via currents induced in the pole pieces by the moving charged particle.

Next, the particle is brought into a vacuum environment, and its mass is determined via the procedure outlined in Section 2.5.

Then, as particles usually have some residual charge after rough neutralization, the particle can be completely neutralized by the method developed in Section 2.6.3. This

method utilizes UV light to knock electrons off of the nearby (grounded) metal pole pieces and onto the particle until its net charge is zero.

The chamber is then baked overnight to temperatures of at least 125 °C, (see Section F.1.3). This is absolutely critical for removing the main source of out-gassing in the chamber (water on the chamber surfaces), which is generally the limiting factor in vacuum chamber pressure prior to baking (and, the higher pressures prior to baking are often the limiting factor in cooling as well). The size of the particle is chosen such that it remains trapped throughout the baking procedure without any feedback mechanisms. After baking and switching to a specialized pumping source, the chamber can reach Ultra-High Vacuum pressures, with pressures as low as $P \approx 1 \times 10^{-10}$ Torr regularly achieved.

After the chamber cools back down, we prepare the system for feedback cooling. The particle is illuminated by a diode laser and imaged onto a position sensitive detection device. The full optical system is discussed in Section 2.3.2.

The most common method utilized for generating the feedback signal is a digital filter running on an Arduino microcontroller, which is essentially the same as the code in [23] (Analog filters can be used (and were tested) in place of the digital filter). The filter uses the position data generated by the quadrant photodiode detector (see Section 2.3.2.4) to generate a signal proportional to the particle's velocity. This velocity signal modulates the intensity of a control laser to provide a damping force to the particle via radiation pressure, as suggested graphically in Fig. 5.

We record the position data from the quadrant photodiode detector, whose calibration is obtained on a per particle basis as described in Section 2.7.

2.3 OPTICAL AND FEEDBACK DESIGN

2.3.1 High Level Summary

This generation of the experiment was designed to utilize only optical interactions with the particle for control. As discussed in Section 2.4.1, the chamber design was developed to keep all illumination and collection optics outside of the chamber, to allow for heating or cooling of the chamber without damaging the objective lens. For illumination, an 830 nm diode laser was chosen, as the peak efficiency of the photodiodes used for detection occurs at or near that wavelength. For control of the particle, a separate 660 nm diode laser was chosen. This allows easy filtering of the control light by way of a long pass filter. In addition, the wavelength lies within the range of the anti-reflective coatings chosen for the lenses and minimizes chromatic aberration from the objective (which is designed specifically for 830 nm light), and is easily visible, thus aiding alignment.

There are at least two main detectors in the system at any time: a split photodiode detector (meaning at least two photodiodes per detector) and a high speed camera. The split photodiode detector, usually a quadrant photodiode detector (QPD), is used to acquire position measurements of the particle in real time by generating electrical signals and supplying them to the feedback mechanisms. The high speed camera is used mainly for alignment and mass calibration. A galvo mirror preceding both of the detectors is necessary for precise positioning of the particle's image on either detector.

Control of the particle is achieved by modulating the intensity of the control laser (and thus, the radiation pressure on the particle) via the drive current to the 660 nm diode laser. All three degrees of freedom are controlled via the one control laser.

2.3.2 Description of Optical Components

A full diagram of the system is shown in Fig. 8, while a list of component part numbers is provided in Table 11. The key points of note in the figure are the paths of the two lasers: the blue path represents the 830 nm illumination and collection path, while the red path represents the 660 nm control beam path. Details of the system will be elaborated on by

discussing groups of components: Diode Lasers, Illumination and Collection, Support Optics, Quadrant Photodiode, High Speed Camera, and Galvo.

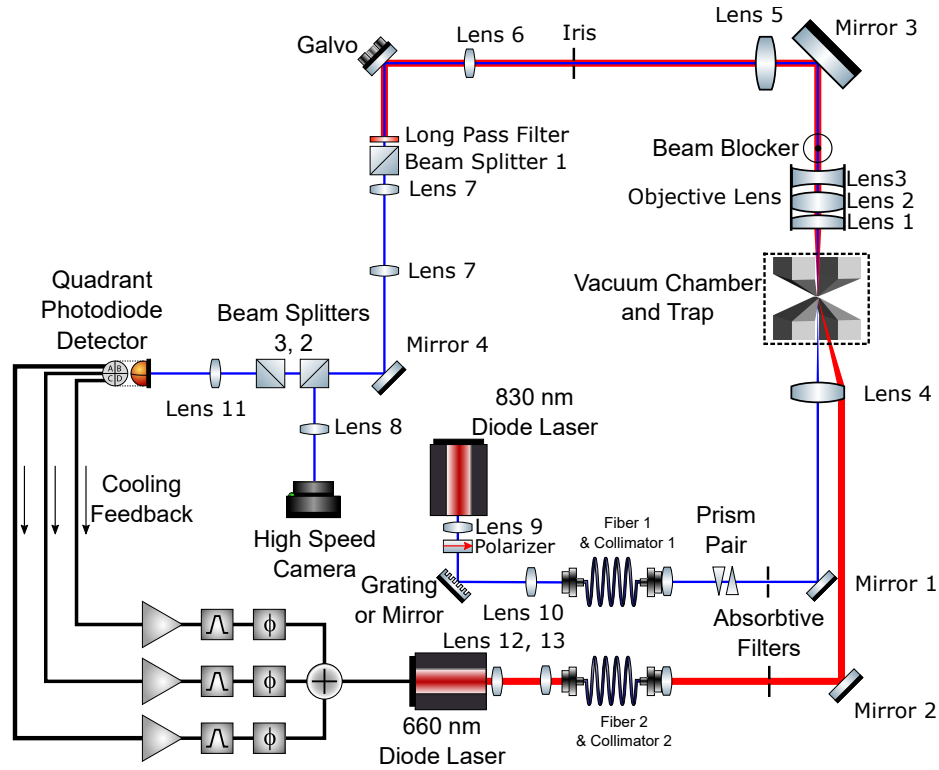


Figure 8: System diagram showing the main optical components and feedback path. Blue beam path represents 830 nm illumination and collection. Red beam path represents 660 nm control beam. The system always has at least one camera and one split detector (like the Quadrant Photodiode Detector).

2.3.2.1 Diode Lasers The lasers are first fiber coupled and then collimated on the output of the fiber; since the shape of the beam emerging from the diodes is asymmetric, a single mode fiber is used to clean up the beam and achieve a single-mode Gaussian output. Both laser diodes are housed in laser mounts with built in thermo-electric coolers to aid in their amplitude and frequency stability. This is achieved by the set of components (Lens 9, Lens 10, Fiber 1, Collimator 1) and (Lens 12, Lens 13, Fiber 2, Collimator 2) for the 830 nm and 660 nm lasers, respectively. Since both lasers are vastly overpowered compared to the power output typically utilized (mW powers are attenuated to μW for the illumination, and up to tens of μW for the control), light from each laser is then attenuated by a neutral density filter, designated as Absorptive Filters.

The 830 nm laser has an extra component, Polarizer, which is a polarizer to set the polarization into Fiber 1. In addition, ‘Grating or Mirror’ in Fig. 8 represents either a mirror or a diffraction grating; a diffraction grating helps frequency stabilize the laser by reflecting a portion of the laser output back into the laser cavity [47, 48]. While the diffraction grating certainly helps stabilize the laser frequency, we did have some skepticism that it came at the cost of amplitude stability, possibly caused by small vibration of any component in the grating setup. Both a mirror and grating were utilized, but no appreciable difference in the cooling results was noticeable between the two setups.

2.3.2.2 Illumination and Collection Both the illumination and control laser beams are loosely focused onto the particle by focusing Lens 4. Beam sizes and Lens 4 were chosen with an appropriately low numerical aperture to allow light to be focused into the trapping region without scattering off of the pole pieces. Images of the illumination and control beams, focused in the plane of a trapped particle, are shown in Fig. 9 (a) and (b), respectively.

The overall size of the two beams is quite similar; in Fig. 9, the control beam (b) appears slightly larger due to an increased intensity compared to the illumination beam in (a). However, there are two important differences between the illumination and control beams.

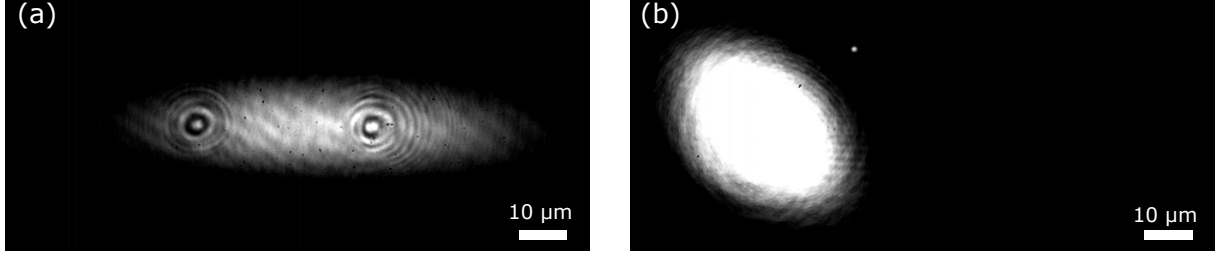


Figure 9: (a) An image of the 830 nm illumination beam, which has been stretched out axially. (b) An image of the 660 nm control beam. Scale bars are 10 μm .

First, the illumination beam is shaped to accommodate the differences in the particle's thermal amplitude in the axial and vertical directions. By examining Eq. 1.18, we see that the thermal amplitude at a given temperature in a particular direction is inversely proportional to the natural angular frequency in that direction; typically, the ratio of the axial frequency to the vertical is about 1:10. As such, to efficiently sample the thermal motion in both directions (as discussed in Section 2.5.3), without making the beam so large in the vertical direction as to cause scattering from the pole pieces, the beam is shaped to illuminate the axial direction more broadly than the vertical. This is accomplished by the Prism Pair, which is a 4:1 asymmetric prism pair. The size of the visible beam region shown in Fig. 9 (a) is roughly measured as $\sim 84 \mu\text{m} \times 18 \mu\text{m}$.

Second, each beam strikes the focusing Lens 4 at a different location on its face. The illumination beam is centered on the lens, and the particle location is designed to share the same location along the optical axis. This ideally means the illumination light only couples strongly to the transverse (x) motion of a particle. However, the control beam is intentionally aligned off-center (to a corner of the lens). The light focuses to the same location as the centered illumination beam, but originates from the corner of the lens, creating a nonzero projection of the control beam along all three trap directions and allowing us to control all three particle DOF with a single laser beam. This off-centering is evident in Fig. 9 (b), as the control beam shape has been slightly skewed (if the beam was centered on the lens, it

would be circular instead of oblong). Presumably, this is an effect of the spherical aberration caused by using a corner of the lens instead of the lens center.

The transmitted light of both beams and light scattered by the particle are collected by the objective lens OL, which is actually a triplet of lenses designed specifically to correct for aberrations to the 830 nm light that are introduced by the 5 mm glass window (see Section 2.4.1) on the chamber. The objective is assembled from 2" diameter lenses to allow for larger numerical aperture with a long effective focal length (calculated as $f_{eff} \approx 46$ mm). Since the main method of motion detection is the quadrant photodiode, the transmitted light from both beams must be removed before reaching the detector. This is accomplished for the control beam by placing a Long Pass Filter (actually, 2 identical filters) in the beam path. For the illumination light, a beam blocker was created to block the transmitted illumination light.

Since the illumination light is focused onto the particle's location, and since the focusing Lens 4 has a longer focal length than the Objective Lens, the transmitted illumination light leaving the back of the objective is essentially collimated and confined to a small region in the center of the optical axis. In contrast, illumination light scattered from the particle reaches the objective lens's full aperture. Thus, by centering a small, opaque object on the optical axis after the objective lens, the transmitted illumination beam can be completely blocked, while the scattered light remains mostly unaffected. It should be noted that the effect on the scattered light is not null, and that this method does decrease the collection efficiency of scattered light, as well as introduce some artifacts in the final image. A photograph of the beam blocker is shown in Fig. 10. It is created by placing a piece of dark tape onto a 2" diameter, anti-reflection coated window. The window is mounted in a two-axis stage to allow precise positioning of the blocker.

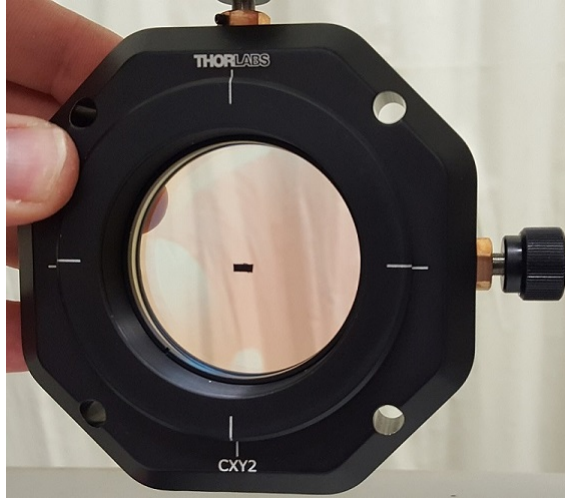


Figure 10: Photograph of the transmitted illumination beam blocker.

If the beam blocker is removed, the transmitted illumination beam can be imaged along with the scattered light. In this case, the transmitted and scattered light interfere, creating a sort of homodyne measurement. This can be seen in Fig. 11 (b) and (c) as a bright or dark center, respectively, along with a series of bright and dark fringes in a ring around the center. The bright or dark center occur when the particle is displaced on one side or the other of the objective's focus. In principle, this could allow for motion detection in the transverse (x) direction. A 'dark-field' image obtained by blocking the illumination light is shown in Fig. 11 (a).

2.3.2.3 Support Optics The rest of the optical system consists mainly of supporting optics to achieve specific requirements of the system. The Objective Lens, turning Mirror 3, and Lens 5 are all 2" compatible optics. To make the beam a reasonable size (or said alternatively, to increase the magnification of the image), 2" Lens 5 and 1" Lens 6 form a 10:1 relay system. After the relay, the beam is small enough to bounce off the galvo mirror without clipping.

The galvo position is chosen as the first element after the 10:1 relay so that any imaging

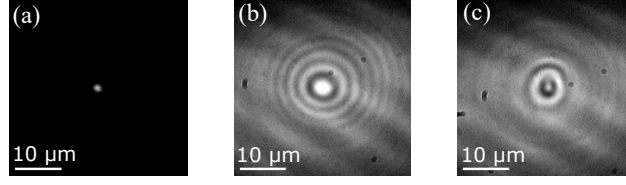


Figure 11: (a) Image obtained by blocking the illumination light. (b) and (c) show the imaging of the transmitted light along with the light scattered by the particle. Scale bars are $10\ \mu\text{m}$.

detector can be aligned relative to the galvo; in this way, (angular) motion of the galvo will move the image on any detector after this point. The galvo is vital for keeping a particle properly centered on the main split photodiode detector, as discussed in Section 2.3.2.6.

Beam Splitters 1 (8:92) and 3 (50:50) are not used in the simplified setup, but are included in the diagram as they were present for all experiments. Both splitters were placed in order to use an additional detector arm in the setup; Beam Splitter 3 was used when an additional split detector was tested and used (as in Section 4.3.4), and BS1 was intended to create a detection arm for the homodyne detection mentioned in Section 2.3.2.2. As such, a pair of Lens 7 forms a 1:1 relay, whose main purpose was to allow placing a beam blocker after the relay, thus having both a ‘homodyne’ detection arm and a dark-field arm.

Beam Splitter 2 (8:92) splits the dark-field arm’s light onto the high speed camera and quadrant photodiode detector. Lens 8 and Lens 11 are imaging lenses for these detectors.

2.3.2.4 Quadrant Photodiode Detector (QPD) The main detector used for both cooling and monitoring is the quadrant photodiode detector (QPD). The detector itself is a Hamamatsu S5980, consisting of 4 Silicon PIN photodiodes in a square array. Each quadrant is $5\ \text{mm} \times 5\ \text{mm}$, and is separated by gaps of $30\ \mu\text{m}$. A homemade amplifier and conditioning circuit, listed in Fig. 79, computes sum and difference currents from the array to generate signals proportional to the axial (z) and vertical (y) particle displacements, and to some degree the transverse (x) displacement. As depicted in Fig. 12, the circuit generates three

voltages (V_z, V_y, V_x):

$$\begin{aligned}
 V_z &\propto (I_{Q1} + I_{Q4}) - (I_{Q2} + I_{Q3}) \\
 V_y &\propto (I_{Q1} + I_{Q2}) - (I_{Q3} + I_{Q4}) \\
 V_x &\propto (I_{Q1} + I_{Q2}) + (I_{Q3} + I_{Q4})
 \end{aligned}
 \tag{2.1}$$

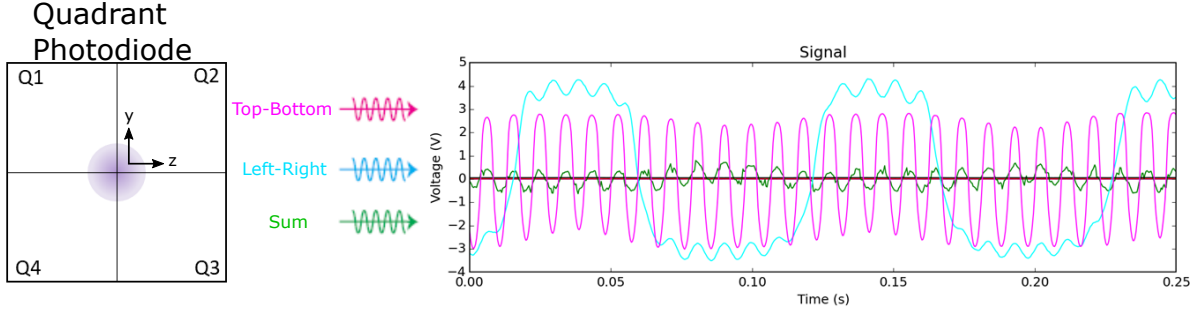


Figure 12: A depiction of a particle imaged onto the quadrant photodiode, and example signals generated by a real particle.

By examining the dimensions of the QPD, it should be seen that care must be taken to choose the size of the particle's image on the QPD (the overall system magnification). If the magnification is too small, a large percentage of the light from the particle will be lost in the gaps of the detector. If the magnification is too large, the image could more easily move beyond the edges of the detector, causing unwanted problems with the signals. For instance, once the particle reaches and moves beyond one of the boundaries, the signal generated will look much the same as when the particle is centered on the detector and moving in the opposite direction. This would have catastrophic consequences for the feedback, which relies on the correct phase information to provide a damping force instead of a driving force.

It can be seen in the example signal shown in Fig. 12 that the Left-Right (cyan) time signal approaches that of a square wave. This occurs when the amplitude of the particle's motion is large - the difference signals will only be proportional to displacement for small displacements when the particle is centered on the QPD. This is further discussed in Section 2.7.2.1.

2.3.2.5 High Speed Camera The high speed camera is a Mikrotron MC1364, with sensor diagonal of 22.9 mm, pixel size 14 μm square (for a total of 1280 pixels \times 1024 pixels). The camera is used as a general purpose tool while working with the optical system. In particular, it is used to view the system essentially any time there is a particle trapped. It also plays a crucial role in the mass determination of a particle, as discussed in Section 2.5, and in the distance calibration of the QPD, as discussed in Section 2.7.

The focal length of the final imaging lens L8 is chosen such that the magnification of the system allows the majority of the camera’s CCD region to be utilized.

As determined in Section C.6, the magnification of the system as measured on the high speed camera is 54.4. Utilizing the ratio of the focal lengths of the imaging lenses L11 and L8, we estimate the magnification on the quadrant photodiode is $\sim (300/250) \times 54.4 = 65.3$.

2.3.2.6 Galvo The inclusion and placement of the galvo mirror is instrumental for both the calibration and operation of the system. The galvo mirror provides the ability for precise alignment, either manually or automatically.

The galvo is placed in a location where the light that is scattered from the particle is collimated. Hence, a small change in the mirror’s pointing corresponds to a small displacement in the location of the image at any image plane, specifically at any of the detectors. Thus, properly aligning all of the optics and detectors relative to each other, after the galvo in the optical path, allows the location of the particle’s image to be controlled on all detectors simultaneously.

Specifics on the usage of the galvo are provided in Section 2.3.3 in regard to control, and in Section 2.7 in regard to calibration.

2.3.3 Electronics and Feedback System

As mentioned in the summary, the feedback system relies on a split photodiode detector to generate electrical signals proportional to the particle’s displacement in real time. An overview of the path that these signals take through the feedback loop is shown in Fig. 13.

The quadrant photodiode generates three signals (see Section 2.3.2.4), so all feedback

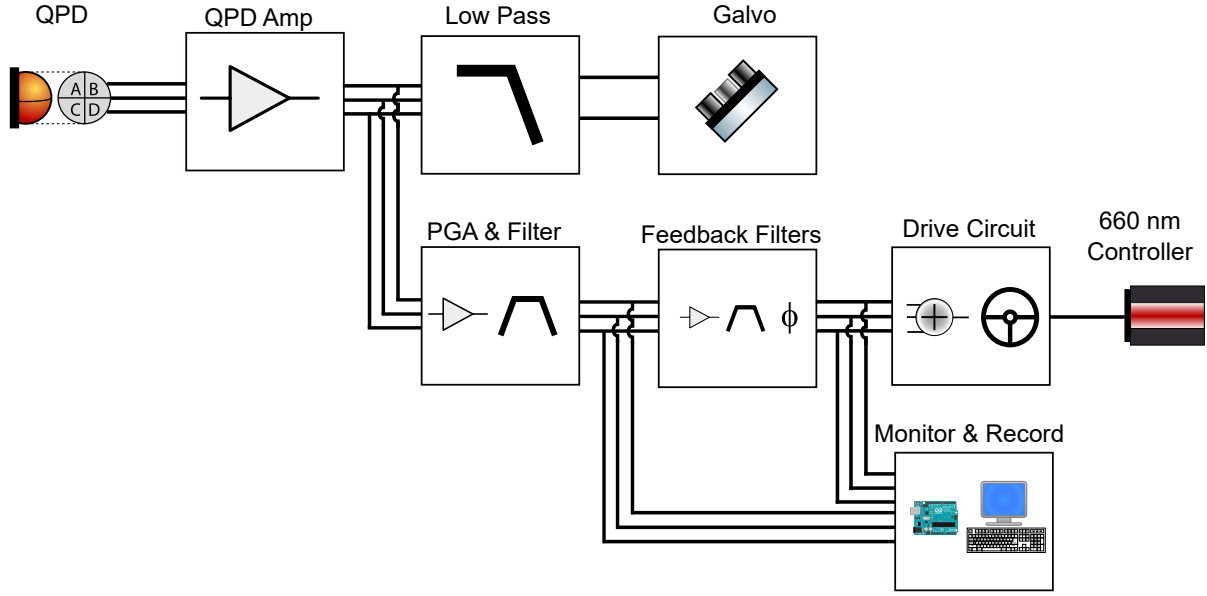


Figure 13: A system diagram displaying the feedback loop in its entirety.

related circuitry (aside from the output to the galvo) is designed with three identical copies of the signal paths (corresponding to the three DOF of a trapped particle). In practice, the axial and vertical signals from the quadrant photodiode are always used, while the third set of components is usually used for testing or for a second split detector channel. After amplification from the on board circuit (See Fig. 79), the motion signals are split and sent on two distinct paths: a path monitoring the low frequency components (DC signals) and a path monitoring AC signals ($f > 1.0$ Hz).

The top path in Fig. 13 creates DC signals by low-pass filtering the motional signals with a ~ 1.0 Hz cutoff frequency (See Fig. 80). This essentially provides a measurement for how well centered the particle is on the detector. The DC signals are sent to individual Keithley digital multimeters, whose measurements are read out by an attached computer over the HP-GPIB bus. A computer program written in Python (for Pythics) provides control logic for creating correction signals to send to the galvo mirror to keep the particle well centered on the detector. This is also the computer program that is utilized for the calibration discussed

in Section 2.7.

The middle path in Fig. 13 treats the AC signals, which corresponds to the oscillatory component of the particle’s motion. The signals are first conditioned by a band-pass filter with optional additional gain from a programmable gain amplifier (PGA), shown in Fig. 13 as ‘PGA & Filter’. A 4th-order low pass filter (4th-order refers to how fast the frequency rolls off after the cutoff frequency) is used to remove unwanted high frequency contributions, mainly to prevent the aliasing high frequency noise into the frequency region of interest during digitization. The schematic for the PGA and filter is shown in Fig. 82. The signals are then sent to the feedback filters, which are responsible for additional gain, filtering, and phase shifting to generate signals proportional to the particle’s velocity. In practice, this is done utilizing either an Arduino Due micro-controller with digital filter code (listed in [23]), or with analog filters (like Fig. 93 or Fig. 95).

A final driving circuit sums the feedback signals and switches the signal voltage reference to a dedicated power supply to drive the 660 nm laser diode controller (Thorlabs LDC202C). There is additional circuitry, with a high current op-amp (OPA548) that can be used to drive components requiring a lot of current - for example, it can be used to drive transducers (for shaking the table, as in Section 4.4), or for the previous method of driving current through a wire in the trap. This circuit is shown in Fig. 83.

2.4 MECHANICAL SUPPORT, VACUUM CHAMBER, AND VACUUM SYSTEM DESIGN

The mechanical support of the magnetic trap and the vacuum chamber setup were designed with the specifics of the illumination of and collection of light from a trapped particle in mind. It is crucial to maximize the amount of light captured from the particle scattering whilst enabling the system to reach ultra-high vacuum (UHV) pressures and allowing for illumination and control of a particle via optical access into the chamber. Specifics of the vacuum system design were chosen to reach UHV pressures, and to minimize transmission of vibrations from the external vacuum equipment to the chamber.

2.4.1 Vacuum Chamber Design Considerations

The chamber was designed to accommodate placing the collection objective outside the vacuum. In past experiments [24], the collection objective was placed inside the vacuum chamber. This places limitations on the system, namely the ability to achieve UHV pressures. To reach such low pressures, all parts of the chamber must be baked to relatively high temperatures (~ 150 °C) to remove water from their surfaces. Most commercial objectives cannot tolerate such temperatures, or are manufactured in ways that are incompatible with UHV environments (for example, epoxies may have been used that will outgas and limit the final pressure of the system). In addition, if the system needs to reach cryogenic temperatures, an objective inside the chamber may have mechanical breakdown during the cool-down or warm-up cycles. By placing the objective outside the chamber, we completely decouple the vacuum requirements from the objective's design, accepting a somewhat reduced numerical aperture by moving the objective farther from the particle.

As such, a home-made objective was designed (by another student in the lab, see [49]). The objective was designed before the chamber, with the requirements:

1. The imaging light is to be 830 nm. This is chosen to maximize the efficiency of the photodiode detectors.
2. The objective shall correct for aberrations from looking through 5 mm of glass. A thickness of 5 mm was chosen to keep the glass surface as flat as possible when used as a vacuum sealing surface.
3. The objective should have as short a focal length as reasonably possible (alternatively said, its numerical aperture [NA] should be maximized).

In the end, the objective has roughly 0.50 NA, with an effective focal length calculated as $f_{eff} \approx 46$ mm. It is a triplet of 2" lenses with anti-reflective coatings in the NIR wavelength range.

2.4.2 Vacuum Chamber

The main vacuum chamber, which houses the magnetic trap and trapped particle, is a 4.5" spherical octagon (Kimball Physics MCF450-SphOct-E2A8), as shown in Fig. 14 (a). The front and back of the chamber are 4" conflat flanges, providing a large opening for light collection via an external objective. There are also 8 1.33" conflat flanges arranged symmetrically about the chamber, which act as all-purpose ports for uses such as a additional optical access, loading, or electrical feed-throughs. The ~ 1.5 " total depth of the chamber is crucial for maximizing the collection of light from an external objective, by minimizing the distance from the objective to the trapped particle.

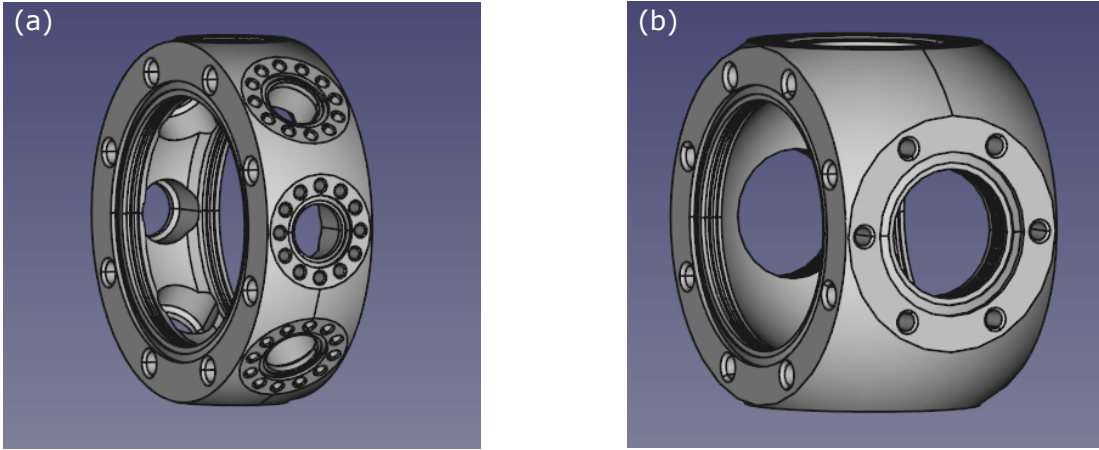


Figure 14: (a) The main vacuum chamber, which houses the magnetic trap. (b) The secondary chamber, mounted on the rear of the main chamber, serves as an adapter for larger pumping ports.

Since there are no large ports on this chamber, a second vacuum chamber is placed at the back of the main chamber for increased pumping speed. This second chamber, shown in Fig. 14 (b), is a 4.5" spherical square (Kimball Physics MCF450-SphSq-E2C4), with two 4" and four 2.75" conflat flanges. The chamber depth is shallow enough to accommodate back illumination of the particle through both chambers, while the 2.75" openings allow for larger connections to vacuum equipment (compared to the 1.33" flanges on the main chamber).

To maximize the quality of the imaging system, a home-made window design was cho-

sen. Typical glass-to-metal seals that are available commercially use relatively thin glass (~ 1.5 mm) with sometimes unspecified surface flatness. Our home-made design allows us to utilize a 5 mm, anti-reflection coated, $\lambda/10$ surface flatness window (Edmund Optics #84-468) . The thickness of the window minimizes any warping caused by the sealing surfaces, decreasing aberration from the air-glass transition. This required the in-house creation of UHV gaskets, discussed in Section 2.4.3.

2.4.3 PEEK Gaskets

In order to keep the chamber UHV compatible, a UHV compatible glass-metal seal is necessary to utilize the chosen windows. Viton gaskets could be used in high vacuum environments, but begin to outgas and even decompose (confirmed accidentally) when baked to high enough temperatures. As mentioned, commercially available view-ports generally use glass windows thinner than we prefer. As such, a PolyEtherEther-Ketone (PEEK) UHV gasket design, as outlined in [50], was chosen and modified to accommodate our vacuum chamber. PEEK is an organic thermoplastic polymer. It is hard enough to withstand the large pressures needed to make a seal, yet soft enough to deform at sharply machined edges to create a sealing surface. In addition, PEEK has been shown to withstand baking temperatures at least up to 200 °C [50], which allows the system to be baked, a necessary component of a UHV system.

As shown in Fig. 15, the gasket design is hexagonal, with relatively sharp points on the top and bottom, which are the glass and metal sealing surfaces. Wire frame design drawings of the gaskets are shown in Fig. 15 (a) and (c), as the hexagonal shape is hard to discern in Fig. 15 (b) and (d).

Our first set of PEEK gaskets were machined from ordinary PEEK rod, purchased from McMaster-Carr (8503K666). During the first machining attempt, the pointed sealing surfaces came out visibly rounded compared to the design - this was from the way the machinist parted off each gasket as they were turned. In addition, sandpaper was used for deburring, which caused some excess rounding of the points. These gaskets were found to function too poorly to reach UHV pressures, with small leaks evident, likely due to the poor uniformity of the

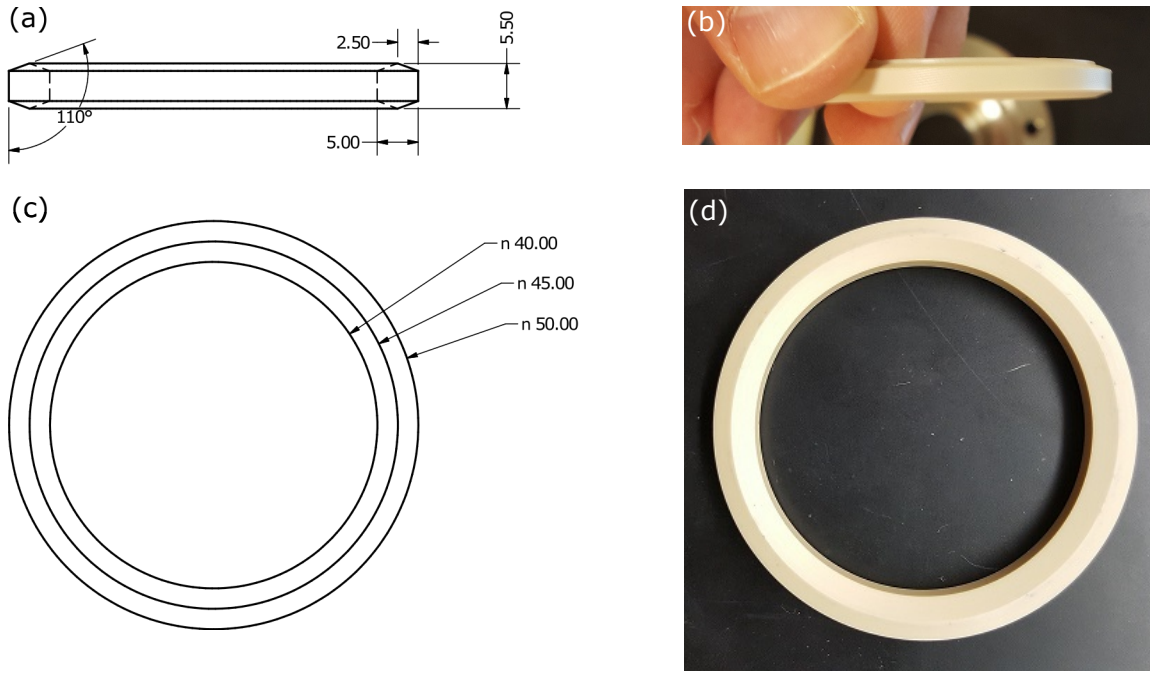


Figure 15: The hexagonal PEEK gasket design creates a glass to metal seal and is UHV compatible. All dimensions are in mm, with n referring to diameter.

sealing surface.

For both the rounded gaskets and a second set of gaskets, which were not deburred, a second turning of the angled edges on a diamond turning machine was necessary to obtain high quality, sharp points. The program for turning the gaskets is listed in Appendix E.1. These gaskets provide a suitable leak-free glass-to-metal seal.

These gaskets survived baking to temperatures up to 150 °C, albeit with some caveats. Once the gaskets were baked (with the chamber) to temperatures at or above ~ 125 °C, there was evidence to suggest that the sharp peaks began to deform as a result of the combination of high temperature and high pressures at the sharp points. As the chamber cooled, the sealing surface had to be re-tightened as much as twice per cycle (see procedure in Section F.1.5) - if they weren't, leaks would begin occurring as the PEEK material was now permanently deformed. This limited the re-usability of the gaskets to several heating

cycles. Once the gaskets were removed to be swapped out, it was blatantly obvious that the gaskets were irreversibly deformed at the points, and even significantly flattened.

In an attempt to increase the longevity of the gaskets, the next set was machined from high temperature PEEK (Boedeker Plastics R902-02000, also called PEEK HT, or Victrex G45). This high temperature PEEK has a slightly higher glass transition temperature of ~ 157 °C, compared to the standard PEEK transition temperature of ~ 143 °C, with a claim of mechanical property retention of up to 30 °C higher than standard PEEK. In addition, this set was machined differently, such that the second step of diamond turning was not necessary.

Only one set of the PEEK HT gaskets have been used, as they were tightened only once during the first baking. They have been cycled many times since without the need for re-tightening.

2.4.4 Re-entrant UHV Flange

A custom UHV flange designed to accommodate the PEEK gaskets is shown in Fig. 16.

The design utilizes a re-entrant backing to move the window as close to the trapped particle as possible, thus allowing more room to maneuver the objective. The assembly of the conflat flange and glass to metal sealing stack is shown in Fig. 16 (d). The realized version of the flange is shown in Fig. 16 (a)-(c), with the PEEK gasket against the flange visible in (a), the re-entrant nature of the back of the flange visible in (b), and the final stainless steel cover that applies pressure to the glass-to-metal sealing stack shown in (c). The sealing structure will also support ‘75 Viton, Size 325’ o-rings (McMaster-Carr 9464K47).

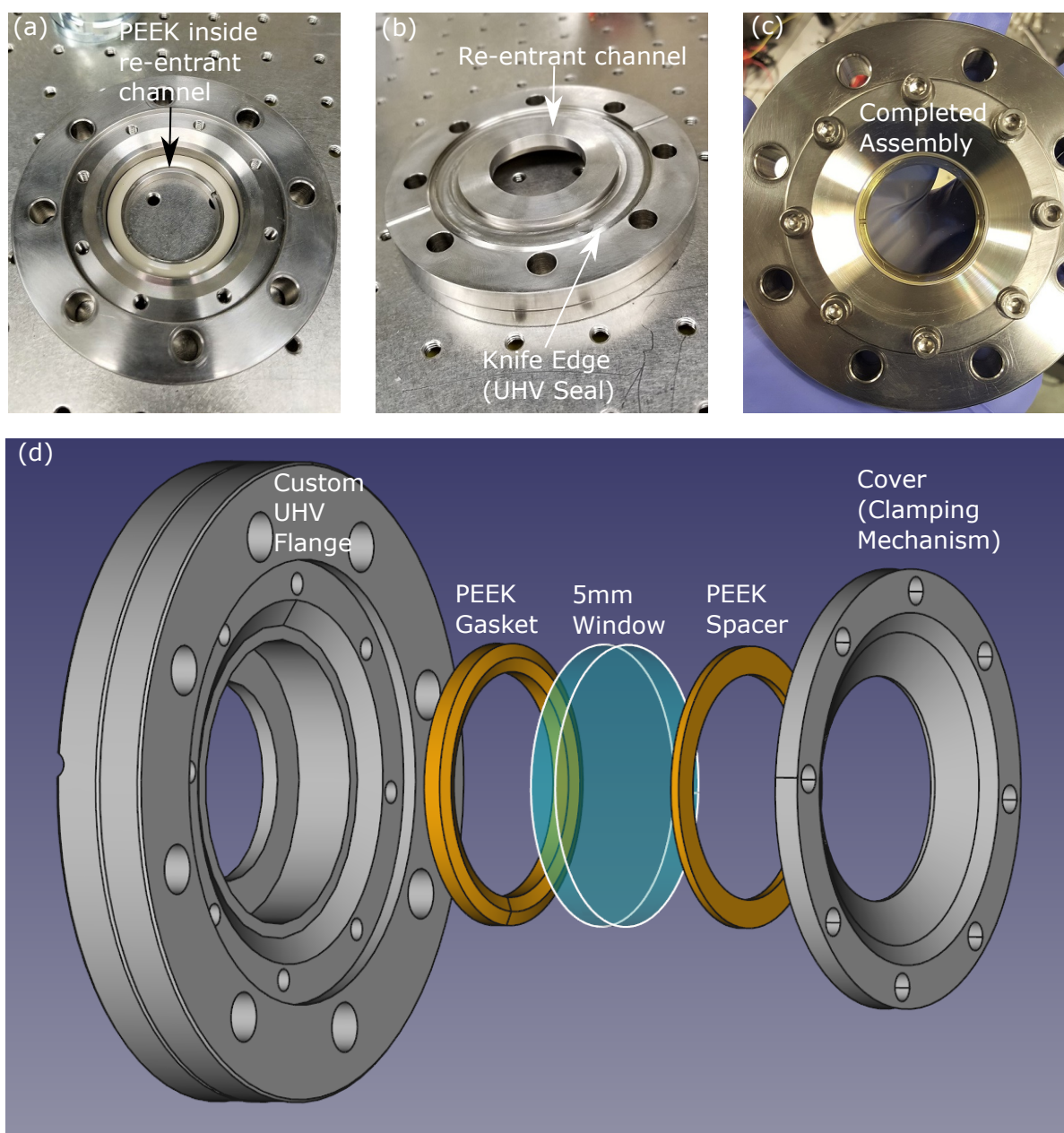


Figure 16: The design of the window flange, incorporating the PEEK glass-metal seal. PEEK components are shaded orange, 316 stainless steel in grey, and the window in blue.

2.4.5 Mechanical Support

All mechanical support for the objective, chamber, and magnetic trap were custom designed and machined in house.

A rigid mount for the objective was created out of aluminum. The mount mates with 5 axis stage Newport 9082. The model for the mount is shown in Fig. 17 (a), and a photograph of the mount in use is shown in Fig. 17 (b).

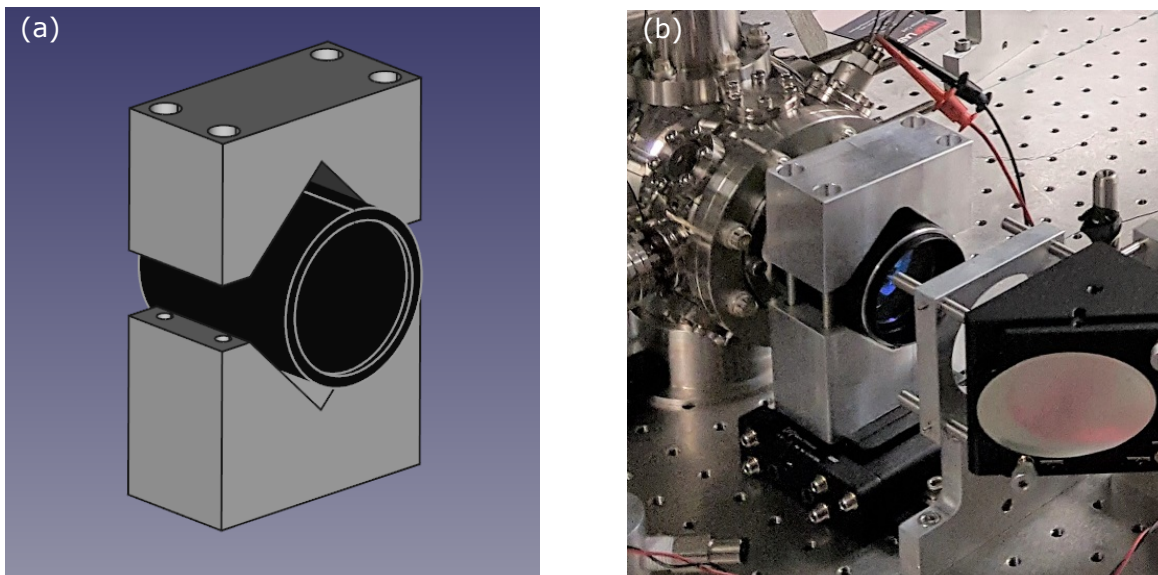


Figure 17: (a) The design of the objective mount. (b) Image of the objective mount in use.

To support the chamber, several iterations of mounting it on a movable platform were attempted; however, due to mechanical instability of even the most rigid designs, a fixed mount was chosen to minimize vibrations. The fixed mount is a stainless steel ‘top hat’ structure, mounted to the table with large clamps. The top hat height is chosen such that the particle location is at the optical axis height (4”). The walls of the mount are very thin (1/16”), so that the path for heat flow from the chamber to the table is minimized (to reduce heat conduction and heating of the optical table when baking the chamber). The model is shown in Fig. 18 (a), while the realized mount is visible beneath the chamber in Fig. 18 (b).

The trap plate (Fig. 19) is the main support structure for holding the magnetic trap in place. In a previous version of the trap plate, which was made out of aluminum, the baking

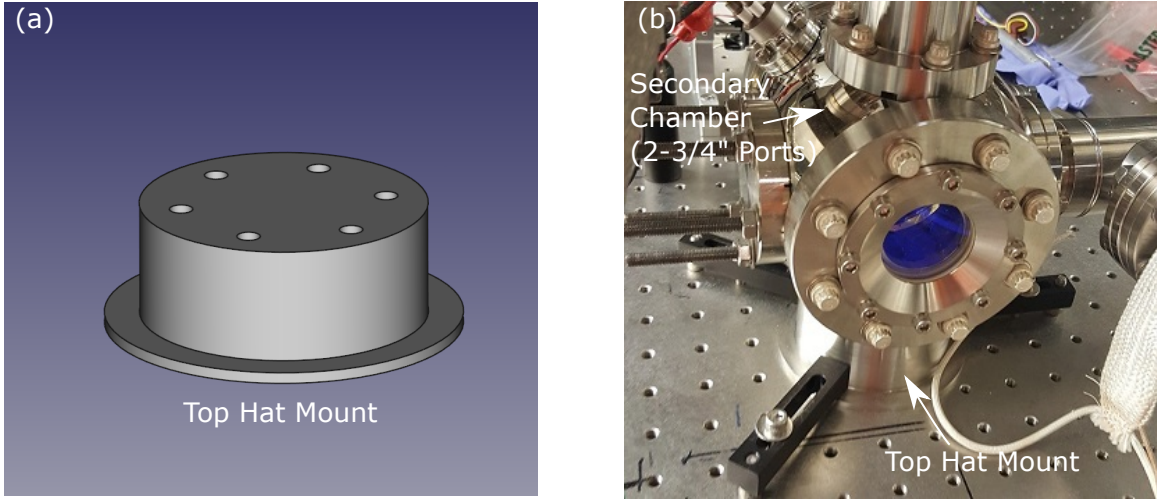


Figure 18: (a) Model of the “top hat” chamber mount. (b) Image of the mount in use.

and cooling process was seen to cause random, large kicks to the particle, in some cases causing it to exit the trap. We believed it likely that this was caused by the trap and plate ‘slipping’ relative to each other as they were heated or cooled, due to a large mismatch in their thermal expansion coefficients. In an attempt to minimize this sort of occurrence, the trap plate is machined out of grade 5 titanium, which has a temperature expansion coefficient that is close to Hipercro 50A (Hipercro 50A ~ 10.4 ppm/ $^{\circ}$ C, Grade 5 titanium ~ 9.2 ppm/ $^{\circ}$ C, copper ~ 17 ppm/ $^{\circ}$ C, aluminum ~ 24 ppm/ $^{\circ}$ C). The plate mates to an aluminum adapter, which itself mates to groove grabbers (Kimball Physics MCF450-GrvGrb-C01). There are several features of the trap plate (and clips) design that are worth noting:

- The plate and clips were originally designed as OFE copper, and the thickness of the clips was intended to keep them from bending when tightening on the far ends. The design remained the same when switched to grade 5 Titanium. The thickness limits the NA of the objective to roughly 0.50.
- The length of the clips and location of the bolts is chosen such that UV light can reach the particle from any of the corner 1.33” conflat flange ports on the vacuum chamber.
- The extra holes in the plate are present to aid in the mounting of electrical connections

to feed-throughs (or anything else useful), like shown in Fig. 35.

- The trap sits in a channel that is slightly larger than the pole piece width (0.375”), and on a ”ledge” at the bottom of the channel. This channel helps to align the trap’s center both horizontally and vertically.
- The horizontal channel on either side aligns the loading horn (shown in Fig. 36 and Fig. 112) into the correct location.
- The hole behind the trap is necessary for “back” illumination of the particle.
- The corners of the plate are removed in order to fit the plate into the vacuum chamber.

The trap plate is shown in detail in Fig. 19 (a), while the mounting and assembly of a typical trap setup with all in-house machined parts is shown in Fig. 19 (b).

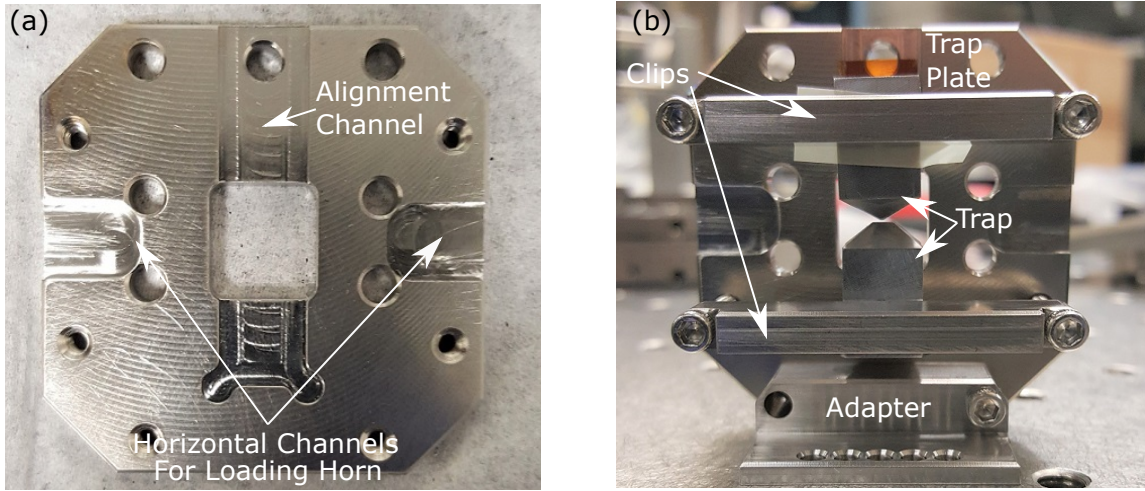


Figure 19: (a) The bare design of the trap plate. (b) A realized assembly of all in-house machined parts, including trap plate, clips, trap, and plate to groove grabbers adapter.

2.4.6 Vacuum System Design

The design of the vacuum system is the result of adhering to well known practices of creating High Vacuum (HV) and Ultra-High Vacuum (UHV) systems, as well as trial and error during system setup and use. A schematic of the vacuum system is displayed in Fig. 20. The entire vacuum system is displayed, with noted divisions between rough vacuum ($\sim 10^{-3}$ Torr), high vacuum ($\sim 10^{-8}$ Torr), and ultra-high vacuum ($\sim 10^{-10}$ Torr).

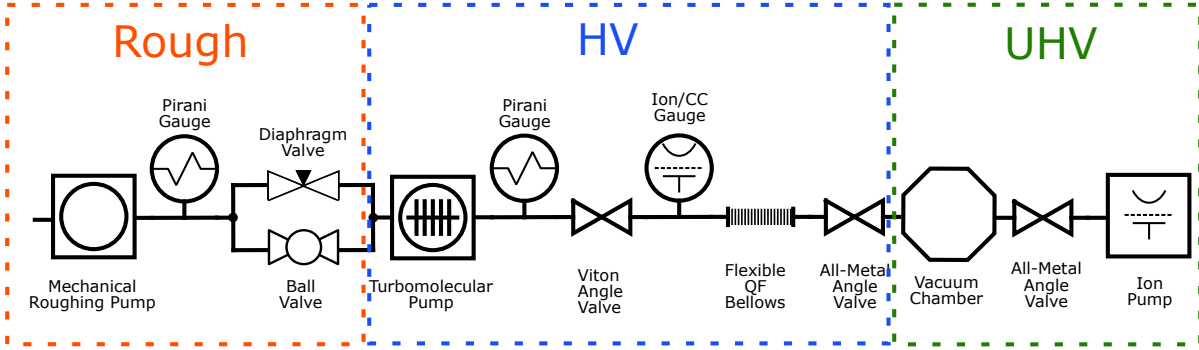


Figure 20: Schematic of the entire vacuum system, including rough, HV, and UHV divisions.

In the section labeled “Rough” in Fig. 20, a mechanical pump is used to provide the backing pressure for the turbomolecular pump. A Pirani gauge is utilized in this section to ensure that the backing pressure reaches, and remains at, an adequate value ($\sim 5 \times 10^{-3}$ Torr). Somewhat unconventional is the use of two separate valves in this section: a diaphragm valve (or leak valve) and a ball valve. This pair of valves is situated in parallel to provide two different paths with different pumping speeds. The diaphragm valve is necessary to slowly evacuate the vacuum system when a small ($\leq \sim 1.5 \mu\text{m}$) particle is trapped - trying to pump too fast causes strong enough forces from air flow to knock small particles out of the trap. Since the diaphragm valve has a small conductance even when fully opened, the ball valve is then opened to provide a high-throughput path for backing the turbomolecular pump.

The rough pumping section is shown in Fig. 21. The bellows on the left leads to the mechanical roughing pump, which is situated on the shelf below. A Pirani gauge is used to check the backing pressure levels. The slow valve (leak valve, with knob) and ball valve

(blue valve with long handle) are situated in parallel to provide different pumping speeds to the vacuum system.

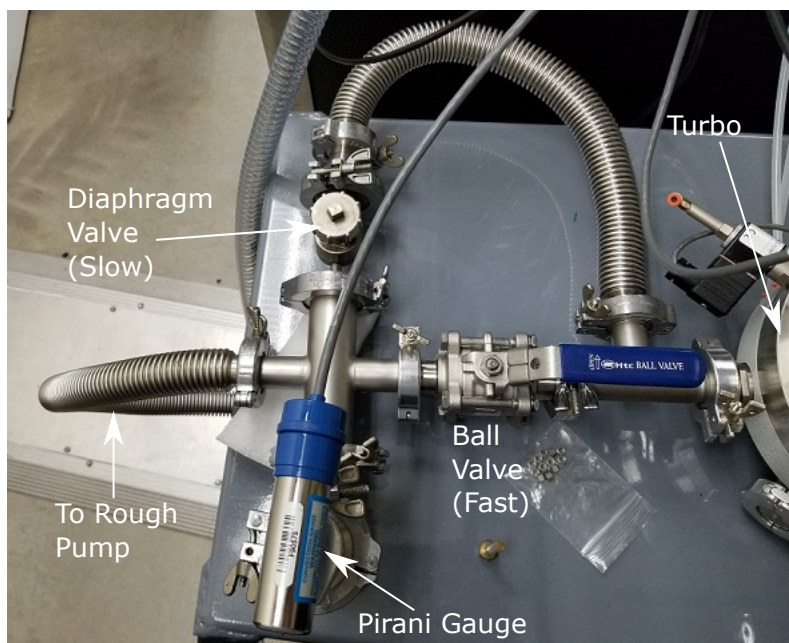


Figure 21: The rough vacuum section of the vacuum system, including mechanical pump, diaphragm valve, ball valve, and Pirani gauge.

Technically, the remainder of the vacuum system, including the UHV section, encompasses the high vacuum portion of the system, but here we name only the non UHV components as part of the HV division. A turbomolecular pump provides the base pumping for the entire system, reaching pressures down to $\sim 10^{-8}$ Torr (at the absolute best). Since the turbomolecular pump creates a pressure differential between the HV and rough vacuum sections, a second Pirani gauge is used in the HV section to ensure an adequate rough vacuum is reached in the HV section before turning on the turbomolecular pump and a gauge for reading lower pressures (either a hot cathode ion gauge with maximum pressure 10^{-4} Torr, or a cold cathode gauge with maximum pressure 10^{-3} Torr). The low pressure gauge is situated after a Viton-sealing angle valve; this configuration allows the turbo to be valved off, providing an accurate pressure reading of the chamber, and allowing for calibration of the ion pump's pressure reading.

The final piece of the HV section is a connection to an all-metal valve on the chamber, made with a removable QuickFlange (QF) bellows. It is important that this bellows is floppy, with the optimal shape decidedly a “U”. When any bellows is evacuated, it tends to shrink considerably, with more shrinking for the “floppier” the bellows. If there is not adequate length for shrinking, undue stresses are placed on the chamber in the form of lateral forces or torques, either when the system is at atmospheric pressure, or when the system is evacuated. The U shape enables the contraction of the bellows to occur freely, without adding stress to any of the rigid connections of the system. The removable bellows also enables easy disconnection of the HV components from the chamber - this completely isolates the chamber from the external vacuum system components, minimizing any vibration transfer from pumps or from the bellows itself (the chamber would then need to be pumped by the local ion pump).

The HV pumping section is shown in Fig. 22.

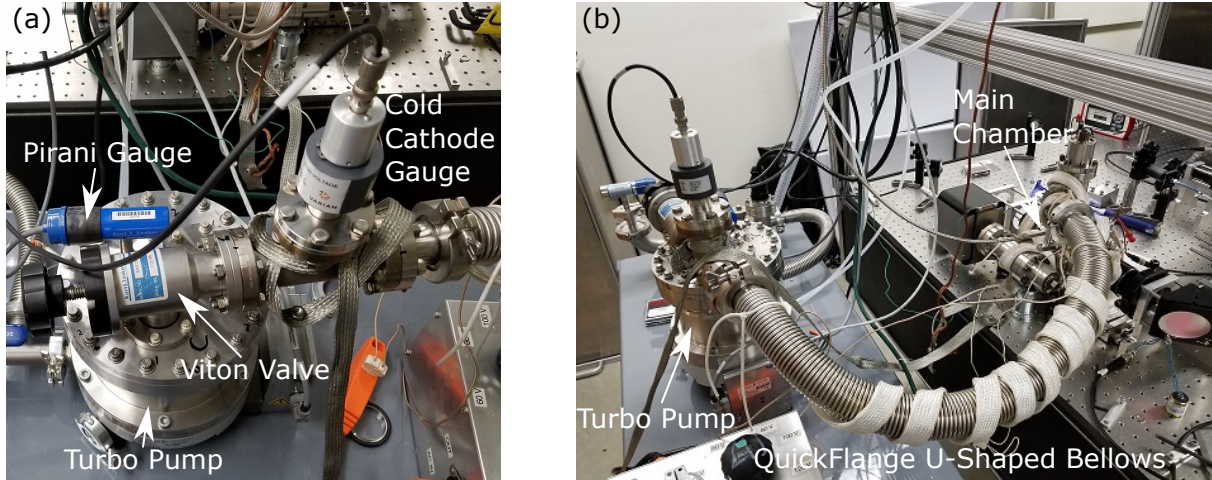


Figure 22: The HV section of the vacuum system. The turbomolecular pump, Pirani gauge, Viton angle valve, and cold cathode gauge are shown in (a). The long, QF bellows with a U-shape is evident in (b).

In Fig. 22 (a) the turbomolecular pump is seen as the base, with the second Pirani gauge (blue) directly attached. Also attached is a Viton angle valve, followed by a cold-cathode

(low pressure) gauge. The remainder of the HV section, namely the floppy U shaped QF bellows, is shown in Fig. 22 (b).

Finally, the dual vacuum chamber, two all-metal angle valves, and an ion pump comprise the UHV section of the vacuum system. Everything in this section is designed to be baked to a high temperature (up to 150 °C) for long periods. An ion pump, attached to its own all-metal angle valve, is attached to the secondary vacuum chamber to provide the sole source of pumping after the system has been baked and the QF bellows removed. As mentioned in Section 2.4.2, the main purpose of the secondary chamber is to increase pumping speed by pumping through 2.75” ports, as compared to the 1.33” ports on the main chamber.

Once the chamber is fully baked (see full procedure in Appendix F.1.3), the all-metal valve leading to the ion pump is opened, while the all-metal valve leading to the turbo pump is closed. This considerably reduces the surface area to volume ratio of components that need to be pumped by the ion pump, allowing the chamber to reach very low pressures ($\sim 1 \times 10^{-10}$ Torr). Closing the all-metal valve to the turbo pump allows the bellows to be disconnected from the main chamber, eliminating one path for external vibrations to couple into the system. The all-metal valve for the ion pump is necessary to keep the ion pump running in its own environment while the rest of the system is vented (the ion pump remains on at all times). Without the all-metal valve for the ion pump, the pump needed to be shut down when the system was vented; subsequently, turning the pump back on caused excessive outgassing at the start (similar to an ion gauge), which was strong enough to knock out a trapped particle.

The UHV segment of the vacuum system is shown in Fig. 23. The all metal valve for the QF bellows is seen directly on top of the chamber in Fig. 23 (a). The second all metal valve and local ion pump are shown in Fig. 23 (b). The ion pump extends over the optical table at a low height and is supported at three points by adjustable jacks (McMaster-Carr 3757K15) to minimize torques on the chamber.

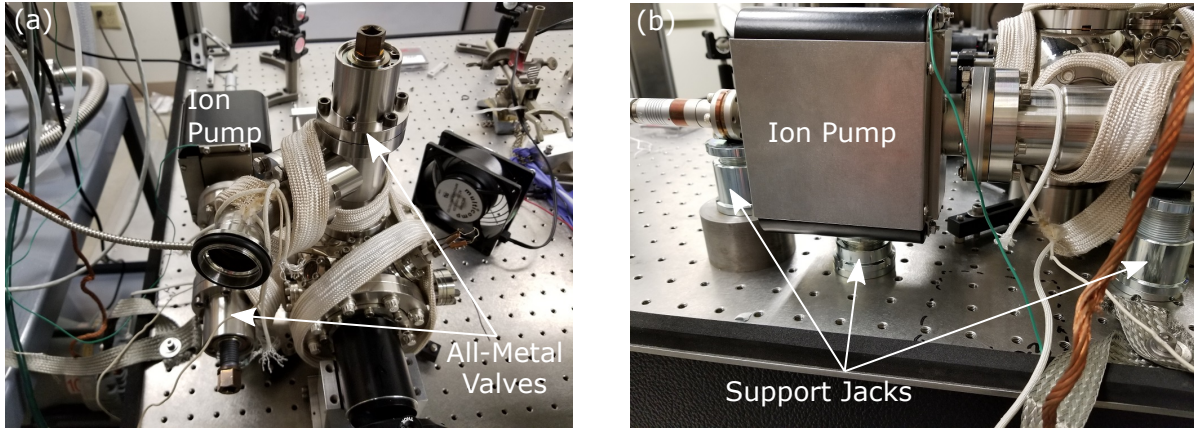


Figure 23: The UHV section of the vacuum system. The all-metal valve for the detachable QF bellows is visible in (a). The local ion pump, second all-metal valve, and adjustable supports are shown in (b).

2.4.7 Previous Setups

As with any experiment, several iterations of the experiment were realized before the final design was chosen. While it is not necessary to mention all failed designs, it is worth pointing out some aspects of the previous designs, in case the information is useful.

Two of the previous mounting designs for the chamber involved either a 5-axis translation plus rotation stage, and a 2-axis translation only stage, shown in Fig. 24 (a) and (b), respectively.

The 5-axis stage (Newport 9082), shown in Fig. 24 (a), was clearly too unstable for mounting the chamber. Trap vibration was visible on the camera; in addition, the torques on the chamber from the bellows (remedied in Section 2.4.6), made it very difficult to obtain stable setpoints at both atmospheric pressure and vacuum.

A 2-axis translation stage design was used successfully for a while. The pair of slides (Velmex B6909C-SLR, B9012C-S9-SLR) were fit with a hand-machined adapter plate of aluminum, all of which can be seen in Fig. 24 (b). The stages provided translation in

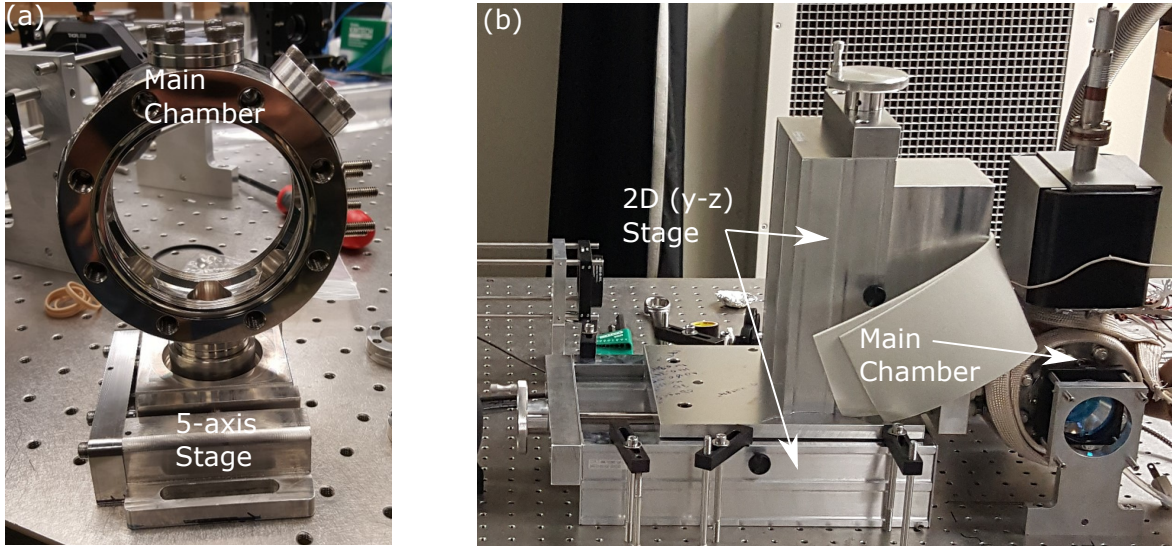


Figure 24: (a) The 5-axis stage, which was not stable enough to support the chamber. (b) The 2-axis translation stage was sturdy enough to suspend the chamber and the ion pump.

the vertical and axial trapping directions. While successful, it was determined that the translation provided by the stages was not worth the possible transfer of vibration, so the change to the rigid top hat mount shown in Fig. 18 was made.

The original vacuum design had 4 main pumping options: a turbo pump, a cryo-pump, a large ion pump, and a titanium sublimation pump, all attached to a large volume via a 6-way cross. All of the pumps rested on top of an adjoining optical table. Fig. 25 shows the full vacuum system, which was indeed much larger than the design in Section 2.4.6.

The turbo pump served the same purpose as it does in the current setup. The ion pump and titanium pump were intended to be used to do the pumping at UHV pressures; however, the large volume they were attached to, coupled with the poor conductance through the long sections of the system, made this impractical. It was found that the ion pump only marginally increased the system's pumping speed over that of pumping with only the turbo. The cryo-pump did indeed significantly increase the pumping speed of the system; however, due to the nature of the compression and expansion cycle of the helium through the pump,

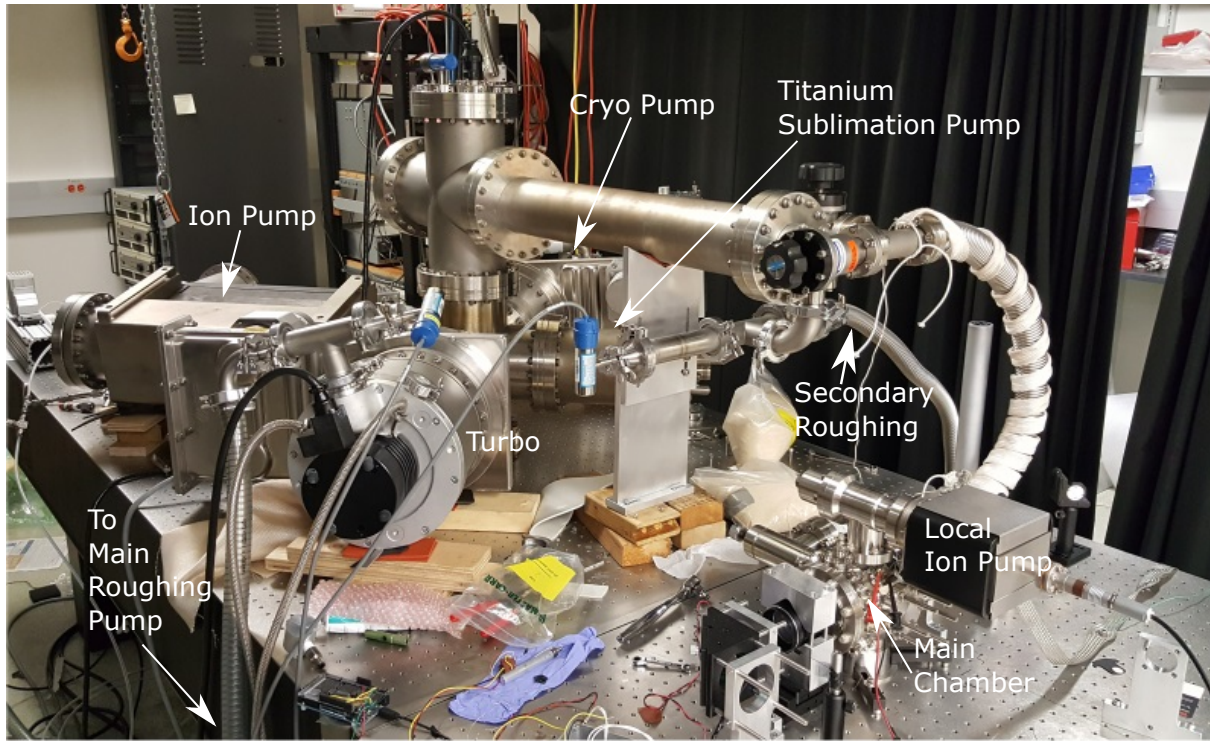


Figure 25: The original vacuum system was much larger, supported 4 different pumps, and sat directly on top of an adjoining optical table.

significant vibration was transferred to the chamber through the bellows, enough so that it was unsafe to trap small particles in high vacuum with the cryo-pump on. Instead of the parallel pumping path discussed in Section 2.4.6, this system had a full second roughing vacuum path (with diaphragm valve) to perform the initial, slow pumping.

It should be noted that the small ion pump was configured in different orientations, as seen in Fig. 23, Fig. 24 (b), and Fig. 25. While none seemed to limit the final cooling ability of the particle, there is some evidence that suggests the orientation does have an effect on a trapped particle's motion, seen as peaks in the particle's motional spectra at specific frequencies.

2.5 MASS DETERMINATION

To determine the mass of a trapped particle, we start with a particle that is in thermal equilibrium with its environment. As mentioned in Section 1.4.1.1, we write Eq. 1.18 for the average amount of potential energy for a single DOF, which is copied here for convenience:

$$\langle V \rangle = \frac{1}{2}k_B T = \frac{1}{2}m\omega_i^2 \langle x_i^2 \rangle$$

where m is the particle's mass, ω is the natural angular frequency, x the particle's displacement from equilibrium, and subscript i denoting the DOF.

We examine the probability density function for the particle's total energy, which follows a Boltzmann distribution of energies $P(E) \propto \exp(-E/k_B T)$. Substituting the classical Hamiltonian in Eq. 1.10 for E , we arrive at :

$$P(v_i, x_i) \propto \exp\left(-\frac{\frac{1}{2}mv_i^2 + \frac{1}{2}m\omega_i^2 x_i^2}{k_B T}\right) \quad (2.2)$$

where v is the magnitude of the particle's velocity.

Integrating out the particle's velocity and accounting for proper normalization, we are left with the probability density function of the particle's displacement from equilibrium:

$$P(x_i) = \sqrt{\frac{1}{\pi} \frac{m\omega_i^2}{2k_B T}} \exp\left(-\frac{m\omega_i^2 x_i^2}{2k_B T}\right) \quad (2.3)$$

To utilize either Eq. 1.18 or Eq. 2.3 to determine the mass m , we need:

- A. A measurement of the angular oscillation frequency, ω_i .
- B. A measurement of the average displacement squared $\langle x_i^2 \rangle$, OR a random sampling of the particle's displacement distribution with a fit to Eq. 2.3.
- C. The temperature, T , of the thermal bath that the particle is in. This is always assumed to be room temperature, $T = 295$ K.

The system has two types of detectors: split photodiode detectors (like the Quadrant Photodiode Detector (QPD) in Section 2.3.2.4, and a high speed camera. While in principle either detector alone could be used to determine a particle's mass, the method chosen requires

the use of both detectors. Further discussion about this choice will be presented in the appropriate sections below.

2.5.1 Angular Oscillation Frequency

Time data of the particle's thermalized motion is recorded by an Arduino micro-controller as a voltage from the QPD (as discussed in Section 2.3.2.4). The time signal is converted to the frequency domain by a Fast Fourier Transform, as defined in Eq. 1.34. The power spectrum ($|X|^2$) of the motion is computed, for which the expected curve is the theoretical curve predicted in Eq. 1.29, which is copied here for convenience:

$$PSD_{x_i}(f) = \frac{A}{(f_i^2 - f^2)^2 + \gamma^2 f^2}$$

Upon examination of Eq. 1.29 and Eq. 1.32, fitting the parameters (A , f_i , and γ) from this function would provide us all the information we need to determine the particle's mass. However, as discussed in Section 2.7.2.1, the QPD has a small linear range due to the nature of its detection scheme. The thermal amplitude A of small particles (meaning a mass $m < 1 \times 10^{-14}$ kg, or specifically silica microspheres of diameter 1.86 μm and below) is much larger than the amplitude corresponding to the linear range of the detector; therefore, the true amplitude of the motion is not adequately detected, and the parameter A from fitting the data does not represent the true value.

For the purpose of obtaining the angular oscillation frequency, $\omega_i = 2\pi f_i$, the only relevant fitting parameter is f_i . In fact, fitting the width of the curve (γ) is frequently just as unreliable as the amplitude A . For one, a computed curve has already been altered due to the issues mentioned with A . In addition, depending on the background pressure of the gas in the chamber during the time that the data was recorded and the rate and duration of the sampling, γ could be much too small for the resolution of the Fourier Transform to make a fit meaningful (this is due to the small damping rates the system is capable of reaching in the UHV regime). In the case where the frequency resolution of the curve is Fourier Transform limited, the resonant frequency can be determined by the single point maximum in the transformed data with an uncertainty of half of the frequency spacing ($\Delta f = 1/(N\Delta t)$),

see Eq. 1.38).

An example of a full axial and vertical power spectrum, computed from voltage data recorded from the QPD of a thermalized, $1.54\text{ }\mu\text{m}$ silica microsphere is shown in Fig. 26 (a).

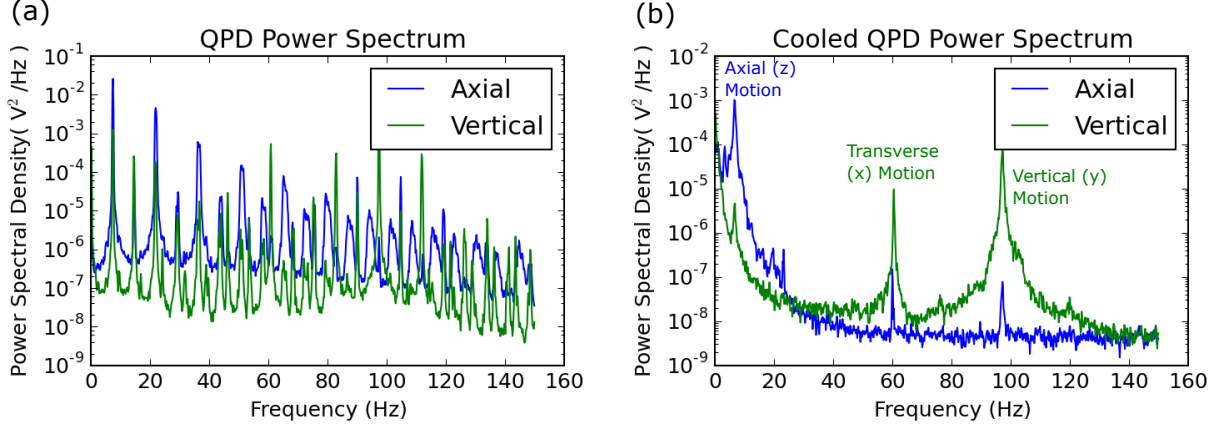


Figure 26: (a) Power spectra of an uncooled particle. (b) Power spectra of the same particle, but with its motion cooled. Particle utilized is a $1.54\text{ }\mu\text{m}$ SiO_2 sphere from 06-06-2017.

Each thermal spectrum contains many different peaks; without prior knowledge of the frequency of each DOF, it would be very hard to separate the particle's motional peaks from other artifacts. There are many different mechanisms for multiple peaks to present themselves in the frequency spectrum:

- Imperfect alignment of the photodiode axes with the particle's vertical and axial axes, coupling the measurement axes together. This exhibits itself as the axial motion being evident in the vertical signal (and vice versa), albeit several orders of magnitude lower in amplitude.
- Imperfect alignment of the measurement (objective) axis with the particle motion's transverse axis, including any alignment and assembly artifacts in the objective itself. This allows the transverse motion to be present in either the vertical or axial signals.
- Anharmonicities in the trapping potential will cause peaks at harmonics of the natural frequency. The larger amplitude of the thermal motion allows these signals to be seen.

- Nonlinearities caused by the detection scheme. The use of the quadrant photodiode provides a linear position signal when the particle's image is nicely centered between the four quadrants, and when the particle's motion is small. Once the motion is large enough that the particle's image falls fully on any one of the quadrants, harmonics of the motion will be present in the spectrum.
- Nonlinearities caused by the particle moving completely off the detector, which is mostly a problem only in the axial direction.
- Sidebands at sum and difference frequencies of the vertical, axial, and even transverse motion will be present as a result of many of these effects.

Rough values of the frequency for each motional peak can be obtained by trial and error with feedback cooling, along with camera data and prior knowledge of the trap. For instance, the axial frequency is quite easy to estimate by viewing camera images since it is always low (~ 10 Hz); the vertical and transverse peaks should be the largest and second largest, respectively, in the vertical signal. Once the true natural frequencies are determined and the particle motion is cooled to a reasonable degree, a cleaner spectrum of the motion is obtained, as seen in Fig. 26 (b). The rough frequencies obtained from the cooled spectrum are then used as guesses to fit the uncooled spectrum. Note that in Fig. 26 (b), the axial motion peak ($f_z \approx 7.3$ Hz) is quite obvious. The larger of the two peaks in the vertical signal is the vertical motion peak ($f_y \approx 97.3$ Hz), while the smaller is the transverse motion peak ($f_x \approx 60.4$ Hz). The mechanism for the transverse peak coupling so strongly into the vertical signal is not fully understood.

Results of fitting on the spectra from Fig. 26 (a) are shown in Fig. 27. The fits are obtained by using a non-linear fitting routine that is included in the numpy[39] package. Fig. 27 (a) and Fig. 27 (b) display the fits to Eq. 1.29 for the spectra shown in Fig. 26 (a) for the axial frequency ($f_z \approx 7.3$ Hz) and vertical frequency ($f_y \approx 97.3$ Hz), respectively. The uncertainty in each center frequency is on the order of 10^{-3} Hz as computed by the non-linear fitting routine; we could alternatively call the uncertainty half of the frequency spacing, which in this case is $\Delta f/2 = 0.043$ Hz ($\Delta f = 1/(N\Delta t)$, see Eq. 1.38). In any case, errors in other measurements will always dominate the effective temperatures reported. Notice that, as discussed, the fits for the widths (γ) and amplitudes (A) clearly aren't reliable (for

instance, the maximum value for the vertical motion peak in Fig. 27 (b) is clearly much too large), due to the issues listed above.

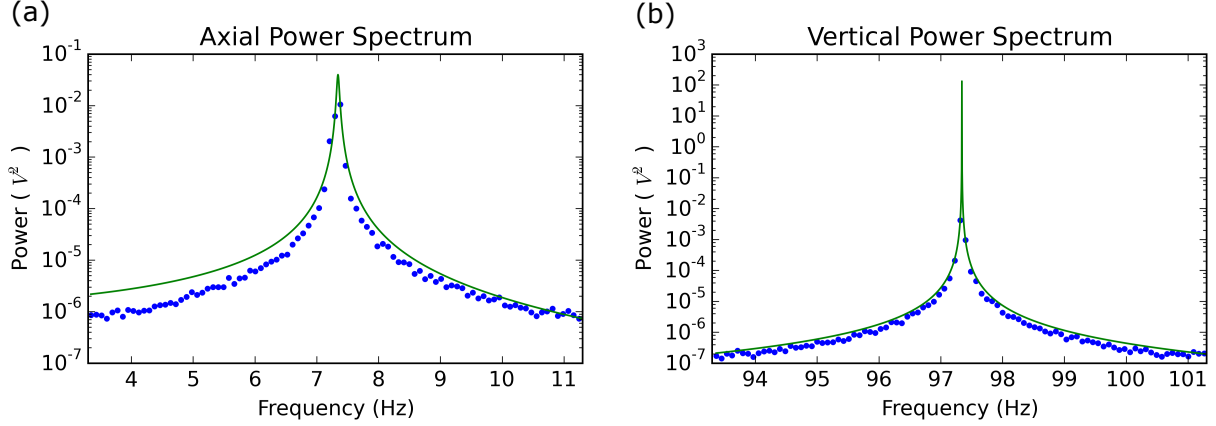


Figure 27: (a) The axial spectrum from Fig. 26 (a), but zoomed in and with an overlay of the fit function. (b) The vertical spectrum from Fig. 26 (a) with fit overlay.

2.5.2 Position Sampling

At relatively high pressures ($\sim 10^{-3} - 10^{-4}$ Torr), the damping time ($1/\Gamma$ in Eq. 1.13) of a trapped particle is on the order of 1-10 s (as estimated from [41] and confirmed experimentally). As such, the particle reaches thermal equilibrium with its environment in a short time. By imaging the particle onto a sufficiently high speed camera and recording its position data, a sampling of the probability density function for the particle's displacement (given in Eq. 2.3) is obtained.

In practice, many images of the particle are saved over a time that is long compared to the damping time ($1/\Gamma$). The images are then processed with the open source tracking package, trackpy [51], which determines the (y, z) pixel position of the Gaussian center of the particle within the image. To convert the data to physical displacements, the mean location of the particle in each direction is determined and subtracted, and the known magnification and pixel size of the camera (as mentioned in Section 2.3.2.5) are used to convert pixels to meters.

A histogram of the (absolute value of the) particle's displacement is generated for each degree of freedom, examples of which are shown in Fig. 28. Since a histogram places data into bins, the midpoint of each bin is used as the displacement value for a Gaussian fit to equation 2.3. The following equation is used for the Gaussian fit of a discrete sampling of Eq. 2.3:

$$F(m') = 2N\Delta x_i \sqrt{\frac{m'}{\pi}} \exp(-m'x_i^2) \quad (2.4)$$

where N is the total number of samples, Δx_i is the width of the histogram bin, and the factor of 2 accounts for the fact that the fit is to only one half of the Gaussian. The fit parameter m' is related to the position variance σ^2 of the distribution as $m' = 1/2\sigma^2$. Comparing Eq. 2.4 to Eq. 2.3, it is seen that the mass is related to the fit parameter m' by:

$$m = \frac{2k_B T m'}{\omega_i^2} \quad (2.5)$$

Fig. 28 shows histograms of a 1.54 μm silica microsphere's thermalized axial and vertical displacement (particle 11/20/2017). The Gaussian profile of the histograms confirms that the particle is indeed in thermal equilibrium.

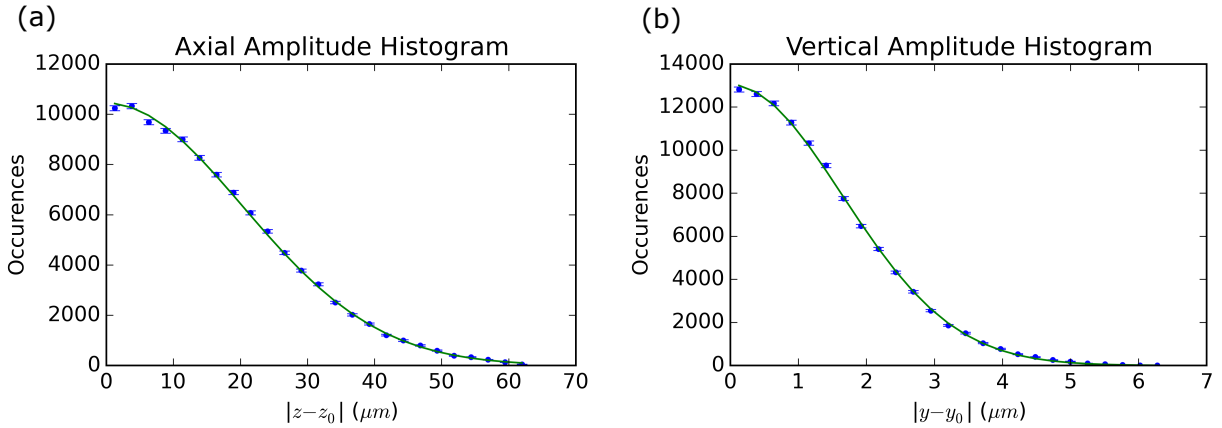


Figure 28: Histograms of the thermalized amplitudes of a 1.54 μm silica microsphere (particle 11/20/2017) in the (a) axial and (b) vertical directions.

For the data shown in Fig. 28 (a), $\langle z^2 \rangle = 408 \text{ } \mu\text{m}^2$, with an extracted mass of $m = (3.37 \pm 0.04) \times 10^{-15} \text{ kg}$. The axial frequency for this particle was $f_z = 8.60 \text{ Hz}$. For the data shown in Fig. 28 (b), $\langle y^2 \rangle = 2.73 \text{ } \mu\text{m}^2$, with an extracted mass of $m = (3.38 \pm 0.04) \times 10^{-15} \text{ kg}$. The vertical frequency for this particle was $f_y = 106.11 \text{ Hz}$.

As a final check, the histograms can be displayed on a semi-log scale and plotted against displacement squared. If the data is nicely Gaussian, these plots will display as a straight line, as shown in Fig. 29.

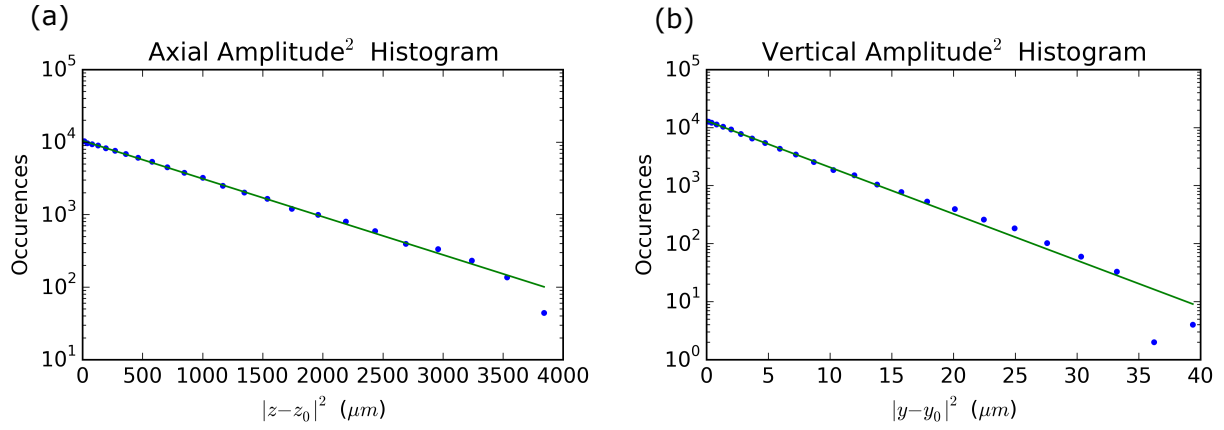


Figure 29: The same histogram data from Fig. 28 in the (a) axial and (b) vertical directions, but displayed on a semi-log plot and plotted as a function of amplitude squared

2.5.3 Discussion

As suggested in Section 2.5.1, all of the information for obtaining the mass of a particle can be extracted from a single experimental result by fitting a particle's thermalized power spectral density to Eq. 1.29. As discussed, use of this method for the QPD is unreliable due to nonlinearities in that detection scheme. However, using a high speed camera to generate the position sampling and computing its power spectral density could be a perfectly legitimate method, as long as some care is taken to avoid a few experimental difficulties or oversights.

First, generating a histogram of the displacement data provides distinct evidence that the particle is indeed in thermal equilibrium with its environment, which is a crucial requirement

for determining the particle's mass correctly, and not as easy to confirm from a power spectrum. If a particle has not yet reached thermal equilibrium, or if the particle motion is viewed on a time scale that is much shorter than the thermalization time, the probability density function will take a form resembling that of a non-thermal harmonic oscillator, in which the sampling of the particle's motion will have a maximum at the classical turning points. Such a curve is distinctly non-Gaussian, as evidenced in Fig. 30.

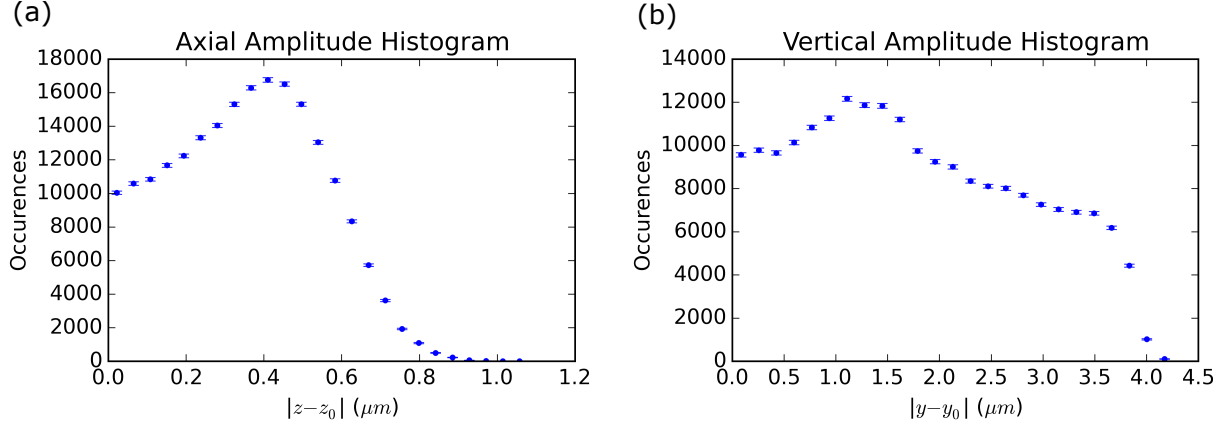


Figure 30: A histogram of a particle that is not in thermal equilibrium. Both the axial motion (a) and vertical motion (b) show signatures of an isolated oscillator. Particle utilized was a 1.54 μm SiO_2 microsphere from 05-14-2017, which is not listed in the mass results table.

Fig. 30 displays the histogram of a particle that is not in thermal equilibrium. Notice that, for the axial motion shown in Fig. 30 (a), there is a distinct maximum at the classical turning points based on the particle's current total energy. There is still evidence of the thermal bath, given the large probability of the particle being near its equilibrium point. The vertical histogram of the same particle, shown in Fig. 30 (b), is additionally obviously non-Gaussian, though its resemblance to an isolated oscillator is less distinct. Similar histograms for artificially created harmonic motion are shown in Fig. 44 (a)-(d).

Second, care must be taken to choose a sampling frequency that works well with the frequency in question. For example, sampling the motion at integer multiples or fractions

of the motional frequency will lead to a strobe effect, continually sampling the particle at the same location. Again, this is very easy to see in histogram data, but not as easy to determine from a power spectrum.

Third, given that the particle motion is determined by a finding algorithm (here, trackpy[51]), it is crucial that the entire thermal range of the particle’s motion is illuminated by the illumination source. If the particle cannot be found in a given image, some phase uncertainty will be introduced when computing the power spectrum. A related issue is the clock jitter of the high speed camera; if the frame rate of the camera is unstable, the frequency spectrum of the motion will clearly suffer. For instance, the location of the peaks in each of the individual samplings will change if the wrong sampling rate is provided to the transform, as evidenced in Fig. 44 (e). If this happens during the course of a single sampling, unphysical broadening of the resonance will occur.

It is a combination of these issues that leads us to choose the method presented. Obtaining the frequency from the QPD provides the best measurement of the location of the peak, given the better sampling rate control of the Arduino. Using the high speed camera as a sampling of the position does not rely on the specific timing of the sampling, and a large enough sample size even helps minimize errors from dropped or missing frames. In addition, the histogram method allows us to verify that the particle is well thermalized.

At any rate, it is a nice check, when possible experimentally, to compute the mass in several ways. An example of a power spectrum generated from the high speed camera sampling is shown in Fig. 31.

As with the quadrant detector data, we can compute fits to Eq. 1.29; however, though for different reasons, the amplitude and width parameter fits are still unreliable. Fits for the spectra displayed in Fig. 31 are shown in Fig. 32. Again, it is noticeable that the fits, particularly the widths, are not reliable.

When the data was available (meaning the camera data was a full set, not missing any frames), the masses quoted in Section 2.5.4 were also calculated by a simple calculation of $\langle x_i^2 \rangle$, and via a fit to the power spectral density obtained from the camera data. The average percentage difference in these two methods compared to the probability distribution method are -0.7 % and +16.4 %, respectively. This confirms the suspicion that the jitter in the

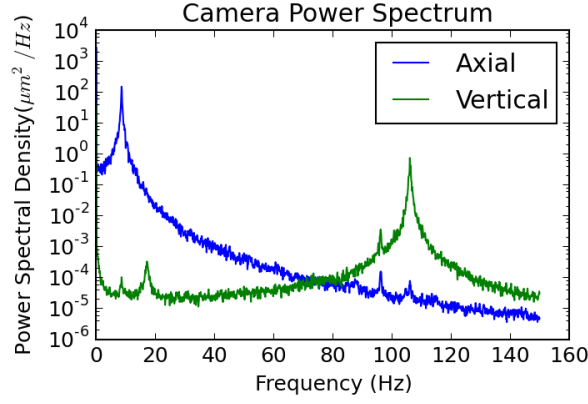


Figure 31: A power spectrum generated from camera data for the particle whose histograms are shown in Fig. 28.

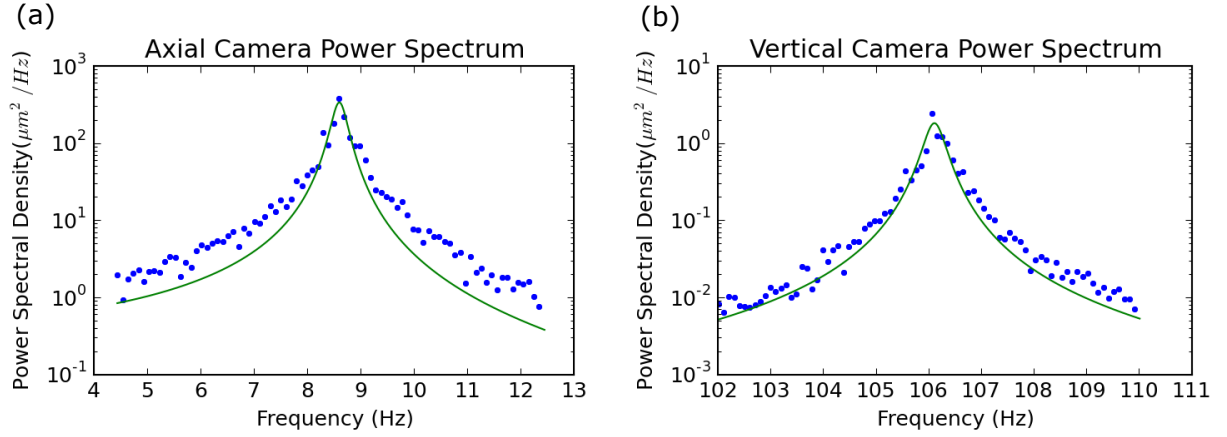


Figure 32: Fits to Eq. 1.29 using the camera data shown in Fig. 31, for both the axial (a) and vertical (b) directions.

camera's sampling rate is substantial enough to artificially inflate the measurement.

The last item that deserves special note is the visibility of the transverse peak in any and

all of the data sets, whether viewing the signal from the QPD or the high speed camera. In all data, there is a strong transverse signal coupling mainly into the vertical DOF. While the mechanism for this is unknown, two likely scenarios are poor vertical alignment or imperfect objective lens holders.

In some cases, particularly when the transverse frequency is well below the vertical (which means its thermal amplitude is significantly larger than the vertical amplitude), the transverse signal can be quite large. An example of this is shown in Fig. 33.

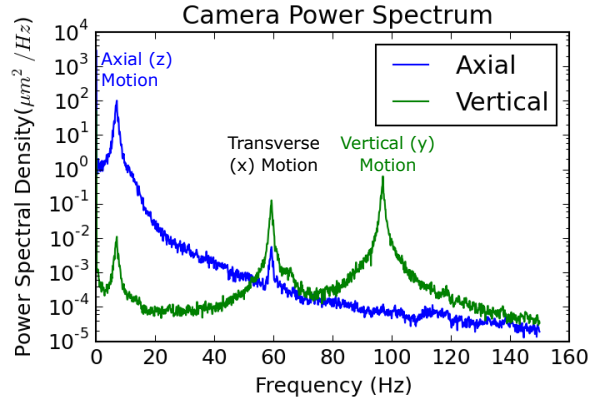


Figure 33: A camera spectrum showing the strong coupling that the transverse motion can have to the vertical signal, especially when the transverse frequency is well below the vertical. Particle is a 1.54 μm SiO_2 microsphere from 10-15-2017.

In such a case, it is reasonable to assume that calculating $\langle y^2 \rangle$ without utilizing the frequency domain data (i.e., without ignoring data at frequencies unrelated to the DOF chosen) could lead to incorrect results for the mass, as the transverse motion clearly adds to the calculation. However, given how well the results of the vertical and axial DOF match, and that the vertical peak is larger than the transverse, we still believe the Gaussian calculation method to be the most reliable calculation of the mass.

2.5.4 Mass Results

There are several different sizes of silica (SiO_2) microspheres measured, listed in Table 2. All SiO_2 microspheres were purchased from CoSpheric, LLC. In addition, polystyrene spheres and diamonds were trapped.

Type	Diameter (μm)	CV (%)	Expected Mass (kg)	Product Name
SiO_2	0.96	3.1	$(8.34 \pm 0.8) \times 10^{-16}$	SiO2MS-1.8 0.96um - 1g
SiO_2	1.54	9.6	$(3.44 \pm 1.0) \times 10^{-15}$	SiO2MS-1.8 1.54um - 1g
SiO_2	1.86	3.2	$(6.06 \pm 0.6) \times 10^{-15}$	SiO2MS-1.8 1.86um - 1g
SiO_2	7.75	3.7	$(4.39 \pm 0.5) \times 10^{-13}$	SiO2MS-1.8 7.75um - 1g
Diamond	2.0	-	1.47×10^{-14}	Pensco
Polystyrene	1.75	-	2.92×10^{-15}	C-PS-1.75

Table 2: Table of particles used for mass calculations.

Table 3 summarizes the full results of the mass measurements performed. For the 1.54 μm data, only particles confirmed to be single particles were included in this calculation; however, those that were larger nicely agreed with integer multiples of particles. It can be seen from the table that we have a good match with the expected mass, except for the cases of the smallest particles (0.96 μm , which only had one data point) and polystyrene (none was believed to be a single particle). The diamonds had a large size variance, so a match was not expected with a small sample size.

Type	Expected Mass (kg)	Measured Mass (kg)
SiO_2 -0.96	$(8.34 \pm 0.8) \times 10^{-16}$	1.43×10^{-15}
SiO_2 -1.54	$(3.44 \pm 1.0) \times 10^{-15}$	3.56×10^{-15}
SiO_2 -1.86	$(6.06 \pm 0.6) \times 10^{-15}$	5.43×10^{-15}
SiO_2 -7.75	$(4.39 \pm 0.5) \times 10^{-13}$	4.62×10^{-13}
Diamond	1.47×10^{-14}	1.40×10^{-15}
Polystyrene	2.92×10^{-15}	1.40×10^{-14}

Table 3: Table of average of mass results.

Table 4 contains a succinct version of every mass measurement made. An inspection of the data in Table 3 shows that the mass measurements are reliable and reproducible, providing good agreement with expected results over a wide range of particle sizes and trap frequencies. Polystyrene spheres are manufactured by parent company Corpuscular Inc., were purchased from Fisher Scientific and provided by Microspheres-Nanospheres.

Date	Type	Mass(kg)	f_z (Hz)	f_y (Hz)	f_x (Hz)
12/12/2017	Poly-1.75	9.29×10^{-15}	8.44	106.34	94.41
12/10/2017	Poly-1.75	2.90×10^{-14}	7.92	110.70	77.99
12/07/2017	*Poly-1.75	4.11×10^{-15}	8.53	104.44	93.70
12/02/2017	SiO2-1.54	3.43×10^{-15}	8.46	105.77	95.69
11/28/2017	SiO2-1.54	4.03×10^{-15}	8.50	105.28	95.11
11/26/2017	SiO2-1.54	7.10×10^{-15}	8.53	106.21	96.25
11/22/2017	SiO2-1.54	1.03×10^{-14}	8.75	105.89	96.06
11/20/2017	SiO2-1.54	3.37×10^{-15}	8.60	106.11	96.10
11/20/2017	SiO2-1.86	1.13×10^{-14}	8.07	105.39	95.99
11/19/2017	SiO2-0.96	1.43×10^{-15}	6.87	97.08	60.94
11/18/2017	SiO2-1.86	5.26×10^{-15}	6.87	97.08	60.11
11/18/2017	Diamond	1.74×10^{-14}	6.95	97.36	62.72
11/16/2017	SiO2-1.86	5.22×10^{-15}	6.82	96.92	59.33
11/16/2017	Diamond	1.06×10^{-14}	6.12	97.93	63.22
11/10/2017	SiO2-7.75	4.42×10^{-13}	6.86	97.14	59.90
11/01/2017	SiO2-1.54	4.20×10^{-15}	6.52	97.62	61.92
10/31/2017	SiO2-1.54	3.22×10^{-15}	6.72	96.90	59.50
10/15/2017	SiO2-1.54	3.09×10^{-15}	7.02	96.89	59.57
10/09/2017	SiO2-1.54	3.60×10^{-15}	6.84	96.91	60.26
06/06/2017	SiO2-1.54	3.69×10^{-15}	7.34	97.31	60.39
05/25/2017	SiO2-1.54	3.76×10^{-15}	8.53	133.21	123.72
05/22/2017	SiO2-1.86	5.54×10^{-15}	9.65	93.85	57.45
05/22/2017	SiO2-1.86	1.46×10^{-14}	10.02	93.77	56.71
05/19/2017	SiO2-1.86	5.69×10^{-15}	10.24	93.67	56.03
05/17/2017	SiO2-1.54	1.13×10^{-15}	10.27	94.03	56.47
05/16/2017	SiO2-1.54	3.55×10^{-15}	9.89	93.64	57.14
05/11/2017	SiO2-1.54	3.71×10^{-15}	9.98	93.55	56.58
04/20/2017	SiO2-1.54	4.00×10^{-15}	7.17	115.69	89.09
03/27/2017	SiO2-1.54	3.61×10^{-15}	8.05	115.69	89.60
03/15/2017	SiO2-7.75	4.82×10^{-13}	7.72	121.48	81.81
03/15/2017	SiO2-1.54	3.26×10^{-15}	7.06	115.27	88.15
03/08/2017	SiO2-1.54	3.54×10^{-15}	7.55	115.38	88.79
02/15/2017	SiO2-1.54	4.03×10^{-15}	7.46	86.02	62.46
02/02/2017	SiO2-1.54	4.33×10^{-15}	9.31	107.36	94.50

Table 4: Table of all mass measurements. Particle with * may have been SiO₂.

2.6 PARTICLE NEUTRALIZATION

Any type of particle loaded via the ultrasonic horn, and in particular silica microspheres loaded from a dry powder, will typically have some non-zero amount of charge. Since the pole pieces are quite close to the particle ($\sim 50 - 100 \mu\text{m}$), several complications could arise if a microsphere is highly charged. Any voltage fluctuations in the pole pieces (whether

thermal fluctuations from Johnson noise or electrical pickup) could create a direct noise source for driving the particle. In addition, a moving charge in the trap could generate currents in the nearby pole pieces, which are susceptible to resistive dissipation, which in turn provides a damping mechanism for particle motion.

At the very least, interaction between charged spheres and localized charges on the pole pieces can cause clear changes in the behavior of trapped particles. The electrostatic attraction (or repulsion) between a trapped particle and localized charges has been seen to create local minima in the trapping potential or alter the trapping frequencies. These localized charges occur, for instance, if a pole piece has developed some oxidation with a localized charge patch, or when a particle with some charge is stuck to a pole piece near the trapping region. An example of the latter is shown in Fig. 34.

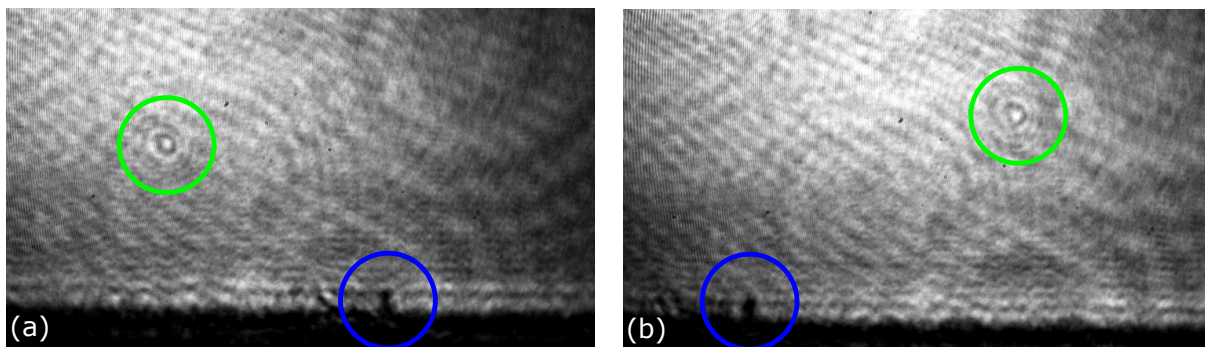


Figure 34: Change in particle location in the trap after rough neutralization.

When this particle was first loaded, its position in the trap was to the left of a clump of microspheres that was stuck to the pole pieces, as seen in Fig. 34 (a). After the rough neutralization process (Section 2.6.2), the particle's position shifted to the right of the clump of microspheres (Fig. 34 (b)). It is not always obvious, as it was in Fig. 34, that a localized charge is nearby, and the movement of particles during neutralization is commonplace. However, the large clump provided a nice reference point to compare the location change in this case.

Obviously, it is important to neutralize the microsphere as well as possible to avoid any of these direct effects.

2.6.1 Loading and Verification of Charge

The charge on a particle is easily verified by creating an electrical field between the top and bottom pole pieces. This is achieved by supplying a DC voltage difference across the top and bottom poles, supplied via an electrical feed-through on the chamber. An image of the usual electrical connections to do this is shown in Fig. 35.

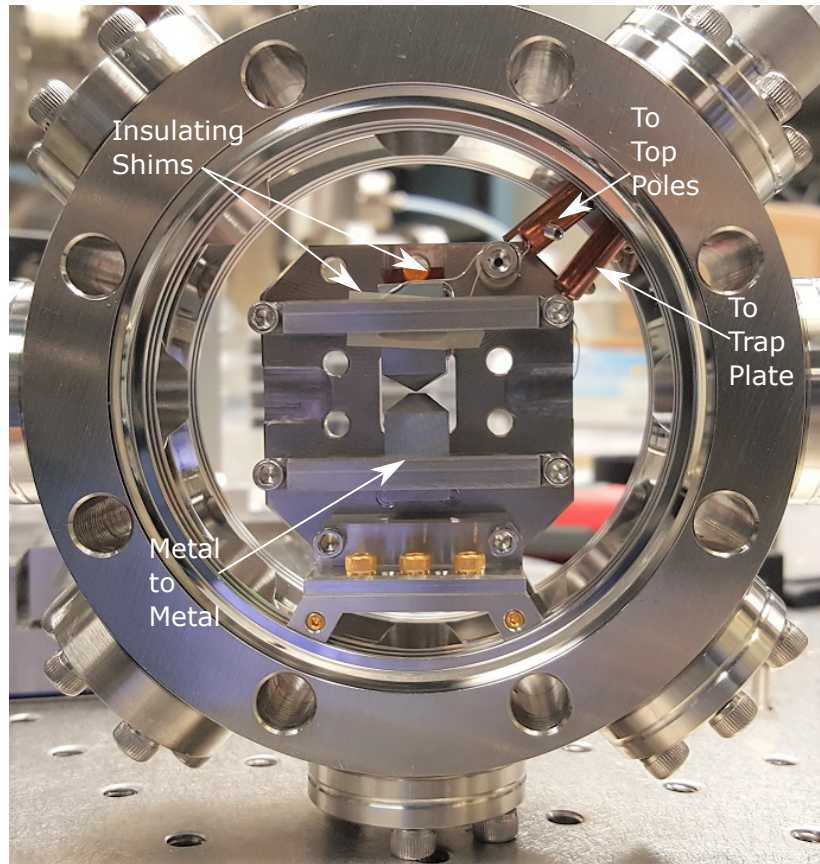


Figure 35: View of typical electrical connections to the trap pole pieces.

The two top pole pieces are shorted together via copper shims between the magnet and pole pieces, as are the two bottom pole pieces. The bottom pole pieces are shorted to the trap plate via direct connection, which is also a ground connection (by way of direct contact with the grounded optical table). The top pole pieces are electrically isolated from the plate via Kapton (dark orange) or PEEK (tan) shims, which can also be seen in Fig. 35.

A silver-plated copper wire is clamped to the top pole pieces, and attached to an electrical feed-through on the vacuum chamber (an intermediate connection to a ceramic standoff is used to aid in the connection process).

A second feed-through pin is connected to the trap plate, which provides a point of contact for supplying a voltage via a differential source. By placing a voltage difference across the top and bottom pole pieces, we create (essentially) a parallel plate capacitor. Placing a positive DC voltage on the top pole pieces will attract (and lift up) negatively charged particles and vice versa, which is easily monitored on a camera.

The ultrasonic horn terminal has three connections, as seen in Fig. 36. Two of the connections (red and white) drive the piezo (which shakes the horn tip), while the third is provided to bias the horn tip with a supplied voltage in order to control the charge of the spheres.

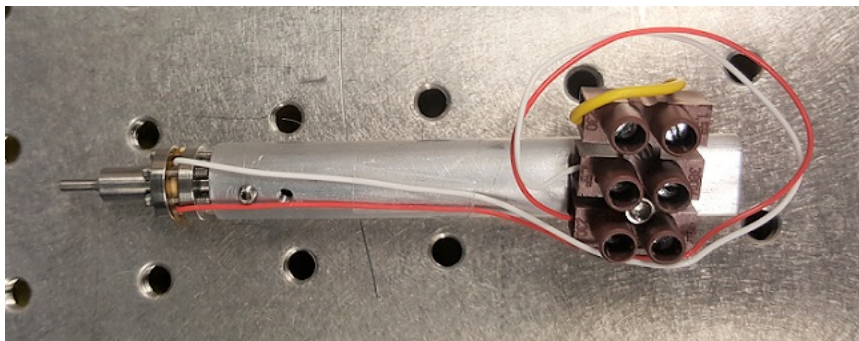


Figure 36: View of the ultrasonic horn and electrical connection. The top wire terminal (yellow) is used to place a voltage bias on the horn.

If the bias wire is grounded, the majority of trapped single particles is negative. If the bias wire is floating, most particles are still negatively charged, but a large distribution of charge occurs. Supplying the bias wire with a moderate positive voltage (15 V) creates a majority of positively charged trapped particles. However, this method is not recommended for loading, as the horn will be attracted to the grounded pole pieces. In addition, the entire horn handle must be wrapped in an electrically insulating material such as Kapton, which creates an additional, strictly physical, complication: since the metal horn must be rested

against the guide in the grounded trap plate (see Fig. 19 (a)) for proper loading alignment, the Kapton film makes the alignment significantly more difficult.

The most effective (and easiest) method of loading particles with either charge is to ground the horn and supply a small (~ 0.1 - 0.2 V) positive or negative bias to the top pole piece. This creates a vertical separation between all microspheres with different charge to mass ratios, which keeps the positive and negative particles from sticking to each other and forming clumps. To trap only positive or negative particles, the voltage should be chosen with the correct polarity and size (not much larger than 0.1 V) to pull the desired polarity of spheres up toward the top pole pieces, and as such push the opposite polarity of charges out of the trapping region (through the bottom pole pieces).

2.6.2 Rough Neutralization

For most experiments to date, there has been no evidence that charge plays the limiting role in the effectiveness of the feedback damping; as such, rough neutralization is usually the only step taken. Microspheres are stored in an aluminum-foil lined cup (to minimize charge accumulation) and loaded onto the tip of the ultrasonic horn by direct pressure. The horn is held grounded, and particles are generally loaded with negative charge. A small (1 - 5 V), slowly oscillating voltage (0.5 - 2 Hz) is placed on the pole pieces, which drives the trapped microsphere if it is charged. A radiation source (Americium-241) is brought very near the trapped particle in atmospheric pressure. This is an α source; however, by utilizing the source in atmospheric pressure (which allows ionization of gas molecules), both positive and negatively charged spheres can be neutralized. The typical proximity of the source to the trap can be seen in Fig. 37, at which time there was an actual trapped particle present.

The motion of the particle is monitored until the driven oscillation is no longer evident on the camera. For 1.54 μm diameter particles, a large voltage (up to 35 V) can be used to continuously view particle motion until there appears to be no more benefit to leaving the radiation source near the particle. The neutralization process starts immediately after inserting the source, with the entire process taking just a few minutes (usually, less than 5). At this point, the charge on the spheres is still generally nonzero. From the plots in

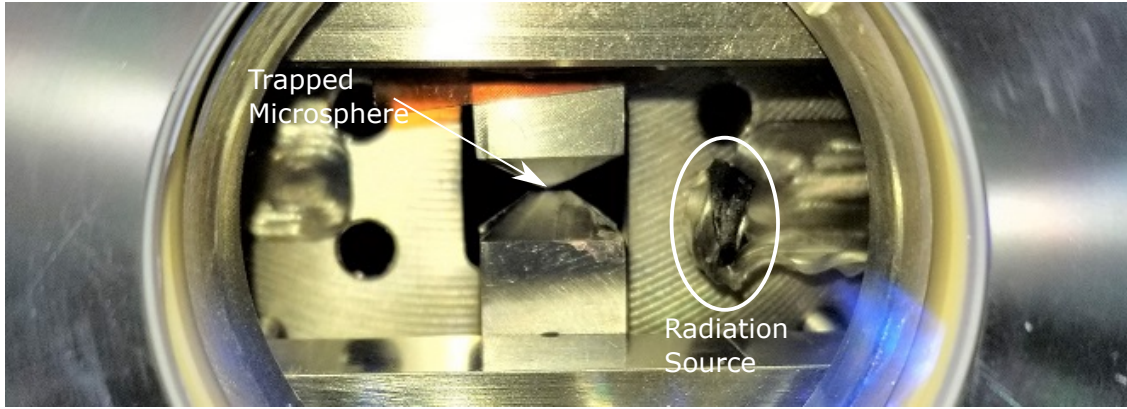


Figure 37: View of the radiation source during rough neutralization, showing that it is brought quite close to a trapped microsphere.

Section 2.6.3, it is estimated that a particle is left with 1-2 excess electron charges. With a 3 Hz drive frequency, the driven amplitude is about 3 μm vertically.

2.6.3 Complete Neutralization

To fully discharge the sphere, we elect to illuminate either the particle or the surrounding pole piece metal with a UV light source. The source contains a 185 nm spectral line; photons with this wavelength have enough energy to knock electrons off of the nearby (mostly iron) pole pieces, which then collide with the particle (decreasing charge on the particle). These photons should also have enough energy to knock electrons off of the sphere itself, thereby increasing charge on the sphere. An illustration of the described process is shown in Fig. 38.

In order to utilize this illumination, the trap chamber components had to be carefully designed to allow UV light from the two corner 1.33" conflat ports on the vacuum chamber to reach either the particle or the surrounding metal. This design can be seen in Fig. 39.

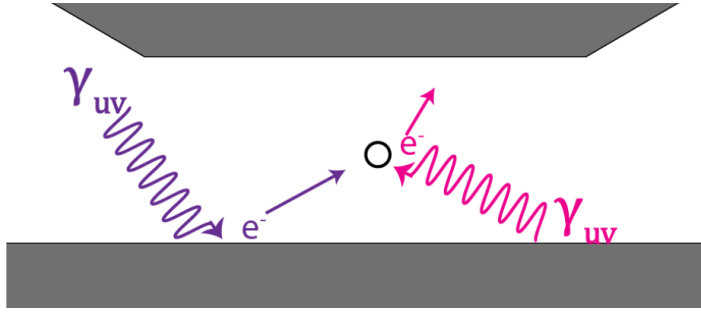


Figure 38: Depiction of the effect of UV light on the trap (purple) and sphere (magenta).

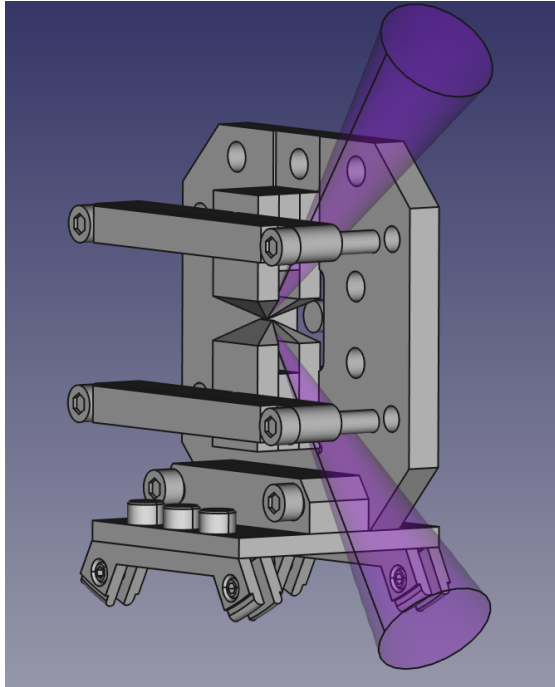


Figure 39: View of the mounting design to accommodate UV light illumination, represented by magenta cones, from the 1.33" corner flanges on the vacuum chamber.

The asymmetry of the process is allowed by the geometry of the pole pieces. The top UV light cone will illuminate a wide area of metal on the bottom pole pieces, allowed by the sharp cut of the top pole pieces. This should negatively charge the sphere as electrons are knocked off the pole pieces. The UV light from the bottom port should be mostly blocked by the long length of the bottom pole pieces - this should shield most of the UV light from hitting metal near the particle, and the majority of the light should directly hit the particle, knocking electrons off and increasing charge on the sphere.

In practice, positively charging the sphere is inconsistent; it has worked, but is highly dependent on the geometry of the trap. It works best when the gap between the bottom pole pieces is small ($< 75 \mu\text{m}$), suggesting the theory of operation is correct.

The UV lamps chosen are small, U-Tube shape lamps. The lamps require a 12 V DC supply voltage to the boards that came with the lamps. When supplying voltage to the lamps, the supply will generate around 100 mA of current while the lamp warms; the lamp will be lit when the current roughly doubles to the 200 mA range.

UV light will generate ozone when run in atmosphere; in addition, excess UV light should be blocked to avoid direct or indirect exposure. As such, a small cap for the UV lamps was created to fit onto the outside of a 1.33" UV glass view-port. The cap has an inlet for the lamp, as well as an NPT gas connection to flow nitrogen into the cap and prevent the generation of ozone. The realization of these caps can be seen closeup in Fig. 40 (a), and its location on the chamber, along with electrical and gas connections, is shown in 40 (b).

The method utilized to check for charge neutralization was to again drive the vertical motion of the particle by placing an oscillating voltage across the top and bottom pole pieces. However, compared to rough neutralization and to quantify results, the output of the vertical channel of the quadrant photodiode detector was directed to a lock-in amplifier, with the drive signal as its reference. In this way, it is unambiguous to verify a change in the sign of the particle's charge by a phase flip in the output of the lock-in amplifier.

Several different parameters were attempted for neutralization, many of which yielded results of some sort, but most of which were inconsistent. For example, the following parameters were attempted: high vacuum, low vacuum, slow drive frequency for measurement (below resonance), high drive frequency for measurement (above resonance), varying strengths

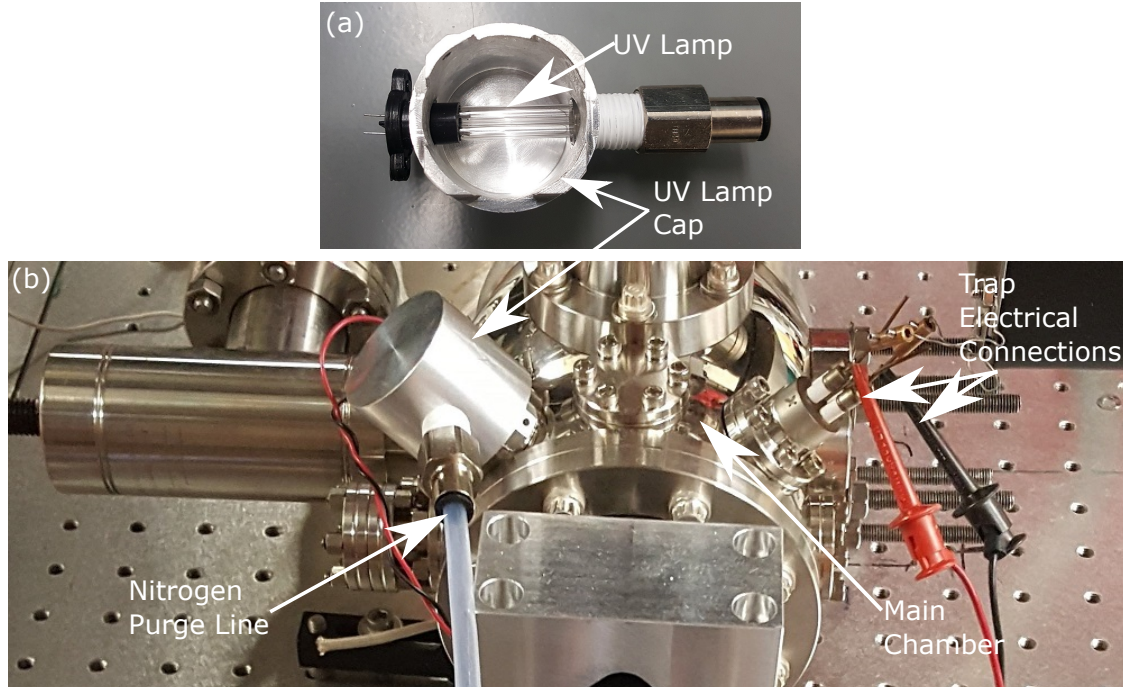


Figure 40: (a) UV lamp is visible inside the UV lamp cap. (b) The UV lamp cap fits over a corner 1.33" conflat viewport on the main chamber.

of drive amplitude, and varying amounts of attenuation of the UV light. In general, the UV light was so intense that the spheres became highly charged in a very short time (seconds). In order to slow down the rate of charging, the UV window (MDC Vacuum 9722013) was covered with 4 pieces of thickness 130-170 μm microscope coverglass. The final method is similar to that described in [52].

Since negative charging had been the most consistent, it is important to load a positively charged microsphere to begin. To do so reliably, the horn is grounded and a small DC bias is placed on pole pieces (the top pole pieces are biased with a negative voltage, to attract positive particles and push negative particles down and out of the trapping region). The rough neutralization procedure from Section 2.6.2 is followed first.

The chamber is then pumped to high vacuum ($\sim 10^{-6}$ Torr). The sphere is electrically driven with a small amplitude (0.5 V) at 78.54 Hz, which is slightly below the then vertical

resonance frequency of 96.9 Hz. The output of a lock-in amplifier is monitored for changes as (attenuated) UV light is injected in the top port of the chamber. In Fig. 41, discrete steps in the magnitude of the signal are seen, which is a feature of the discrete nature of charge. In addition, the rate of change is sufficiently slow that it is easy to identify the zero charge state and turn the lamp off before continuing.

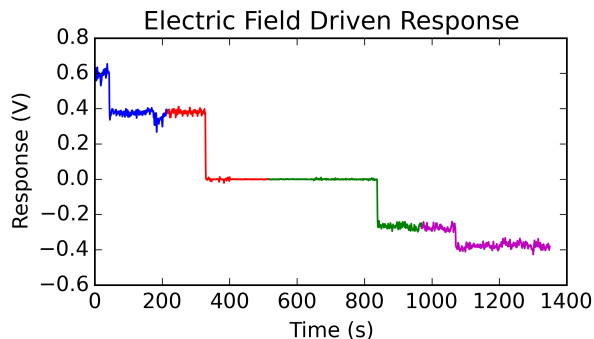


Figure 41: Demonstration of particle neutralization and a charge sign change. Particle utilized was a 1.86 μm SiO_2 microsphere from 06-19-2017 (not listed in mass table).

The different colors in Fig. 41 and Fig. 42 represent the fact that the data was not taken continuously. Once the charge state changes, the particle's equilibrium position changes. After a charge change event, the UV lamp was extinguished while the particle was re-centered on both the galvo mirror and position sensitive detector, so data was not collected during this time. Note that, intentionally, no changes to the objective focus or illumination location were made.

In the data shown in Fig. 41, the particle was purposely continually charged to verify a phase flip, signifying the change from positive to negative charge, and eliminating any explanations other than charging. The data also shows that the magnitude of the discrete changes are not equal. One possible explanation for this is that differing numbers of electrons crashed into the particle during each discrete change. However, the most likely explanation is that the sensitivity of the detector changes as the particle's charge changes. There are many observations to support this claim:

- The particle's equilibrium position in the trap measurably changes each time the charge is changed.
- The QPD is very sensitive to the overall intensity of the scattered light and careful focusing. Three things can contribute to a signal amplitude change when the equilibrium position changes:
 - A. The location of the particle relative to the maximum of the illumination beam can change, causing an overall increase or decrease in intensity.
 - B. An equilibrium change along the optical axis will affect the focusing of the optical system, which will result in greater or weaker sensitivity to position changes (see Fig. 102).
 - C. A large equilibrium change in the vertical or axial directions will move the particle away from the center of all the optical system lenses, which could cause a loss of collection efficiency.
- The amount of time between single events is significantly long (\sim hundreds of seconds); for such a slow event rate, it is unlikely that multiple events occur simultaneously.
- The steps sizes are not integer multiples of each other. This suggests a continuum in the signal amplitude, which could only be attributed to charge in the regime of large numbers of charge.

The process has been repeated at least two more times, with two more particles, demonstrating that the neutralization procedure is indeed repeatable. Both additional charging attempts were stopped when the particle reached zero response amplitude, indicating a neutral particle. These are shown in Fig. 42 (a) and (b).

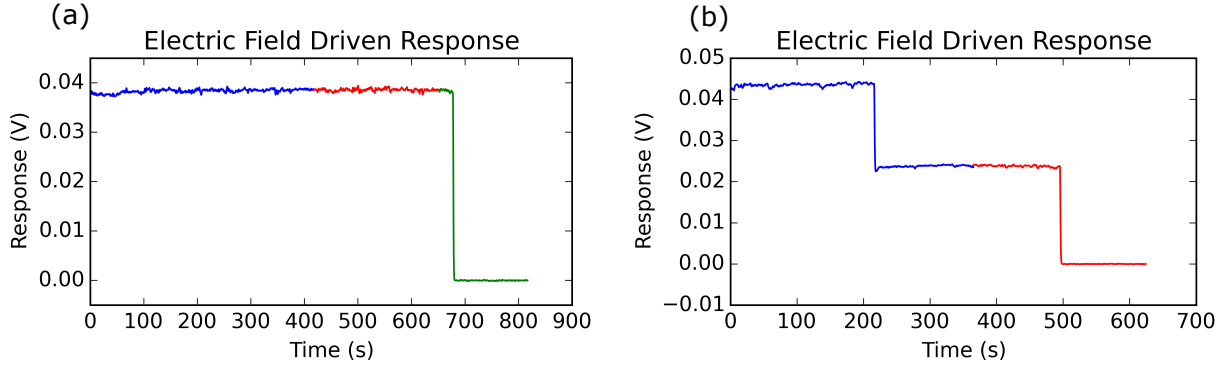


Figure 42: Two additional demonstrations of charge control, both stopped at zero particle response, indicating complete neutralization. Both were $1.54 \mu\text{m}$ SiO_2 microspheres, from (a) 10-09-2017 and (b) 10-15-2017.

2.7 DETECTOR CALIBRATION

Measurement of the maximally cooled position of a particle requires the use of the QPD, as the motion is too small ($\sim 1 - 10 \text{ nm}$) and the resolution of the camera too coarse to be accurately measured by the high speed camera. As mentioned in Section 2.3.2.6, the galvo is absolutely necessary for calibrating the quadrant photodiode detector (QPD) voltage to units of distance. The method we utilize also requires the use of the high speed camera. In short, moving the galvo mirror with a small amplitude moves the image of the particle at any image plane. We then use the known magnification of the high speed camera to calibrate the voltage of the QPD to a distance.

The process is described mathematically below. A critical assumption made in this analysis is that the displacement of the particle is linear in the drive amplitude (a voltage) applied to the galvo driving circuit (listed in Fig. 81), an assumption that will hold for small angular galvo displacements:

$$x = \alpha a \tag{2.6}$$

where x is the particle's displacement on a detector, α is the proportionality constant (in detector units per galvo unit), and a is the amplitude of the galvo drive signal (in galvo units).

For some function of a

$$a(A, t) = AF(t) \quad (2.7)$$

with A a constant and $F(t)$ any function of time, we write:

$$x(A, t) = \alpha AF(t) \quad (2.8)$$

The time average of some parameter, for instance the average amplitude of the displacement $\langle |x(A, t)| \rangle_t$, is simply:

$$\langle |x(A, t)| \rangle_t = \alpha A \langle |F(t)| \rangle_t \quad (2.9)$$

Performing the time averaging in Eq. 2.9 leaves us with a function $x'(A)$:

$$x'(A) = \alpha \langle |F(t)| \rangle_t A \quad (2.10)$$

Utilizing the same drive function for another detector, and defining the particle's displacement on this detector as $y'(A)$ and the detector's constant of proportionality as β , we have:

$$y'(A) = \beta \langle |F(t)| \rangle_t A \quad (2.11)$$

We perform the time averaging measurement for a variety of amplitudes A on both detectors, which yields two straight line data sets. The slopes m_α and m_β of these lines are then:

$$m_\alpha = \alpha \langle |F(t)| \rangle_t \quad (2.12a)$$

$$m_\beta = \beta \langle |F(t)| \rangle_t \quad (2.12b)$$

Finally, taking the ratio of Eq. 2.12a to Eq. 2.12b leads us to the desired calibration:

$$c_{\alpha,\beta} = \frac{\alpha}{\beta} \quad (2.13)$$

where $c_{\alpha,\beta}$ gives the desired unit conversion in (detector x units)/(detector y units). For all calibrations performed, we choose the drive function:

$$F(t) = \cos(\omega t) \quad (2.14)$$

As we know the function $F(t)$, we could obtain the desired conversion from a single measurement on each detector. However, making several measurements and fitting a line gives a more accurate estimate of the proportionality constants. Making several measurements and plotting them also allows us to visually check the linearity of the galvo and of the detector in the region of interest, which is not possible via a single measurement.

2.7.1 Camera Calibration

Given that the particle's location on the camera is extracted from the 2-dimensional grid of pixels based on a Gaussian filter (trackpy), the calibration is essentially independent of parameters like the particle size or illumination intensity. As such, for a given configuration of the optical setup, the camera calibration need only be performed once. The calibration can be done in two ways: by creating a 'pinhole particle' instead of a real particle, or by trapping and cooling an actual particle. In either case, the galvo is driven with a sinusoidal input at a frequency close to but not overlapping with the frequency of the particle in the axial and vertical directions. The movement of the galvo moves the location of the image on the camera, simulating particle movement.

In order to make the measurement as clean as possible, a 'pinhole particle' can be used instead of a cooled particle. This removes any additional movement of the image from particle motion. A 30 μm pinhole can be placed at the first image plane in Fig. 8, between lenses L5 and L6 (at the same location as the iris). Laser light is injected through the system just as if a particle was trapped, but the beam blocker is removed to allow the illumination light through. The result is an image that looks nearly identical to a particle. (This is the

method utilized for optimizing the location of the quadrant photodiode lens, Section C.8.)

The method chosen for the most recent incarnation of the optical setup was to trap and cool an actual particle, namely a $1.54\text{ }\mu\text{m}$ SiO_2 microsphere. The particle is cooled to the extent that the drive amplitude to the galvo creates significantly larger movement than the actual particle motion. When this is the case, we can use a simple calculation of $\langle|x|\rangle$ or $\sqrt{\langle x^2 \rangle}$ for the measurement metric: for all data in this document, $\langle|x|\rangle$ was used. Care must be taken to ensure that the large drive amplitude is small enough to make the linear approximation of Eq. 2.6. In the case that the drive amplitude is close in magnitude to the particle motion amplitude, we can work in the frequency domain to analyze only contributions to the measurement metric from the galvo induced movement at frequency $\omega/2\pi$. As with the mass determination in Section 2.5, care must be taken when choosing the pair of camera sampling rate and drive frequency so that no strange beating effects occur.

For the sake of clarity in the analysis, a galvo unit (henceforth written as g.u.) corresponds to an analog voltage output provided to the galvo driving circuit (Fig. 81) from an Arduino. As shown by Eq. 2.13, the conversion from g.u. to a voltage is not necessary for analysis, and thus is left as this somewhat arbitrary unit. Physically, a g.u. represents a single, integer unit of change in the analog output of the Arduino, with the full output range roughly 4000 g.u.. In addition, the unit px refers to a single, physical pixel on a camera.

Data from an axial calibration is shown in Fig. 43. In the data presented, a drive frequency of $\omega/2\pi = 7\pi \approx 22\text{ Hz}$ was chosen, which is sufficiently above the axial frequency $\omega_z/2\pi \approx 7\text{ Hz}$. A total of 4 different amplitudes for the sinusoidal drive were chosen (50, 100, 150, and 200 g.u.).

Histograms of the particle's displacement from equilibrium for each of the drive amplitudes are shown in Fig. 43 (a)-(d). The shape of these distributions matches that expected for the sampling of the motion of an isolated harmonic oscillator, where the particle spends more time at the classical turning points. Obtaining a well defined distribution throughout the full displacement range confirms that the motion was adequately sampled.

Fig. 43 (e) is a single plot displaying the amplitude spectra (computed with a flat top windowing function) for the same set of data. The linearity of the amplitude response with the drive amplitude is clearly evident.

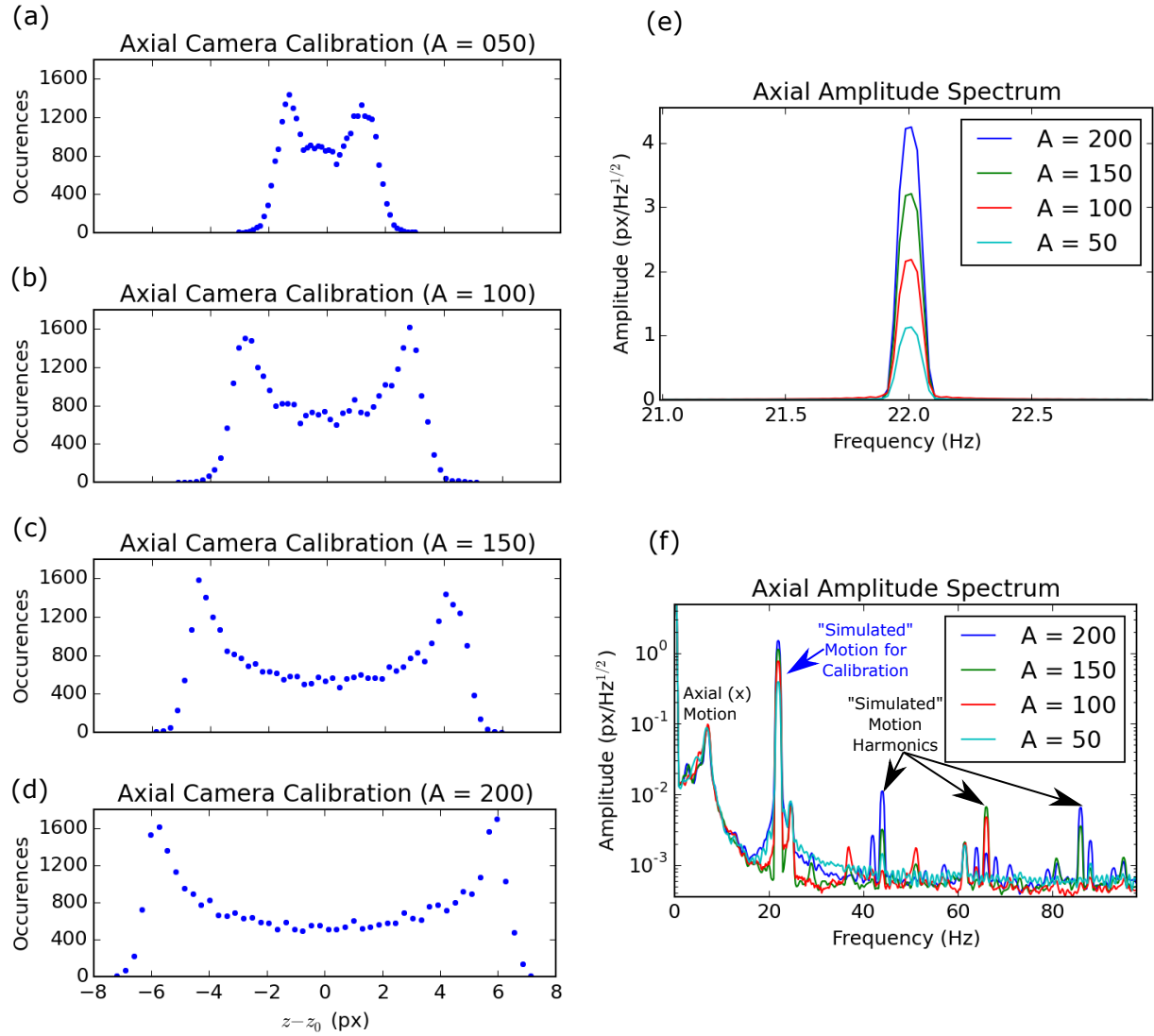


Figure 43: Analysis of amplitude calibration for high speed camera in the axial direction. Histograms for particle displacement at various drive amplitudes are shown in (a)-(d). Linear amplitude spectra comparing all 4 drive amplitudes is shown in (e). A semi-log plot showing the full amplitude spectra is shown in (f).

Fig. 43 (f) displays a larger frequency range for the amplitude spectra on a semi-log plot. The cooled axial motion peak is noticeable near $f_z \approx 7$ Hz, where its width is broadened by

the applied feedback damping. The peak corresponding to the drive is visible as the sharp peak near $f_z \approx 22$ Hz. Additional peaks are evident at harmonics of the drive frequency (in particular, at $f'_z = \{2f_z, 3f_z, 4f_z\}$). Since the response of the camera as a detector is linear over its entire sensor area, the peaks at harmonics must be attributed to nonlinearities in either the driving voltage or in the response of the galvo. At any rate, the amplitudes of the harmonic peaks are orders of magnitude smaller than the amplitude of the drive peak, so their contribution to the measurement is negligible. In addition, the axial motion peak is significantly smaller than the drive peak, so no frequency domain analysis is necessary in this case; calculating the amplitudes using the frequency domain data yields a change on the order of 0.5 %.

The same method is utilized to calibrate the vertical motion, with one caveat: the measurement of the vertical amplitudes was found to be lightly dependent on the drive frequency. This is evident on both the camera and the QPD. While the QPD signals are filtered to some extent (see Section B.4), the camera signal is not, which suggests that the reason for the dependence is the frequency and amplitude response of the galvo, and not of the QPD. The chosen way to deal with the response is to calibrate the vertical motion on either side of the resonant frequency and compute the average of the two. For this purpose, the frequencies $\omega_{low}/2\pi = 25\pi \approx 78.5$ Hz and $\omega_{high}/2\pi = 37\pi \approx 116$ Hz were chosen, with the vertical resonant frequency roughly $\omega_y/2\pi = 96$ Hz.

The set of data analogous to the axial motion data in Fig. 43 is shown in Fig. 44. While it is similar to the axial data set, there are several differences that are worthy of discussion.

First, comparing Fig. 43 (a)-(d) to Fig. 44 (a)-(d), it is noticeable that the amplitude response of the vertical motion is smaller (by about 33 %) than the axial amplitude response for the same drive. This is most likely due to the response of the galvo, as there is no guarantee that components in each direction of the drive circuitry are identical. However, this might suggest a fundamental alignment issue breaking the cylindrical symmetry of the optical system, and could conceivably be related to the transverse motion coupling seen in the vertical signals (as mentioned in Section 2.5.3).

Second, Fig. 44 (e) shows yet another confirmation of the reliability issues created by working in the frequency domain with the camera data and mentioned in Section 2.5.3; while

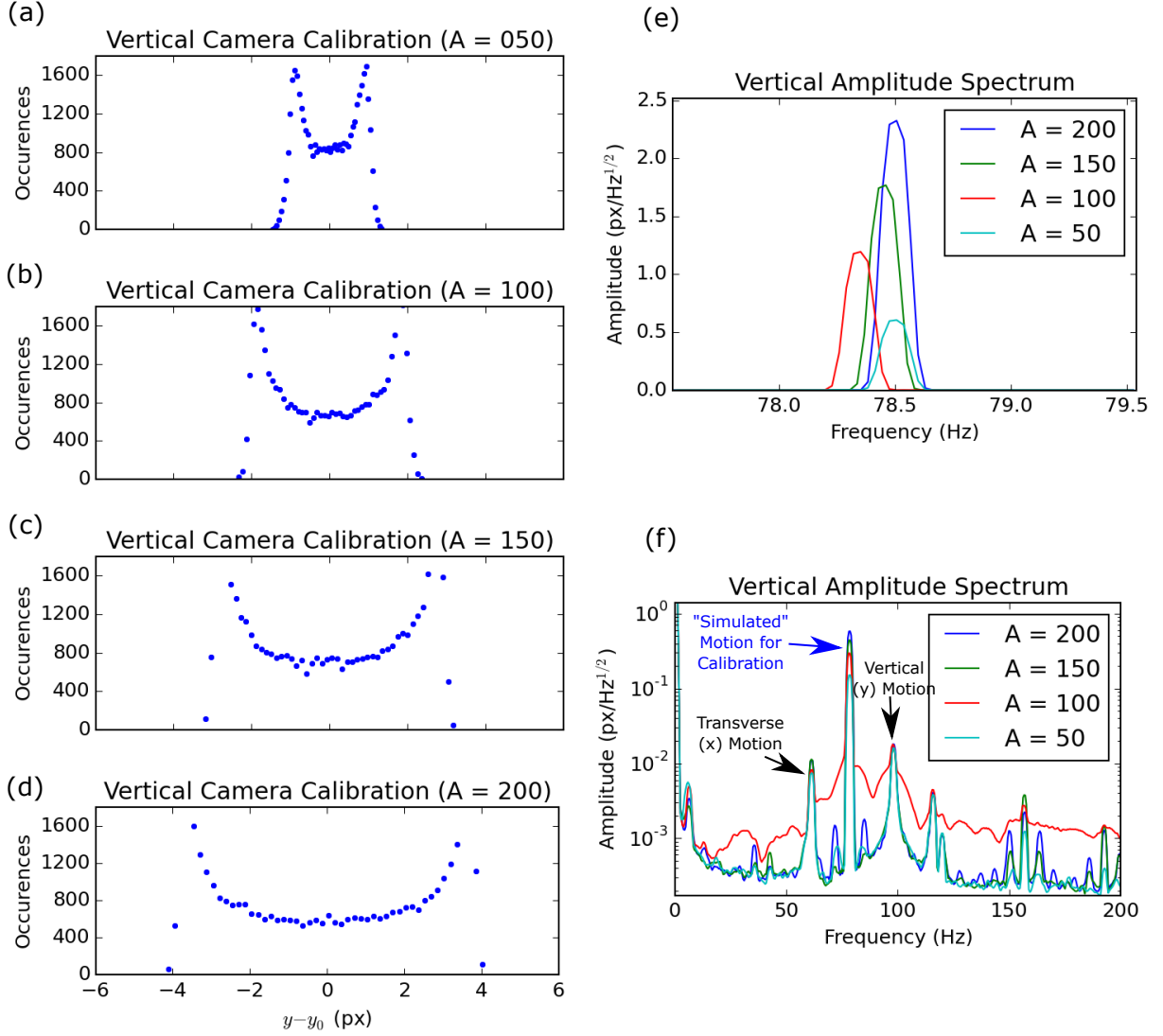


Figure 44: Analysis of amplitude calibration for high speed camera in the vertical direction. Data shown is for the low drive frequency, $\omega_y/2\pi \approx 78.5$ Hz. Histograms for particle displacement at various drive amplitudes are shown in (a)-(d). Linear amplitude spectra comparing all 4 drive amplitudes is shown in (e). A semi-log plot showing the full amplitude spectra is shown in (f).

the drive frequency is certainly identical in all instances, the location of the peak slightly changes during different measurements. This is most likely a result of using a higher sampling rate for the vertical motion (the vertical motion was sampled at ~ 500 Hz, while the axial was sampled at ~ 200 Hz). The rates were chosen to achieve adequate sampling of the distributions in Fig. 43 (a)-(d) and Fig. 44 (a)-(d), to account for the factor of ~ 5 difference in the drive frequencies chosen. A similar issue is visible as an increased background level in the $A = 100$ curve in Fig. 44 (f). Again, this has no effect on the calculation performed - it is likely due to a purely hardware issue, such as occasional unrecorded frames of data.

Finally, Fig. 45 displays the fits for the axial and vertical calibration slopes. For the curves presented, the axial slope is determined as $m_{\alpha,z} = (18.96 \pm 0.1) \times 10^{-3}$ px/g.u., and the average of the two vertical slopes is determined as $m_{\alpha,y} = (11.2 \pm 0.1) \times 10^{-3}$ px/g.u..

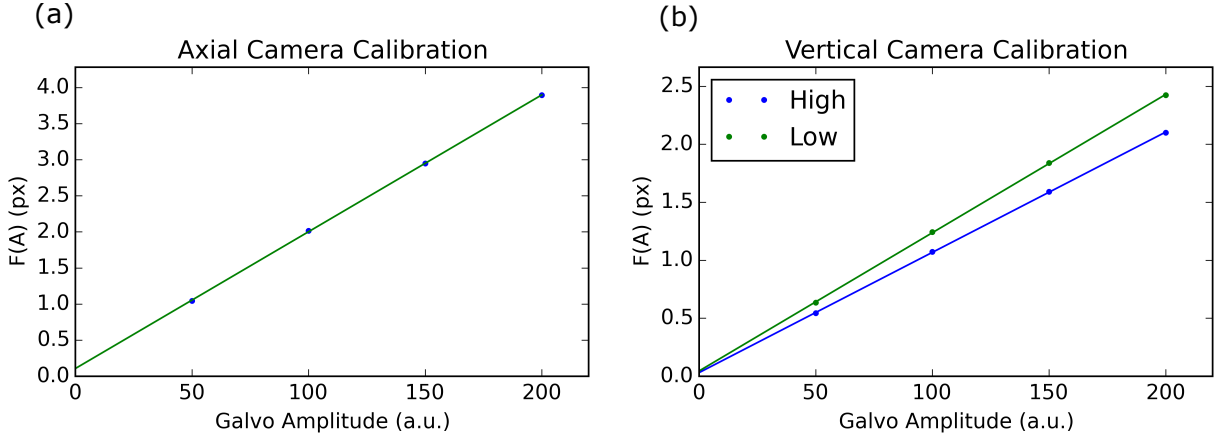


Figure 45: Fits to Eq. 2.12a for (a) the axial and (b) the vertical directions to determine the camera distance to galvo drive amplitude calibration.

Using the calibrated magnification of the system ($1 \text{ px} = 0.259 \text{ } \mu\text{m}$, which is the size of a single pixel ($14 \text{ } \mu\text{m}$) divided by the magnification of the system (54.4)), we have

$$m_{\alpha,z} = (4.91 \pm 0.03) \times 10^{-3} \text{ } \mu\text{m/g.u.} \quad (2.15)$$

$$m_{\alpha,y} = (2.89 \pm 0.02) \times 10^{-3} \text{ } \mu\text{m/g.u.} \quad (2.16)$$

Finally, knowing that $\langle |\cos(\omega t)| \rangle_t = 2/\pi$, we extract α_z and α_y :

$$\alpha_z = 7.72 \pm 0.04 \text{ nm/g.u.} \quad (2.17)$$

$$\alpha_y = 4.54 \pm 0.04 \text{ nm/g.u.} \quad (2.18)$$

Given that the range of the output to the galvo is ~ 4000 g.u., the full range R_i of movement accessible to the galvo in the z and y directions is:

$$R_z \approx 31 \text{ } \mu\text{m} \quad (2.19)$$

$$R_y \approx 18 \text{ } \mu\text{m} \quad (2.20)$$

Looking at Fig. 45, it can be seen that none of the calibrations crosses the x-axis at $x = 0$. This implies that there is some slight error in the calibration procedure - however, since there are somewhat large uncertainties in many of the other parameters when reporting cooling results, this will not be the limiting uncertainty in the temperatures reported.

2.7.2 Quadrant Photodiode Calibration

The goal of any of these distance calibrations is to obtain a value for the quadrant photodiode signal conversion from a voltage to meters. The camera calibration in Section 2.7.1 was the first part of this process. The quadrant photodiode part of the process is essentially the same as the camera calibration, but with a few key differences:

- A. The QPD has a much smaller linear range, as mentioned in Section 2.7.2.1 and Section 2.3.2.4, so the drive amplitude for the QPD calibration must be much smaller.
- B. The QPD calibration *IS* sensitive to the scattered light intensity and particle size. It must be performed for *every* particle, and even multiple times for the same particle if considerable time has past, to account for laser power fluctuations or particle drift.
- C. Because of item (B.), the particle image must be well centered on the QPD.

D. Because of the smaller drive amplitude, the particle motion may be much closer in magnitude to the galvo simulated motion. Thus, working in the frequency domain is likely required.

Since this is so crucial to the final measurement, the procedure for doing this is outlined here in the main text as follows:

1. Roughly center the uncooled particle on the QPD by monitoring the low-pass-filtered motion voltage (See Section 2.3.3).
2. Reasonably cool the particle. This generally causes a shift in the centering (for example, since the illumination light is Gaussian shaped, the relation of the particle's equilibrium position to the beam's intensity maximum plays a key role in the "centering" for large motion amplitudes).
3. Recenter the particle. Turn on the galvo tracking program any time the particle is not being driven.
4. Cool the particle with a narrow filtering bandwidth ($\sim 1 - 2$ Hz) in all directions.
5. Drive the particle at a non-overlapping frequency.
6. Filter the obtained data by converting to the frequency domain and zeroing the data outside of a small bandwidth (~ 3 Hz), thus removing particle motion.
7. Calculate the desired function ($\langle |x| \rangle$ or $\sqrt{\langle x^2 \rangle}$), either in the time domain (either) or in the frequency domain (RMS only).
8. Repeat 3-7 for several amplitudes.
9. Extract the slope, m_β .

Presumably because of the large impact these requirements have on the measurement, the calculation of the QPD calibration is frequently the limiting factor when computing the error in any effective temperature measurement obtained.

2.7.2.1 Linear Range Test To determine an acceptable range of drive amplitudes, many measurements are made with drive amplitudes from small to large. The expected result of this test will be a curve that looks linear in some region (from 0 drive amplitude to some undetermined maximum drive amplitude). As the drive amplitude increases, the

turning points of the particle's image on the detector swing further away from the central region. Once it swings all the way from being completely imaged on one side or the other of the center, the signal will approach that of a square wave. At this point, increasing the drive amplitude further will have no effect on the signal response. As such, we expect a linear response for small amplitudes with an asymptotic approach to the maximum (square wave) signal as the drive amplitude increases.

This behavior can be seen in Fig. 46 (a) and (b). For the axial data presented, the drive frequency is $\omega/2\pi = 6\pi \approx 19$ Hz.

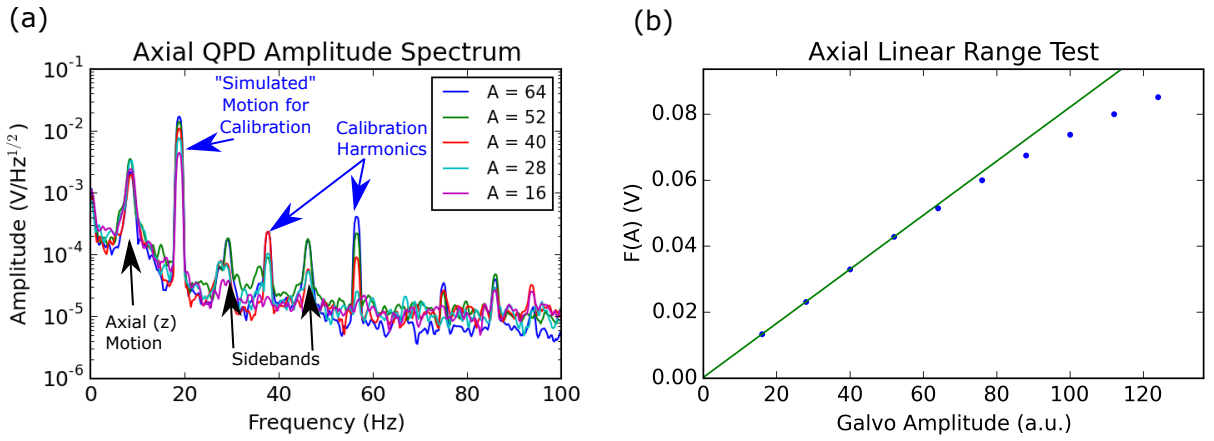


Figure 46: (a) Amplitude spectra of axial QPD linear range testing. (b) Determination of linear range by plotting the measured signal average amplitude, akin to Fig. 45. Particle from 12-07-2017 was utilized for this test.

In Fig. 46 (a), we examine the amplitude spectrum of the axial motion signal for various drive amplitudes. The sharp axial drive peak is evident near $f_z \approx 18$ Hz, while the cooled, broadened axial motion peak is evident near $f_z \approx 7$ Hz. It can be seen that, as the drive amplitude increases, frequencies at the harmonics of the driven motion start appearing, which is a clear sign of a nonlinearity. In addition, sideband peaks are evident on either side of the second harmonic ($f_z \approx 36$ Hz). As the amplitude increases, the amount of signal in the harmonics increases. Only contributions from the first harmonic of the driven motion (as further explained in Section 2.7.2.2) are included in the calibration calculation.

In Fig. 46 (b), we plot the measured amplitude of the signal (as in Fig. 45). While the result is difficult to describe mathematically with a smooth function of amplitude, it is obvious visually that the curve is no longer linear at the data point of $A = 64$.

In an attempt to quantify this, linear fits to the smallest 3, 4, and 5 drive amplitude data points were calculated; fitting 3 points instead of 4 results in a change of $\sim 0.3\%$ to the extracted slope, which is in line with the error allowed in the camera measurement. In comparison, fitting 5 points instead of 4 results in a change of $\sim 2.3\%$. The fit for 4 data points is the smooth green line displayed in Fig. 46. By this measure, no drive amplitude greater than 54 g.u. was used in the calibration for any particles.

Based on the result Eq. 2.17, this corresponds to a linear range R of:

$$R_{z,qpd} \approx 400 \text{ nm} \quad (2.21)$$

The test had also been performed previously in the vertical direction. Given that the 4 quadrants of the QPD are identical, there is no reason to believe the physical linear range would be any different than the range axially. However, for completeness, the data for the vertical channel is shown in Fig. 47.

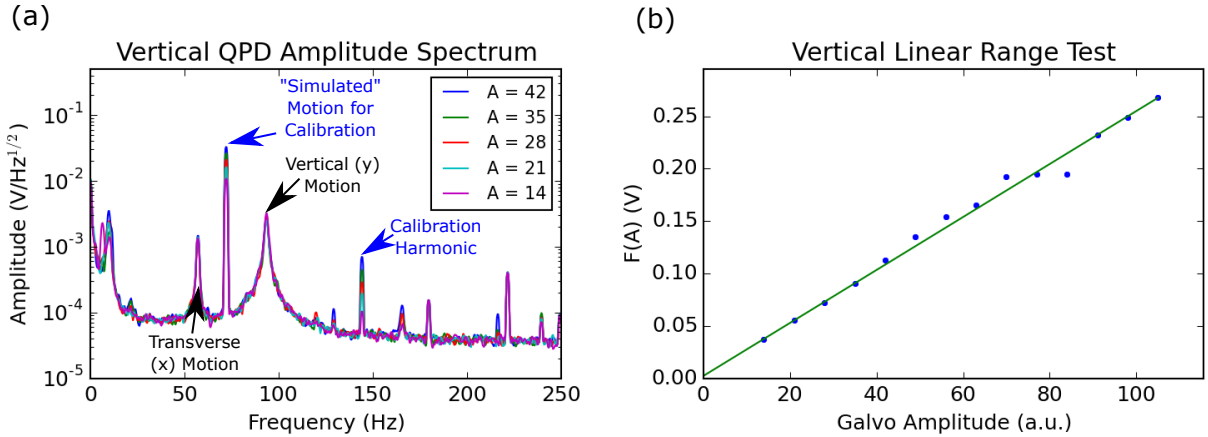


Figure 47: (a) Amplitude spectrum of vertical QPD linear range testing. (b) Determination of linear range by plotting the measured signal average amplitude, akin to Fig. 46. Particle from 05-17-2017 was utilized for this test.

It is clear that the data taken was not as clean as the axial data - I believe this is simply coincidental, but this test should be performed again on a particle to make sure. In this case, it is again the lowest 4 data points that are used to fit the linear range. Using results Eq. 2.17, Eq. 2.18, and Eq. 2.21, and assuming the physical linear range to be equal in both directions, I would expect the linear vertical linear range to extend to ~ 88 g.u., given that the galvo response seems to be roughly $\alpha_y/\alpha_z = 0.58$ times weaker in the vertical direction. This explains why there is not strong evidence of nonlinearity in the larger drive amplitudes, compared to the obvious evidence in Fig. 46.

Note that the overall amplitude is different for the axial and vertical data, which corresponds to different experimental parameters (for instance, illumination intensity). For these tests, the overall amplitude is irrelevant - it is the relative amplitudes that we are examining.

2.7.2.2 Example Particle Calibration An example of the calibration for an actual particle is now analyzed. As discussed, we work in the frequency domain for this calibration. Fig. 48 shows the amplitude spectra obtained from running the calibration process on a silica microsphere (specifically, the particle from 10-15-2017).

In Fig. 48 (a), the axial spectrum for the smallest drive amplitude ($A = 16$ g.u.) is displayed. The particle's cooled axial motion is visible as a wide peak near $f_z \approx 7$ Hz, with the simulated motion evident as a sharp peak near $f_z \approx 18$ Hz. Additionally, a peak near $f_z \approx 60$ Hz is evident, caused either by electrical interference or the coupling of transverse motion into the axial signal. In Fig. 48 (b), the vertical spectra for the smallest drive amplitude ($A = 16$ g.u.) for the low and high drive frequencies are displayed. The cooled vertical frequency ($f_y \approx 96$ Hz) and cooled transverse frequency ($f_x \approx 60$ Hz) are visible as broadened resonances, while the peaks corresponding to the low and high frequency simulated motion near $f_y \approx 79$ Hz and $f_y \approx 116$ Hz, respectively, are sharp. As evidenced from all three spectra, it is necessary to remove contributions from the particle's true motion, as they are similar in magnitude to the drive amplitude.

To perform the calculation chosen ($\langle |x_i| \rangle$), a single FFT with no windowing function (or the so-called rectangular window) is computed for the entire data set for a given drive amplitude. This frequency domain data is then filtered around the drive frequency, meaning

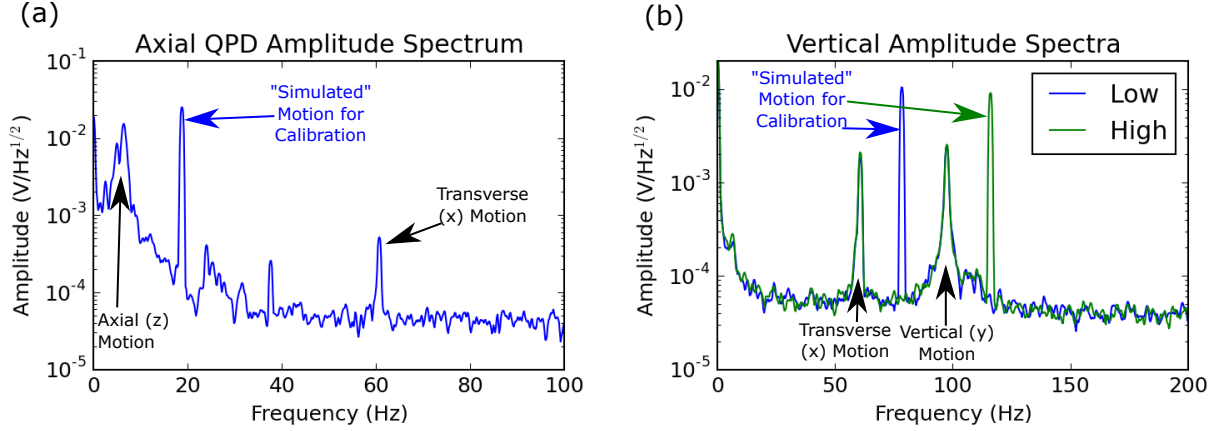


Figure 48: Amplitude spectrum for the smallest galvo drive amplitude ($A = 16$ g.u.) for (a) axial QPD calibration and (b) vertical QPD calibration. A flat-top FFT window was used. Particle utilized is a $1.54 \mu\text{m}$ SiO_2 microsphere from 10-15-2017.

any points in the FFT corresponding to frequencies outside a small bandwidth (here, $\Delta f = \pm 3$ Hz) are set to zero. Two examples of the amplitude spectra computed are shown in Fig. 49.

Note the spectra obtained in Fig. 49 are artificially broadened due to spectral leakage when computing the FFT. This is a well-known occurrence in FFT computation when the data is not strictly periodic with the sampling time period. This is usually dealt with by multiplying the data by a ‘windowing function’ that will force the data to smoothly approach 0 at the start and end of the dataset. Since we are calculating $\langle |x_i| \rangle$ from this data, we have chosen not to use a windowing function to avoid normalization issues. It has been determined that the values calculated are not adversely affected by this broadening.

To compute the average amplitude, the data is first returned to the time domain using the inverse FFT. Note that if we had chosen to utilize $\langle x_i^2 \rangle^{1/2}$ as the metric, we could use the frequency domain data via Parseval’s theorem Eq. 1.35.

There is likely an opportunity for improvement here - it may be better to have higher frequency resolution, as the FFT data is always limited in resolution by the frequency spacing

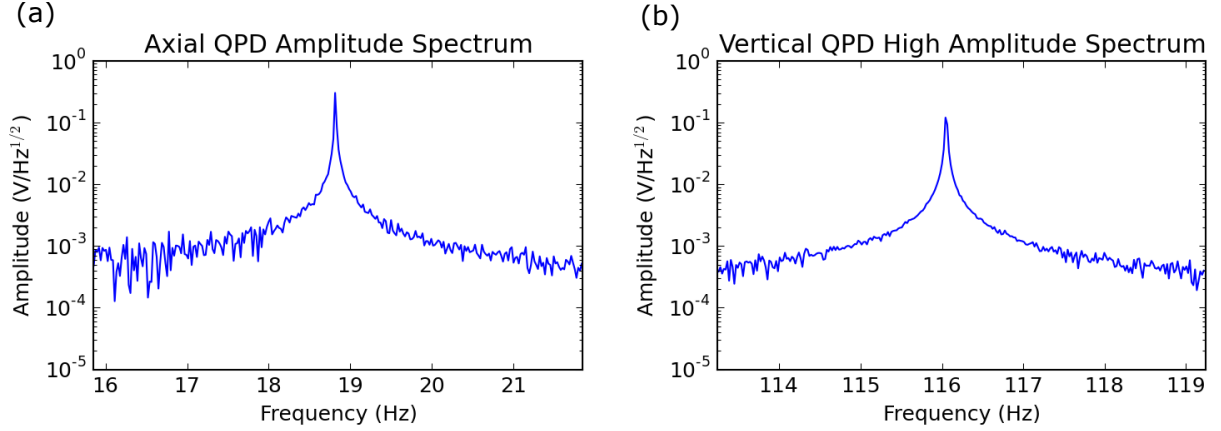


Figure 49: Amplitude spectra for the smallest galvo drive amplitude ($A = 16$ g.u.) filtered around the drive frequency for the (a) axial, $f_z = 6\pi \approx 19$ Hz and (b) vertical high, $f_y = 37\pi \approx 116$ Hz for the same particle used in Fig. 48.

of the Fourier Transform.

The final calibration data set, analogous to Fig. 45, is displayed in Fig. 50. It is noticeable in the axial calibration (Fig. 50 (a)) that the final data point *may* be outside of the linear range of the QPD; however, given the results from Fig. 46, the slope was still computed with all data points.

The values obtained for the fits are

$$m_{\beta,z} = (3.55 \pm 0.08) \times 10^{-3} \text{ V/g.u.} \quad (2.22)$$

$$m_{\beta,y} = (2.06 \pm 0.01) \times 10^{-3} \text{ V/g.u.} \quad (2.23)$$

As in Eq. 2.17 and Eq. 2.18, we can extract β_z and β_y :

$$\beta_z = (5.58 \pm 0.10) \times 10^{-3} \text{ V/g.u.} \quad (2.24)$$

$$\beta_y = (3.23 \pm 0.02) \times 10^{-3} \text{ V/g.u.} \quad (2.25)$$

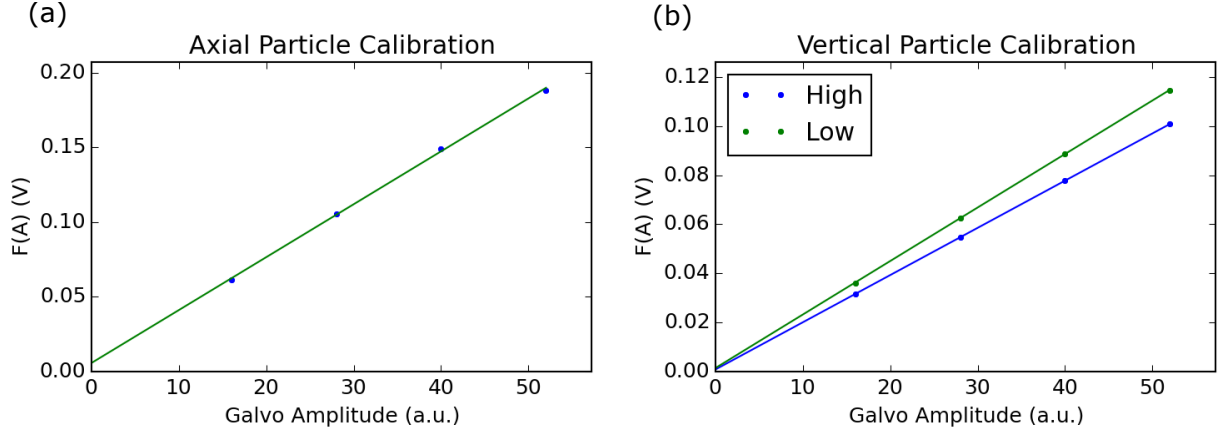


Figure 50: Fits to eq Eq. 2.12a for (a) the axial and (b) the vertical directions to determine the QPD voltage to galvo drive amplitude calibration for the same particle used in Fig. 48.

Finally, we obtain the desired calibrations c_z and c_y :

$$\begin{aligned}
 c_z &= \frac{m_{\alpha,z}}{m_{\beta,z}} \\
 &= \frac{4.91 \times 10^{-3} \text{ } \mu\text{m/a.u.}}{3.55 \times 10^{-3} \text{ V/a.u.}} \\
 &= 1.38 \pm .01 \frac{\mu\text{m}}{\text{V}}
 \end{aligned} \tag{2.26}$$

$$\begin{aligned}
 c_y &= \frac{m_{\alpha,y}}{m_{\beta,y}} \\
 &= \frac{2.89 \times 10^{-3} \text{ } \mu\text{m/a.u.}}{2.06 \times 10^{-3} \text{ V/a.u.}} \\
 &= 1.40 \pm .02 \frac{\mu\text{m}}{\text{V}}
 \end{aligned} \tag{2.27}$$

As discussed, these results are performed every time a temperature measurement is to be reported. Since we generally utilized the same illumination intensity, particle size, and optical setup, the results are most commonly in the range of $c_i \approx 1 \text{ } \mu\text{m/V}$.

3.0 FEEDBACK COOLING RESULTS AND DISCUSSION

3.1 CHAPTER OUTLINE

Once the mass of the trapped particle has been determined, and the optical system has been calibrated for the same particle (see Section 2.2 for a quick overview), the feedback mechanism is enabled and the particle motion is damped to some minimum value. This chapter contains the primary results and discussion of this dissertation. The results contained in Section 3.3 are the best confirmed temperature vertically, and close to the best obtained result axially.

3.2 TARGET RESULTS

The target result of this work is to remove energy from the particle's motion until further removal is fundamentally prohibited by the laws of quantum mechanics; in other words, we would like to cool the particle to its quantum mechanical ground state. In the regime that the energy remaining in a DOF is on the order of its ground state energy, the particle motion would be damped to the extent that the fluctuations (or uncertainty) in position measurements would match that predicted by quantum mechanics. Namely, referring to Eq. 1.59:

$$\langle x_i^2 \rangle = \frac{\hbar}{2m\omega_i}$$

For the average mass of spheres typically utilized (1.54 μm diameter SiO_2) and typical

axial and vertical trapping frequencies ($f_z \approx 7.0$ Hz, $f_y \approx 100.0$ Hz), the ground state average amplitude fluctuations are:

$$\sqrt{\langle z^2 \rangle}_{gnd} = 1.85 \times 10^{-11} \text{ m} \quad (3.1)$$

$$\sqrt{\langle y^2 \rangle}_{gnd} = 4.90 \times 10^{-12} \text{ m} \quad (3.2)$$

Using Eq. 1.58 and the same parameters for the mass and frequencies, we assign effective temperatures to the ground states:

$$T_{gnd,z} = 1.68 \times 10^{-10} \text{ K} \quad (3.3)$$

$$T_{gnd,y} = 2.40 \times 10^{-09} \text{ K} \quad (3.4)$$

In practice, the minimum value obtained for the motion in any DOF is dependent on a whole host of system and experimental parameters that must be optimized to reach the ideal results. If we assume perfect experimental conditions (like noiseless feedback and perfect collection efficiency), we would expect the current limitation to be imposed by the background gas pressure in the chamber. As discussed in Section 1.4.1.4, we can relate the predicted natural damping rate Γ_A to the background pressure via Eq. 1.47:

$$\Gamma_A(P) = \frac{P}{\rho r} \sqrt{\frac{8}{\pi} \frac{m_g}{k_B T}}$$

Utilizing common values for these parameters (i.e. $1.54 \text{ } \mu\text{m SiO}_2$, $T = 295\text{K}$), and the pressure from the example results of Section 3.3 ($P \approx 2.0 \times 10^{-10}$ Torr), we expect a natural damping rate of:

$$\Gamma_a(P_{best}) \approx 1 \times 10^{-7} \text{ s}^{-1} \quad (3.5)$$

Utilizing Eq. 1.43 ($\Gamma_A \leq \frac{T_{fb}}{T_A} \Gamma_{fb}$) and the damping rates of the examples results of Section 3.3, we estimate the absolute best temperature we can achieve based purely on current vacuum limitations:

$$T_{z,target} \approx 3 \times 10^{-6} \text{ K} \quad (3.6)$$

$$T_{y,target} \approx 7 \times 10^{-7} \text{ K} \quad (3.7)$$

The cooling results from Section 3.3 represent the best vertical temperature and nearly the best axial temperature recorded to date:

$$T_z \approx 0.6 \times 10^{-3} \text{ K} \quad (3.8)$$

$$T_y \approx 1.2 \times 10^{-3} \text{ K} \quad (3.9)$$

These estimates suggest that we are obtaining temperatures that are factors of roughly 200 and 1800 higher than the target temperatures for the axial and vertical directions, respectively.

Notably, performing the same calculations for the best case axial cooling results (11-17-2017-Midnight, pressure $P = 5.0 \times 10^{-10}$ Torr, $T_z = 0.14 \times 10^{-3}$ K, $\Gamma/2\pi = 1.5$ Hz, $2r \approx 1.96 \text{ }\mu\text{m}$), we obtain results that are only a factor of ~ 20 away from the best case estimates. This suggests we are actually able to do quite well in the axial direction, considering these are estimates from a theoretical prediction. However, we are doing quite poorly vertically, in comparison.

Example results and a table of all results are reported in Section 3.3 and Section 3.4, followed by a discussion of possible explanations for the current limitations.

While still far from the ground state, these results represent a significant $\sim 10^3$ improvement in both the axial and vertical directions from the previously reported results in a magneto-gravitational trap [24].

3.3 EXAMPLE RESULTS

For all of the data reported in this section (Sec. 3.3), the particle used was the SiO₂, 1.54 μm diameter microsphere trapped on 10-15-2017. The mass determination, camera calibration, and quadrant photodiode calibration were performed as described in Sections 2.5, 2.7.1, and 2.7.2, respectively. The particle was fully neutralized via the method presented in Sec. 2.6, with its specific neutralization confirmation displayed in Fig. 42 (b). Additional results for this particle were also obtained in the fully enclosed table top described in Appendix D.1, so this particle represents the best effort to date of full experimental control.

3.3.1 Experimental Parameters

The experimental parameters for this particular particle (1.54 μm SiO₂ microsphere from 10-15-2017) were:

- Pressure $P = 2.0 \times 10^{-10}$ Torr, as reported by the ion pump.
- Particle fully neutralized.
- Scattered illumination power reaching the QPD $P_{830,qpd} \approx 1$ nW.
- Scattered illumination power (830 nm) $P_{830,s} \approx 5$ nW (accounts for beamsplitters, collection efficiency).
- Incident illumination power (830 nm) $P_{830} \approx 6$ μW (measured).
- Incident cooling power (660 nm) $P_{660} \approx 2.4$ μW (measured) for z cooling.
- Incident cooling power (660 nm) $P_{660} \approx 15$ μW (measured) for y cooling.
- Estimated scattered cooling power (660 nm) $P_{660,s} \approx (0.5 \text{ nW}, 3 \text{ nW})$ for (z, y) .

The detector utilized was the QPD, with an extra gain of 10 from the Programmable Gain Amplifier (noted as PGA in Fig. 13).

The total incident illumination power is $P_{830} \approx 6$ μW , as measured prior to the focusing lens L4 on an optical power meter, which is the nominal operating level for most experiments. More importantly, this corresponds to roughly $P_0 = 1.0$ nW of (scattered) optical power reaching the QPD. This value was chosen empirically first to provide a maximum signal in

the 1-2 V range. With the gain of the QPD amplifier from Eq. B.1, the extra factor of 10 gain from the PGA, and the detector efficiency $\epsilon \approx 0.6$ A/W, this leads to a maximum voltage signal from the QPD of:

$$\begin{aligned} V_m &\approx 1.0 \times 10^{-9} \text{ W} \times 0.6 \frac{\text{A}}{\text{W}} \times 2.41 \times 10^9 \Omega \\ &\approx 1.45 \text{ V} \end{aligned}$$

This value was then later verified by measuring the total (scattered) power at the QPD, but with much higher incident illumination powers (increasing factors of 10 up to ~ 13 mW, which increased the scattered power to a value measurable on an optical power meter) and extrapolating to 6 μW .

The scattering for each individual particle was not measured - it was just ensured that the maximum signal was always $1 \text{ V} < V_m < 3 \text{ V}$, while the total incident illumination power was always verified as $P_{830} \approx 6 \mu\text{W}$.

As mentioned above, we estimate the total scattered illumination power P_s :

$$P_s \approx 5 \text{ nW}$$

We compare this to the optimal value of P_s , which can be computed by determining the radiation pressure shot noise of the illumination on the particle with Eq. A.8 from Appendix A.1:

$$P_s \leq 2m\alpha c \lambda f_i^2$$

Here, α is an experimental parameter related to the bandwidth of the cooling, which is empirically determined as $\alpha \approx 0.1$. For an axial frequency of $f_z = 7.0$ Hz, a vertical frequency of $f_y = 97.0$ Hz, and a typical mass ($m = 3.5 \times 10^{-15}$ kg), this leads to different optimal powers in each direction:

$$P_{s,z} \approx 1 \times 10^{-11} \text{ W}$$

$$P_{s,y} \approx 1 \times 10^{-9} \text{ W}$$

This means we are right in line with the correct power vertically, but a factor of ~ 100 higher than the optimal axial power. However, since the PSD of shot noise (see Eq. A.11) is linear in the scattered power, this would limit us to an effective temperature ~ 100 times larger than the ground state temperature, which we are still several orders of magnitude (~ 4) above.

The total incident cooling power was $P_{660,z} \approx 2.4 \mu\text{W}$ and $P_{660,y} \approx 15 \mu\text{W}$ for the axial and vertical cooling, respectively, as measured prior to lens L4 with an optical power meter. These are determined experimentally as the minimum amount of optical power required to reach the best cooling (as determined by the final damping width being near the $\alpha \approx 0.1$ value. Of course, the cooling power has shot noise as well, which must be considered. However, since the total cooling and illumination powers are roughly equal, so too will the cooling shot noise power be roughly equal to the illumination shot noise power. As such, we are still well below power levels that would cause the primary cooling limitation via shot noise.

3.3.2 Results

The particle's cooling results in the axial and vertical DOF are shown in Fig. 51 (a) and (b), corresponding to effective temperatures of $T_z = 0.6 \pm 0.1 \text{ mK}$ and $T_y = 1.2 \pm 0.1 \text{ mK}$, respectively. The data points shown in Fig. 51 are the computed, normalized power spectrum (Eq. 1.39) of the particle's motion, with fits to Eq. 1.29. The fit parameter results are displayed in Table 5.

The method for determining these effective temperatures is to fit data in a region near each DOF resonance to the theoretical power spectral density (Eq. 1.29), thereby obtaining $\langle x_i^2 \rangle$ (Eq. 1.40) and thus T_{eff} (Eq. 1.18). To focus on the shape of the data and the fits, and to obtain the most accurate fits for the data, the plots in Fig. 51 are shown only over the frequency range for which the fit to Eq. 1.29 are performed. Calculating the effective temperature this way allows us to ignore contributions to the signal that we know are unrelated to the harmonic motion in the DOF of interest in a mathematically rigorous way.

For instance, to ensure that the result calculated using the power spectral density fits in

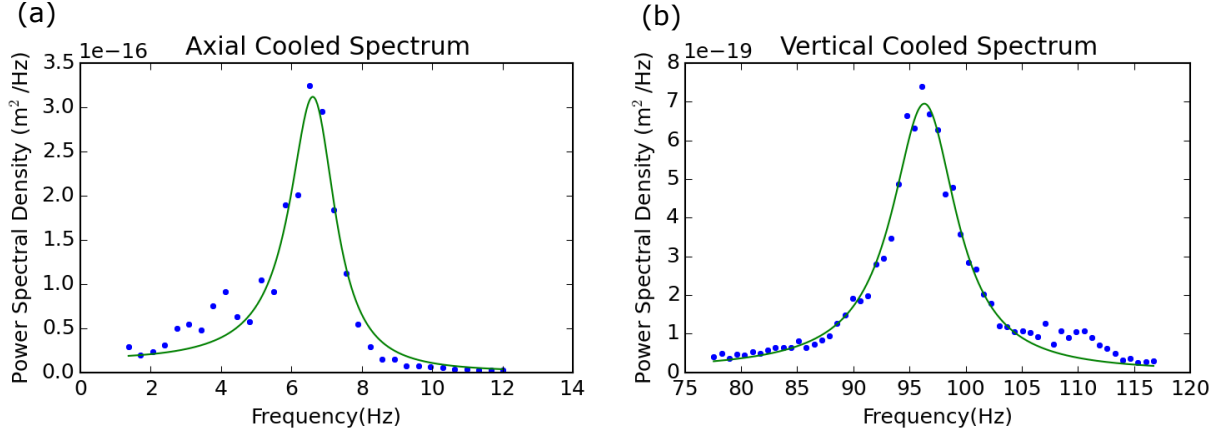


Figure 51: Plots of the power spectral density of the maximally cooled motion of the 10-15-2015, 1.54 μm SiO_2 particle are shown for (a) the axial (b) the vertical DOF.

DOF	T (mK)	A (m^2)	f_i (Hz)	γ (Hz)
Axial (z)	0.6 ± 0.1	$(3.4 \pm 0.4) \times 10^{-14}$	6.70 ± 0.05	1.6 ± 0.1
Vertical (y)	1.2 ± 0.1	$(3.1 \pm 0.2) \times 10^{-13}$	96.45 ± 0.08	7.0 ± 0.2

Table 5: Table of temperature results and fit parameters for 10-15-2017 particle.

Fig. 51 are accurate, we always double check the result by a straightforward calculation of $\langle x_i^2 \rangle$. Like discussed in Section 2.7.2.2, to report a temperature describing only the DOF of interest, we should not include contributions at unrelated frequencies (like the signal of the transverse motion coupling into the axial or vertical signals). The same data from Fig. 51 is shown with a broad frequency range in Fig. 52. The shaded area corresponds to the region of data used to compute a check of $\langle x_i^2 \rangle$, with its frequency range equal to that plotted in Fig. 51.

By calculating $\langle x_i^2 \rangle$ via Parseval's theorem (Eq. 1.35) with the bandwidths shown ($\Delta f_z = 11.0$ Hz, $\Delta f_y = 40.0$ Hz), we obtain values identical (to the specified precision) for the effective temperatures but with smaller uncertainties ($T_z = 0.60 \pm 0.02$ mK and $T_y = 1.18 \pm$

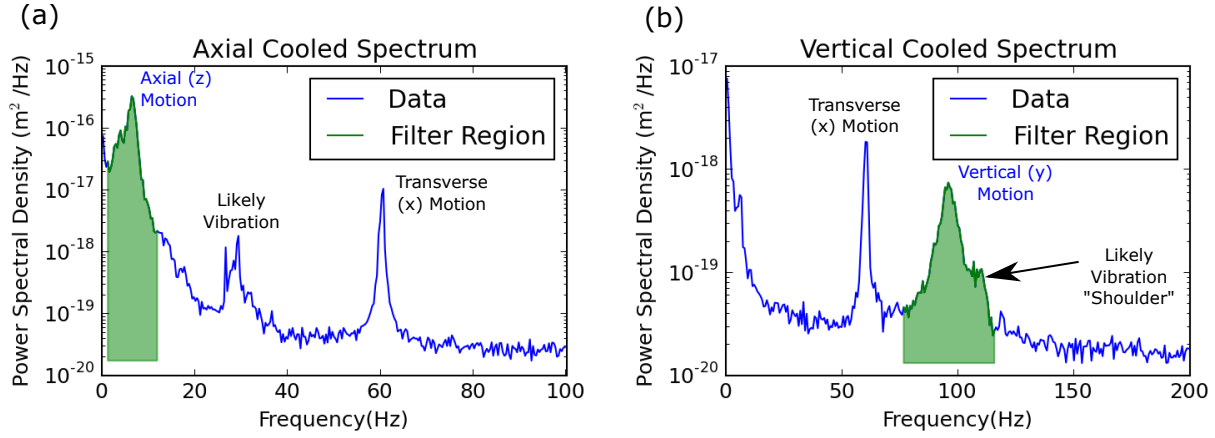


Figure 52: A larger frequency range of the power spectral density of the maximally cooled motion is shown for (a) the axial DOF and (b) the vertical DOF. The green, shaded area corresponds to the plotting windows of Fig. 51.

0.03 mK). It is evident in either spectrum shown in Fig. 52 that a calculation using either the power spectral density or the filtered straightforward calculation will remove contributions from unwanted frequencies.

Most notably, the transverse motion is strongly evident in both spectra near $f \approx 60.0$ Hz (while this is near the frequency of electrical line noise, these peaks have in fact been verified as the transverse motion); the relative strengths of the transverse peaks in the two cases should not be directly compared, as the cooling strength of the transverse motion is most certainly not identical in each case. In addition, a strong signature of $1/f$ type noise is evident in both spectra.

A third region of excitation is evident in the axial motion shown in Fig. 52 (a) in the frequency range of $f_z \approx 30.0$ Hz. It is strongly suspected that this peak is caused by vibrations somewhere on the optical table, with its source being yet unknown. This is substantiated by the vibration data displayed (for a different particle) in Fig. 63 (a,c,d), which clearly displays the same qualitative shape and effect in the motional data in the range from $f_z = 25 - 30$ Hz. A similar region is visible on the right shoulder of the vertical

peak shown in Fig. 52 (b) in the range $f_y \approx 110$ Hz, and again the main suspect is vibration. In addition, the correlation plots displayed in Fig. 64, again for a different particle, also show that the vibration sensor data is correlated with particle motion strongly in the regions mentioned.

A final calculation is completed for comparison in which $\langle x_i^2 \rangle$ is computed from its definition with no filtering whatsoever. This calculation yields temperatures of ($T_z = 0.67 \pm 0.03$ mK and $T_y = 6.79 \pm 0.20$ mK), which highlights the effect of filtering. For the axial motion, which has a much larger peak amplitude, filtering has almost no effect on reported temperature. For the vertical motion, the contributions from $1/f$ noise and the transverse and axial signal coupling are on the same order as that from the actual vertical motion, and so have a similar order effect on the reported temperature.

In practice, the power spectrum is obtained by an incoherent average of many power spectra. Continuous time data is recorded (typically, ≥ 90 s worth) and then partitioned into smaller sets of points. The total time (T_s) always corresponds to a sample size that is a power of 2, allowing the partitioned sets to be powers of 2 in length (which maximizes efficiency of the FFT algorithm). The total length is also chosen as a number $T_s \gg 1/\gamma$ (where γ is the width of the resonance and is on the order of $\gamma \approx 1 - 10$ Hz) to ensure the particle is in thermal equilibrium (with the cooling laser contributions included), and to allow at least several partitions for averaging. The overall number of partitions is determined solely on the basis of required frequency resolution (since $\Delta f = 1/N\Delta t$, the choice of the partition length determines the frequency resolution). With a given total time T_s , we can choose to decrease noise by choosing a smaller N (and thus performing more averaging) at the expense of frequency resolution, and vice versa.

While Fig. 51 or Fig. 52 contain all the necessary information for reporting the cooled temperature, neither gives a feel for the large degree of cooling that has been achieved. To show this, we plot the power spectral density of the particle's thermal motion and its cooled motion on the same plot, shown in Fig. 53. The cooled data plotted in Fig. 53 is the same data shown in Fig. 51 as captured from the quadrant photodiode detector, while the thermal data is a spectrum generated from the particle's thermal motion and captured on the high speed camera.

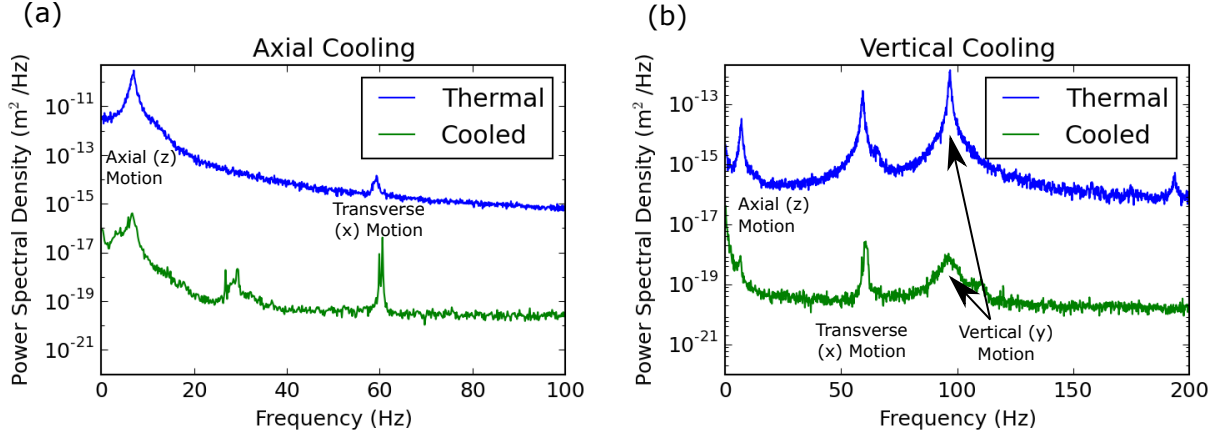


Figure 53: The power spectral densities of both the thermal motion and cooled motion are shown for (a) the axial DOF and (b) the vertical DOF for the same particle as the data shown in Fig. 51 and Fig. 52.

The total energy can be read off of this figure as the area underneath a given curve. It is easy to estimate, based on the ratio height of the peaks at $f_z \approx 7.0$ Hz (axial, Fig. 53 (a)) and $f_y \approx 96.9$ Hz (vertical, 53(b)), that between 5 and 6 orders of magnitude of cooling have been achieved. Of particular note is the drastic difference in the background levels of each. This can be attributed to a physical difference in the experiment for each (the thermal data was taken at a much higher pressure ($\sim 10^{-4}$ Torr) than the cooled data ($\sim 10^{-10}$ Torr), as well as to noise in the measurement (the thermal data contained fewer samples than the cooled data, and the camera has a higher noise level than the quadrant photodiode, since there is an extra step of signal processing to find the Gaussian centers in the camera data).

For clarity, a summary of the results discussed are provided as Eq. 3.10 and Eq. 3.11, and Table 6.

$$T_z = (0.6 \pm 0.1) \times 10^{-3} \text{ K} \quad (3.10)$$

$$T_y = (1.2 \pm 0.1) \times 10^{-3} \text{ K} \quad (3.11)$$

$$\bar{n}_z = 1.9 \times 10^6 \quad (3.12)$$

$$\bar{n}_y = 2.7 \times 10^5 \quad (3.13)$$

$$\sqrt{\langle z^2 \rangle} = 3.9 \times 10^{-8} \text{ m} \quad (3.14)$$

$$\sqrt{\langle y^2 \rangle} = 3.9 \times 10^{-9} \text{ m} \quad (3.15)$$

DOF	Measurement Type	T_{eff}	$\sqrt{\langle x_i^2 \rangle}$
Axial (z)	Power Spectral Density Fit	$0.604 \pm 0.08 \text{ mK}$	39 nm
Axial (z)	Filtered $\langle z^2 \rangle$	$0.599 \pm 0.02 \text{ mK}$	39 nm
Axial (z)	Unfiltered $\langle z^2 \rangle$	$0.665 \pm 0.03 \text{ mK}$	41 nm
Vertical (y)	Power Spectral Density Fit	$1.250 \pm 0.09 \text{ mK}$	3.9 nm
Vertical (y)	Filtered $\langle y^2 \rangle$	$1.182 \pm 0.03 \text{ mK}$	3.8 nm
Vertical (y)	Unfiltered $\langle y^2 \rangle$	$6.792 \pm 0.18 \text{ mK}$	9.1 nm

Table 6: Summary of T_{eff} for example cooling results for different calculation schemes.

3.4 SUMMARIZED RESULTS

A graphical summary of all results with a valid mass and distance calibration is displayed in Fig. 54:

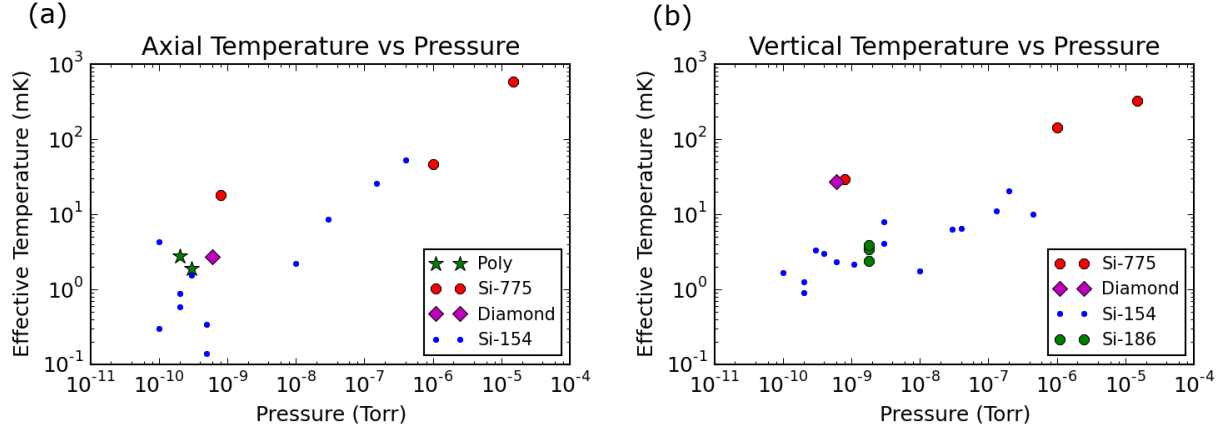


Figure 54: Graphical summary of cooling results obtained in the (a) axial and (b) vertical directions corresponding to results tables.

Fig. 54 shows two clear trends:

1. Lower temperatures are achieved axially than vertically for similar pressures.
2. Lower temperatures are archived for smaller particles.

These trends will be discussed in more detail in the following discussion sections.

Summarized tables of all cooling results where a valid detector calibration are given in Table 7, Table 8, and Table 9. Table 7 provides results from Bozeman, Montana using the ‘top hat’ mount for the chamber; Table 8 provides results from Pittsburgh using the ‘top hat’ mount for the chamber; Table 9 provides results from Pittsburgh using the translation stage as a chamber mount. A graphical summary of the results from all of these tables is displayed in Fig. 54. Spectra from all cooling results in the table are displayed in Appendix G.

Particle Date	ID	Type	Temp (mK)	P (Torr)	f_i (Hz)	γ (Hz)
12/12/2017	A	Poly	1.90 ± 0.61	0.3E-9	8.93	1.14
12/10/2017	A	Poly	2.80 ± 0.32	0.2E-9	8.30	1.06
12/07/2017	A	Poly?	0.87 ± 0.17	0.2E-9	9.14	1.30
12/02/2017	A	Si-1.54	0.30 ± 0.03	0.1E-9	8.68	1.06
11/26/2017	A-8P	Si-1.54*	0.34 ± 0.05	0.5E-9	8.80	1.28
11/26/2017	A-MN	Si-1.54*	0.14 ± 0.04	0.5E-9	8.68	1.51
11/18/2017	A	Diam.	2.72 ± 0.42	0.6E-9	7.34	1.48
11/18/2017	V	Diam.	26.9 ± 4.20	0.6E-9	98.09	9.06
11/10/2017	AE5	Si-7.75	588.79 ± 133.3	1.5E-5	7.00	1.74
11/10/2017	VE5	Si-7.75	323.49 ± 26.9	1.5E-5	96.71	2.12
11/10/2017	AE6	Si-7.75	46.09 ± 5.80	1.0E-6	6.91	1.34
11/10/2017	VE6	Si-7.75	144.70 ± 10.2	1.0E-6	96.86	0.93
11/10/2017	AE9	Si-7.75	18.04 ± 1.83	0.8E-9	6.78	0.51
11/10/2017	VE9	Si-7.75	29.06 ± 43.8	0.8E-9	96.37	1.52
10/15/2017	V17	Si-1.54	9.85 ± 2.53	4.5E-7	94.24	10.10
10/15/2017	V16	Si-1.54	6.33 ± 1.52	3.0E-8	96.49	2.19
10/15/2017	VP	Si-1.54	1.25 ± 0.09	0.2E-9	96.45	6.97
10/15/2017	AP	Si-1.54	0.58 ± 0.09	0.2E-9	6.70	1.48
10/15/2017	A2.17	Si-1.54	53.15 ± 12.8	4.0E-7	6.71	1.51
10/15/2017	A.17	Si-1.54	25.96 ± 2.72	1.5E-7	6.58	0.61
10/15/2017	A.16	Si-1.54	8.56 ± 1.48	3.0E-8	6.55	1.02
10/09/2017	12V	Si-1.54	3.34 ± 0.30	0.3E-9	97.97	6.05
10/09/2017	12A	Si-1.54	1.53 ± 0.20	0.3E-9	6.37	0.42
10/09/2017	11V	Si-1.54	2.99 ± 0.40	0.4E-9	97.23	6.72
10/09/2017	10V	Si-1.54	6.46 ± 0.64	4.0E-8	96.92	5.44
10/09/2017	9V	Si-1.54	20.47 ± 1.81	2.0E-7	96.37	5.86

Table 7: Cooling results obtained in Bozeman, using the ‘top hat’ chamber mount. ID column specifies A for axial and V for vertical, along with a label corresponding to the labels in Appendix G. * indicates double particle, particle with ? may have been SiO₂.

Particle Date	ID	Type	Temp (mK)	P (Torr)	f_i (Hz)	γ (Hz)
06/06/2017	A	Si-1.54	2.20 ± 0.16	1.0E-8	6.56	0.85
06/06/2017	V	Si-1.54	1.76 ± 0.27	1.0E-8	95.11	6.98
05/25/2017	V	Si-1.54	3.85 ± 0.38	??	133.29	1.07
05/22/2017	VLG	Si-1.86	3.41 ± 0.37	1.8E-9	94.63	14.39
05/22/2017	VML	Si-1.86	2.37 ± 0.29	1.8E-9	94.33	11.11
05/22/2017	V	Si-1.86	3.87 ± 0.39	1.8E-9	97.23	20.19
05/17/2017	V	Si-1.54*	0.90 ± 0.08	0.2E-9	93.51	14.77
05/16/2017	V	Si-1.54	2.88 ± 0.45	??	92.86	23.88

Table 8: Cooling results obtained in Pittsburgh, using the ‘top hat’ chamber mount. ID column specifies A for axial and V for vertical, along with a label corresponding to the labels in Appendix G. * indicates particle was known to be abnormally small.

Particle Date	ID	Type	Temp (mK)	P (Torr)	f_i (Hz)	Notes	γ (Hz)
05/11/2017	V12	Si-1.54	1.76 ± 0.24	??Baked	86.73		13.86
05/11/2017	V	Si-1.54	11.10 ± 1.10	1.3E-7	86.37		11.79
04/20/2017	V	Si-1.54	2.14 ± 0.44	1.1E-9	116.20		6.40
03/27/2017	V20	Si-1.54	1.85 ± 0.31	3.0E-9	119.36	Bad Fit	??
03/27/2017	V4	Si-1.54	1.47 ± 0.46	3.0E-9	117.97	Bad Fit	??
03/27/2017	V35	Si-1.54	4.09 ± 0.65	3.0E-9	116.16		5.80
03/27/2017	V28	Si-1.54	7.99 ± 1.22	3.0E-9	116.74		7.42
03/15/2017	V	Si-7.75	2258.12 ± 349.4	0.2E-9	119.84	Not maximum cooling	0.18
03/15/2017	A	Si-7.75	269.29 ± 114.9	0.2E-9	8.25	Bad Fit	??
03/08/2017	V13	Si-1.54	4.25 ± 0.64	$\geq .1E-9$	117.47		7.88
03/08/2017	A13	Si-1.54	4.26 ± 1.72	$\geq .1E-9$	7.18		0.79
03/08/2017	V10	Si-1.54	1.67 ± 0.35	0.1E-98	116.26	2 Day Bake	11.71
03/08/2017	Anti	Si-1.54	4.25 ± 1.13	??	117.65	Has interesting (x) peak	11.63
02/15/2017	v16	Si-1.54	2.29 ± 0.39	0.6E-9	85.04		7.68
02/15/2017	v17	Si-1.54	1.92 ± 0.19	0.8E-9	86.00	Bad Fit	??
02/13/2017	V	Si-1.54	3.40 ± 1.00	1.4E-8	86.14	Mass assumed	3.04
02/01/2017	A	Si-1.54	0.24 ± 0.07	??	??	Mass assumed	??

Table 9: Cooling results obtained in Pittsburgh, using the translational stage mount. ID column specifies A for axial and V for vertical, along with a label corresponding to the labels in Appendix G. ?? Indicates data was not recorded. Bad fit means fit parameters untrustworthy.

3.5 DISCUSSION

We now discuss several important characteristics of the cooling results, including cooling data and other analyses.

3.5.1 Cooling Efficiency

For the estimates for best case cooling that were described in Section 3.2, we had assumed a perfect feedback mechanism, meaning one that provides only a damping term to the particle's motion. In experimental reality, we do not expect a perfect feedback mechanism - at the very least, we will certainly be feeding back some noise, whether it be from the measured position signal or excess laser noise. This means the best case results we estimated in Section 3.2 are overestimates for the best cooling attainable.

To demonstrate this, we examine Eq. 1.44 $\left(T_{fb} = T_A \frac{\Gamma_A}{\Gamma_{fb}}\right)$. Recalling that the damping constant Γ and the FWHM of the PSD curve γ are related by $\gamma = \Gamma/2\pi$, we have:

$$T_{fb} = T_A \frac{\gamma_A}{\gamma_{fb}} \quad (3.16)$$

This equation states that the cooled effective temperature (T_{fb}) is inversely proportional to the FWHM (γ_{fb}) of the particle's cooled motion. We have direct control over γ_{fb} as an experimental parameter, which is the gain (G) of the feedback loop. In the ideal case, as we increase G (and thus γ_{fb}), the temperature will decrease proportionally. However, as alluded to in other sections, there are generally experimental limitations to the maximum cooling width, and thus the lowest temperature. As a rule of thumb, $\gamma_{max} \approx 0.1f_i$, which is essentially a statement that the oscillator remains under-damped. We experimentally and graphically demonstrate this relationship in Fig. 55 (a) and (c).

In Fig. 55 (a) and (c), we plot the PSD of the particle's motion in the (a) axial and (c) vertical directions for several different values of the feedback gain G (and thus γ_{fb}). Qualitatively, we see that as the gain is increased to larger values, the area underneath the curve (which is proportional to the effective temperature) decreases until some minimum value. At some point, as particularly evident in (c) in the $G = 256$ curve, the gain becomes

too large to continue to ‘squash’ the peak, and we actually end up exciting motion outside of the bandwidth of the cooling feedback (i.e. outside of the $\gamma_{max} = \alpha f_i \approx 0.1 f_i$ region). These curves qualitatively match similar curves and analysis provided for feedback cooling of a cantilever’s fundamental mode [53].

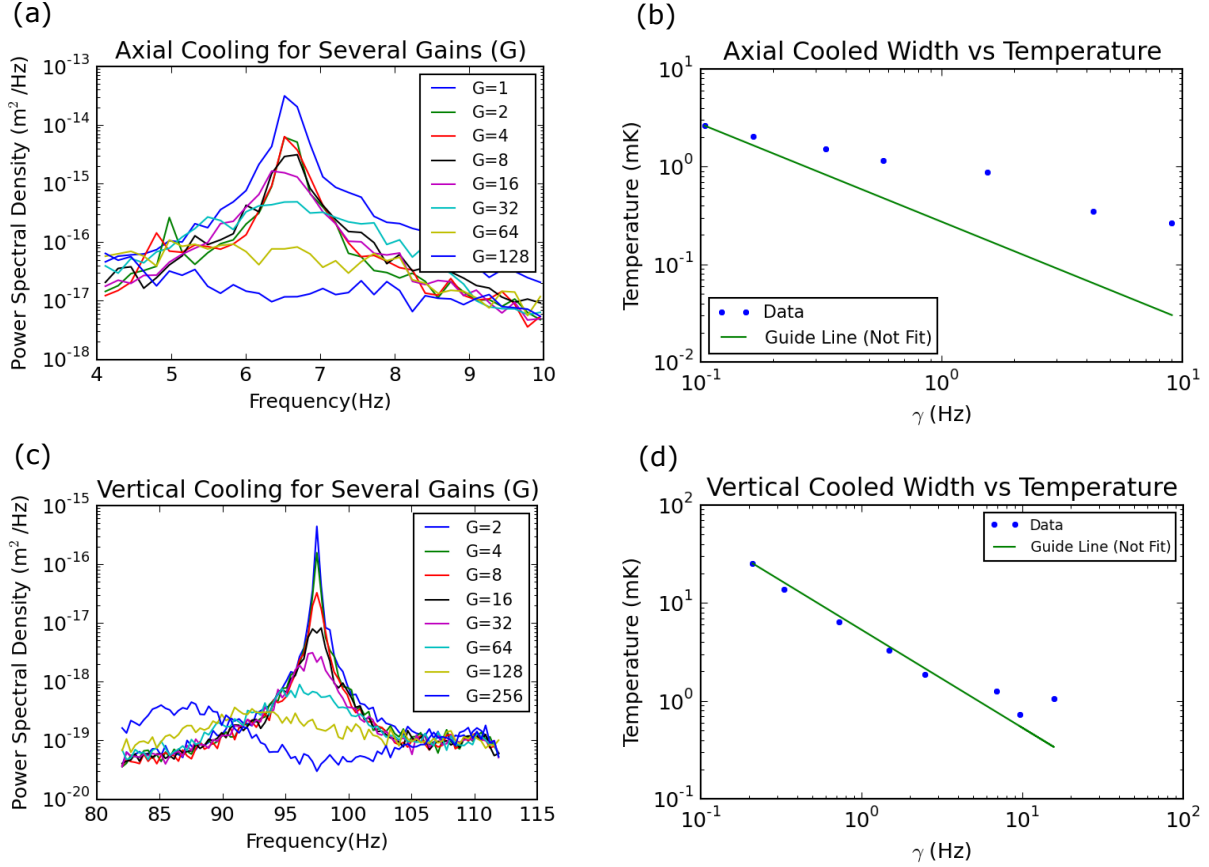


Figure 55: Plots examining cooling vs damping width provided by the feedback.

However, even before we start exciting motion, the feedback may not be performing as well as theoretically predicted as we increase the damping width γ_{fb} . In order to check this, we plot the computed temperature T_{fb} for each curve as a function of its FWHM (γ_{fb}) in Fig. 55 (b) and (d) for the axial and vertical directions, respectively. The green line in each curve is not a fit - it is the line computed by plotting Eq. 3.16, starting at the largest temperature data point. The point of plotting the data and line in this way is simply to compare the perfect (inversely proportional case) to the actual results.

We see in Fig. 55 (b) that, as we increase γ_{fb} , the temperature achieved is higher than the ideal case. We see the same behavior in the vertical direction displayed in Fig. 55 (d), where we note that we have not included the $G = 256$ or $G = 128$ data points. In each case, we see that the estimate of $\gamma_{max} \approx 0.1f_i$ is a good estimate, as it seems that the temperature to width relationship only worsens after $\gamma_z > (0.1 \times 7.0)$ Hz and $\gamma_y > (0.1 \times 97.0)$ Hz.

We also see that the temperatures in the vertical directions start at values far worse than that of the axial for similar widths, which is consistent with the results reported in Section 3.4.

We specifically call out this analysis as the factor of **23** quoted in Section 3.2 is likely fully explained by this relationship and an uncertainty in the measured pressure, which suggests that we can reach pressure limited results in the axial direction.

3.5.2 Pressure

As suggested in Section 3.2, pressure plays a large role in the natural damping rate (Γ_A) of the system, and our expectations have been that we will be limited in our cooling ability by the background pressure in the chamber. First, we add to the discussion in Section 3.2 and Section 3.5.1 by utilizing again the relation of Eq. 1.43 $\left(\Gamma_A \leq \frac{T_{fb}}{T_A} \Gamma_{fb}\right)$. Copied here to highlight the methodology, we examine the ideal case (equality):

$$\Gamma_A = \frac{T_{fb}}{T_A} \Gamma_{fb} \quad (3.17)$$

All cooling results were summarized graphically in Fig. 54; however, said figure does not account for differences in the the final cooled damping widths (γ_{fb}). To place the results on equal footing, we utilize the results to extract Γ_A from Eq. 3.17. In addition, we plot the expected damping rate Γ_A from Eq. 1.47, which represents the theoretical best possible Γ_A assuming that background pressure is the limiting factor. These results are shown in Fig. 56 (a) and (b) for the axial and vertical results, respectively.

In particular, Fig. 56 highlights the stark contrast in the cooling ability in the (a) axial and (b) vertical directions as the background pressure is reduced, suggesting a fundamental difference either in the system itself or in our detection and feedback mechanism in the

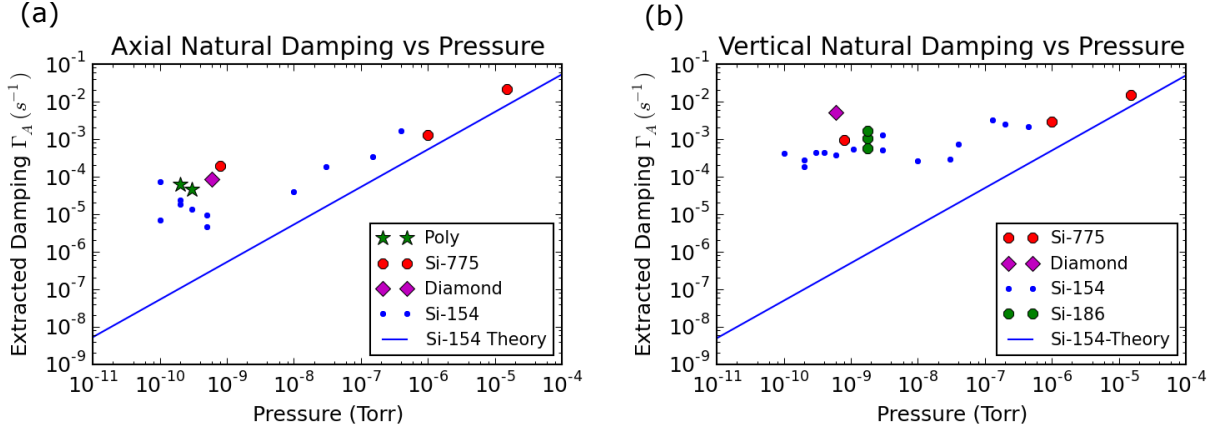


Figure 56: Extracted natural damping rates (Γ_A) for results in the (a) axial and (b) vertical directions. The solid curves are a calculation of Eq. 1.47, representing expected damping rates for a $1.54 \mu\text{m}$ SiO_2 microsphere.

vertical direction. Still visible is the trend that larger particles have significantly worse results than smaller particles, however this is now only evident at low pressures and in the axial case. What is not clear, however, is whether this is a fundamental difference in the system or in the detection and feedback mechanism.

In an attempt to answer this, we attempt to measure Γ_A instead of extracting it from cooled data, which is now discussed in Section 3.5.2.1.

3.5.2.1 Large Particle, Large Amplitude Damping We now attempt to relate P and Γ_A by experimentally measuring Γ_A via a damping time measurement.

Squaring the homogeneous solution of the damped harmonic oscillator (Eq. 1.14) yields a function proportional to the energy in the oscillator as a function of time:

$$E(t) \propto e^{\Gamma t} \cos^2(\omega' t + \phi) \quad (3.18)$$

By measuring $\langle x_i^2 \rangle$ with sufficient experimental conditions, a fit for the envelope of the oscillation ($e^{\Gamma t}$) yields a direct measurement of Γ_A . However, as discussed at length, we do not have an isolated harmonic oscillator, but rather a randomly driven harmonic oscillator. To combat this, we start the measurement by exciting the particle to an amplitude much larger than the thermal amplitude (we multiply our feedback phase by -1 to provide positive feedback instead of negative, thus driving the particle). This way, the random fluctuations in the particle's energy should be small compared to the particle's overall energy.

Experimentally, this large amplitude is not possible to achieve with a particle of small mass (meaning the desired $1.54 \text{ } \mu\text{m SiO}_2$) - given that the axial thermal amplitude of such a particle is $\sqrt{\langle z^2 \rangle} \approx 20 \text{ } \mu\text{m}$, excitation to an amplitude of $|Z'| \approx 10|Z|$ would extend the particle near the edges of the trap dimensions (which are $\sim 200 - 400 \text{ } \mu\text{m}$), assuredly kicking the particle out of trap. Even though the vertical motion is in a much stronger field (requiring a smaller excitation amplitude), the tighter dimensions of the trap vertically and the bias toward the bottom poles due to gravity create exactly the same issue.

To combat this, a particle with a much larger mass ($7.75 \text{ } \mu\text{m SiO}_2$, $m_{7.75} \approx 125m_{1.54}$) and thus much smaller thermal amplitude ($|Z_{7.75}| \approx \sqrt{125} |Z_{1.54}|$) was utilized. Specifically, the particle used was that from 11-10-2017, with $\sqrt{\langle z^2 \rangle}_{th} = 2.2 \text{ } \mu\text{m}$ and $\sqrt{\langle y^2 \rangle}_{th} = 0.17 \text{ } \mu\text{m}$.

The results are neatly summarized in Fig. 57. Data points for the axial and vertical motion are displayed, with the solid lines corresponding to a linear fit for Γ_A as a function of pressure P . To obtain these fits, the uncertainties were defined as relative uncertainties at each pressure (if each point was defined with the same absolute uncertainty, the smallest points would essentially be ignored). As in Fig. 56, the solid magenta ‘Calculated’ curve is a calculation of Eq. 1.47 for the size of particle utilized. Individual results for the axial and vertical motion are displayed in the Appendix in Fig. 58 and Fig. 59, respectively.

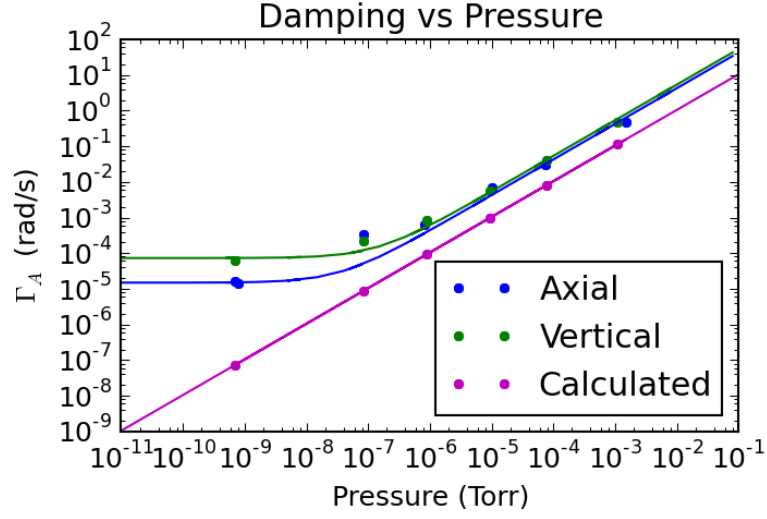


Figure 57: Summary of large particle, large amplitude damping measurements at various pressures. All axial and vertical data points were obtained with the same 7.75 μm SiO_2 particle (11-10-2017). The solid curves for the axial and vertical data represent linear fits to the data. ‘Calculated’ data is a calculation of Eq. 1.47 representing the expected damping rates for said particle.

While this plot seems to suggest the damping rate Γ_A is no longer linear in the pressure below $\sim 10^{-7}$ Torr, we note that we should exercise caution in drawing this conclusion for several reasons.

The individual results for the large amplitude, large particle damping tests are given in Fig. 58 and Fig. 59 for the axial and vertical directions, respectively. Each figure displays the average energy of the particle (as determined by its average amplitude), expressed as a ratio of its thermal energy. Green solid lines are a fit to an exponential damping function, which is the exponential envelope in Eq. 3.18.

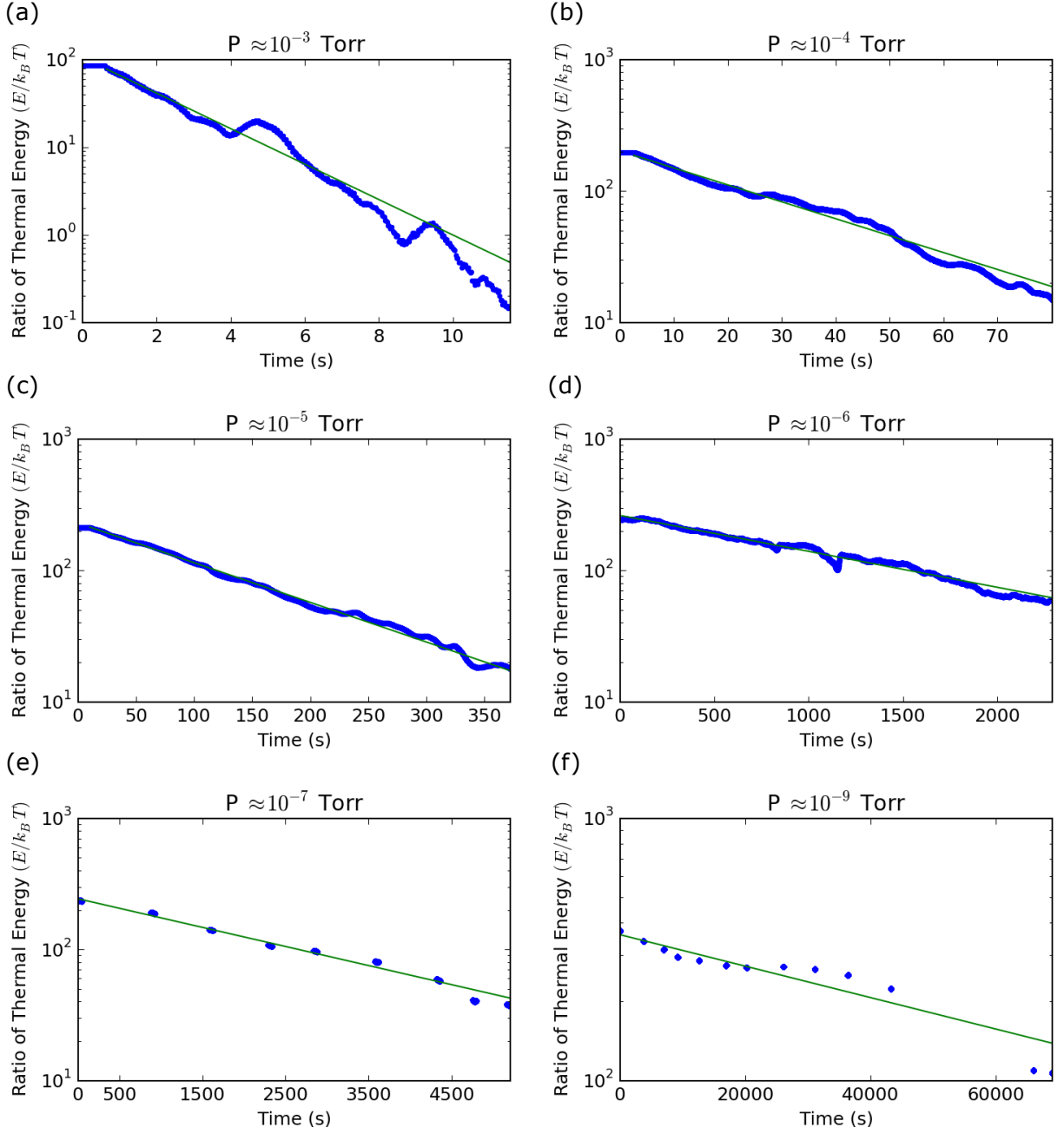


Figure 58: Plots showing the damping of the axial energy (expressed as a ratio of thermal energy) of a particle, as a function of time, in various background pressures (corresponding to data points in Fig. 56). Note that in (f) the fit is poor in comparison to the fits in (a - e).

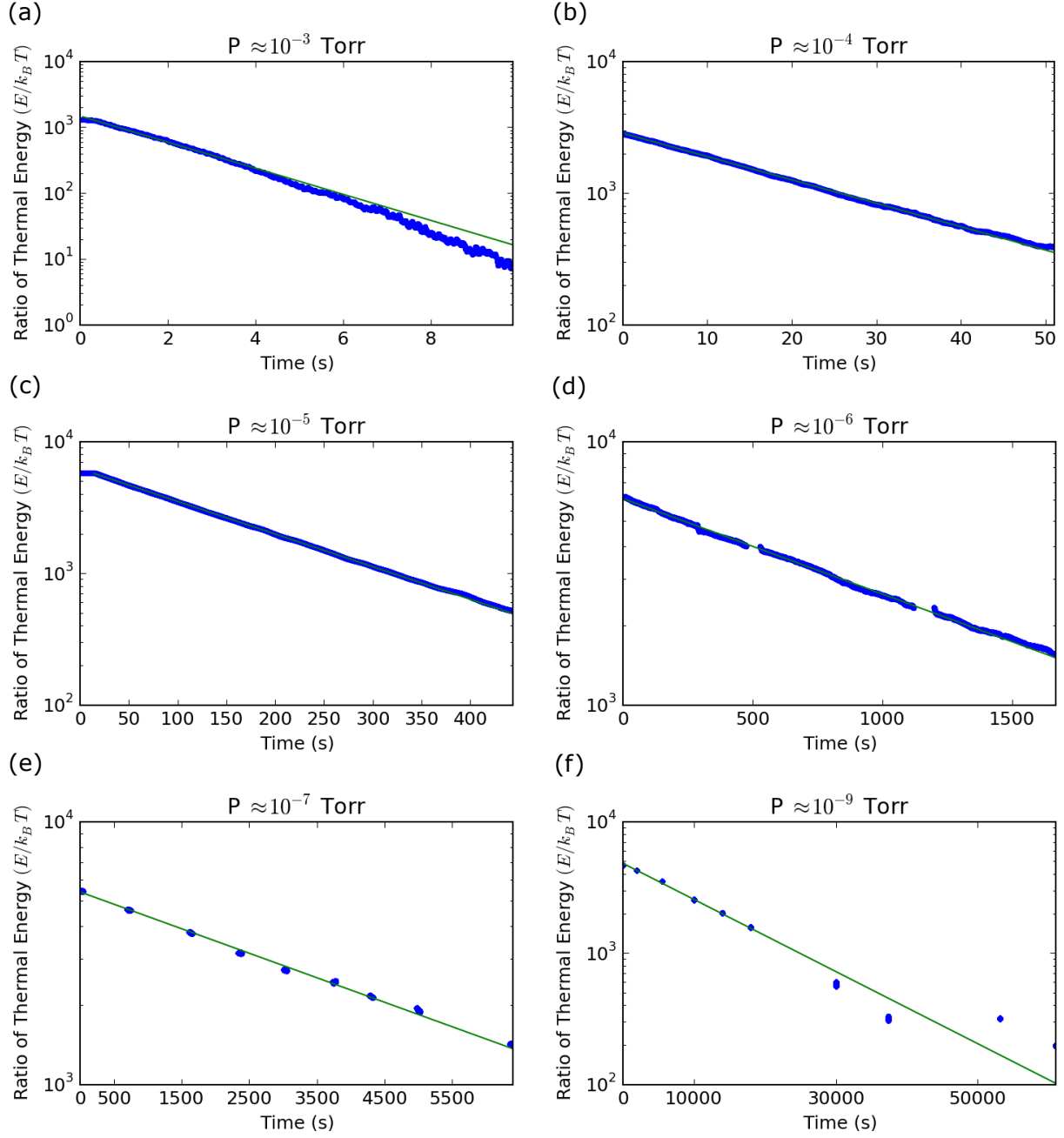


Figure 59: Plots showing the damping of the vertical energy (expressed as a ratio of thermal energy) of a particle, as a function of time, in various background pressures (corresponding to data points in Fig. 56). Note that in (f) the fit is poor in comparison to the fits in (a - e).

First, the pressure reported for the data points in the $P \approx 10^{-7}$ Torr has a large uncertainty. To obtain data in the 10^{-3} Torr to 10^{-6} Torr range, we were able to either completely close or significantly throttle the Viton right-angle valve separating the turbo from the chamber - this ensures that the pressures in this range were adequately measured. However, in the 10^{-7} Torr range, the valve had to be opened significantly, which means the measured pressure was likely *lower* than the true pressure in the chamber, meaning those data points likely fall more in line with the expected values than they appear to.

Second, for pressures at the $P \leq 10^{-7}$ Torr range, the damping time $1/\Gamma_A$ is predicted to be quite long (~ 1 day), and even the measured damping time is already several hours. These are becoming very long times - so long that trying to obtain data becomes difficult. It can be seen in (e) and (f) of Fig. 58 and Fig. 59 that we started taking data intermittently in order to make data storage feasible. However, in doing so we lose the ability to view the motion continuously, which may enlighten us to what occurs to the motion. For instance, in (f) of both figures the data clearly becomes non-exponential at some point during the process, which makes the values of Γ_A extracted rather uncertain. Considering this data is taken over ~ 10 hours, it is entirely plausible that a random occurrence (like a door slamming and shaking the table) can significantly alter the results by way of a sudden removal or addition of energy to the particle's motion. We could make the data more robust by repeating the experiment, but given the time requirements and ease of ruining the data, this is not particularly feasible. With that said, while Fig. 58 (f) is clearly altered by fluctuations, Fig. 58 (f) *may* indicate a fast damping time predicted by the first several data points.

Third, performing a test with very large amplitudes ignores the original approximations we make in the system - namely, we generally consider oscillations that are small compared to the size of the trap to treat the motion harmonically. Large amplitude motion, especially the large vertical amplitudes used, do not lie within this approximation range. In fact, it is obvious when exciting the vertical motion that the particle's equilibrium position shifts in both the axial and vertical directions by several μm .

For a final comparison of rates, we plot extracted damping rates from the cooled motion (akin to Fig. 56) along with the measured damping rates, all for the same particle (11-10-2017, $7.75 \mu\text{m}$ SiO_2). Fig. 60 again confirms that the cooling is not working optimally,

since all of the results from the extracted rates (circles) are worse than the results from the measured rates (dots).

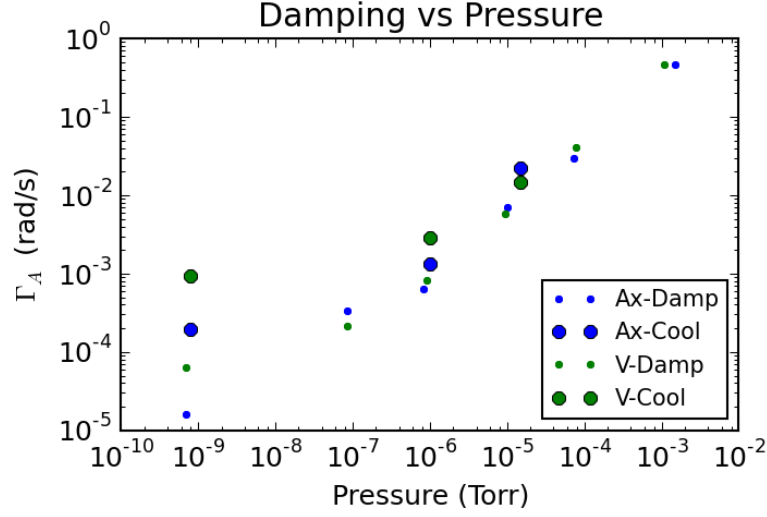


Figure 60: Comparison of measured damping rates (dots, same data points as Fig. 57) with rates extracted from cooling (circles, as done in Section 3.5.2). All data was obtained from the same 7.75 μm SiO_2 particle from 11-10-2017. This data suggests that the feedback cooling of large particles is not optimal (optimal cooling would see the dots and circles overlap in this plot).

3.5.2.2 Other Considerations For our last visual description of pressure effects, we plot the power spectral densities of particle motion for a 1.54 μm SiO_2 particle (10-15-2017) in Fig. 61 and a 7.75 μm SiO_2 particle (11-10-2017) in Fig. 62. In both figures, it is evident that both the effective temperature (given by the area under the curve) and the background of the curves decreases as the pressure decreases. In Fig. 61, we see that the background of the signals ends up being dominated by the noise floor of the detector. The signals stay above the detector noise floor in Fig. 62, but other features of the spectra obscure the noise floor in (d).

Most interestingly, when both particles reach their lowest pressures (10^{-10} Torr and 10^{-9} Torr for the 1.54 μm and 7.75 μm particles, respectively), motional peaks at non-

resonance frequencies arise. Surprisingly, especially in the case of the 7.75 μm particle in Fig. 62, the additional peaks extend well beyond the previous noise floor levels for the same particle at lower pressures. This suggests there is a fundamental change in the system. I suspect that these are vibrational peaks, which will be discussed in the following Section 3.5.3, but I cannot explain why the large particle is so much more strongly effected. The peak at ~ 27 Hz can actually be seen in data dating all the way back to the Pittsburgh lab (see Mar 15 - PGH in Appendix G).

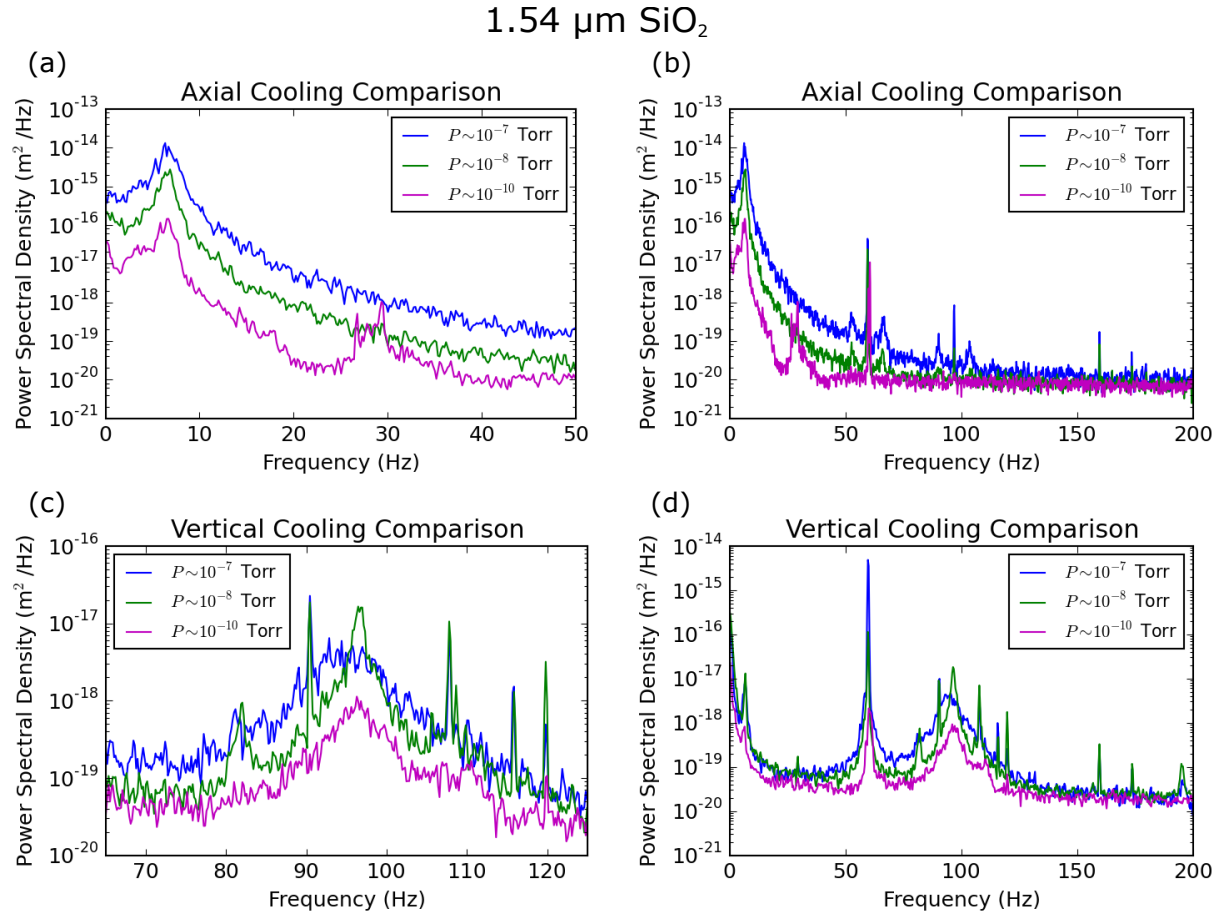


Figure 61: Comparison of cooling results at several pressures for a 1.54 μm SiO_2 particle (10-15-2017). (a) and (c) are the same spectra as (b) and (d), respectively, but zoomed in on the frequency region near particle resonances.

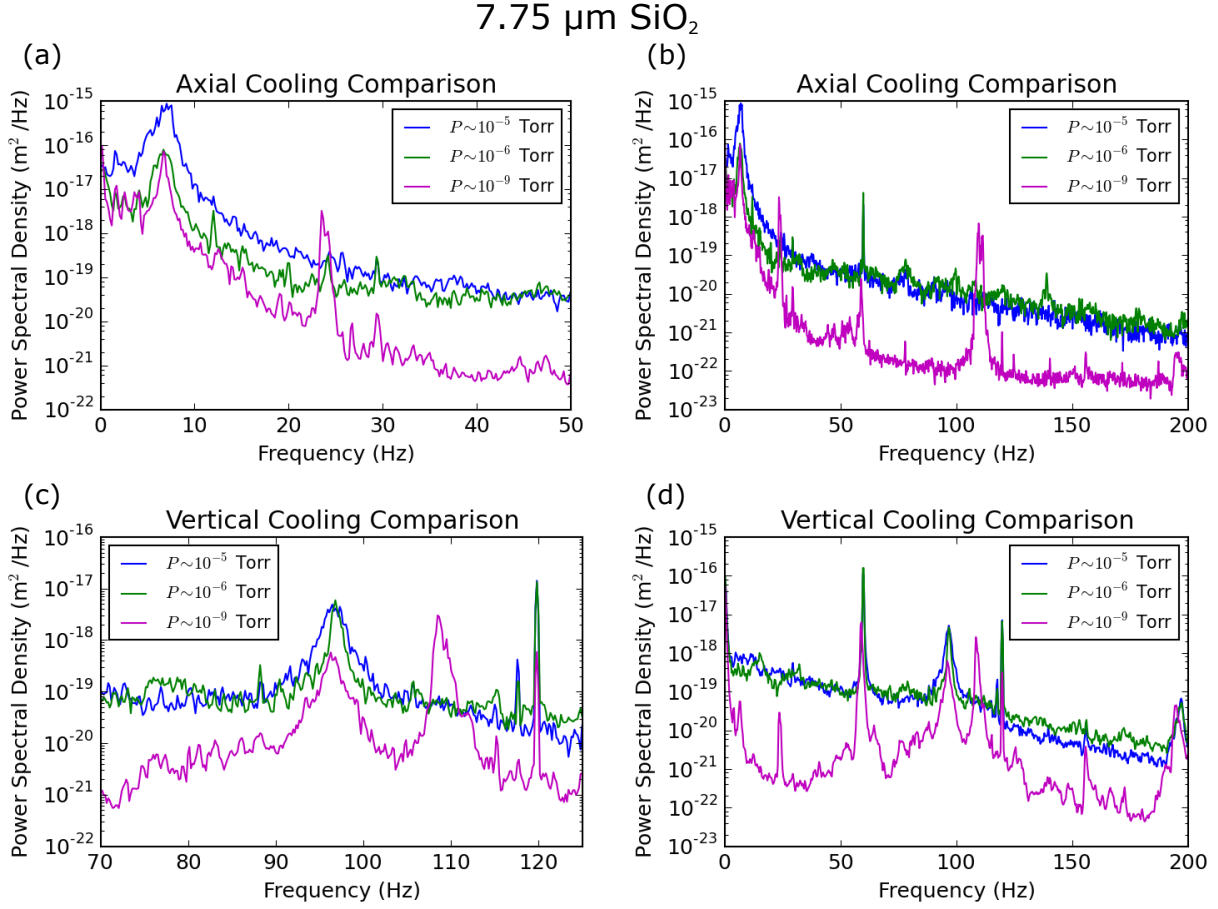


Figure 62: Comparison of cooling results at several pressures for a $7.75 \mu\text{m SiO}_2$ particle (11-10-2017). (a) and (c) are the same spectra as (b) and (d), respectively, but zoomed in on the frequency region near particle resonances.

3.5.3 Vibration Sources

There is much anecdotal evidence on the effect of vibrations on the motion of a trapped particle, particularly when the particle is in a high-vacuum (or better) environment. Observations supporting this claim stem from witnessing an increase in the motion of the particle in the real-time monitoring of its motion while environmental factors are at play, such as:

- Doors shutting.
- Tools being dropped.
- Lightly tapping on the table.
- Turbo and roughing pump being on and near the particle.

In all of these cases (with ample experimental spectra recorded as evidence), it is quite clear that the environment perturbation effects the results of cooling. What is not clear, and has been hard to prove, is whether or not events of a smaller amplitude, i.e. the typical environment of the laboratory, have a limiting effect on the particle motion.

The best evidence to date of vibrations coupling into the particle motion come from monitoring the vibration strength at several places on the optical table while simultaneously cooling the particle. To monitor vibration data we utilize a velocity sensor device, the SM-24 Geophone (SENSOR Nederland b.v., Sparkfun SEN-11744). The geophone utilizes a magnet and coil to translate movement into a voltage.

To generate the data, we compare the cooled power spectra of a particle (in this case, polystyrene from 12/10/2017) in Ultra-High Vacuum ($P \approx 2 \times 10^{-10}$ Torr) to the power spectrum simultaneously obtained from the geophone. To convert the recorded geophone signal, which is a velocity measurement, to a position measurement we numerically integrate the data after subtracting off the mean velocity. Since we know the sensitivity of the geophone in units of velocity ($28.8 \text{ V}/\frac{\text{m}}{\text{s}}$), we can directly compare the magnitudes of the particle to that of the geophone. The particle environment is as quiet as possible, with all connections to the ‘outside world’ (as outlined in Section 2.4.6) fully disconnected.

The data shown in Fig. 63 serves as an excellent demonstration of both evidence for vibrations coupling into the motion and as an illustration of the difficulty in interpretation of the results. Fig. 63 displays cooling data and vibration data for several different positions

of the geophone on the optical table: (a) on top of the chamber's top 1.33" conflat blank, (b) on top of the all-metal valve, (c) on the optical table, and (d) again on the chamber, but with the support jacks (see Fig. 23)) underneath the ion pump removed.

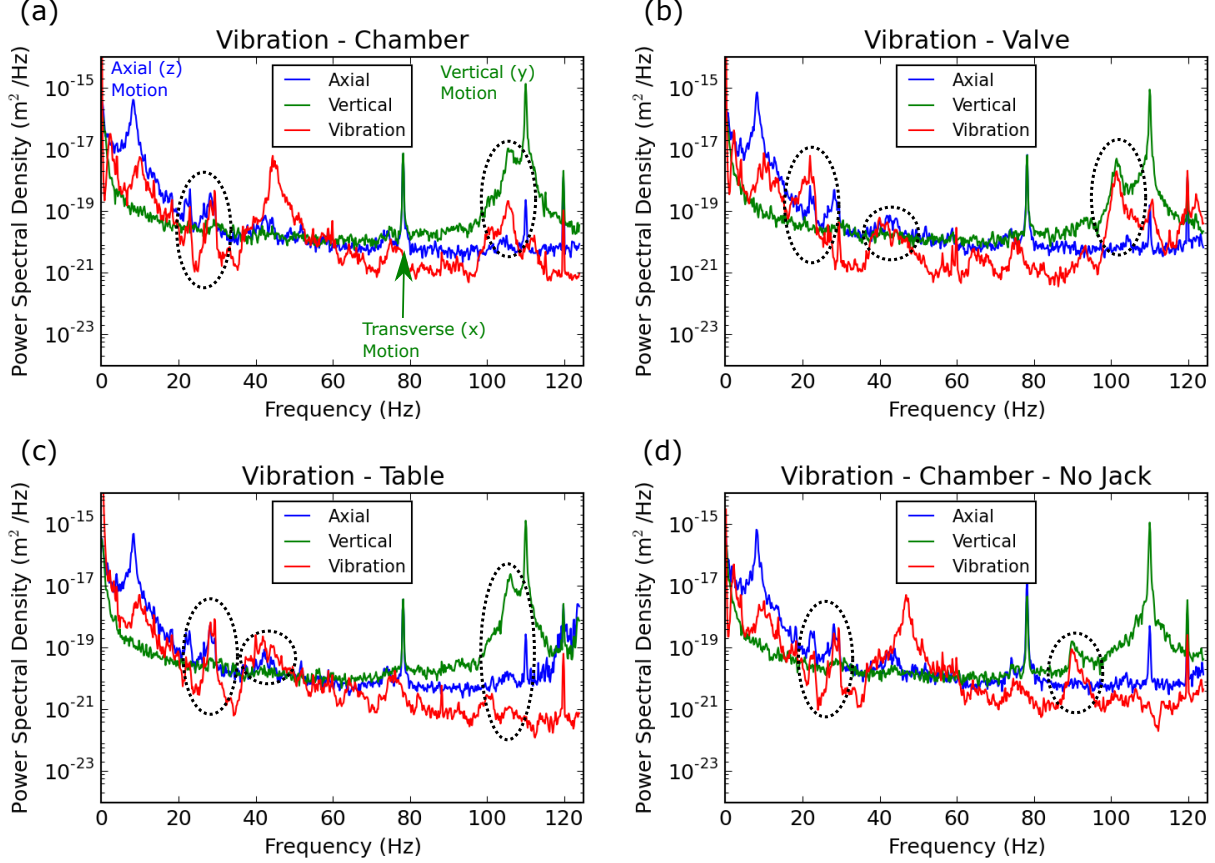


Figure 63: Comparison of cooling data and vibration data for several different positions of the velocity sensor on the optical table. Regions of interest as discussed in the text are circled. Particle used for all spectra is a polystyrene sphere from 12-10-2017.

First, we point out the main features of the spectra in (a)-(d): the large peak near $f_z \approx 8$ Hz is the axial motion; the peaks at $f_y \approx 80$ Hz and $f_y \approx 110$ Hz are the transverse and vertical motion, respectively; and the peak at $f \approx 120$ Hz is power line noise. The power line noise is most likely electrical interference or stray light reaching the photodiode detector.

Then, we note several observations about the data. Most notably, there is a peak visible

in the vertical spectrum of the particle in (a, b, c) at $f_y \approx (106, 101, 106)$ Hz in (a, b, c) (just left of the main large peak at $f_y \approx 110$ Hz). The peak is evident in the motional peaks of all three spectra - the vibration sensor data contains the same peak in (a) and (b), when the sensor is placed on the chamber itself, while it is not visible in the sensor data in (c). We interpret this as vibration of the chamber, where we have caused a shift in the frequency when we placed the sensor on the valve (which has a very long lever arm to the chamber). We also see in (d) that a peak near $f_y \approx 90$ Hz is visible when we removed the support jacks underneath the ion pump - a decrease in the frequency would be expected since we have decreased the stiffness of the support of the system.

In addition, the slope of the axial data and of the vibration data seem significantly similar, particularly at low frequencies where the motional signals are well above the noise floor of the detector. Several of the vibrational peaks in these regions also display in the axial data. However, we also see clear examples of cases where the vibration is very large with no corresponding signal in the motion, such as the large peak at $f \approx 45$ Hz in Fig. 63 (a). It is these conflicting observations that make it difficult to attribute these findings completely to vibration.

In an attempt to quantify these results, we look at the cross-correlation ($f \star g$) of the vibration data and motional signals in the frequency domain. To do so, we compute [54]:

$$\mathcal{F}[f \star g] = \mathcal{F}[f]^* \cdot \mathcal{F}[g] \quad (3.19)$$

where f or g correspond to the motional or vibrational data, and \mathcal{F} denotes the Fourier Transform. In practice, we take many averages of this function, so that any data that is not-correlated should average to zero. We then normalize each by the amplitudes:

$$Norm_{f \star g} = \frac{|\mathcal{F}[f]^* \cdot \mathcal{F}[g]|}{|\mathcal{F}[f]| \cdot |\mathcal{F}[g]|} \quad (3.20)$$

Fig. 64 shows just two of these functions corresponding to the data shown in Fig. 63 (a), as all data showed very similar correlation. In fact, the axial correlation calculation was practically identical in all 4 cases, whereas the vertical data showed small differences in relative amplitudes. Fig. 64 (a) and (b) plot the calculation of Eq. 3.20 for the axial motion and vertical motion, respectively.

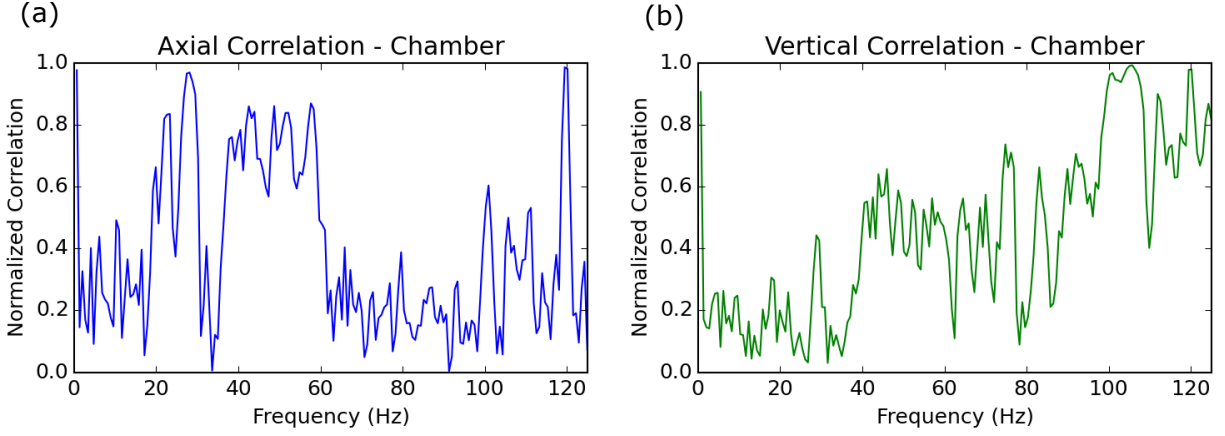


Figure 64: Normalized cross-correlation plots of (a) the axial motion with vibration data and (b) the vertical motion with vibration data.

In Fig. 64, there is clearly strong correlation in parts of the $f_z < 60$ Hz region; however, correlation is suspiciously absent below $f_z \approx 20$ Hz. In Fig. 64 (b), we see that the vertical data has nearly perfect correlation at the previously mentioned $f_y \approx 105$ Hz peak, and somewhat strong correlation in the $f_y = 50 - 120$ Hz region.

As such, while there is undeniable proof that there is correlation between vibration and motion, we cannot claim that vibration is the limiting factor in cooling at this point.

Some of the uncertainty in the measurement could come from the fact that the sensor is not fully attached to the chamber or table - it is possible that the BNC cable and wire connection add some vibration noise, which would explain some of the instances where there appears to be strong vibration with no corresponding peak in the motional data.

3.5.4 Particle Rotation

Most likely, particles undergo some amount of rotation or ‘wobbling’ in the trap. For a perfectly spherical and uniform particle, this motion would be completely undetectable on our detectors. However, even if our detectors can’t see the rotation, it could still interfere

with the translational cooling by providing a thermal source of heating.

Consider a particle rotating along some axis as it translates in the trap. If an air molecule collides with this spinning particle, the particle could impart a very large momentum change in the air molecule by transferring angular momentum (with a corresponding momentum change to the particle itself). As an example, consider spinning a large object (like a basketball) very fast and throwing another object (say a tennis ball) at it, the tennis ball can gain momentum in a perpendicular direction from the frictional interaction with the spinning basketball. If energy is continually added to the particle's rotation by some mechanism, it is feasible that this rotation can then act as an excitation source once the linear degrees of freedom have been cooled.

This becomes even more likely if we consider a slightly non-spherical or non-uniform particle. In such a case, angular momentum can be imparted to the particle via the radiation field interactions (for instance, if the illumination light has elliptical polarization). While our particles are believed to be nicely spherical on average, there is no guarantee that individual particles do not have defects.

In cases where the trapped particle is clearly non-spherical (like a large, deformed single particle or a cluster of small particles), there can be clear indication of the non-uniformity of the object even on the camera. Fig. 65 shows three different images of the same polystyrene object (12/10/2017). Because of a large measured mass and visual non-uniformities, it is highly unlikely to be a nicely formed, single sphere. In the figure, it is quite obvious that the scattering profile of the particle changes as the particle moves around in the trap. Presumably, this occurs with smaller particles as well, but may be impossible to detect with the limited camera resolution.

In addition to being visible on the camera, particles that are believed to be deformed or clusters also frequently display extra noise in their power spectra. Several power spectra for the same polystyrene object shown in Fig. 65 are shown in Fig. 66, where the only difference between the spectra is that they are taken at different times. In the spectra, the large peak near $f_z \approx 8$ Hz is the axial motion; the peaks at $f_y \approx 80$ Hz and $f_y \approx 110$ Hz are the transverse and vertical motion, respectively; the “shoulder” at $f_y \approx 105$ Hz in (a,c,d) is a vibrational source; and the peak at $f \approx 120$ Hz is power line noise. There are very

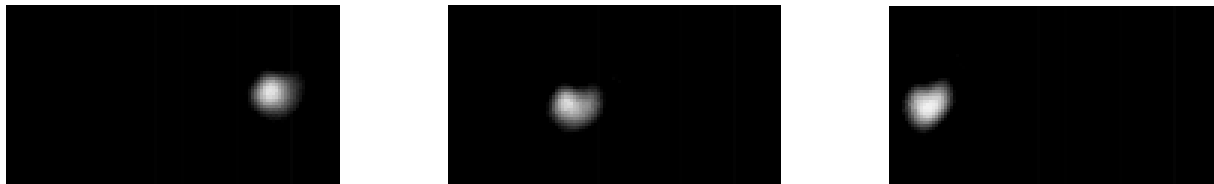


Figure 65: Three separate images of the same polystyrene object (12-10-2017), which is most likely not a single sphere, showing scattering changes as it moves in the trap.

obvious additional features in both the axial and vertical motions in the $f \approx 120 - 160$ Hz regions. Four different runs are displayed to demonstrate that these peaks change in time in both strength and width. The peaks appear very wide because these are incoherently averaged spectra over many seconds - the actual peaks are likely narrow and move around in that frequency region much faster than the data is being averaged, causing essentially inhomogeneous broadening.

These are believed to be rotation of the particle. There are several experimental properties that support this:

1. The peaks “move around” in frequency space - rotations will have no fixed frequency in this system
2. The peaks change in strength - rotation speed can be variable in this system
3. The peaks are not always present
4. The visibility of the peaks is correlated with the particles being non-uniform looking or large

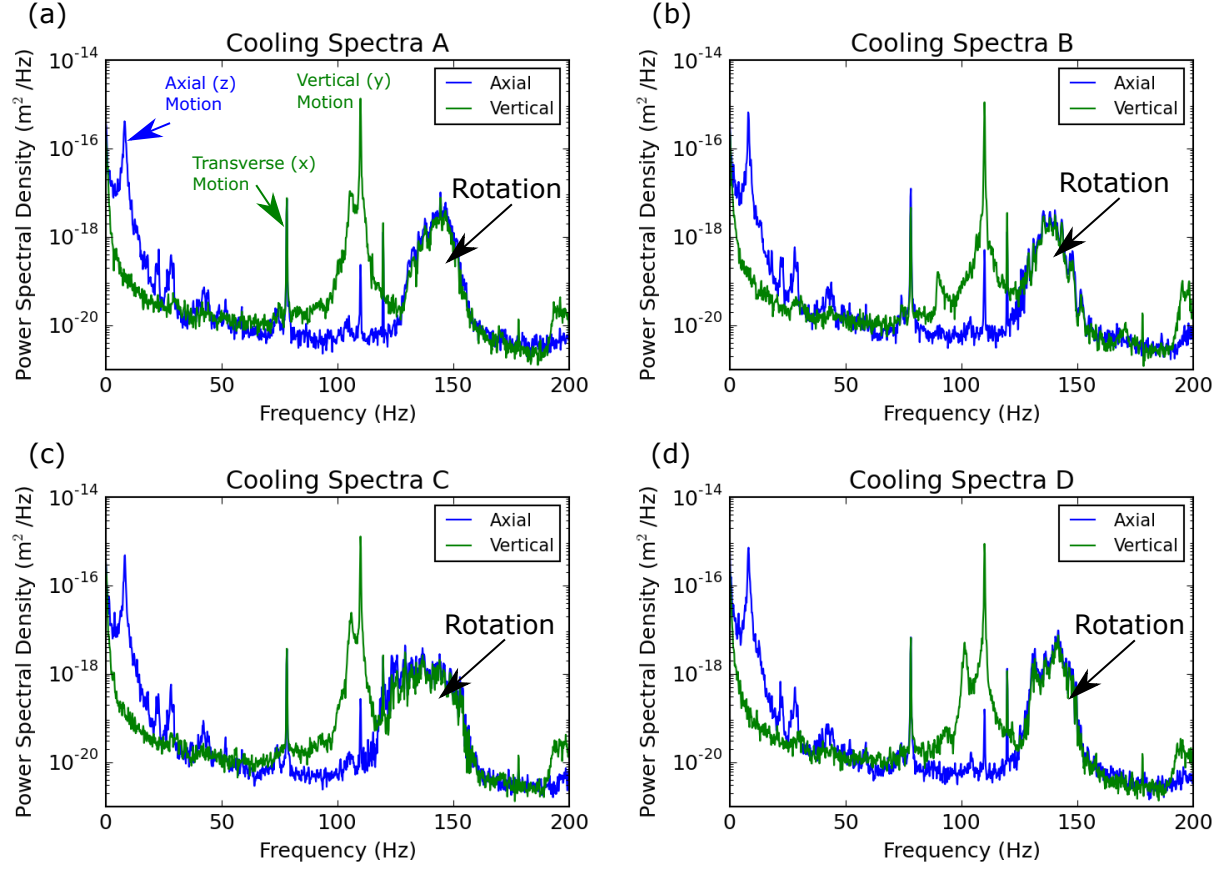


Figure 66: Four spectra of the same polystyrene particle (shown in Fig. 65) taken at different times, showing additional peaks in the motional output in the $f \approx 120\text{--}160$ Hz region, which are believed to be rotational motion of the particle.

3.5.5 Detection Noise Floor and Detector Sensitivity

In order to reach effective temperatures near the quantum ground state, a very sensitive detection system is needed. The quadrant photodiode detector does not have the sensitivity required to reach the quantum ground state. In addition, our monitoring (and digital filtering) system utilizes 12-bit Analog to Digital Converters (ADC), which will also end up being a limitation before reaching motion at amplitudes near the ground state amplitude fluctuation magnitudes. However, there is no evidence that either of these is the current

limitation in cooling, despite the fact that the ADC resolution in particle is very close to being so.

We record the noise signal from the quadrant photodiode detector circuit while it is powered on, but with the photosensitive areas completely covered. This signal is then the lower bound on a detectable signal. In Fig. 67, we plot the same cooling signals from Fig. 51 and Fig. 52 alongside the power spectral density of the noise signal. For direct comparison, both signals are left in their absolute units of V.

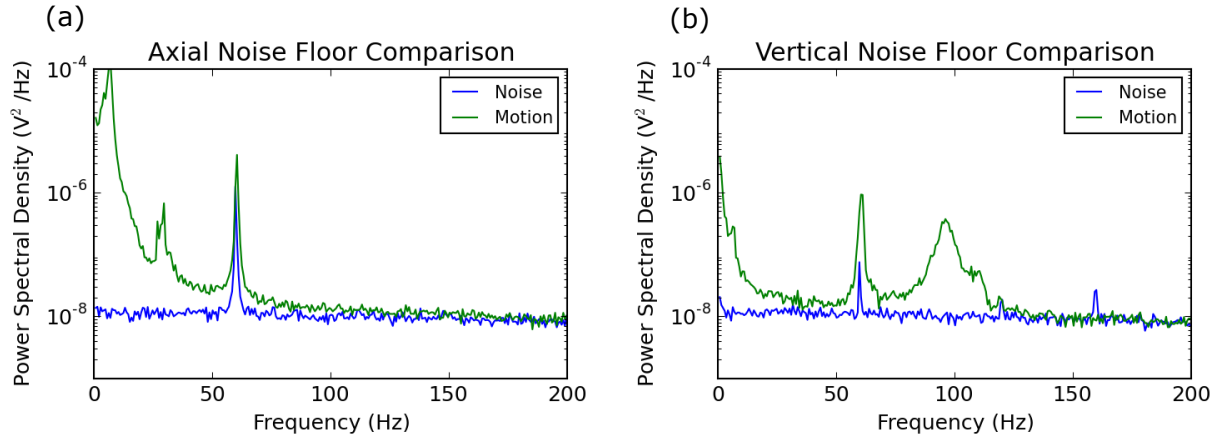


Figure 67: Comparison of quadrant photodiode noise floor and cooling results in the (a) axial and (b) vertical directions. Particle spectra are the same as those shown in Section 3.3 for a 1.54 μm SiO_2 particle.

3.5.5.1 Expected Noise Floor We first check that the noise floor shown in Fig. 67 is close to the expectation of the noise generated by the QPD circuit (and subsequent amplifier and filter circuitry). In general, if a large enough feedback resistor is used in the first stage of the amplification (i.e. the trans-impedance operational amplifier AD824ARZ in Fig. 79), the signal to noise ratio of the overall signal will be limited by the signal to noise in this first stage. Alternatively stated, if the signals leaving the first stage of the amplifier are large compared to the noise of subsequent amplifiers, the noise generated in later stages is insignificant overall.

As such, we examine noise sources related to the first stage of amplification circuit. These noise contributions are:

- Resistor thermal noise (Johnson-Nyquist noise).
- Photodiode dark current (not technically ‘noise’).
- Photodiode noise, provided as Noise Equivalent Power (NEP).
- Op-amp voltage noise.
- Op-amp current noise.

Many of these are specified by the manufacturer in units of $\{\text{unit}/\sqrt{\text{Hz}}\}$, which is what we will use for comparison.

Johnson-Nyquist Noise The (single-sided) power spectral density (i.e. V_n^2) of thermal noise in a resistor is given by the equation [55]:

$$PSD_{V_n}(T, R, f) = 4k_B T R \quad (3.21)$$

For $2 R = 22.1 \text{ M}\Omega$ in series at room temperature, this amounts to $864 \text{ nV}/\sqrt{\text{Hz}}$. To convert to a two-sided density, we simply divide this by 2.

Photodiode dark current The dark current for the Hamamatsu S5980 is specified as 0.3 nA typical to 2.0 nA max. This corresponds to a background of $V_{dark} = 13 - 89 \text{ mV}$. Since the final signal is a difference signal, we assume that these cancel to first order, and simply mention them for completeness.

Photodiode NEP The photodiode NEP is specified as the amount of optical power falling onto the sensor that would result in the equivalent noise signal. The NEP is determined as a combination of many factors, for instance photodiode shunt resistance thermal noise and dark current shot noise. For the S5980, this is specified as $NEP = 1.4 \times 10^{-14} \text{ W}/\sqrt{\text{Hz}}$, corresponding to a voltage noise (by multiplying by efficiency and R) of $446 \text{ nV}/\sqrt{\text{Hz}}$.

Op-amp voltage noise The AD824ARZ voltage noise density is specified at 1 kHz as $16 \text{ nV}/\sqrt{\text{Hz}}$, which is comparatively negligible. It is also specified as $2 \text{ }\mu\text{V}$ peak to peak in the range from 0.1 to 10 Hz , which corresponds to $25 \text{ nV}/\sqrt{\text{Hz}}$, which is also comparatively negligible.

Op-amp current noise The AD824ARZ current noise density is specified at 1 kHz as $1.1 \times 10^{-15} \text{ A}/\sqrt{\text{Hz}}$, which corresponds to $50 \text{ nV}/\sqrt{\text{Hz}}$, which is comparatively negligible.

Given all these, we take the sum of the all of the noise contributions (in quadrature) as our overall first stage voltage noise:

$$\bar{V}_n \approx 0.623 \text{ } \mu\text{V}/\sqrt{\text{Hz}}$$

The signal is then amplified thrice by the second stage, third stage, and external programmable gain amplifiers by factors of 0.91, 10 and 10, respectively. In addition, due to the sum and differencing of the signals, we gain an extra factor of 2 in noise from adding the noise from each quadrant in quadrature. This means that we expect to measure a voltage noise of:

$$\bar{V}_{n,calc} \approx 113 \text{ } \mu\text{V}/\sqrt{\text{Hz}}$$

Measurement of the noise power (which is pretty simple just by looking at Fig. 67, but also computed mathematically) yields a noise power and voltage noise of roughly:

$$\begin{aligned} \bar{V}_{n,meas}^2 &\approx (100 \text{ } \mu\text{V})^2/\text{Hz} \\ \bar{V}_{n,meas} &\approx 100 \text{ } \mu\text{V}/\sqrt{\text{Hz}} \end{aligned}$$

This indicates that the circuit is operating quite close to its expected noise profile.

Notably, as determined by the peak heights of the cooled motion axially (Fig. 67 (a) and vertically Fig. 67 (b), there seems to be a signal-to-noise ratio (SNR) of $\sim 10^5$ and $\sim 10^2$, respectively, in the motional signals. While it has not been determined what exact SNR is needed for optimal cooling, it is safe to assume there is plenty of overhead to cool to lower temperatures axially.

We had been suspicious that signal to noise or simply the small absolute magnitude of the vertical signal may be limiting us from better cooling. In particular, the average signal amplitude for the particle motion in Fig. 67 (b) is only $\sqrt{\langle V^2 \rangle} = 2.77 \text{ mV}$. The resolution of a 12-bit ADC (range of 4096 units) with a voltage range of $\pm 5 \text{ V}$ is roughly 2.44 mV/unit . This

means that the signal recorded for vertical motion is essentially at the single bit resolution of the ADC. However, we have determined that this is not currently the limitation for cooling.

Of particular note is the electrical line noise near $f \approx 60$ Hz visible in both noise spectra, which clearly interferes with the cooling of the transverse peak which is (unluckily) measured at $f_x \approx 59.57$ Hz, and which knowingly couples into both the axial and vertical signals. This electrical line noise was **NOT** present in the same testing when performed before the lab move, and is likely due to a grounding issue. This should absolutely be investigated and addressed in any current and future experiments.

3.5.5.2 Detector Sensitivity (Volts per Meter of Movement) We now calculate the signal that we expect to receive from the detector for a typical particle and motion. We copy Eq. A.28, which provides us the signal in one dimension from the full QPD circuit (detector and amplifiers), assuming a quadrant photodiode detector with an infinitely small gap between the quadrants:

$$S_{qpd} = \left(\frac{2}{\pi}\right)^{1/2} \frac{P_0}{\sigma} G \epsilon x_i(t)$$

where P_0 is the total amount of power falling onto the detector, $\sigma = 0.42\lambda/2NA$ [56] (see Appendix A.3), ϵ the sensitivity of the detector at the given wavelength λ , G the total gain factor, and $x_i(t)$ the particle's displacement as a function of time. For this system, $NA \approx 0.5$, $\epsilon \approx 0.6$ A/W, $\lambda = 830$ nm, $G = 2.41 \times 10^9 \Omega$, and $P_0 \approx 0.72$ nW (P_0 was determined by extrapolating scattered power as a function of illumination intensity).

We simply calculate the conversion factor for $x_i(t)$, which yields:

$$S_{qpd} = (2.38 \text{ V}/\mu\text{m}) x_i(t)$$

We compare this to the typical QPD calibrations, like those reported in Section 2.7.2.2 (c_y from Eq. 2.27):

$$\begin{aligned} c_y &\approx 1.40 \text{ } \mu\text{V} \\ 1/c_y &\approx 0.71 \text{ V}/\mu\text{m} \end{aligned}$$

These estimates are quite close, differing only by a factor of ~ 4 , which means the detector is decently well aligned and operating quite well, considering we did not account for light lost in the gaps of the detector.

3.6 SUMMARY AND OUTLOOK

As discussed, it appears as though we are doing a pretty good job cooling in the axial direction, but a comparatively poor job vertically. This is an important conclusion, as there are several benefits to using the vertical motion for cooling instead of the axial, mostly because of the factor of 10 increase in oscillation frequency:

1. The vertical frequency is much better separated from low frequency noise, which we know can be an issue (for instance, illumination location wobble causes some low frequency noise).
2. The ground state energy is $\sim 10\times$ larger, so we don't have to cool as far in (in terms of energy).
3. The bandwidth of the cooling is $\sim 10\times$ larger, which means we can remove energy $10\times$ faster (and cool $10\times$ better), compared to the axial direction.
4. The optimal illumination power is $\sim 100\times$ larger (this is from the two factors of 10 above), making detection easier (although, the ground state amplitude fluctuations are also a factor of 10 smaller, so this is really only a factor of 10 overall).
5. Because of the cooling bandwidth increase, the pressure requirement is $10\times$ lower vertically.

As such, I believe the first step for proceeding is to determine why we are doing a poor job at cooling vertically. Several possible reasons for poor vertical cooling are listed in the following section.

3.6.1 Possible Reasons for Vertical Limitation

3.6.1.1 Energy Transfer and Signal Coupling Between DOF The most worrisome of the possible causes for a limitation vertically is a combination of signal coupling and cooling-feedback coupling of the vertical and transverse DOF. As discussed in several sections, the transverse motion signal always strongly couples to the vertical channel (and not usually into the axial channel). As such, cooling of the transverse DOF is usually done by feeding back this ‘rogue’ signal from the vertical channel. This means there is a direct path for one signal to effect the other, especially considering feedback signals have a frequency dependent phase shift that may cause a driving response at the other frequency.

The cooling laser itself is also oriented (intentionally) to couple to all three DOF simultaneously. This creates a direct energy transfer mechanism between the degrees of freedom, as well as possible amplitude dependent coupling. In short, this could lead to a ‘side-band’ energy transfer effect. Specifically, once the axial motion is broadened, we most certainly are driving the cooling laser at the difference frequency of the vertical and transverse motion. This could cause energy to transfer from the transverse motion to the vertical motion (or vice versa). This could actually explain some of the observations seen in the system, such as both the vertical and transverse motions being well behaved or poorly behaved simultaneously, or the vertical motion being difficult to cool when the transverse motion is highly excited.

This type of coupling is actually mentioned explicitly in [46], even though in that case there are three independent lasers with very little coupling to other DOF, meaning it is certainly a problem that others have seen and have worked to remedy.

3.6.1.2 Signal to Noise As mentioned in Section 3.5.5.1, the average amplitude of the vertical motion is essentially at the single bit level of the ADC of the monitoring hardware (and also the digital filter hardware), which must mean that we are reaching a point where the digital conversion is just too inherently noisy to operate efficiently. To combat this, we have designed a new 16-bit ADC board which will provide much better dynamic range.

It should be noted that tests **were** performed to check this. For one, in many cases, an extra factor of 10 gain in the signal loop was used to ensure that the ADC resolution wasn’t

the issue. This never yielded any statistically significant improvement in final temperature.

Tests were also performed to check if this was a signal to noise limitation by changing the illumination and the gain in the signal loop by a factors of 10. This is why there are 3 data points for the 05-22-2017 data (see Table 8: LG means Less Gain, where the illumination light stayed the same but the gain was decreased, and ML means More Light, where the gain was decreased whilst increasing the illumination light). This can be seen as the noise floor in the ML case is actually increased (see Appendix G, May 22 - lgml - Silica 11.86 - PGH). None of the three results (normal, LG, and ML) had any statistical difference.

Judging by these results, it doesn't seem overwhelmingly likely that this is the current limitation. In particular, the noise floor increase from the ML case (without a decrease in temperature) implies that the signal represents the particle's actual motion, and as such would not be a signal to noise issue. However, the fact that larger particles are harder to cool could stem from this signal to noise issue, as the QPD is measured to be less sensitive when using larger particles.

At any rate, even if this is not the current limitation, it is obvious that it very soon will be. As such, the new ADC boards and a new detector should be utilized to increase the signal to noise and resolution of the measurement.

3.6.1.3 Filtering Limitations Many of the components in the system have a frequency dependent phase response. For instance, the Sallen-Key filter in Fig. B.4 has a known frequency dependent phase response. However, while we ensured all components had adequately large specifications for bandwidth, many other components (like the cooling laser controller) displayed some amount of unexpected frequency dependence even at the 100 Hz range (which is our vertical frequency).

Regardless of the type of filter utilized for feedback (analog or digital), these extra, somewhat unknown phase shifts will decrease the effectiveness of the cooling by shifting the phase response of the feedback away from its optimal value.

To minimize these effects, all components should be adequately tested and redesigned if necessary to ensure that the phase response is as flat as possible in the region of interest.

3.6.1.4 Laser Noise Since the particle’s scattering is mostly forward oriented and we have a single cooling laser coupled to all three DOF, any fluctuations in the laser will have a direct effect on the particle’s motion (this is mentioned in Section 4.3.5 as a limitation of the current system). However, even assuming worst case laser power fluctuations, the laser noise would still not limit the vertical cooling to the current temperatures.

But, the current mechanism for controlling the cooling laser is to modulate the current of the laser diode. This will certainly cause all sorts of strange noise-like effects (for instance, mode hopping and frequency shifts) as well as nonlinearities in the laser output power. The plan is to switch to electro-optic modulators (EOM) and balanced cooling for future versions of the experiment - this would allow a stable nominal laser power, and would remove the direct coupling of laser fluctuations by balancing the power from both sides. The use of EOMs is also discussed in [46].

3.6.1.5 Vibration Sources We have certainly shown that vibrations on the optical table (or of the chamber itself) couple into all of the motional DOF. However, we have not proven that this limits the cooling ability of the system, and at this point it is not likely to be the fundamental limitation vertically. In particular, the cooled damping widths Γ_{fb} in the vertical direction are quite large, indicating that the limitation is not a sharp, coherent source such as vibration.

However, as evidenced by the ‘shoulder’ in the cooling spectrum shown in Fig. 52 (b), this may be a real problem in the near future. We have done preliminary tests of using active cancellation of vibration sources, and this may be a viable approach to quieting the environment in a narrow band region around the resonance frequency.

3.6.1.6 Rotational Energy Transfer As we have shown in Section 3.5.4, some particles exhibit traits of rotational motion, and it is likely that any non-uniform particle will have some amount of rotation. If this rotation is caused by external factors (say, our cooling laser), we would constantly be adding energy to this type of motion. It could then transfer its energy (via air molecule collisions or again the laser interaction) to the linear DOF, acting as a thermal reservoir at a temperature much higher than room temperature. Most of the

data to date has shown that these rotation signals are near frequencies closest to the vertical resonance, meaning it may have the largest effect on the vertical DOF.

Care should be taken to use particles as uniform as possible, and to ensure that the laser interaction is strictly with linearly polarized light, to limit the effects of angular momentum transfer.

3.6.1.7 Damping from Magnetic and Electric Field Effects The last possibility would be an issue internal to the material being trapped in the form of damping from electric or magnetic field effects. Since we reach lower temperatures axially, we likely rule out losses due to electric field effects, since they would be equally important in each direction.

However, the vertical direction does have a difference in the magnetic field symmetry that could play a role in damping if there is a lossy (imaginary) part to the diamagnetic susceptibility. But, considering the small nature of these effects in general, coupled with the fact that even enormous changes in parameters like the charge on the particle have no effect at the current temperatures, this seems somewhat unlikely. However, considering that the trapping mechanism fundamentally relies on diamagnetism, this should not be ruled out, and can be easily tested in the future by trapping and cooling several types of materials. If this is done, it should be ensured that the materials used are of excellent quality.

3.6.2 Moving Forward

I believe there is a clear path to move forward in this experiment. As mentioned, the first step will be to determine why the vertical motion cannot be better cooled.

The first steps were already taken in this direction by creating the cooled, balanced detector shown in Fig. 89, which has at least 3 orders of magnitude lower noise floor than the current detector. In addition, the circuit boards for the the 16-bit ADC have already been created, but need to be tested. The combination of these two will greatly improve the efficiency of all of the measurements, not just those on the vertical motion, and will provide a path to get very near the ground state detection requirements.

Next, the feedback cooling system needs to be overhauled now that we know several of

its issues. In particular, instead of modulating the cooling laser power via a current drive of the diode itself (which will certainly cause all sorts of noise), the system should switch to the use of electro-optic modulators to amplitude modulate the laser power. This should be a much more linear process, and will then allow the diode lasers to operate at a single output power. In addition, the cooling modules for the diode lasers will work better if the laser is set to a constant output power. This should drastically reduce the amount of noise in the feedback system.

In addition, the single beam nature of the feedback cooling, while simple and useful, is likely the change of highest priority needed. There is no doubt that using this single laser beam, which directly couples to all three DOF and is modulated from the summed feedback signals of all three DOF, will cause unwanted driving and noise issues. This is corroborated by discussion in the literature [46]. At the least, there should be a single cooling laser in the direction of interest (like in our over-damping experiments) that minimally couples to the other DOF. Even better, if this cooling could be bi-directional (from both sides of the particle), it would eliminate driving to the particle from power fluctuations in the laser (at least to first order).

Finally, the most difficult step that is on the horizon is a move to a cryogenic environment. It is clear that if we are not currently limited by the vacuum pressure, that we are right on the cusp of being so. While we can perform longer and hotter bakes of the system, we will need great (at least ~ 4 orders of magnitude) improvements in background pressure to achieve cooling near the ground state energy level. The only way to do this is to move to a cryogenic environment. This environment would essentially freeze all air molecules that collide with the (cold) chamber, reducing the pressure in the chamber drastically.

Working in the cryogenic system will come with many challenges, as the configuration becomes much more constrained, and vibrations from the compressor have already been seen to cause troubles. However, I am confident that we can apply the lessons we have learned in the current (room temperature) experiment to overcome these challenges.

4.0 OTHER EXPLORED APPROACHES

4.1 CHAPTER OUTLINE

In this chapter, we describe experiments that lay just outside of the primary goal of this dissertation. We describe modified feedback cooling experiments that may be useful in the future, as they address specific potential issues in the primary experiments as outlined in Section 3.5.

4.2 A MICRO-MOLECULE

Since vibration sources on the optical table could be a limiting factor in the limitation of cooling (see Section 3.5.3), we decided to test a system in which a degree of freedom is decoupled from a vibration source that may drive the trap. To do this, we consider placing two similarly charged microspheres into the magnetic trap. The charge on the spheres acts as a repulsion mechanism, while the trapping potential favors the particles joining together. In a harmonic trap and for small oscillations, this combination of forces can be expanded to yield two decoupled degrees of freedom: the internal ‘vibrational’ motion between the two particles, and a center-of-mass motion in the trap. A source of vibration, such as the entire trap shaking, will then couple only to the COM motion of the two particles, leaving the vibrational mode undisturbed.

4.2.1 Description of Motion

We describe the motion of two charged microspheres in a harmonic potential well. For the following analysis, we treat the particles one dimensionally; since the axial restoring force is much weaker than that of the vertical or transverse restoring forces, the particle motions stay well aligned along the axial (z) axis. We examine the one dimensional Newtonian equations of motion with a Coulomb interaction in Eq. 4.1a and Eq. 4.1b:

$$m_1 \frac{d^2 z_1}{dt^2} = -m_1 \omega_z^2 z_1 - \frac{1}{4\pi\epsilon_0} \frac{n_1 n_2 e^2}{(z_2 - z_1)^2} - c_1 \frac{dz_1}{dt} \quad (4.1a)$$

$$\alpha m_1 \frac{d^2 z_2}{dt^2} = -\alpha m_1 \omega_z^2 z_2 + \frac{1}{4\pi\epsilon_0} \frac{n_1 n_2 e^2}{(z_2 - z_1)^2} - c_2 \frac{dz_2}{dt} \quad (4.1b)$$

where we have assumed the natural angular frequency, ω_z , is the same for each particle, the masses m_i are defined as $m_2 = \alpha m_1$, n_i is the number of charges on a particle, e is the electron charge, ϵ_0 is the vacuum permittivity, c_i are damping constants, and the subscripts labeling each particle.

By making the transformations in Eq.4.2a and Eq.4.2b:

$$z_2 - z_1 \equiv r_0 + r \quad (4.2a)$$

$$z_1 + \alpha z_2 \equiv R \quad (4.2b)$$

and taking the appropriate superpositions of the equations (4.1b- α ·4.1a) and (4.1b+4.1a), we have:

$$\frac{d^2 r}{dt^2} = -\omega_z^2 (r + r_0) + \frac{1}{\alpha m_1} \frac{1}{4\pi\epsilon_0} \frac{n_1 n_2 e^2}{(r + r_0)^2} - \left(\frac{c_2}{\alpha m_1} \frac{dz_2}{dt} - \frac{c_1}{m_1} \frac{dz_1}{dt} \right) \quad (4.3a)$$

$$\frac{d^2 R}{dt^2} = -\omega_z^2 R - \left(\frac{c_2}{m_1} \frac{dz_2}{dt} + \frac{c_1}{m_1} \frac{dz_1}{dt} \right) \quad (4.3b)$$

We then expand $1/(r + r_0)^2$ to first order in r about $r = 0$. In doing so (and setting the equilibrium force to 0, by definition, at $r = 0$), we solve for $n_1 n_2$:

$$n_1 n_2 = \frac{\omega_z^2 r_0^3 \alpha m_1}{(1 + \alpha) e^2 / 4\pi\epsilon_0} \quad (4.4)$$

We define $\Gamma \equiv c_1/m_1$ and (assuming $\Gamma_i \propto 1/d_i$ where d is the particle radius [see Section 1.4.1.4]) $c_2/m_1 = \Gamma\alpha^{2/3}$, and utilizing Eq. 4.4 we arrive at:

$$\frac{d^2 r}{dt^2} = -3\omega_z^2 r - \Gamma \frac{d}{dt}(\alpha^{2/3} z_2 - z_1) \quad (4.5a)$$

$$\frac{d^2 R}{dt^2} = -\omega_z^2 R - \Gamma \frac{d}{dt}(z_1 + \alpha^{-1/3} z_2) \quad (4.5b)$$

where R describes the center of mass (COM) displacement from equilibrium and r describes the displacement from the equilibrium separation (r_0) between the particles.

By loading two particles of the same size, we assume $\alpha \approx 1$, yielding:

$$\frac{d^2 R}{dt^2} = -\omega_z^2 R - \Gamma \frac{dR}{dt} \quad (4.6a)$$

$$\frac{d^2 r}{dt^2} = -3\omega_z^2 r - \Gamma \frac{dr}{dt} \quad (4.6b)$$

4.2.2 Experimental Procedure

The particles utilized are SiO₂ microspheres with a mean diameter of 1.86 μm . The particle loading procedure is the same as for single particles (see Appendix F.1), with negatively charged particles desired, until two (and only two) single spheres remain in the trap.

We start by minimizing the charge on the spheres, as very highly charged spheres are difficult to control when pumping, mostly due to the large average separation for highly charged particles. To reduce the separation to a manageable level, the ionizing source (discussed in Section 2.6) is brought near the particles and their separation distance is monitored until the separation is reasonably small.

We then evacuate the vacuum chamber to moderate vacuum ($\sim 10^{-4}$ Torr). At this point, we further tune the separation distance by exposing the interior of the chamber and the trap to an ultraviolet light source (see Section 2.6.3). Since the spheres are selectively negative, the separation distance increases as charge accumulates on either particle. The criteria for the final separation for this demonstration is such that only one of the two

particles is imaged onto the quadrant photodiode detector. Finally, we bring the particles into High Vacuum ($\sim 10^{-8}$ Torr) with a turbo pump.

The detectors necessary are a high speed CCD camera for data recording and analysis and a split detector for detecting the motion of only one of the two spheres. The camera requires a large enough detection area to view both particles simultaneously. We center the image from only one sphere onto the quadrant photodiode; since this single particle's motion is a superposition of the center-of-mass and vibrational motion of the two particle system, we actively manipulate one (or both) of the modes by band-pass filtering the signal around the resonance frequencies, just like in Section 2.2, with the second laser beam (at 660 nm) focused on the same single particle only.

4.2.3 Micro-Molecule Results

We show in Fig. 68 the distinct visualizations of these motions. Fig. 68 displays time sequences of the two-particle motion in the case of (a) thermal equilibrium with the environment, (b) damped COM motion with excited vibrational motion, and (c) damped vibrational motion with excited COM motion. It should be noted that the analysis in Section 4.2.1 assumes small oscillation amplitudes about equilibrium, whereas the motions in Fig. 68 are all highly excited. As such, the motions don't completely decouple. In addition, distinct asymmetries are evident in the excited vibrational mode sequence in Fig. 68 (b), which can be attributed to the higher order terms of the Coulomb repulsion that were ignored in obtaining Eq. 4.6a and Eq. 4.6b.

To show this is another way, and to provide some quantitative analysis of the motion, we start by cooling both degrees of freedom of the particle such that their excitation is somewhat sub-thermal (this is solely to make data collection easier by keeping the amplitudes smaller), and then allow the motion to freely evolve. We then track the motion of the two particles on a camera and compute a power spectrum of each. The power spectral densities for each particle are displayed in Fig. 69 (a).

To experimentally determine the value for α in Eq. 4.2b, we simply compute several power spectra of the transformed COM coordinate R (Eq. 4.2a) and choose the value of α

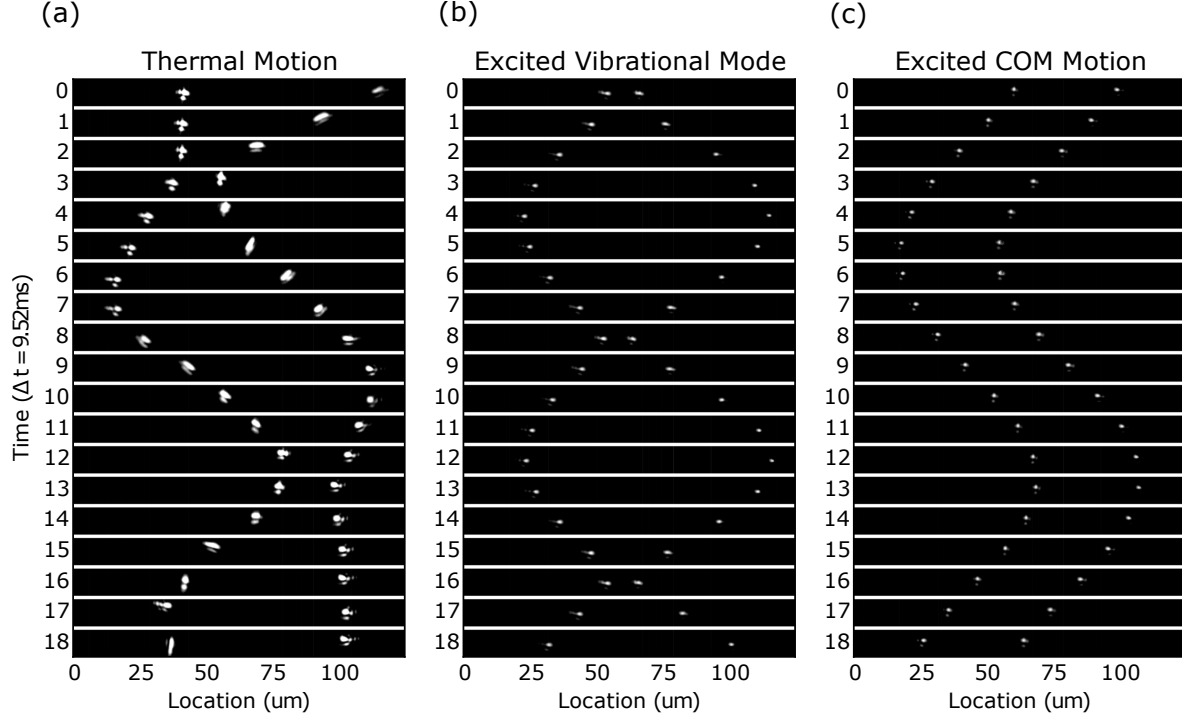


Figure 68: Time sequences of the two-particle motion for (a) thermal excitation, (b) excited COM motion, and (c) excited vibrational motion.

that minimizes the secondary peak (the vibrational mode). Fig. 69 (b) displays the power spectral densities of the transformed coordinates with the experimentally determined value of $\alpha = 1.644$. These spectra nicely identify decoupling of the vibrational and COM motion, even at somewhat large amplitudes. There is, however, evidence of the anharmonicity introduced by the Coulomb potential, which is visible as harmonics in the vibrational spectra, in the same vein as the asymmetries evident in Fig. 68 (b).

Both frequencies (COM and vibrational) are evident in Fig. 69, determined as $f_R = 7.08 \pm 0.15$ Hz and $f_r = 12.46 \pm 0.15$ Hz as the frequency at the maximum value with an uncertainty of the frequency bin size. The ratio of the frequencies is computed as $f_r/f_R = 1.76 \pm 0.04$, which matches with the theoretical prediction of $\sqrt{3}\omega_z/\omega_z = 1.732$ in Eq. 4.6b.

We also demonstrate significant cooling of both degrees of freedom via the same feedback

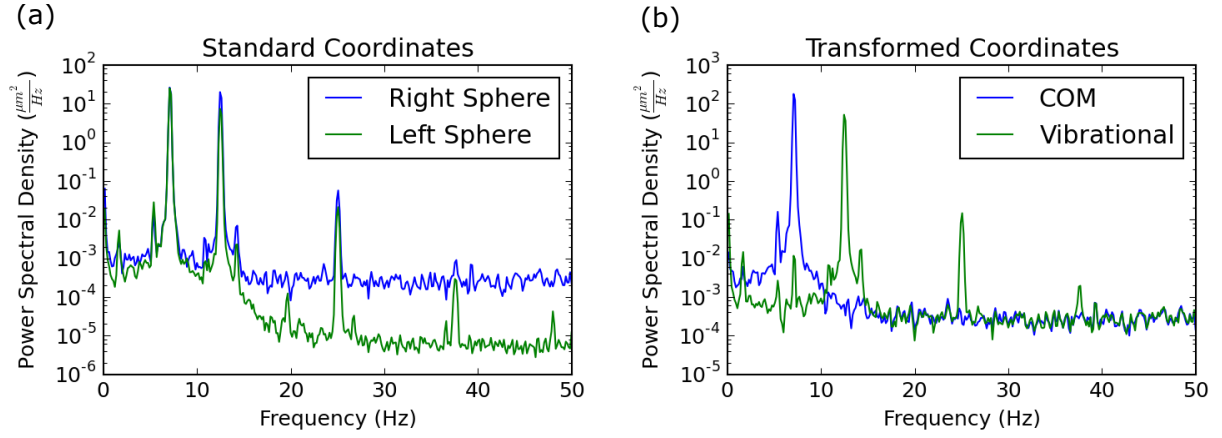


Figure 69: Power spectral densities of (a) the left and right spheres and (b) the transformed coordinates R (COM) and r (Vibrational).

cooling methods discussed in Section 2.2. But, since we use only camera data for the analysis, a calculation of an effective temperature for this data is nowhere near as accurate as the single particle results, and therefore we do not perform the calculation with the power spectral density method. Instead, we simply estimate the effective temperatures achieved by computing the ratios of the thermal amplitude squared displacement to the cooled amplitude squared displacement, as in Eq. 1.42. The cooling results are shown in Fig. 70.

It is interesting to note that the average separation of the molecules (as calculated from the full set of camera images) *decreases* when the particle is cooled (from $r_0 \approx 46 \mu\text{m}$ to $r_0 \approx 38 \mu\text{m}$), which is somewhat evident in Fig. 70 (b) as the cooled motion has a lower offset than the average of the thermal motion. Calculating the ratio of the mean squared displacements of the thermal data to the cooled data presented yields results:

$$T_R \approx T_{th} \frac{\langle R^2 \rangle}{\langle R^2 \rangle_{thermal}} = 30 \text{ mK} \quad (4.7)$$

$$T_r \approx T_{th} \frac{\langle r^2 \rangle}{\langle r^2 \rangle_{thermal}} = 11 \text{ mK} \quad (4.8)$$

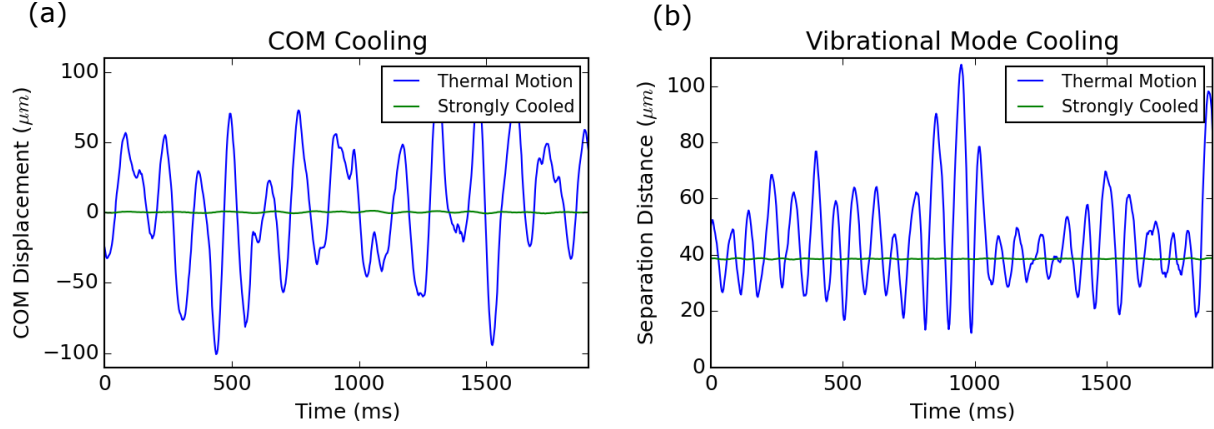


Figure 70: Segment of time domain data demonstrating cooling of (a) the COM motion and (b) the vibrational mode of the micro-molecule.

with $T_{th} = 295$ K, $\langle R^2 \rangle_{thermal} = 1450 \text{ } \mu\text{m}^2$, $\langle R^2 \rangle = 0.145 \text{ } \mu\text{m}^2$, $\langle r^2 \rangle_{thermal} = 300 \text{ } \mu\text{m}^2$, $\langle r^2 \rangle = 0.011 \text{ } \mu\text{m}^2$. However, these correspond to average amplitudes of only $\sim 1/2$ pixels on the camera. The minimum observable amplitude is not exactly known, but an average amplitude of $1/2$ pixels is probably approaching the limit considering the particle images themselves are only $\sim 6 - 8$ pixels in size. Cooling results of $T_R \approx 200$ mK and $T_r \approx 250$ mK were also obtained, which are likely reasonably accurate measurements.

Finally, we estimate the number of electrons on each particle (using Eq. 4.4) as $n_1 n_2 \approx 2050$, or assuming $n_1 = n_2$, $n \approx 45$ electrons on each sphere.

4.3 AN OVER-DAMPED HARMONIC OSCILLATOR AS PSEUDO-FREE PARTICLE

4.3.1 Rationale

While the methodology of providing negative feedback in the under-damped regime of the harmonic oscillator is still considered a viable approach to reaching the quantum mechanical regime, we have begun development on a new methodology to address some of the experimental concerns related to under-damping. We intend to move the feedback into the over-damped regime of the harmonic oscillator, which essentially gives us more cooling “strength” and allows us to overcome some possible limitations in the system. The major difference in this approach is that the time scale that quantum mechanical experiments must be performed is significantly decreased.

As mentioned in Section 3.5, we have not yet determined the cause of the limitation in our cooling ability, with one of the candidates being excess natural damping. As discussed in prior analyses (see Section 1.4.1.3), the effective temperature of the cooled motion is fundamentally limited by the natural damping rate (Γ_A) in the system (copied from Eq. 1.44):

$$T_{fb} = T_A \frac{\Gamma_A}{\Gamma_{fb}}$$

While that analysis assumed a certain description of the power spectral density, the same results can be obtained by a simple argument that the cooled temperature is determined by the heating and cooling processes reaching equilibrium.

In the under-damped regime, Γ_{fb} is limited experimentally (and also as a mathematical definition of under-damping) to about one-tenth of the resonance frequency, $\Gamma_{fb} \approx 0.1\omega_i$. Then, the only way to reach lower effective temperature T_{fb} is to decrease the natural damping rate (Γ_A), for instance by decreasing the pressure in the chamber. If the natural damping cannot be decreased, for instance if it is determined not by external factors like the pressure but by an internal mechanism, such as loss in the magnetic response of the system, we may have no experimental handle for decreasing the rate; or, if we simply want to continue working in a pressure limited (room temperature) experiment, our only choice

to reach lower effective temperatures is to increase Γ_{fb} beyond the under-damping limited values.

4.3.2 RC Feedback Filter Attempt

Moving into the over-damped region requires a stronger damping force (the damping rate Γ and the strength of the interaction are essentially one and the same). The nominal laser setup (shown in Fig. 8) has very weak coupling to the axial motion due to its geometry. As such, simply increasing the illumination intensity of the cooling laser is not an option, as it would cause issues with the other DOF. On top of that, since we are aiming for a strong effect over a large bandwidth, any signal leakage from one DOF to another would lead to disastrous consequences in the feedback filter (i.e., we would likely excite the vertical and transverse motion). As such, a second 660 nm laser is added to the system and aligned such that it couples mainly to the axial DOF. A simplified schematic of the illumination setup is shown in Fig. 91.

In the under-damped regime, we were able to use a band-pass filter around the resonance frequency to provide our feedback; as suggested previously, this method gets difficult as the bandwidth of the filter approaches the resonance frequency. In addition, we want to generate a true derivative signal and extend the feedback all the way to DC. To do this, we started by encoding the motion into an RC circuit as a voltage input.

We read the voltage across the resistor (V_R) of the RC circuit, with the voltage output signal from the particle motion as the circuit's driven input. To explain the predicted response V_R , we plot the analytical amplitude and phase response to a sinusoidal input in Fig. 71.

Defining $f_c \equiv 1/2\pi RC$, we see that the response of V_R in the frequency domain in both amplitude and phase is essentially a derivative (considering a $\pi/2$ phase shift from the input signal). As such, we choose the time constant $\tau = RC$ of the circuit such that we stay well near the $\pi/2$ region.

The full set of changes to the system to enable overdamping is listed in Appendix B.7.

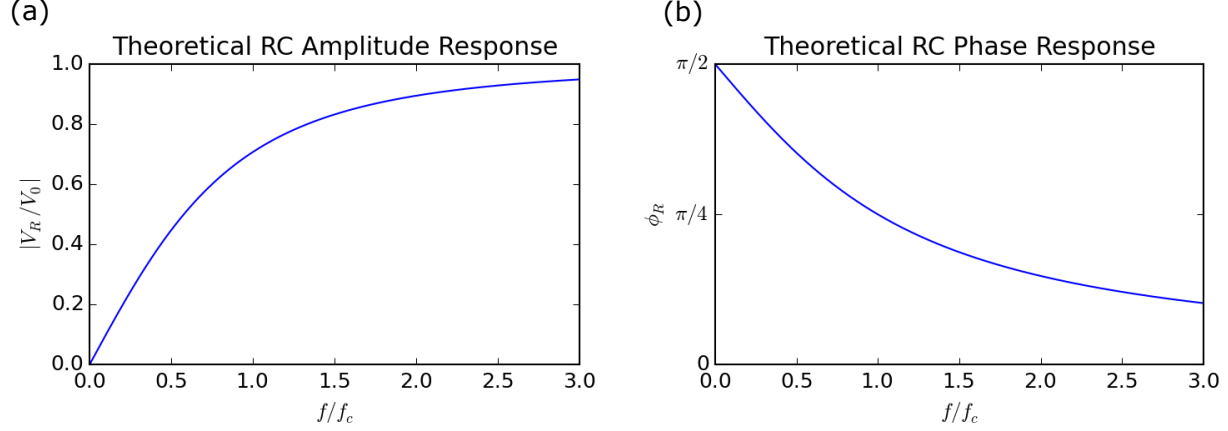


Figure 71: Theoretical amplitude (a) and phase response (b) of V_R in an RC circuit.

4.3.2.1 Results While we no longer need to work in the frequency domain to discuss our results (and in fact, it may no longer makes sense to do so, since in the over-damped regime the time scales of interest are determined not by the oscillator frequencies but by the feedback damping rates), we show in Fig. 72 what the frequency data looks like as we push into stronger and stronger cooling. The legend labels correspond to the amount of gain provided to the drive laser in somewhat arbitrary units - however, the curves increase from the lowest feedback (-20db) to the largest feedback (MAX).

It is evident in the (-20DB) and (-10DB) curves that the motion is still under-damped, as there is still a resonance peak visible in each. As the feedback is increased, we increasingly drive the amount of signal in the low frequency regions toward the noise floor. In fact, for the maximum feedback (MAX), we actually drive the response of the particle *below* the detector noise floor - this means we are driving the particle to cancel detector noise.

We can also see in the MAX curve that we have somewhere around $\Delta f \approx 100$ Hz of cooling bandwidth, as evidenced by the signal increasing to levels above the covered detector signal around that frequency. Essentially, the feedback signal is a derivative of the motion in the frequency range of 0 Hz to roughly the feedback bandwidth; above this ‘cutoff’ frequency, the feedback signal is no longer a damping force, and we end up driving the particle instead.

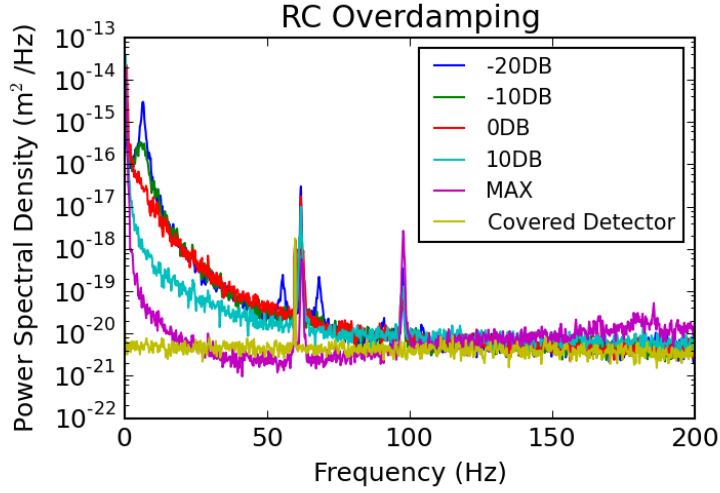


Figure 72: Power spectra showing over-damping of a particle, evident as a lack of resonance peak for higher gain values.

This also brings to light a major issue in this method of cooling, which is the other DOF coupling into the motion. In this case, both the vertical ($f \approx 97$ Hz) and transverse ($f \approx 60$ Hz), as well as 60 Hz line noise are all coupling into the axial signal. Since we are feeding this back to the particle, we likely then drive the particle at those frequencies. In fact, the limitation in this case was likely due to an instability created from the 60 Hz noise.

4.3.3 Parameter Estimates

Since we saw in Section 4.3.2 that over-damping was possible, we decided to make estimates of the parameters needed in the over-damping regime.

In the under-damped regime, we say we have reached the quantum mechanical regime when the energy of particle is on the order of the energy of the ground state of the system:

$$E \equiv k_B T_{fb} \approx \hbar \omega_i \quad (4.9)$$

Then, from Eq. 1.44:

$$k_B T_A \frac{\Gamma_A}{\Gamma_{fb}} \approx \hbar \omega_i \quad (4.10)$$

Now, as an estimate, we assert we can reach the quantum mechanical regime of the over-damped particle with an energy scale determined not by ω_i but by Γ_{fb} :

$$k_B T_A \frac{\Gamma_A}{\Gamma_{fb}} \approx \hbar \Gamma_{fb} \quad (4.11)$$

Solving for Γ_{fb} :

$$\Gamma_{fb} \approx \left(\frac{k_B T_A \Gamma_A}{\hbar} \right)^{1/2} \quad (4.12)$$

We compute $\Gamma_A = \Gamma'_{fb} T'_{fb} / T_A$ from the best damping rate result (11-26-2017 MN). Using $T_A = 295\text{K}$, $\Gamma'_{fb}/2\pi = 1.51\text{ Hz}$ and $T'_{fb} = 0.14\text{ mK}$, we arrive at a value of $\Gamma_{fb}/2\pi \approx 2\text{kHz}$.

We also must perform our measurements at the standard quantum limit (SQL), meaning our measurement accuracy is limited only by the uncertainty principle for position and momentum. An analysis similar to the quantum harmonic oscillator SQL in [23] is performed, in which we aim to calculate the optimal measurement time scale τ for a free particle in order to meet the SQL. This analysis is taken from [57] (pp. 299-300), with key arguments reproduced here for clarity.

Consider making a single position measurement x_1 on a free particle with a measurement uncertainty of Δx_1 . This creates a corresponding uncertainty in the momentum p given by the uncertainty principle [57]:

$$\Delta p \geq \frac{\hbar}{2\Delta x_1} \quad (4.13)$$

We then wait some amount of time τ and perform a second x measurement. Then, we consider the additional uncertainty of $\Delta x_{add} = \Delta p \tau / m$ in addition to the measurement uncertainty Δx_2 . The total uncertainty in the two measurements is then [57]:

$$(\Delta x(\tau))^2 = (\Delta x_1)^2 + (\Delta x_2)^2 + (\Delta x_{add})^2 \quad (4.14)$$

The author sets $\Delta x_2 \equiv 0$ and then minimizes Eq. 4.14 with respect to $(\Delta x_1)^2$ (I think it should probably be done with $\Delta x_2 \equiv \Delta x_1$, but this only changes things by a factor of $\sqrt{2}$).

This leads us to the result [57]:

$$(\Delta x(\tau)) = \Delta x_{SQL} = \sqrt{\frac{\hbar\tau}{m}} \quad (4.15)$$

We now estimate Δx in the case of continuous measurements by asserting $\tau \rightarrow 2\pi/\Gamma_{fb}$. Using $\Gamma_{fb}/2\pi = 2\text{kHz}$ calculated earlier, we contend to make a continuous measurement of x with uncertainty:

$$\Delta x(0.5 \text{ ms}) \approx 4 \times 10^{-12} \text{ m} \quad (4.16)$$

We then make a rough estimate of the detected illumination power by a simple argument that we can localize the particle to roughly the diffraction limit (dl) of the objective divided by the square root of the number of photons (this is essentially the same statement as Eq. A.35):

$$\Delta x_{SQL} \approx \frac{\Delta x_{dl}}{\sqrt{N}} \quad (4.17)$$

In our system, $\Delta x_{dl} \approx 1.66 \text{ }\mu\text{m}$, leading to $N = 1.8 \times 10^{11}$. This needs to be done in τ s. Finally, this means:

$$P_0 = \hbar c \frac{N}{\tau} \frac{2\pi}{\lambda} \approx 90 \text{ }\mu\text{W} \quad (4.18)$$

As a first attempt, we start with $\tau \approx 10 \text{ ms}$, allowing us a scattered power $P_0 \approx 900 \text{ nW}$.

4.3.4 RLC Feedback Filter Attempt

A second experiment was run in an attempt to better match experimental parameters with estimates for optimal performance. Mainly, this means more illumination power. The additional illumination power causes an issue with the QPD detector, in that the signals would saturate in the first stage. As such, it is necessary to utilize a balanced detector, in which we can orient the photodiode connections such that they perform the current subtraction themselves - this keeps the signal small for the first (and now only) stage amplifier. The schematic for this detector is shown in Fig. 89. This also requires a second detection path for the axial motion - the original path is used to keep control of the system, and then feedback is switched to the new detector and feedback path. This setup is described in Fig. 94.

In addition, the analog circuit was changed to a critically damped RLC circuit, with the feedback output taken as the voltage across the resistor. The major difference from the RC circuit performance shown in Fig. 71 is that we match the bandwidth (cutoff frequency $\omega_0 = 1/LC$) to bandwidth estimates. Fig. 73 shows the theoretical circuit response for the critically damped RLC circuit. In effect, compared to the RC circuit, we have a trade-off: the phase response rolls off more quickly in the RLC filter, but we gain an amplitude roll-off as well.

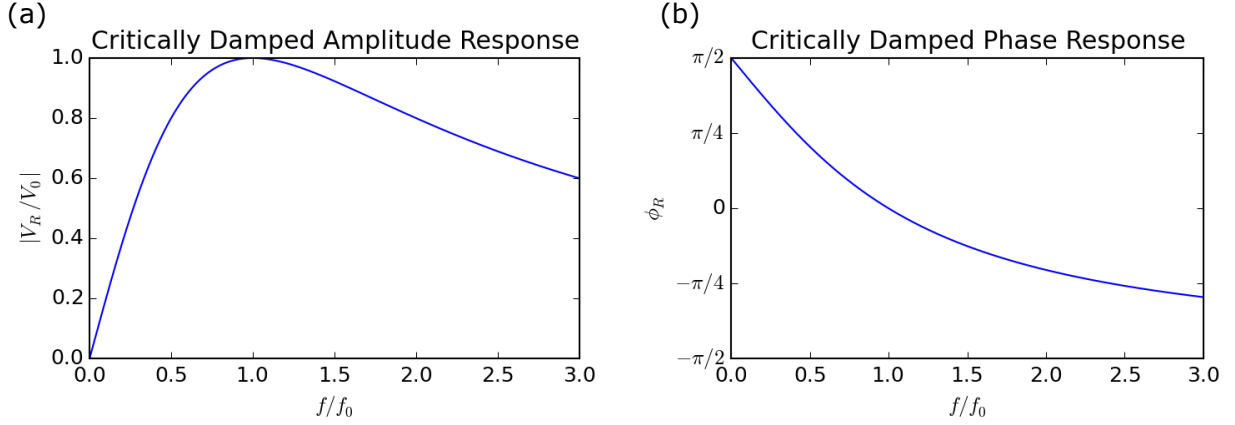


Figure 73: Theoretical amplitude (a) and phase response (b) of V_R in a critically damped RLC circuit.

4.3.4.1 Results We again display the power spectral density of two tests of overdamping - once with roughly 50 nW total scattered power (~ 10 nW detected) and again with roughly 200 nW scattered power (~ 50 nW detected).

We see that we have improved in some respects compared to Fig. 72, as our noise floor has decreased (because of the balanced detector) and the increased illumination has increased our signal to noise, allowing the baseline of the signal to reach about 2 orders lower. In addition, we see that we can scatter a lot of light from the particle and still have good control of the system.

Without cooling, we continued to test the maximum amount of power that we could scatter off the particle before causing trap stability issues. We found that the particle was

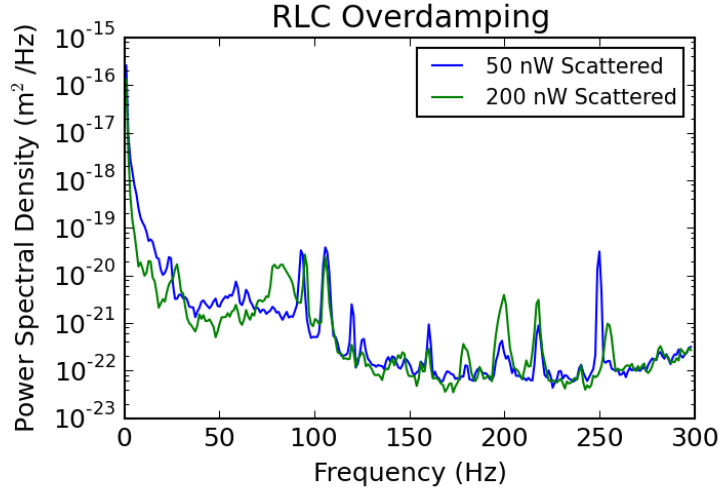


Figure 74: Power spectra of overdamped spectra using the RLC filter.

still stable up to $1.7 \mu\text{W}$ scattered, which was the maximum amount of illumination power available at the time.

4.3.5 Challenges

The biggest limitation of the system at this point is using the feedback laser on only one side in the axial direction. As discussed, for larger cooling bandwidths, more illumination power is necessary. However, since the axial direction of the trap is the weakest, and the leaser beam is oriented along that axis with one specific k-vector, the particle's equilibrium position ends up being significantly shifted once the cooling laser light is turned on. This is demonstrated in Fig. 75. In (a), the particle is at its natural equilibrium position. When the axial feedback laser is focused onto the particle in (b), the particle equilibrium is shifted about $75 \mu\text{m}$ along the axis. Considering the trapping region is at most $\sim 500 \mu\text{m}$ total (the top pole piece is nominally $\sim 200 \mu\text{m}$ wide), this represents a significant alteration to the equilibrium trapping field.

This becomes the primary limitation on the amount of cooling illumination power that

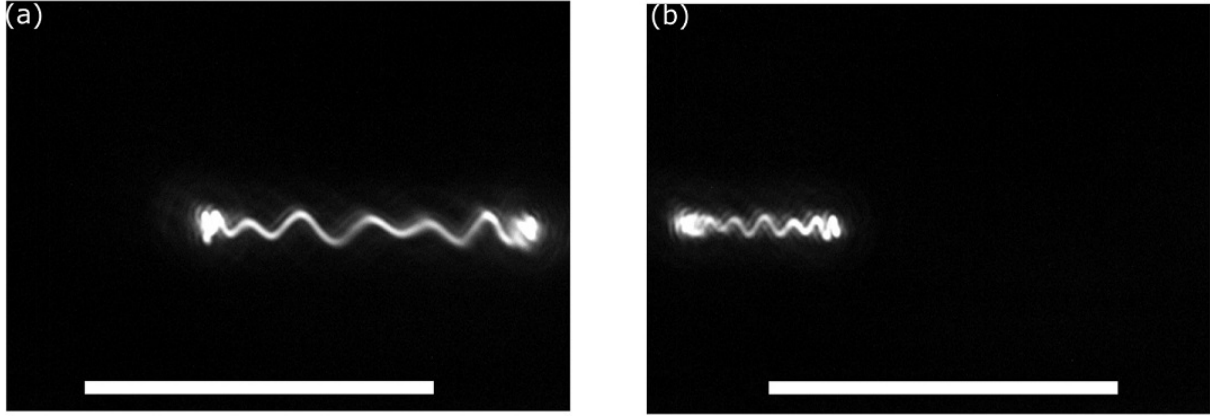


Figure 75: (a) The nominal equilibrium position of the particle in the trap. (b) The equilibrium position is shifted by $\sim 75 \mu\text{m}$ when the axial feedback laser is turned on. Scale bars are $100 \mu\text{m}$.

we can use, as increasing the power any further will completely push the particle out of the trap. It also causes a slow drift in the equilibrium position of the particle over time, making measurements of the variance in the signal much larger than they would appear to be by viewing the power spectral densities in Fig. 74.

4.3.6 Outlook

While there is clearly a lot of work to be done, this demonstration proves that this type of cooling can be performed in our system. This may be important to the future of the experiment if some of the cooling issues discussed in Section 3.5 end up being fundamental system limitations. This is an exciting result: similar to the G measurement, this type of cooling is something unique to our system because of its low oscillation frequencies.

4.4 MOVING THE TABLE VERTICALLY TO DAMP PARTICLE MOTION

As an extra demonstration, we tested cooling the vertical motion of the particle by moving the entire optical table up and down. Aside from the feedback mechanism, the experimental process was exactly the same as the single particle cooling. Instead of sending the vertical feedback signal to the second laser, we send the feedback signal as a current (see Fig. 83 to a set of three transducers wired in parallel, placed on the middle of the optical table, with extra weight on top of them. The surface transducers (SparkFun COM-10975) in a parallel configuration are shown in Fig. 76 (a), with the extra weight placed on top of them shown on Fig. 76 (b).

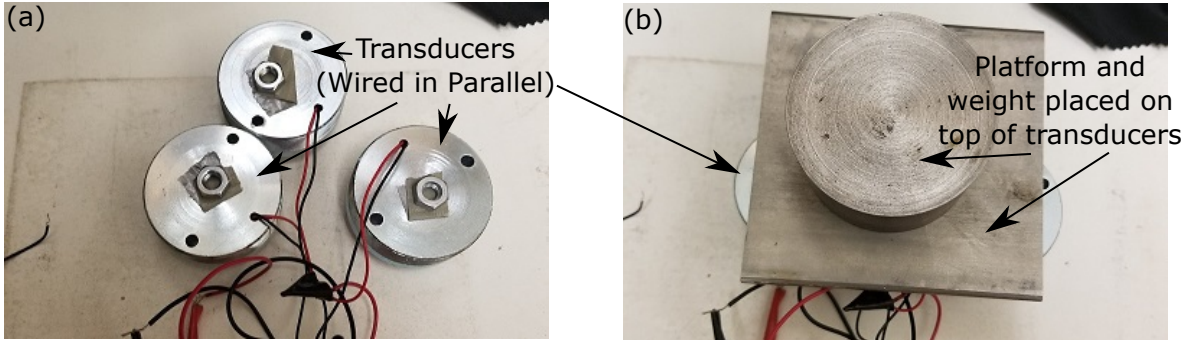


Figure 76: Three surface transducers are wired in parallel in (a) and fit with an extra weight (b). The transducers are placed on the optical table and driven to move the optical table vertically.

A full mass and detector calibration was not performed for the table shaking data. Instead, we display in Fig. 77 (a) comparison between the best laser feedback results and the best table shaking results for the same particle.

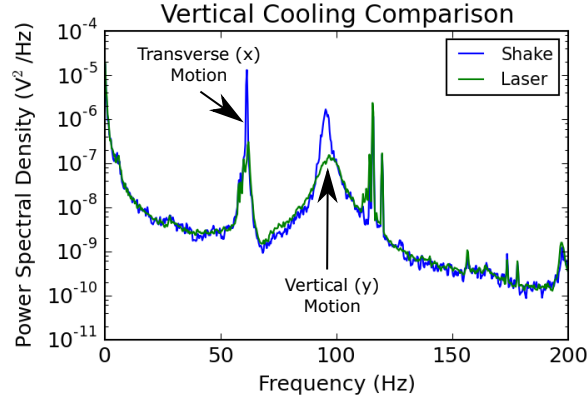


Figure 77: Comparison of laser feedback results and table shaking feedback results for the same particle.

An estimate of the cooling would place a best case temperature for the laser feedback at $T_{eff} \approx 10$ mK, with the table temperature a factor of 10 higher.

As evident from Fig. 77, shaking the table is unable to provide results as good as the laser feedback. This is likely due to bandwidth limitations of the transducers, meaning it is hard to get true wide-band cooling because of circuitry limitations in the transducers (like their own resonance frequencies) and table.

APPENDIX A

SHOT NOISE LIMITED DETECTION

A.1 RADIATION PRESSURE SHOT NOISE

In order to damp the particle motion to the energy scale of its quantum ground state, all drive forces from interaction with the environment must be small enough as to not heat the particle motion on the time scale that energy is removed from the system ($\sim \Gamma$). While all classical noise sources can be removed (such as collisions with residual gas molecules), quantum noise sources are a fundamental fact of nature. In particular, we discuss the shot noise of the light scattered from the particle, which is an unavoidable consequence of a quantum mechanical description of the system.

We aim to compute the maximum allowable amount of optical power scattered from the particle, such that our feedback cooling mechanism can keep the particle at or near its quantum ground state. We will first compute this using straightforward arguments, and then with the power spectral density methodology of Section [1.4.1](#).

We assert that, on average, the particle scatters N_s photons, with the variance in the number of photons scattered referred to as the shot noise:

$$\bar{N} = N_s \quad (\text{A.1})$$

$$(\Delta N)^2 = N_s \quad (\text{A.2})$$

The uncertainty in the number of photons scattered translates to an uncertainty in the amount of momentum imparted to the particle.

$$\begin{aligned} \Delta p &= \hbar k \Delta N \\ &= \hbar k \sqrt{N_s} \end{aligned} \quad (\text{A.3})$$

where $k = 2\pi/\lambda$ is the wave number of the scattered light. We can relate this to the amount of energy required to increase the energy of the particle by one energy quanta $\hbar\omega_i$:

$$E = \frac{(\Delta p)^2}{2m} = \hbar\omega_i \quad (\text{A.4})$$

and solve for N_s , which gives us the number of scattered photons needed to increase knock the particle out of its ground state:

$$\begin{aligned} N_s &= \frac{2m\omega_i}{\hbar k^2} \\ &= \frac{2m\omega_i \lambda^2}{\hbar (2\pi)^2} \end{aligned} \quad (\text{A.5})$$

We can relate this to a scattered power by saying N_s is the number of photons scattered in the time it takes the cooling to respond (Δt):

$$P_s = N_s \frac{\hbar\omega}{\Delta t} \quad (\text{A.6})$$

We then assert:

$$\frac{1}{\Delta t} = \Delta f = \alpha f_i \quad (\text{A.7})$$

which is to say the bandwidth of the cooling is some fraction of the resonance (usually, $\alpha \approx 0.1$). Equating Eq. A.5 and Eq. A.6, we have computed the optimal average scattered power, which we write as an inequality as any power less than this is also acceptable:

$$P_s \leq 2m\alpha c\lambda f_i^2 \quad (\text{A.8})$$

Alternatively, we can use the power spectral density formulation detailed in Section 1.4.1 to compute an even more accurate estimate. We note that the force (divided by mass) on the particle due to radiation pressure is [58]:

$$F'_{rad} = \frac{1}{m} \frac{P_s}{c} \quad (\text{A.9})$$

Like thermal noise, shot noise is a stationary process, with autocorrelation function given by [58]:

$$\langle (F'_{sn}(t) - \bar{F}'_{sn})(F'_{sn}(t + \tau) - \bar{F}'_{sn}) \rangle = \frac{\beta_i}{m^2 c^2} \hbar \omega P_s \delta(\tau) \quad (\text{A.10})$$

Here, β_i represents the fraction of the total power scattered in a given direction. For example, in [58], β_i is obtained via an integral over the emission pattern of a point dipole, and is on the order of 0.1. In the case of larger particles (particles whose size is on the order of the illumination wavelength), the emission pattern is more difficult to calculate, but most of the light is forward scattered along the direction of illumination. As such, in our case, we expect β_x to be much larger than β_y or β_z .

If shot noise from the scattered light is the limiting excitation source, we can simply replace ξ in Eq. 1.28 with the expression in Eq. A.10:

$$\langle x_i^2(t) \rangle_s = \int_{-\infty}^{\infty} \frac{\frac{\beta_i}{m^2 c^2} \hbar \omega_0 P_s}{(2\pi)^4 (f_i^2 - f^2)^2 + \gamma^2 f^2} df \quad (\text{A.11})$$

Then, we utilize Eq. 1.31 to equate Eq. A.11 with the ground state amplitude variance in Eq. 1.59:

$$P_s \leq 2\pi m\alpha c\lambda f_i^2 / \beta_i \quad (\text{A.12})$$

This result matches with the simple formulation result of Eq. A.8, up to a factor of π/β_i , where π is a result of the actual power spectral density integral being used and $1/\beta_i$ accounts

for the fact that only some fraction of the total scattered power is in the direction of interest.

A calculation of the optimal power for the typical particle used (1.54 μm SiO_2) according to Eq. A.8 is given in Section 3.3.1.

A.2 DETECTION - OVERCOMING JOHNSON NOISE IN THE DETECTOR

The detectors utilized to monitor the motion of the particle are photodiode detectors. Since small optical illumination powers are required in order to cool to the ground state (see Section A.1 and Section 3.3.1), an amplification circuit with large gain (like those shown in Fig. 79 and Fig. 89) is required to make the detected signals large enough to record. As mentioned in Section 3.5.5.1, voltage fluctuations from thermal agitation of charge carriers in any resistor (known as Johnson-Nyquist Noise) will create excess noise in the detected signal. In order to detect motion at the quantum-mechanical shot noise limit, the signal generated from the shot noise of the illumination must overwhelm this Johnson-Nyquist noise.

The average noise power of Johnson-Nyquist noise generated in a resistance R and a bandwidth Δf is given by [55]:

$$\bar{v}_{jn}^2 = 4k_B T R \Delta f \quad (\text{A.13})$$

The shot noise current σ_i (generated by the photodiode) in a bandwidth δf is given by [59, 60]:

$$\bar{\sigma}_i = \sqrt{2eI\Delta f} \quad (\text{A.14})$$

where e is the electron charge and I is the photodiode current. This is converted to a voltage noise power by multiplying by the same resistance R in Eq. A.13 and squaring:

$$\bar{v}_{sn}^2 = 2eI\Delta f R^2 \quad (\text{A.15})$$

We then require that the shot noise voltage power given in Eq. A.15 overwhelms the

Johnson-Nyquist noise power given in Eq. A.13:

$$\bar{v}_{sn}^2 \geq \bar{v}_{jn}^2 \quad (\text{A.16})$$

leading to a condition on the voltage ($V = IR$) generated by the photodiode current I across the resistor R :

$$IR \geq \frac{2k_B T}{e} \approx 50 \text{ mV} \quad (\text{A.17})$$

This result states that the signal from the photodiode will be shot noise limited when the voltage generated by photodiode current I across the resistor R is greater than ~ 50 mV. It should be noted that Eq. A.15 can be written in terms of the optical power P_s , illumination angular frequency ω , and photodiode efficiency ϵ (units of A/W) as:

$$\bar{v}_{sn}^2 = 2\hbar\omega\epsilon^2 P_s \Delta f \quad (\text{A.18})$$

A.3 DETECTION SIGNAL TO SHOT NOISE FOR A SPLIT DETECTOR

In addition to momentum kicks from shot noise, we must be able to distinguish between the signal generated by shot noise and our actual signal, based on our detection method. For the current experiment, the detection method is a split photodiode detector (See Section 2.3.2.4). In such a case, this means that the signal from the photodiode is proportional to the difference in optical power on either side of the detector (for the sake of analysis, we will call the two sides ‘left’ and ‘right’, but this could also mean ‘top’ and ‘bottom’:

$$S = (P_r - P_l)\epsilon G \quad (\text{A.19})$$

$$= \left(\int_{A_r} I dA - \int_{A_l} I dA \right) \epsilon G \quad (\text{A.20})$$

where P_r and P_l are the total power on the right or left photodiode, I is the intensity of the light, A_r and A_l represent the area that the light occupies on each side of the detector, ϵ is the photodiode conversion factor, and G is the gain from the photodiode circuit. Since ϵ and

G will be identical for both the signal and shot noise signal, we omit them for the remainder of the analysis.

The particles utilized are typically $d = 1.54 \text{ } \mu\text{m}$ in diameter, which is right around the Abbe diffraction limit of the objective ($2r = \lambda/\text{NA} \approx 1.66 \text{ } \mu\text{m}$), with $\text{NA} \approx 0.5$. For the following, we will assume $d \leq \lambda/\text{NA}$. We can approximate the Airy disk with a Gaussian distribution with $\sigma \approx 0.42\lambda/2\text{NA}$ [56].

$$\sigma \equiv \frac{0.42\lambda}{2\text{NA}} \quad (\text{A.21a})$$

$$I(y, z) = \frac{P_0}{2\pi\sigma^2} e^{-y^2/2\sigma^2} e^{-z^2/2\sigma^2} \quad (\text{A.21b})$$

where P_0 is the total power detected. Integrating out one degree of freedom, we write:

$$I(x'_i) = \frac{P_0}{(2\pi)^{1/2}\sigma} e^{-x_i'^2/2\sigma^2} \quad (\text{A.22})$$

Continuing from Eq. A.20 (and dropping ϵ and G), we look at the signal from the detector when the Gaussian's center is displaced by x_i :

$$S = \int_{A_r} I dA - \int_{A_t} I dA \quad (\text{A.23})$$

$$= \int_{-x_i}^{\infty} I(x'_i) dx'_i - \int_{-\infty}^{-x_i} I(x'_i) dx'_i \quad (\text{A.24})$$

$$= \left(\int_{-x_i}^0 I(x'_i) dx'_i + \int_0^{\infty} I(x'_i) dx'_i \right) - \left(\int_{-\infty}^0 I(x'_i) dx'_i - \int_{x_i}^0 I(x'_i) dx'_i \right) \quad (\text{A.25})$$

$$= 2 \int_{-x_i}^0 I(x'_i) dx'_i \quad (\text{A.26})$$

Since we need to detect a signal from the ground state variance of the particle's motion, we note that $x_i \ll \sigma$, so we expand the Gaussian about $x_i = 0$:

$$I(x_i) \approx \frac{P_0}{(2\pi)^{1/2}\sigma} \left(1 - \frac{1}{2} \left(\frac{x_i}{\sigma} \right)^2 \right) \quad (\text{A.27})$$

And finally, we arrive at:

$$S(x_i) = (2/\pi)^{1/2} \frac{P_0}{\sigma} x_i \quad (\text{A.28})$$

Similar to the shot noise momentum analysis, we now require that the power spectral density (PSD) of the signal in Eq. A.28 be at least as large as the PSD of the shot noise in some bandwidth Δf_i :

$$\int_{f_i - \Delta f_i}^{f_i + \Delta f_i} PSD_{S(x_i)}(f) df \geq \int_{f_i - \Delta f_i}^{f_i + \Delta f_i} PSD_{SN}(f) df \quad (\text{A.29})$$

Then,

$$PSD_{S(x_i)}(f) = \left((2/\pi)^{1/2} \frac{P_0}{\sigma} \right)^2 PSD_{x_i}(f) \quad (\text{A.30})$$

and

$$PSD_{SN}(f) = \hbar \omega P_0 \quad (\text{A.31})$$

Again, we assert that $\Delta f_i = \alpha f_i$. For the function in Eq. 1.29, this is saying that $\gamma = \alpha f_i$, where $\gamma \approx \text{FWHM}$. Now, we complete the integrals in Eq. A.29, noting:

$$\int_{f_i - \gamma}^{f_i + \gamma} PSD_{x_i}(f) df \approx \frac{1}{2} \int_0^\infty PSD_{x_i}(f) df \quad (\text{A.32})$$

$$\int_0^\infty PSD_{x_i, gnd} = \frac{1}{2} \frac{\hbar}{2m\omega_i} \quad (\text{A.33})$$

$$\int_{f_i - \gamma}^{f_i + \gamma} PSD_{SN}(f) df = \hbar \omega P_0 \gamma \quad (\text{A.34})$$

leading to:

$$\left(\frac{2P_0^2}{\pi\sigma^2} \right) \frac{\hbar}{8m\omega_i} \geq \hbar \omega P_0 \gamma \quad (\text{A.35})$$

Solving for P_0 :

$$P_0 \geq \frac{16\pi^3 m c \alpha \sigma^2 f_i^2}{\lambda} \quad (\text{A.36})$$

Finally, we account for collection inefficiencies by stating that P_0 is some fraction of the scattered power P_s :

$$P_s \geq \frac{16\pi^3 mc\alpha\sigma^2 f_i^2}{\eta\lambda} \quad (\text{A.37})$$

where we have introduced the collection efficiency, $\eta \leq 1$.

A.3.1 Radiation Shot Noise Power and Signal Shot Noise Comparison

We can combine Eq. A.12 and Eq. A.37 to place limits on the allowable scattered power:

$$\frac{16\pi^3 mc\alpha\sigma^2 f_i^2}{\eta\lambda} \leq P_s \leq 2\pi mc\alpha\lambda f_i^2 / \beta_i \quad (\text{A.38})$$

or, in terms of NA by substitution with Eq. A.21a:

$$2\pi^2 0.42^2 \leq \frac{P_s \eta \text{NA}^2}{2\pi mc\alpha f_i^2 \lambda} \leq \eta \text{NA}^2 / \beta_i \quad (\text{A.39})$$

which leads to the condition:

$$3.48 \leq \frac{\eta}{\beta_i} \text{NA}^2 \quad (\text{A.40})$$

*Note that this equation seems to imply that the result improves as we improve the NA of the collection objective. While this is true, one should keep in mind that the assumptions originally made stated that the particle size is roughly matched to the Abbe diffraction limit spot size. As such, the NA can only be increased to the point that the scattered light from the particle completely fills the objective lens.

The result of Eq. A.40 suggests that cooling to the quantum ground state by using a split detector is likely **not** possible with the current collection dynamics of the system, assuming $\eta \approx 0.5$, $\beta_i \approx 0.1$, $\text{NA} \approx 0.5$, Eq. A.40 cannot be satisfied:

$$3.48 \not\leq 1.25 \quad (\text{A.41})$$

This is shown graphically in Fig. 78. For the figure, P_s was set to the value given by Eq. A.12, with $\eta = 0.5, \beta_i = 0.1, \text{NA} = 0.5, \alpha = 0.1$. The power spectral densities are arbitrarily normalized for ease of plotting.

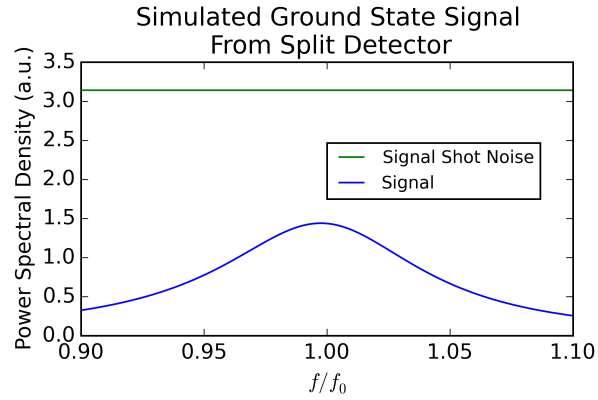


Figure 78: Normalized PSD of the (classical) ground state motion signal and the shot noise in that signal, as determined by setting the scattered power P_s with Eq. A.12.

APPENDIX B

FEEDBACK SYSTEM

The schematics for the boxed sections described in Fig. 13 are listed here. Note that the basis for design for much of the system was performed in [23], and schematics are included here to address changes and additions to the configuration.

B.1 QUADRANT PHOTODIODE AMPLIFIER

The quadrant photodiode detector is designed for use with pretty small optical powers ($P \sim \leq 6$ nW), so a large gain is required. The main changes from the original design in [23] are the first stage amplifier and feedback resistors. The amplifier is changed to AD824 for noise considerations, and the feedback resistors changed to 2, 22.1 M Ω resistors in series. All told, the voltage response for the circuit is computed as:

$$\begin{aligned} V(P_0) &= P_0 \epsilon R_1 G \\ &\approx P (0.6 \frac{\text{A}}{\text{W}}) (44.2 \times 10^6 \Omega) (9.10) \\ &= 2.41 \times 10^8 P_0 \end{aligned} \tag{B.1}$$

where P_0 is the optical power on the detector, ϵ is the detector efficiency at the desired wavelength (830 nm), R_1 is the first stage feedback resistance, and G is the total gain of the remaining stages (which is 0.91 for stage 1 and 10 for stage 2). Sum and difference signals are created in the second and third stages. The schematic is listed in Fig. 79.

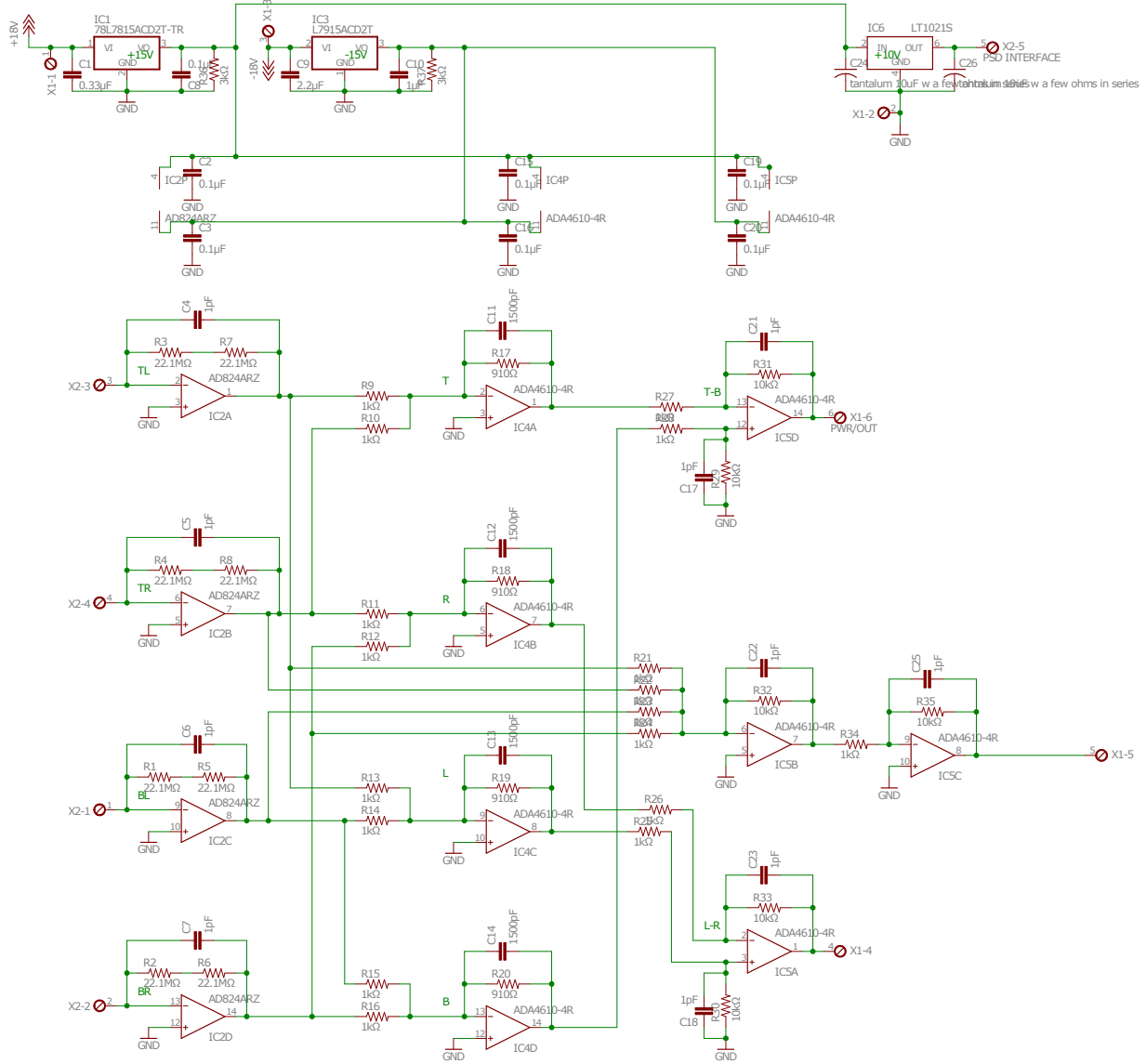


Figure 79: Quadrant photodiode sum, difference, and amplification circuit diagram.

B.2 LOW PASS FILTERS

The low pass filters separate the DC components of the motional signals from the AC components, thus providing a measurement for the centering of the particle on a split detector. The filters are simple passive low-pass filters with a cutoff of $f \approx 1.0$ Hz. The voltages

are read from 3 Keithley multimeters (2000 Keithley), which are communicated to a control computer over the HP-GPIB bus. The main purpose of these filters is to use the offset measured to control the galvo mirror, in order to keep the particle centered on the detector. Such centering is critical for calibration of the final temperature, so automation is critical. The circuit diagram is shown in Fig. 80.

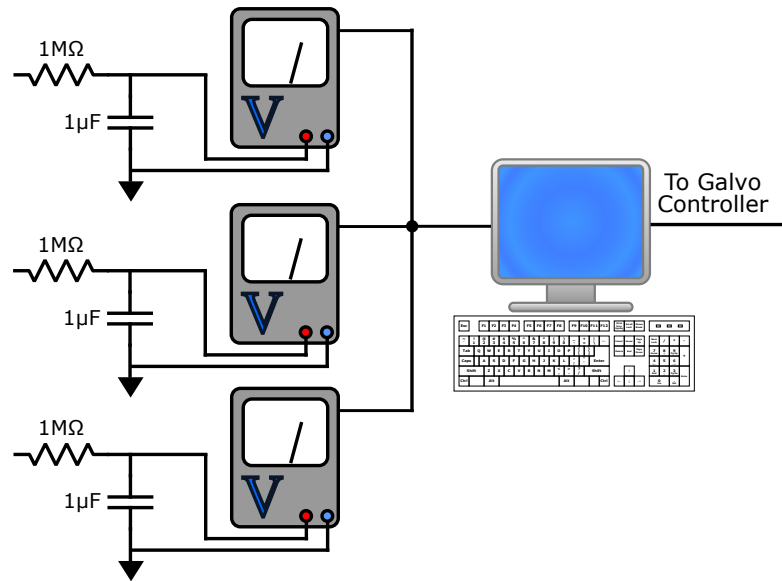


Figure 80: Low pass filters read by Keithley multimeters and a control program automate particle centering on the detector.

B.3 GALVO CONTROL CIRCUIT

The galvo control circuit was designed in [23]. The schematic is copied here, with just a single change to the power resistor. This resistor was changed to $40\ \Omega$ in both arms of the control. This cut the overall range of currents provided to the galvo roughly in half, requiring larger signals to create movement. This was to try to reduce the absolute size of fluctuations in the control signal. The circuit is shown in Fig. 81.

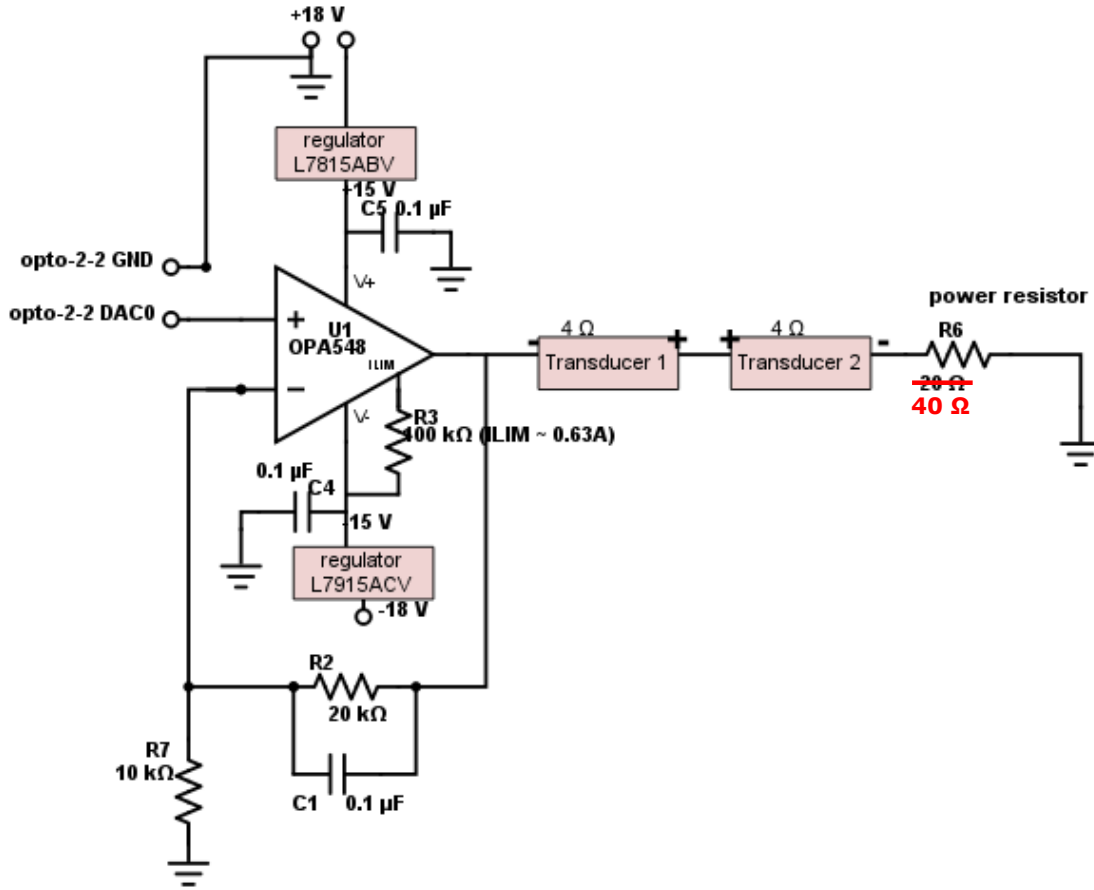
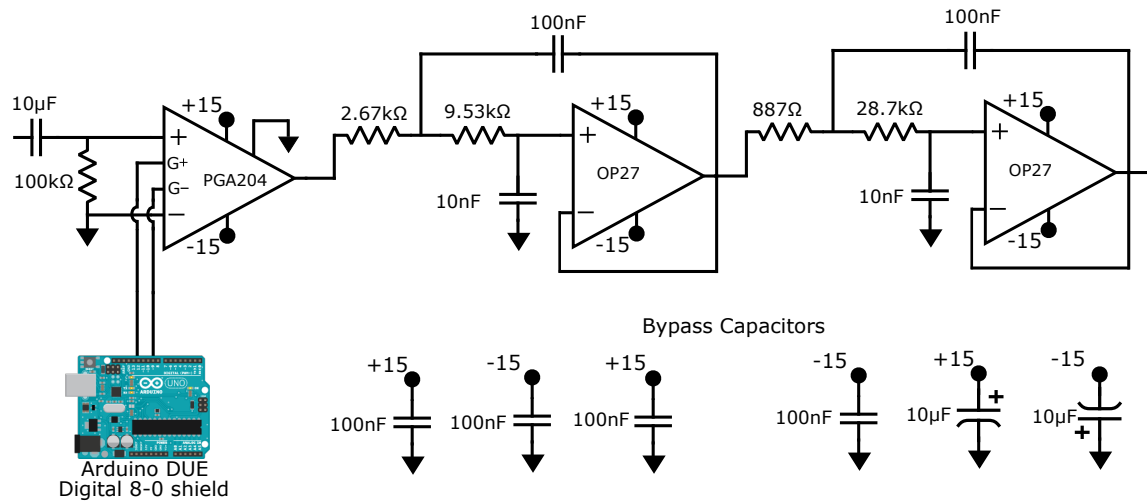


Figure 81: Schematic of galvo drive circuit, copied from [23], with resistance value modified.

B.4 PROGRAMMABLE GAIN AMPLIFIER, HIGH-PASS FILTER, AND SALLLEN-KEY FILTER

The programmable gain amplifier (PGA) and Sallen-Key filter from [23] were modified and combined into a single box. Compared to the original design, the active high pass filter prior to the PGA was changed to a passive filter. Then, the two separate circuits were combined into one. The PGA provides optional additional gain for the motion signals, and the Sallen-Key filter removes high-frequency components to prevent aliasing into the signals

during digitization. The circuit is shown in Fig. 82.



*There are 3 copies of this circuit

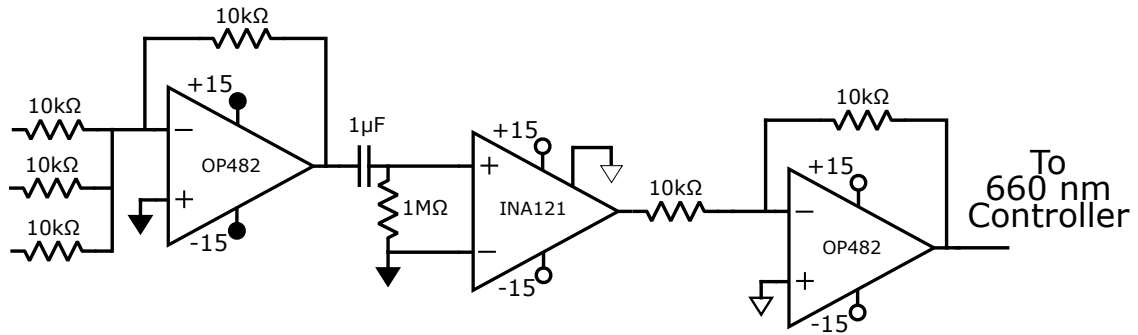
Figure 82: Schematic of the PGA and bandpass filter.

B.5 FEEDBACK DRIVING CIRCUIT

The feedback driving circuit from [23] was originally copied, then modified to the version displayed in Fig. 83. Since the method of feedback is now a voltage signal provided to the 660 nm laser diode controller, the high current op-amp was no longer necessary. In addition, the output of the laser diode can be viewed independently, so the monitoring path was no longer necessary.

The high current op amp and monitor path were separated from the laser drive, but remain in the same box in case a high current drive signal is needed (for instance, when a wire drive was attempted to cool the vertical motion, or when transducers were used to shake the table vertically to cool the vertical motion).

Laser Controller Driver



Transducer or Wire Driver

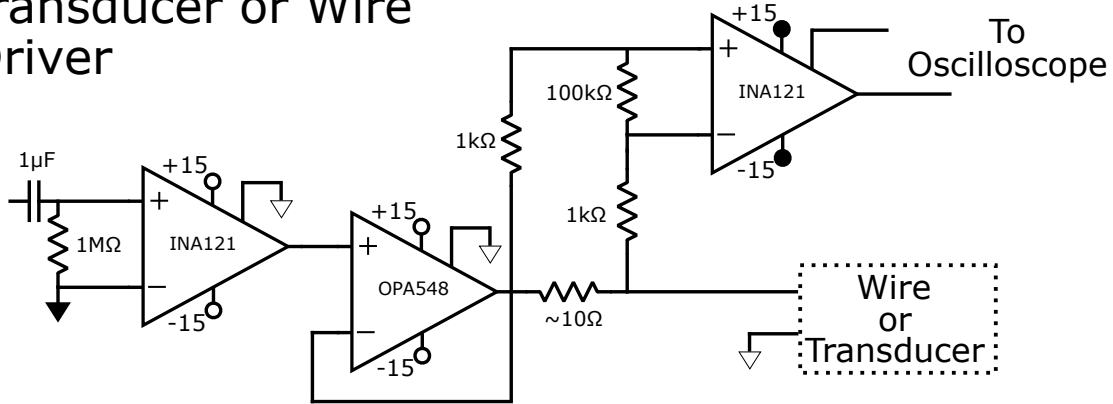


Figure 83: Schematic of the laser drive circuit and high current drive circuit.

B.6 BALANCED AND COOLED DETECTOR

An additional detector was created as a lower noise alternative to the QPD. The detector achieves its lower noise via low noise components (OPA128 op-amp, Eltec Model 104 1 GΩ resistor) and cooling of the photodiodes. In addition, since discrete photodiodes are used, the difference current is created by the detectors themselves without an additional op-amp. In order to cool the photodiodes, they must be placed into a vacuum environment to prevent condensation from forming.

The balanced and cooled detector was originally designed for a different mounting scheme.

Here, we list the important aspects of the hardware design for reference. The designs in Fig. 84 and Fig. 85 are original to the previous design; the supports in Fig. 86 were modified to fit the newly designed vacuum chamber and nipple combination, shown in Fig. 88. The components in Fig. 89 were chosen to deal with the small scattered light levels utilized in the main text (see Section 3.3).

B.6.1 Front and Back Flanges

Some details for detector window flange and thermoelectric cooler flange are included here for completeness. The detector window flange is shown in Fig. 84 (a). It is a 6.0" conflat flange with holes (3.0" apart) for windows to allow light to reach the photodiodes. The TEC flange V3 is also a 6.0" conflat flange machined out of aluminum. Its main purpose is to serve as the mounting point for the detector and to mount the thermoelectric cooler (TEC) (Laird Technologies 9350006-301). The flange has water cooling lines milled out of the aluminum to dump the heat generated from the TEC. The TEC flange is shown in Fig. 84 (b).

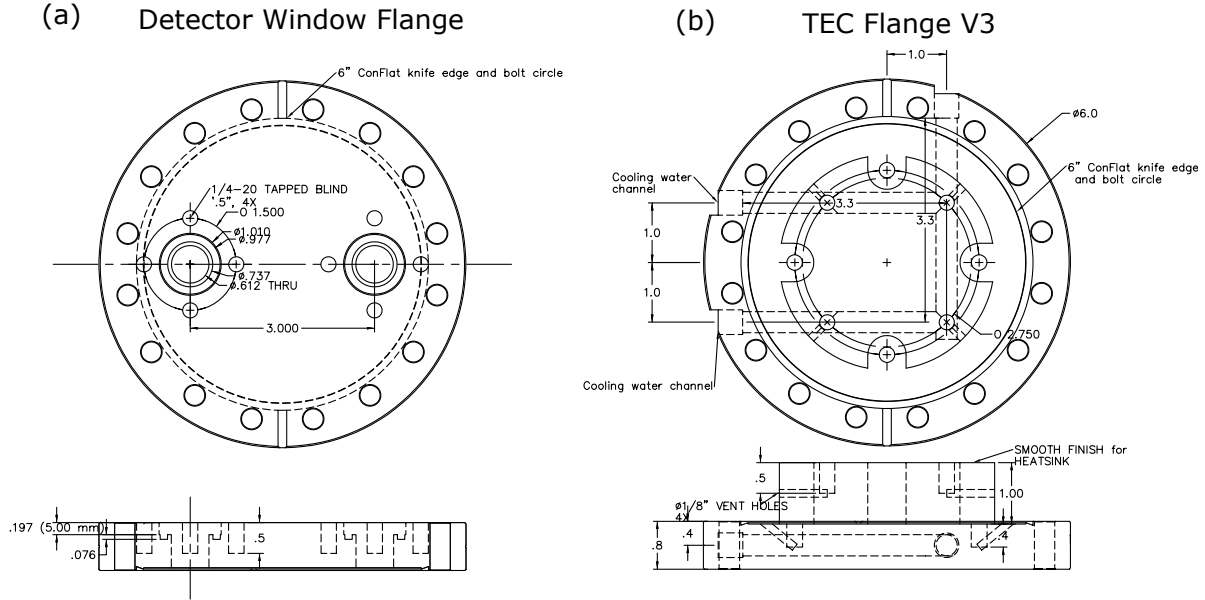


Figure 84: (a) Window flange that allows light to reach the photodiodes. (b) The back (aluminum) flange mounts the (TEC) with internal cooling water channels.

B.6.2 Electronics Mounting Plate

Since a high gain, highly sensitive photodiode circuit is utilized (here, we use a $1\text{ G}\Omega$ feedback resistor and very sensitive OPA128 op-amp), a mounting plate was designed to hold all sensitive components and allow electrical connections to be made ‘floating’ in the air, which is suggested, for instance, by the op-amp specification sheet. In addition, the plate is made out of aluminum, which is a good thermal conductor and allows for the photodiodes to be cooled via direct contact to the plate. The plate is shown in Fig. 85 (a) and Fig. 85 (b).

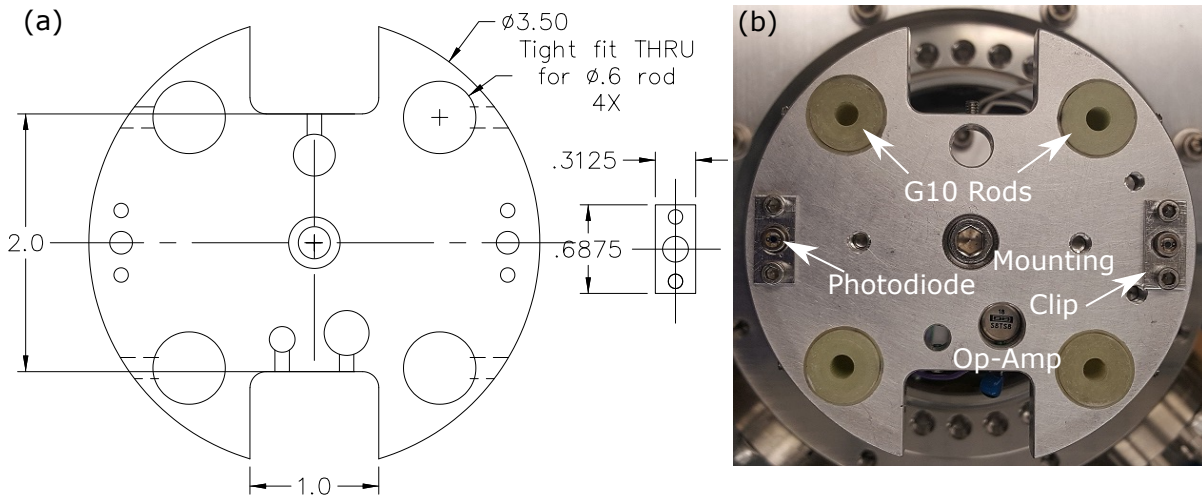


Figure 85: Plate for mounting balanced detector electronics.

B.6.3 Mounting Plate Mechanical and Cooling Supports

The electrical plate is supported by four G10 rods that are connected to the base of the mounting plate. G10 rods are used for thermal isolation from the mounting structure. An aluminum rod and copper braiding, attached to the thermally insulated cold plate, make the thermal connection for cooling the electrical plate (and photodiodes). This support structure is evident in Fig. 86. Both the G10 rods and aluminum rod were shortened roughly 2.125", from 9.625" and 7.5", respectively, to enable mounting the detector in a new vacuum chamber and nipple (shown in Fig. 87 and Fig. 88).

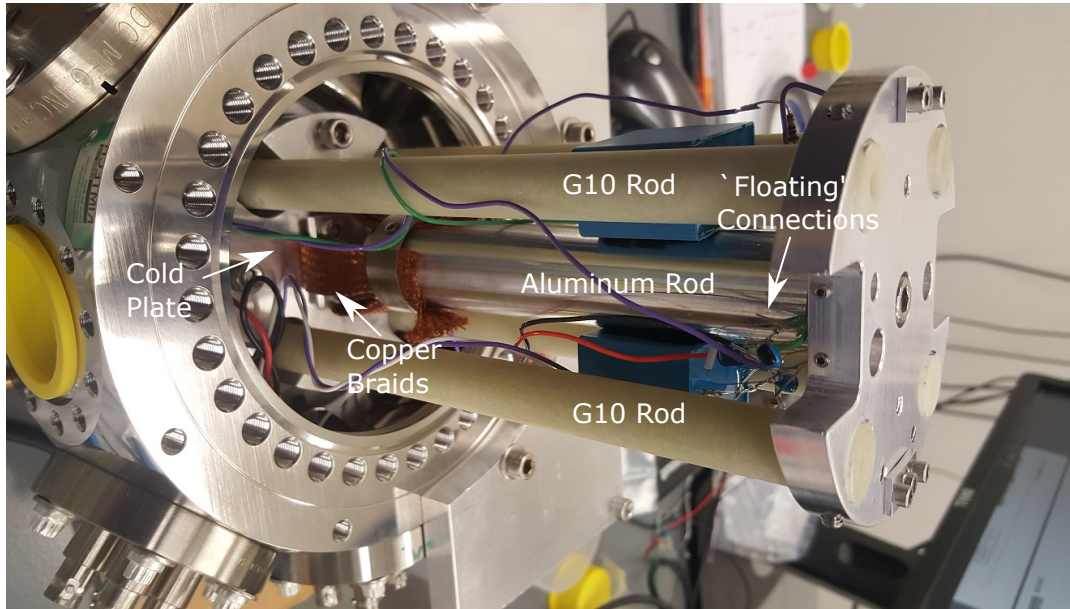


Figure 86: The support for the electronics mounting plate is four thermally insulating G10 rods. The plate is cooled via attachment to a cold plate via an aluminum rod and copper braiding. The ‘floating’ electrical connections are also visible.

B.6.4 Vacuum Chamber and Table Mount

A 6.0” spherical octagon vacuum chamber (Kimball Physics MCF600-SphOct-F2C8) was chosen as the new base structure for this design. The 8 2.75” conflat ports allow for adequate separation of the sensitive electrical connections (reverse bias voltage to photodiodes, power lines, and signal lines) from those that are less sensitive and noisier (thermoelectric cooler and thermistor connections). An aluminum mount was designed and machined to provide support and connection to the optical table. The chamber and mounting structure are visible in Fig. 87.

A custom nipple encloses the remainder of the design (the electrical plate and the support rods), as shown in Fig. 88. An adjustable support jack (McMaster-Carr 3757K13) adds extra support to the front of the chamber.

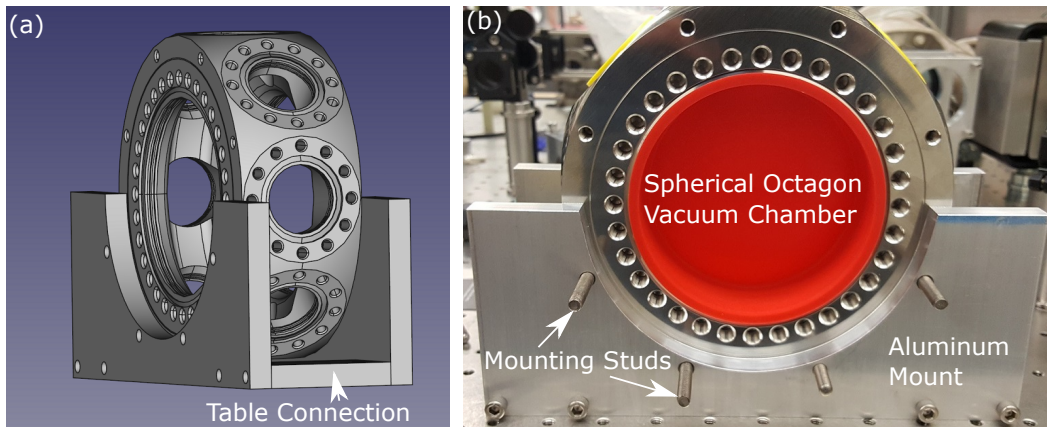


Figure 87: The main vacuum chamber and mounting structure for the balanced detector.

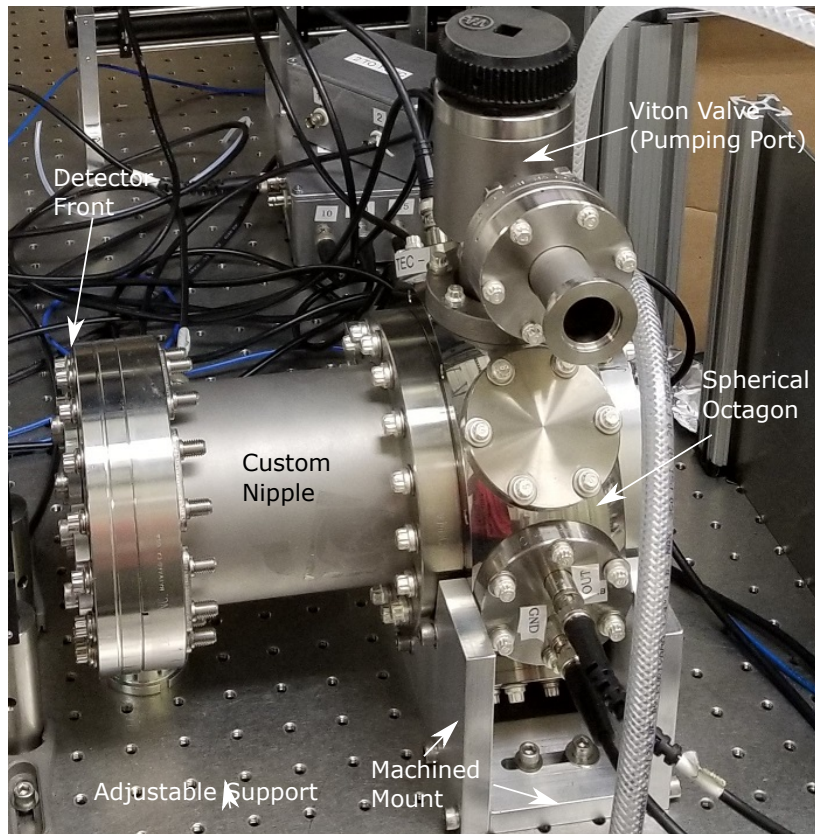


Figure 88: The fully assembled balanced and cooled photodiode detector.

B.6.5 Circuit Diagram

The schematic of the balanced detector is shown in Fig. 89.

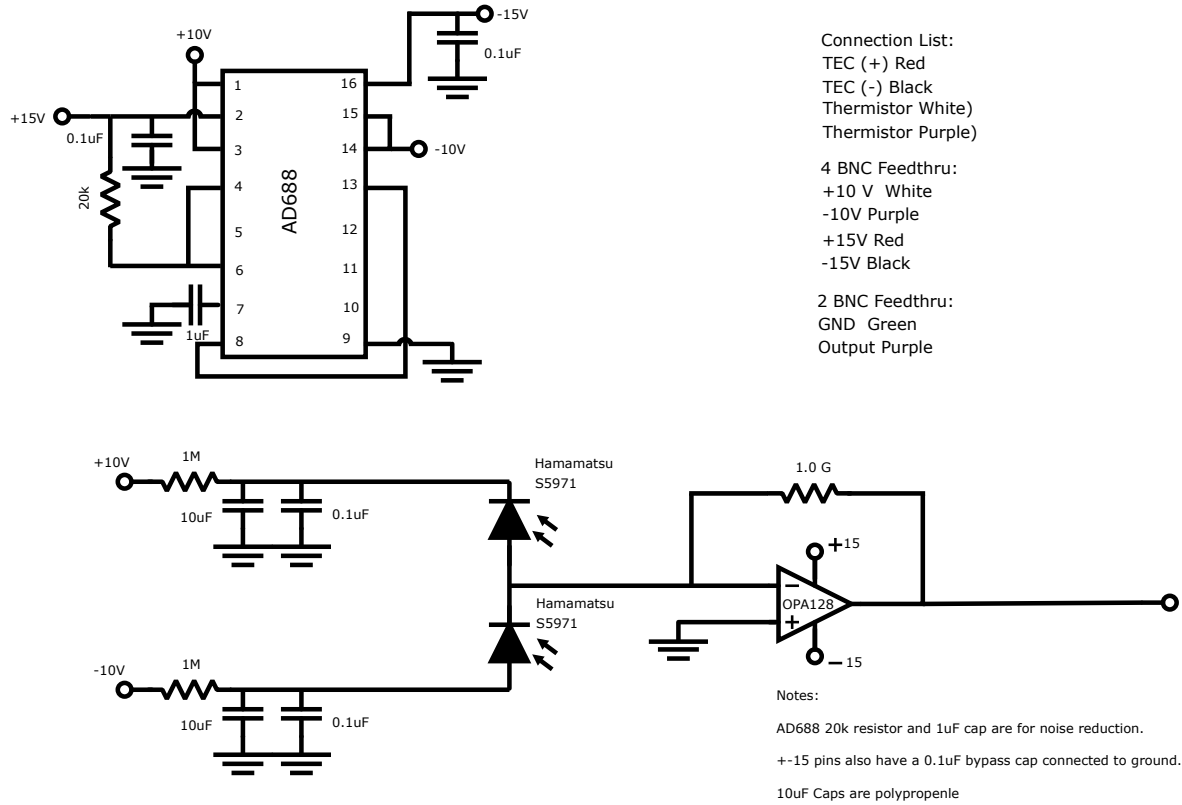


Figure 89: Schematic for a low noise, balanced detector.

B.6.6 Expected Noise Floor

As in Section 3.5.5.1, we calculate the expected noise floor of the balanced detector.

Again, the noise contributions are:

- Resistor thermal noise (Johnson-Nyquist noise).
- Photodiode dark current (not technically ‘noise’).
- Photodiode noise, provided as Noise Equivalent Power (NEP).
- Op-amp voltage noise.

- Op-amp current noise.

Many of these are specified by the manufacturer in units of $\{\text{unit}/\sqrt{\text{Hz}}\}$, which is what we will use for comparison.

Johnson-Nyquist Noise The (single-sided) power spectral density (i.e. V_n^2) of thermal noise in a resistor is given by the equation [55]:

$$PSD_{V_n}(T, R, f) = 4k_B T R$$

For $R = 1 \text{ G}\Omega$ at room temperature, this amounts to $4.1 \text{ }\mu\text{V}/\sqrt{\text{Hz}}$ (note that to convert to a two-sided density, we simply divide this by 2).

Photodiode dark current The dark current for the Hamamatsu S5971 is specified as 0.07 nA typical to 1 nA max. This corresponds to a background of $V_{\text{dark}} = 0.07 - 1 \text{ V}$. Since the final signal is a difference signal, we assume that these cancel to first order, and simply mention them for completeness.

Photodiode NEP The photodiode NEP is specified as the amount of optical power falling onto the sensor that would result in the equivalent noise signal. The NEP is determined as a combination of many factors, for instance photodiode shunt resistance thermal noise and dark current shot noise. For the S5971, this is specified as $\text{NEP} = 7.4 \times 10^{-15} \text{ W}/\sqrt{\text{Hz}}$, corresponding to a voltage noise (by multiplying by efficiency $\epsilon = 0.6 \text{ A/W}$ and R) of $4.4 \text{ }\mu\text{V}/\sqrt{\text{Hz}}$.

Op-amp voltage noise The OPA128SM voltage noise density is specified at 10 Hz as $92 \text{ nV}/\sqrt{\text{Hz}}$, which is comparatively negligible and at 100 Hz as $78 \text{ nV}/\sqrt{\text{Hz}}$. It is also specified as $4 \text{ }\mu\text{V}$ peak to peak in the range from 0.1 to 10 Hz , which corresponds to $50 \text{ nV}/\sqrt{\text{Hz}}$, which is also comparatively negligible.

Op-amp current noise The OPA128SM current noise is specified as 3 fA peak to peak in the range of 0.1 Hz to 10 Hz , which corresponds to a voltage noise density of roughly $37.5 \text{ nV}/\sqrt{\text{Hz}}$, which is comparatively negligible. It is also specific as a current noise density of $0.16 \text{ fA}/\sqrt{\text{Hz}}$ in the range of 0.1 Hz to 20 kHz , which corresponds to a voltage noise density of roughly $160 \text{ nV}/\sqrt{\text{Hz}}$.

In the case where multiple values were provided in the same frequency range, we use

only the worst case (largest) noise estimate. Given all these, we take the sum of the all of the noise contributions (in quadrature) as our overall noise power, with an additional factor of $\sqrt{2}$ due to computing the difference signal:

$$\bar{V}_n \approx 6.87 \mu\text{V}/\sqrt{\text{Hz}}$$

B.6.7 Effect of Cooling

Cooling the photodiodes should have two effects: reduced $1/f$ type noise and a reduced noise floor (cooling the photodiodes reduces the amount of dark current, and a large source of noise is shot noise of the dark current). Both of these effects are shown in Fig. 90. In Fig. 90 (a), it is evident that the $1/f$ type noise of the detector is significantly reduced when the detector is cooled compared to when the detector is at room temperature. In Fig. 90 (b), a slight decrease in the noise floor for the cooled photodiodes is evident.

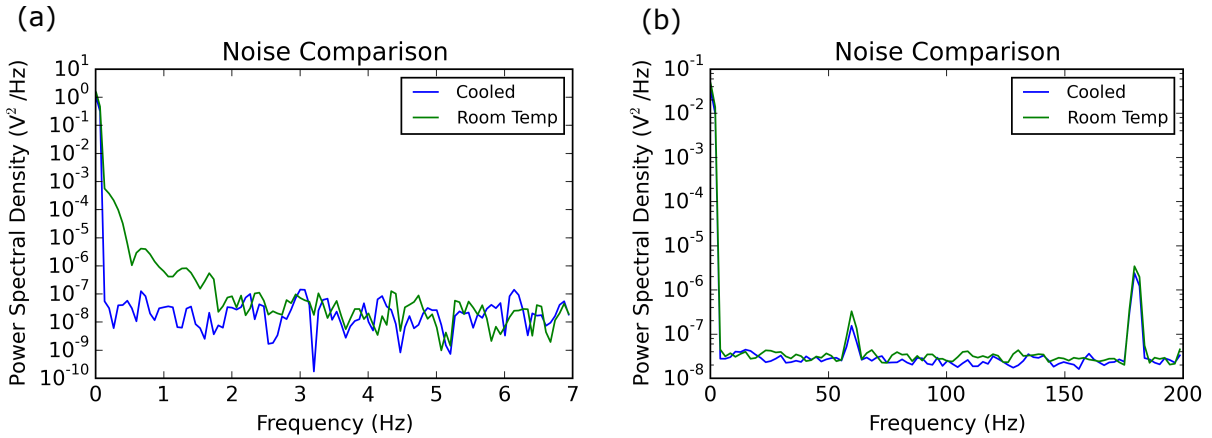


Figure 90: Comparison of noise for the balanced detector when cooled and uncooled. The same spectrum, computed with a hanning window, is utilized for both (a) and (b); the spectrum in (b) has lower frequency resolution to achieve a more evident noise floor via more averaging.

B.6.8 Cooling Notes

The detector is cooled by pumping out the entire chamber to a pressure of $P \approx 10^{-5}$ Torr. An adjustable DC power supply can be used to power the TEC. It is crucial that the cooling water to the detector is connected and running any time the TEC is on, as it generates a lot of heat that needs to be removed. The temperature of the electrical plate (Fig. 85) can be read by reading the resistance of a thermistor (NTCASCWE3) that is attached to the plate.

The conditions utilized for Fig. 90 and for Section 4.3.4 were:

- Pressure $P \approx 10^{-5}$ Torr.
- Plate temperature -10° C (Thermistor value 4.5 k Ω).
- Voltage supplied to TEC $V \approx 13.5$ V.

A table of several resistance-to-temperature conversions are included in Table 10 for a quick guide.

Resistance (Ω)	Temperature ($^\circ$ C)
1215	20
1490	15
1830	10
2270	5
2840	0
3570	-5
4530	-10
5800	-15

Table 10: Table of temperatures and resistance values for thermistor NTCASCWE3.

B.7 MODIFICATIONS FOR OVER-DAMPING

B.7.1 Dual Cooling Laser Modification

A second 660 nm laser is added to couple directly (and nearly exclusively) to the axial motion. This allows a very strong interaction with the axial motion while minimize coupling to the transverse or vertical motion.

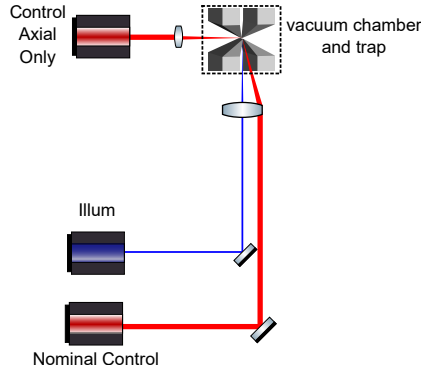


Figure 91: A second 660 nm laser for axial feedback in the over-damping experiment.

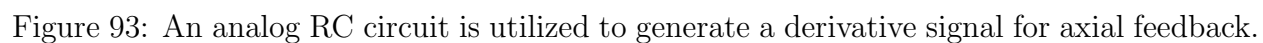
B.7.2 Feedback Circuit Modification

To incorporate the second laser for over-damped axial cooling, the feedback system was fit with another feedback path. A diagram of the system for the RC filter over-damp attempt is shown in Fig. 92. The nominal feedback path remains in place in order to gain control of the system.

Instead of a digital filter, an analog filter was utilized to generate a derivative of the input signal. For the results shown in Section 4.3.2 an analog RC filter was used, where the output of the circuit is the voltage across the resistor. This circuit is shown in Fig. 93.

For the RLC filter over-damp attempt in Section 4.3.4, a second detector was used to monitor the axial motion. The diagram showing the system for this change is shown in Fig. 94.

For the feedback in this case, analog RLC filter was used, where again the output of the circuit is the voltage across the resistor. A second output is the voltage across the capacitor, which is used only as a monitored signal. This circuit is shown in Fig. 95.



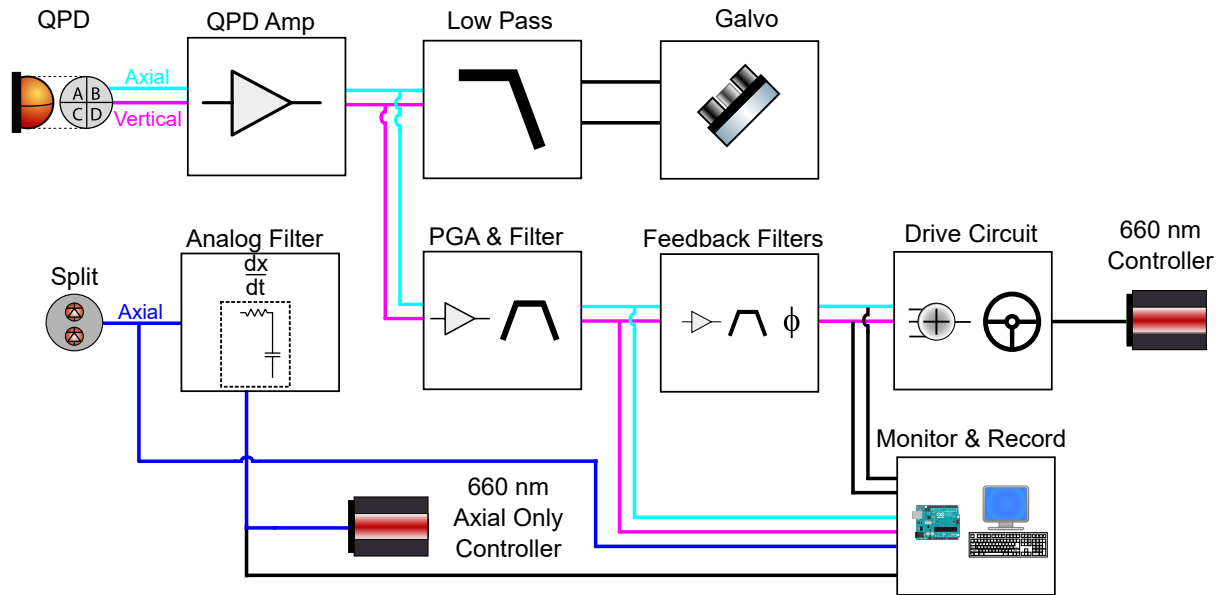


Figure 94: The feedback electronics were modified to utilize a second split detector for another copy of the axial motion (blue).

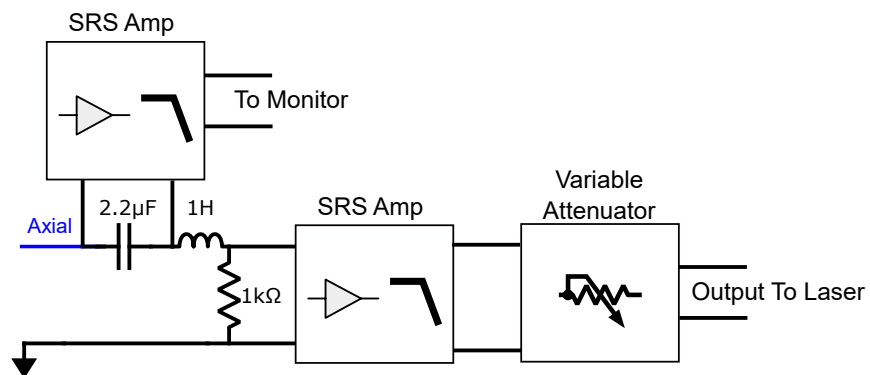


Figure 95: An analog RLC circuit is utilized to generate a derivative signal for axial feedback.

APPENDIX C

ALIGNMENT PROCEDURE

Alignment of the optical system can be done in many ways; the intent of this section is simply to relay the methods that I have used to successfully align the entire system. The simplest version of the optical system is displayed in Fig. 8, and is sufficient for discussion of alignment and resolution checking.

C.1 OPTICAL COMPONENTS LIST

Label	Part No.	Label	Part No.
Lens 1	Edmunds 67-282	Collimator 2	Thorlabs F240FC-B
Lens 2	Thorlabs LB1199-B	Mirror	Thorlabs BB1-E03
Lens 3	Newport KPC073AR.16	Mirror 1	Thorlabs BB1-E03
Lens 4	Thorlabs AC254-150-B-ML	Mirror 2	Thorlabs BB1-E02
Lens 5	Thorlabs AC254-500-B-ML	Mirror 3	Thorlabs BBE2-E03
Lens 6	Thorlabs AC254-50-B-ML	Mirror 4	Thorlabs BB1-E03
Long Pass Filter	Thorlabs FELH0800 (x2)	Beam Splitter 1	Thorlabs CM1-BP108
Lens 7	Thorlabs AC254-100-B-ML	Beam Splitter 2	Thorlabs CM1-BP108
Lens 8	Thorlabs AC254-250-B-ML	Beam Splitter 3	Thorlabs CCM1-BS014
Lens 9	Thorlabs 355230-B	Absorbitive Filters	Thorlabs (Various)
Lens 10	Thorlabs C240TME-B	Prism Pair	Thorlabs PS833-B
Lens 11	Thorlabs AC254-300-B-ML	660	Thorlabs L660P12, LDC202C 200 mA
Lens 12	Thorlabs 355230-B	830	Thorlabs HL8338MG, LDC201CU 100 mA
Lens 13	Thorlabs C240TME-B	Fiber 1	Thorlabs P5-180PM-FC-5
Collimator 1	Thorlabs PAF-X-18-PC-B	Fiber 2	Thorlabs PM630-HP
Beam Blocker	Edmunds 84-468		

Table 11: Table of optical component part numbers

C.2 LASER COUPLING

As discussed in Section 2.3.2.1, all diode lasers are first fiber couple, mainly to clean up the laser beam. Many guides are readily available online to help with choosing the correct components to achieve efficient coupling (see [61]).

Personally, I have had most success in fiber coupling when the collimated beam is well straightened, so I prefer to use two mirrors and the procedure discussed in Section C.3 first. We then typically place the coupling lens, via adapters, into a flexure mount (Thorlabs CP1XY), followed directly by the fiber mounted in a z-translation stage (Thorlabs SM1Z). All fibers are single mode fibers. Generally, the fibers are FC/APC on the end for couple, and FC/PC on the output end.

Since we do no conditioning of the shape of the beam prior to coupling (beams from laser diodes are highly asymmetric), coupling efficiency is generally limited to the range of 15-40%.

C.3 BEAM COLLIMATION AND ALIGNMENT

It is crucial for every section hereafter that the alignment starts with a well aligned, well collimated laser beam. By well aligned, I mean a beam that is parallel to the table, 4" in height, and centered in the middle of two table holes (a requirement of using the homemade cage rod mounts) for its entirety. This leaves no ambiguity in the desired location of the trap, and helps set the translation and angle of all system mirrors.

I use a well known technique to do this, which is a modified two iris method. I set two of the home-made cage rod mounts along the desired axis, ideally a few feet apart. I then use a pair of turning mirrors to adjust the beam so that it propagates through the center of a "t-shirt" detector card (see Fig. 101 for a clear image of the card).

An example of this method is shown in Fig. 96. The mirror and detector card, with 830 nm light striking it, are visible in the forefront. The second mount that acts as the second iris is visible toward the top of the photograph. The distance between the two irises is shorter

than desirable, but still acceptable for some uses (and in particular, for this demonstration).

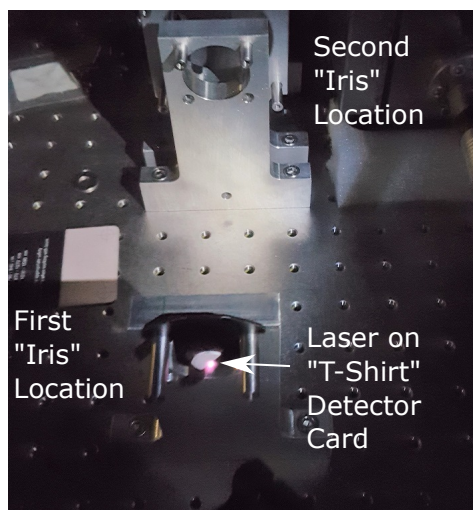


Figure 96: Example setup of the ‘two iris’ method. Instead of an iris, an 830 nm detector card and cage rod mount are used.

The two turning mirror method is preferred as it gives me the necessary degrees of freedom to adjust the beam propagation, and it assumes nothing about the type of mount the laser light originates from. In this way, I need not worry about messing up a possibly well-calibrated fiber coupling port for a temporary use.

Beam collimation is ensured to be as good as possible given experimental room requirements for checking collimation over long distances.

C.4 SETTING FOCAL LENGTHS

Theoretical focal lengths for lenses are an excellent starting point for rough positioning all of the lenses in the system. However, I never find it adequate, even with careful measurement, to rely solely on focal lengths or working distances. As such, all crucial distances (by crucial distances, I refer to focal lengths for lenses in the imaging plane) between optical elements are determined experimentally. In particular, I start with a well collimated laser 830nm laser beam, as discussed in Section [C.3](#).

To set focal lengths of imaging lenses, such as Lens 8, I carefully direct the collimated laser beam at the center of the lens and view the image of the focused light on a camera. I then move the lens along the optical axis until I achieve the smallest possible spot size on the camera. Note that a very small amount of optical power is suggested to do this ($P < 1 \mu\text{W}$), both to make the image easier to interpret (with more power, the diffraction limited spot will saturate the camera pixels and make it hard to determine the optimal focus), and to keep the camera safe from damage. This is a very simple way to recheck camera calibration, or to change the magnification of an image by swapping out the imaging lens.

For relay lens systems, such as the pair of lenses labeled Lens 7, checking the collimation of the beam on the output of the relay system, as in Section C.3, is the simplest method to fix the relative distances of the lenses. The spot size method for a camera could also be used just as efficiently, once the camera lens has been set to its correct position.

For telescoping relays, such as Lens 5 and Lens 6, more care must be taken if the beam size is being changed to a large degree. For instance, the lens pair referenced causes a 10:1 reduction in beam size. Depending on the size of the beam entering the relay, the output beam may not stay collimated for the typically long distances desired (the beam has some divergence before the relay, and shrinking it will make that divergence larger). The same camera spot size method or collimation method is used, but on much smaller distances. My method is to keep the beam visible on a detector card for as long as possible, which ensures that the convergence (or divergence) of the beam is as small as reasonably possible.

C.5 INITIAL ALIGNMENT

The alignment of the system is usually iterative. As such, my first alignment of the system starts after all lens focal lengths are set. I then start alignment by using the 660 nm laser, which is easily visible to the naked eye with small optical powers.

I begin by removing the chamber (and trap), Lens 4, and the objective from the optical path, and send a beam that is carefully straightened (both vertically and horizontally) along the illumination path. This allows me to unambiguously adjust turning mirror M3, the galvo

(while powered on and at the midpoints of its output range), and turning mirror M4, keeping the beam (close to centered) at all times. Until much later in the process, all of these mirrors remain a fixed reference point for a straight laser beam.

Next, I place the objective in its mount and adjust its tip, tilt, and height until the red laser light is reasonably centered throughout the optical system. This ensures that the objective is reasonably aimed at the correct location, as determined by the straightened laser beam. With the objective reasonably in place, this is a good time to test the resolution of the system, if it hasn't been done already.

C.6 OBJECTIVE RESOLUTION AND MAGNIFICATION

The magnification of the system is very important for calibrating distances for any of the non-imaging (split photodiode) detectors. To test the resolution and magnification of the objective, a negative 1951 USAF test target (Thorlabs R1DS1N) is placed in the optical path in front of the objective. Since the objective is corrected for a 5 mm glass chamber window, it is crucial to place a 5 mm window (Thorlabs WG41050-B) between the target and the objective. It is also imperative to use illumination at the wavelength that the objective is corrected for, which in this case is 830 nm. A laser can be used, but images are harder to analyze and focus because of diffraction and interference from the single wavelength light. Alternatively, using an 830 nm LED provides enough of a broad spectrum in illumination to avoid diffraction, but the spectrum is still centered at the corrected frequency.

Illumination can be directed at the target from behind the objective (reflection image) or behind the target (transmission image). I found it best to back-illuminate the target with the LED and a short focal length lens to limit the divergence of the output light. The most recent testing setup for this is shown in Fig. 97, in which a 60 mm focal length lens was used (Thorlabs AC254-060-B-ML).

Images obtained from doing this can be seen in Fig. 98. The resolution of the system is determined by the smallest set of distinguishable line pairs, which in this case is Element 6 of Group 7 at 228 line pairs/mm (it is hard or impossible to see in Fig. 98 (a), only because

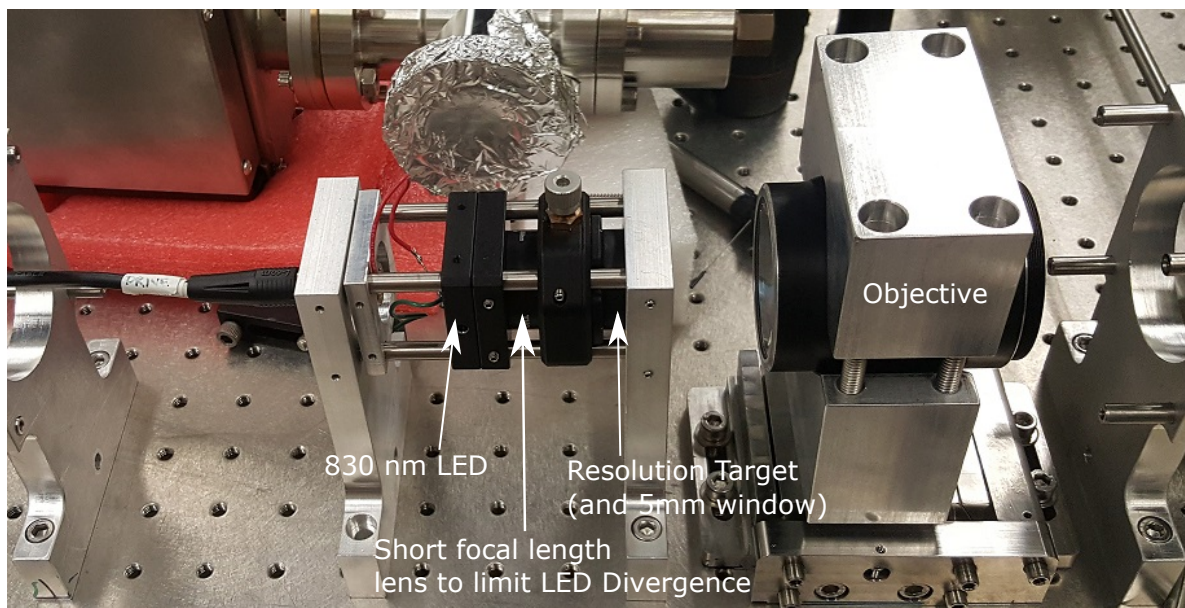


Figure 97: Setup for testing the resolution and magnification of an objective, including 830 nm LED, 60 mm lens, USAF negative target, and 5 mm window.

it is dim and the image is scaled down significantly). The magnification is determined by separately imaging Groups 4-7 of the target, converting the values of line pair per millimeter (lp/mm) that are provided with the target to pixels (which are $(14 \times 14)\mu\text{m}^2$ for camera Mikrotron MC1364), and averaging.

Front illumination (such that light is reflected off of the target) is also a reasonable method, and a simple testing setup for this is shown in Fig. 99 (a), with the key difference being that this requires a beam splitter to direct illumination light into the objective while not blocking light collected from the objective. An 8:92 uncoated beam splitter is best, as it allows most of the light collected through on its return path. A reflection image can be seen in Fig. 99 (b).

Note that the image in Fig. 99 (b) was actually acquired in a previous setup than the example shown in Fig. 99 (a).

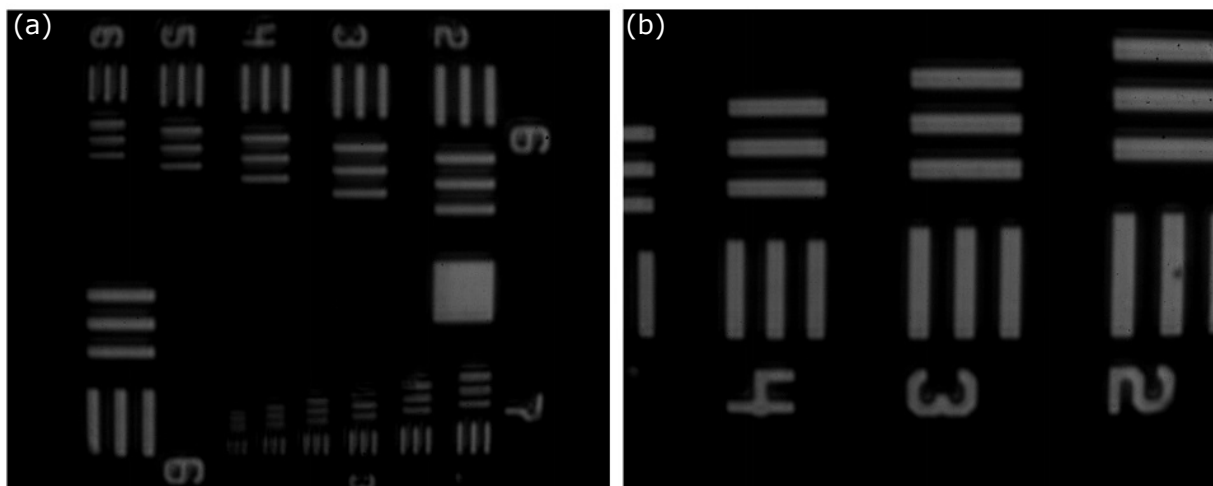


Figure 98: Transmission images of the USAF 1951 resolution target Group 7 (a) and Group 5 (b). Resolution is 228 line pairs/mm and magnification $\sim 54.4x$.

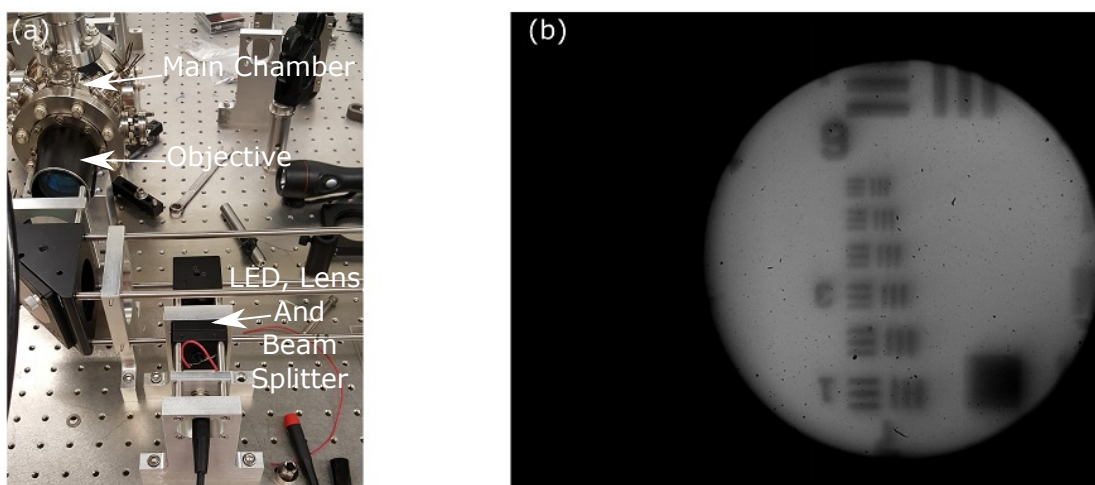


Figure 99: (a) A beam splitter can be used to illuminate the resolution target with LED light from the 'front', generating the 'reflection' image of the target shown in (b).

C.7 PLACING THE CHAMBER

Following from Section C.5 and still utilizing the red laser light, the chamber (and trap) are placed into the optical path for the sole purpose of setting the (currently rigid) location of the trap. If everything was machined and assembled correctly, the center of the trap should be very nearly 4" off of the table, so it should be relatively easy to find. Because the 660 nm laser light is collimated to a size much larger than the trap size (mm compared to $\sim 100\text{ }\mu\text{m}$), a shadow "image" of the trap can be seen on our detector card.

Since we believe the objective to already be well aligned to the optical axis, the trick is to rotate and translate the chamber simultaneously to line the center of the trap image up with the hole in the detector card (the rotation is necessary because of the possibility that an off-center translation coupled with beam deflection from rotation will also center the trap on the hole). A picture showing the trap shadow, with the detector card placed directly behind the objective, is shown in Fig. 100. Looking very closely, one can make out an image of the upright trap bottom pole pieces (long) and top pole pieces (sharp point), with the center of the trap aligned with the hole on the detector card.

We now add back the objective to fine tune its direction by using a very similar method; this time, I place the detector card at several locations, but most importantly the first image plane (between Lens 5 and Lens 6) and center the trap on the detector card hole, as seen in 101. I do this by changing the tip, tilt, theta, height, and translation of the objective ONLY, leaving all other parameters in tact. I now know that my objective is aimed directly at the center of the trap and the desired illumination location - at this point, focus is not yet a concern.

The final and most difficult step is to use the 830nm laser and add in the focusing Lens 4. I undo some of the work I did in centering my trap, as the 830nm focused spot was not immediately visible. This has always been because the beam is either too high or (in my case) too low, and as such hits the bottom pole piece. I designed the chamber mount to be machined slightly shorter than necessary, so that I could shim the trap to the proper height; however, likely owing to assembly differences in the trap itself, I still end up with the trap slightly higher than 4" (I estimate it is a few hundred μm).

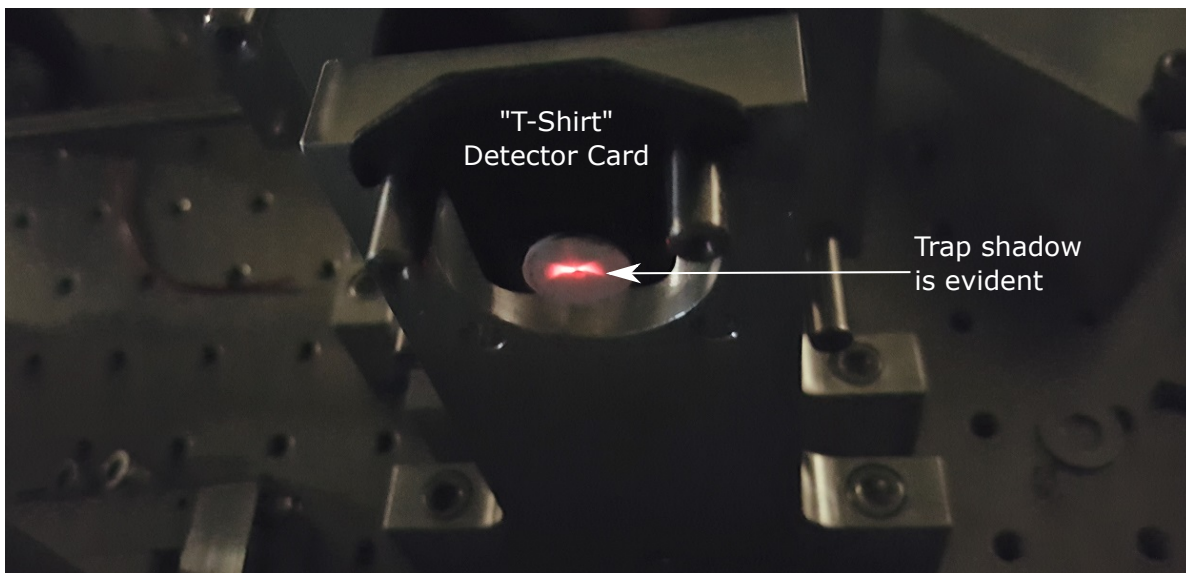


Figure 100: The shadow of the trap, as illuminated by a the collimated 660 nm laser, is visible on the detector card placed directly behind the objective.

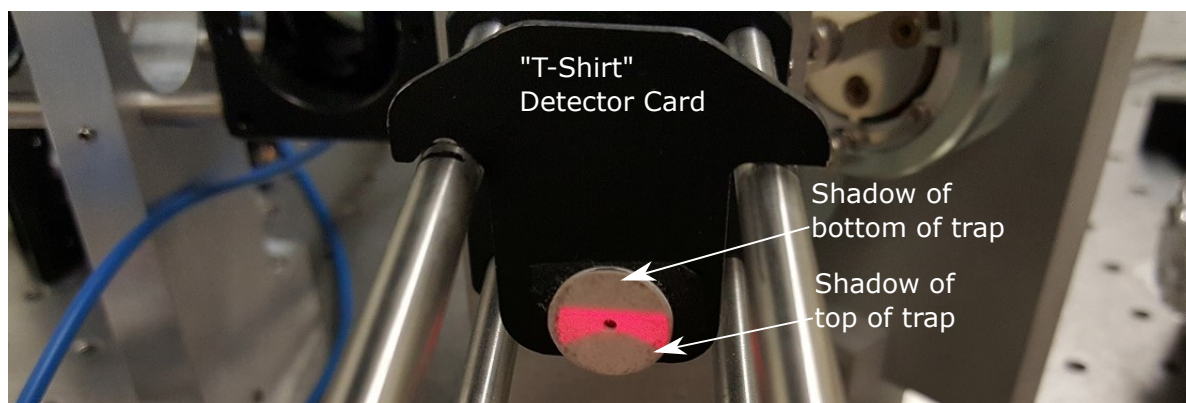


Figure 101: An image of the shadow of the trap at the first image plane, as illuminated by the 660 nm laser.

I move the chamber left and right to find the laser spot on either side of the trap to orient my direction. I then slowly change ONLY the height of the beam until I no longer lose the spot. It is now that I can carefully tilt and translate the chamber, being sure NOT

to change any other parameter.

As such, I am able to align the beam to the center of the trap touching ONLY the vertical adjustment of the laser beam and the translation and rotation of the chamber. At last I can move either the objective or the focusing lens to find the smallest spot size available, and I am done (for now).

I have done this alignment several different ways, including both 660 nm and 830 nm LED, either laser, and transmission or reflection, and have found that the described procedure is the most reliable method, as it allows no assumptions in beam height, location, or adjustment of any other aspect of the system.

C.8 QUADRANT PHOTODIODE FOCUS AND ALIGNMENT

With either (or both) lasers correctly focusing through the trap, we can align the quadrant photodiode detector (QPD) and set its focusing lens. Rough alignment is achieved trivially by utilizing either laser and, by eye, centering either laser spot onto the center of the quadrants with mirror M4 and Lens 11's XY1 stage. This works well enough to get some signal from the QPD.

It is not trivial, however, to set the focus of Lens 11, since the QPD is inherently not an imaging detector. In addition, utilizing either laser for focus or alignment would cause some ambiguity in result, given that the laser spot size is much bigger than the size of a microsphere image (for which the magnification was designed). As such, the 830nm laser is focused into the trap, but a 30 μm pinhole is placed at the first image plane after the objective, which is between Lens 5 and Lens 6. This size is chosen to give a spot size on the camera that is very close to the size of an actual microsphere (here, 6-8 pixels).

Then, the galvo is driven with a small sinusoidal signal in one (or both) directions, generating a pseudo-particle oscillation signal (just like in Section 2.7). Iteratively, the focusing lens is moved along the optical axis, the particle is re-centered on the photodiode, and then a signal is generated and recorded. The location that provides the sharpest transitions and largest signal strength fluctuations is taken to be the optimal focusing location.

An example of the output of this procedure is shown in Fig. 102. Fig. 102 (a) shows the signal obtained for several iterations of the focal length; it also stresses how important it is to find the optimal location, as the initial guess for the focus (the blue curve) can provide quite poor results. Once a rough location of the optimal position is found, it is carefully selected by moving to either side of the optimal location, as shown in Fig. 102 (b).

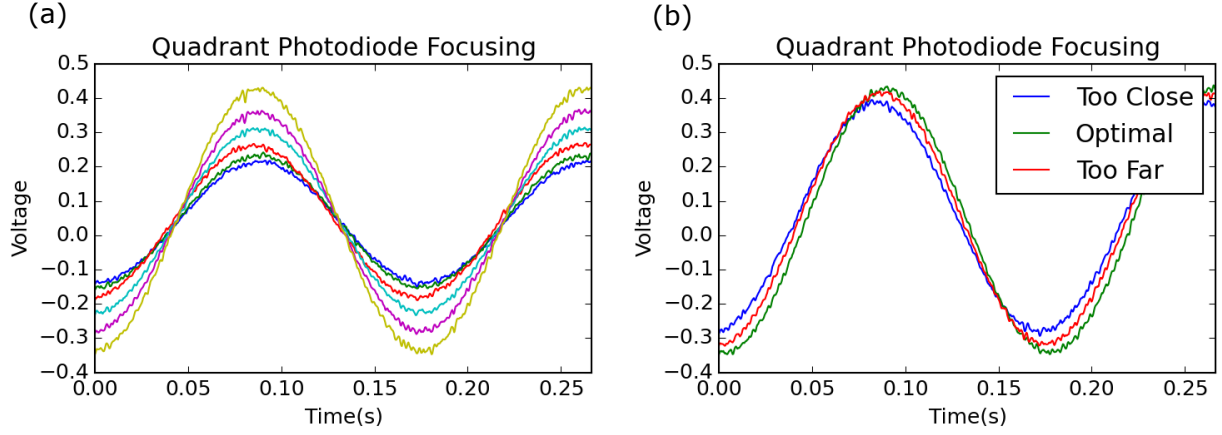


Figure 102: Plots of the signal generated by simulating movement on the quadrant photodiode detector. In (a), a rough location is found, while in (b) the optimal location is determined.

APPENDIX D

HARDWARE

This appendix contains descriptions, schematics, and procedures related to the experimental hardware.

D.1 TABLE ENCLOSURE

While vibrations of the entire table are a worry, vibrations of individual optical components are also a worry. In particular, it has been seen that air currents in the room cause fluctuations in the location of the illumination beam. This is evident as $1/f$ type noise in spectra, and even visible on the camera.

To combat this, an aluminum enclosure was designed to cover the entirety of the optical table. This should rid the system of any additional noise due to fluctuations of optical components due to air currents. The completed table enclosure can be seen in Fig. [103](#).

The enclosure was designed with 4 removable L-shaped panels, to allow a user to work on the table and place the panels in place when a measurement is being performed. All electrical connections are fed through the end panels, which have thick foam insulation across the bottom as a feed-through mechanism, and to keep all electrical connections stable. To place the panels on with a particle trapped, it is important to enable the feedback cooling mechanism.

There is no evidence at this time that the enclosure has improved the cooling ability of

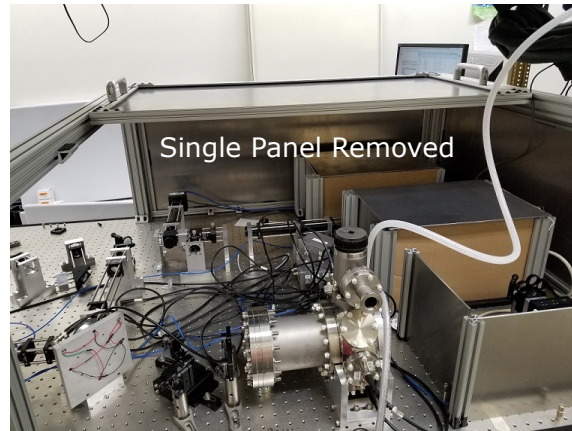
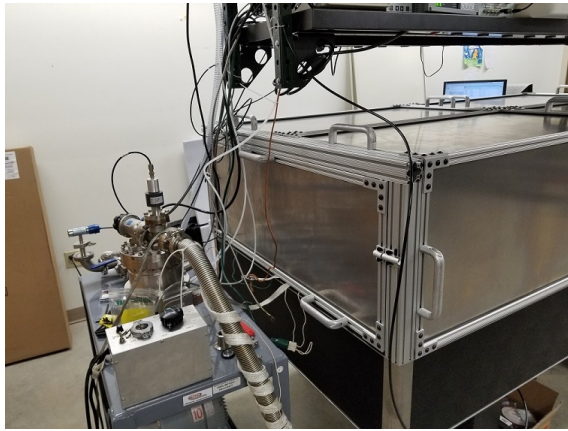


Figure 103: Images of the table top enclosure.

the system. I believe the enclosure will be important when we reach smaller amplitudes of motion. Currently, we detect ~ 1 nm amplitudes, and we need to detect ~ 1 pm to see the ground state motion in the vertical direction. We already know that air currents can cause illumination direction changes, and this enclosure will completely eliminate those effects.

D.2 POLE PIECES

The material, design, and assembly of the pole pieces is discussed in the following sections.

D.2.1 Materials

The pole pieces are machined from a highly magnetic material, Hiperco 50A (Ed Fagan, Inc). It is an alloy of 49 %Cobalt, 2 %Vanadium, and the balance iron, and was chosen as it has the largest saturation magnetization of any soft magnetic alloy. The data sheet is provided in Fig. 110.

The magnets utilized are $\text{Sm}_2\text{Co}_{17}$, grade 26M from Stanford magnets. The magnets were chosen for their strength and low corrosion characteristics for use in a UHV environment. The data for the magnets is shown in Fig. 111.

D.2.2 Design

The pole pieces for this generation of the experiment were designed to have opening angles that match the numerical aperture of the objective lens (30° half angle). The length of the flat part of the pole pieces is chosen to allow for UV light to reach the area near the particle (see Fig. 39) without being blocked by the magnets. The dimensions for the top and bottom pole pieces are displayed in Fig. 104 (a) and (b), respectively.

These drawings have two extra features to note. First, the machine shop is instructed to bring both the top and bottom poles to a sharp point (when viewed from the side), as the flat features needed are not really possible with machining alone - we then lap the pieces by hand to obtain the flat features intended (see Fig. 105). Second, the design is specified for a magnet of width 0.125" - to make sure we end up with functional pole pieces, several thousandths of an inch are removed from the **inside** faces of the pole pieces. The dimensions discussed are those listed at 0.120" in Fig. 104 (a) and (b). By intentionally making these thinner, we ensure that if anything, the pole piece tips will be too close together when assembling the trap. In this way, we can shim the pieces to the necessary gap size: if they were machined with gaps too large due to imprecision or error, there's nothing we could do

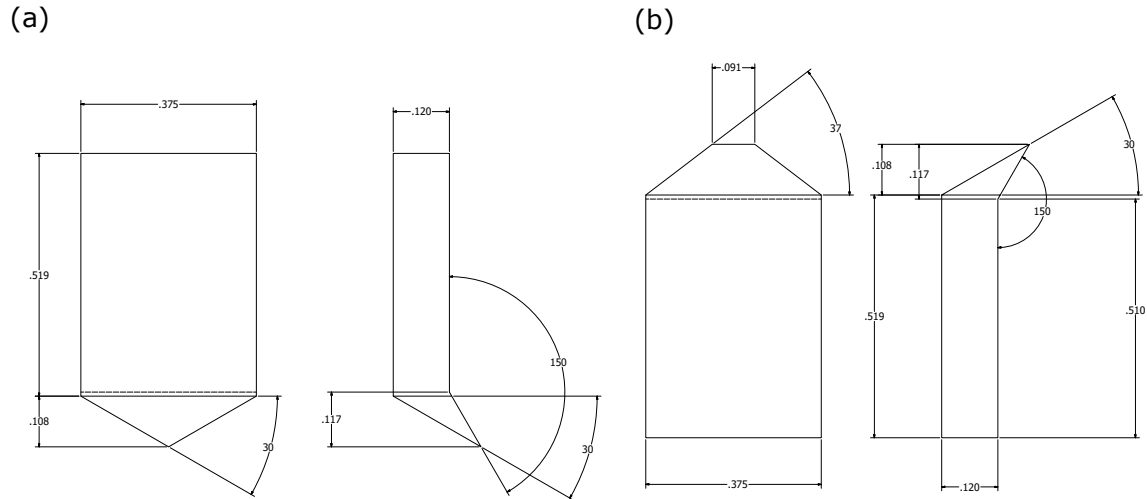


Figure 104: Dimensions of top (a) and bottom (b) pole pieces, machined from Hiperc 50A.

in the lab to fix it. It should be noted that these drawings list a contraction of .005", but in practice, only .002-.003" are required.

The nominal design for assembling the pole pieces into a trap is to align them such that lines extended from the lapped surfaces meet in the center of the trap, or in other words, if the tips weren't lapped all trap points would meet in the center. This is shown in Fig. 105, with the poles lapped to create flat surfaces. The dimensions are μm .

D.2.3 Lapping Procedure

As discussed, the pole pieces are machined such that lapping is necessary to obtain a finished product. The lapping procedure requires use of the following equipment:

- A granite, precision surface (for flatness).
- Fine (2000 grit) wet-dry sandpaper.
- The lapping-specific pole piece holder discussed in [23].
- A microscope.

We start with the pole pieces as received from the machine shop. The sandpaper and

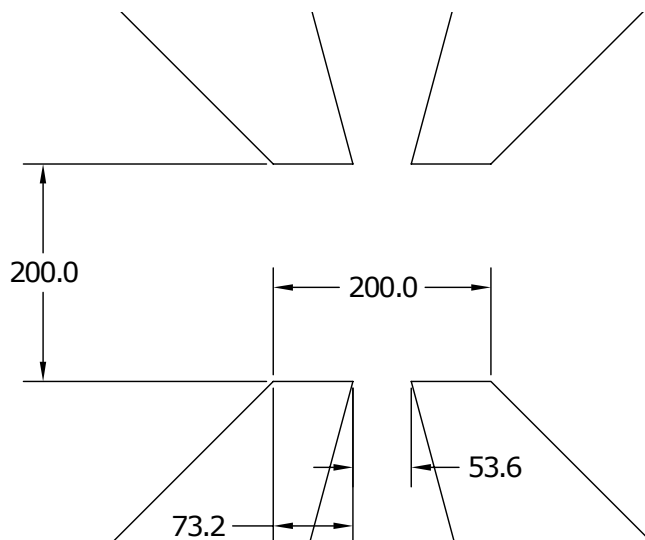


Figure 105: Nominal dimensions (in μm) for lapping of pole piece tips and trap alignment.

a small amount of water are placed on the granite block, and by hand the flat surfaces of the pole pieces are sanded. This is simply to create a smooth surface and remove excess machining irregularities.

Next, the tips of the pole pieces are “sharpened” by lapping. As mentioned above, and can be seen in Fig. 106 (a) and (d), the sharpness of the tips is really limited by the machining precision - we are clearly pushing the limits of what is possible with conventional machining tools. In order to get the nice features desired in Fig. 105, the tips must start with dimensions smaller than the final dimension. To make the tips sharp, we lap (again by hand) the flat backs and sides of the angled portions of the pole pieces. This part of the process is quite important, and extra care **must** be taken, especially when lapping the sides, so that the tips do not become irreparably rounded. The sharpened tips are shown in Fig. 106 (b) and (e).

Finally, the flat portions of the tips are created by lapping the tips vertically. This step requires the use of the lapping-specific pole piece holder mentioned in [23], which ensures the correct orientation of the lapping region. In any case, since it is quite easy to remove material from the sharp tips compared to the flat surfaces (since the pressure is much greater), all tip

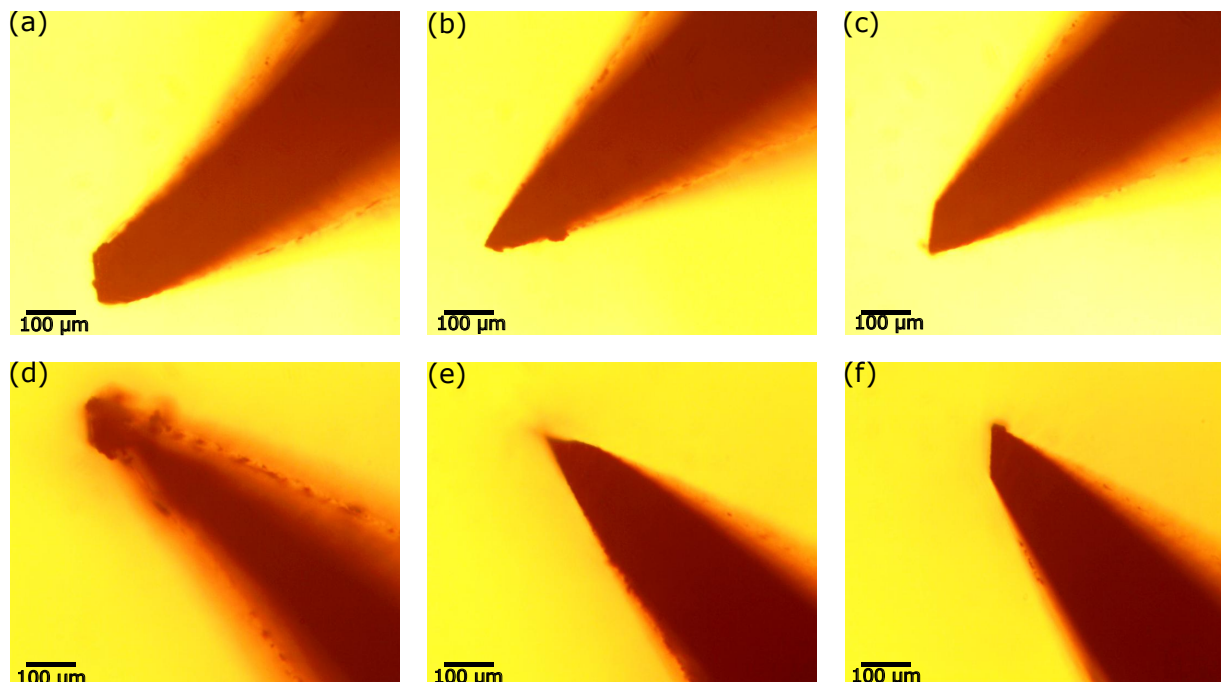


Figure 106: Example of top (a)-(c) and bottom (d)-(f) pole pieces as machined (a,d), after sanding (b,e), and after lapping (c,f). Scale bars are 100 μm

lapping should be done “in the air”. By this, we hold the (wet) lapping paper in one hand, and the lapping holder with pole piece in the other, with both surfaces vertical. The holder is then placed against the lapping paper and moved in a figure 8 pattern to remove material in a uniform way.

For the bottom pole pieces (Fig. 106 (d)-(f)), it usually takes several large, sweeping figure 8 patterns to remove sufficient material. However, for the top pole pieces (Fig. 106 (a)-(c)), it generally required less than 10 very small figure 8 patterns. As such, only one or two figure 8 patterns were usually performed at a time, to ensure we did not remove too much material. This is also why the lapping was done “in the air” instead of on the granite block - I found it much more difficult to control the pressure when placing the holder surface directly on top of the lapping paper horizontally.

An example of the finished top and bottom pole pieces are shown in Fig. 106 (c) and (f),

respectively. All scale bars are 100 μm .

The alignment and lapping of one of the most commonly used traps is shown in Fig. 107. For this trap, the top pole piece width (a) is $\sim 200\mu\text{m}$, the top (b) and bottom (c) horizontal gaps are $\sim 50 \mu\text{m}$, and the vertical gap (unfortunately, not displayed) was $\sim 250 \mu\text{m}$. The frequencies for this trap were $f_z \approx 6.7 \text{ Hz}$, $f_y \approx 96.9 \text{ Hz}$, $f_x \approx 60 \text{ Hz}$.

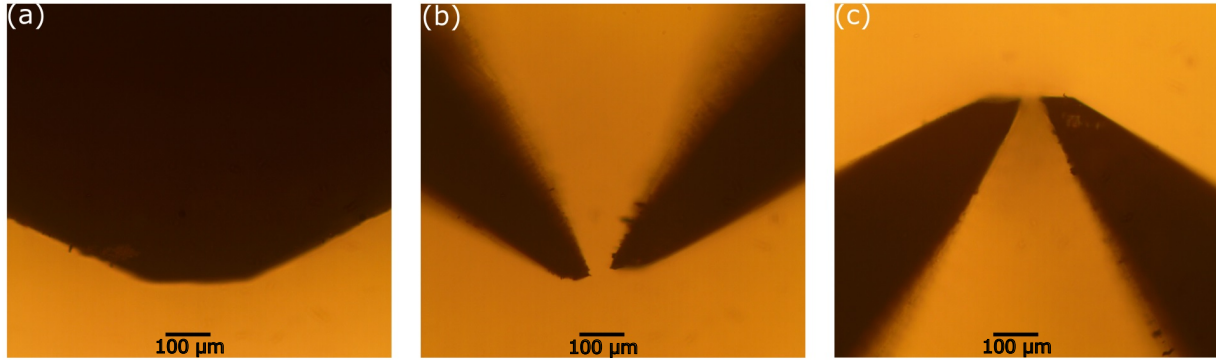


Figure 107: Commonly used trap assembly. Horizontal gaps are $\sim 50\mu\text{m}$. Vertical gap was $\sim 250\mu\text{m}$. Scale bars 100 μm .

D.2.4 Trap Assembly

While certainly dependent on personal preferences, some tips for trap assembly are now discussed. I have found that the most important aspects of trap assembly (meaning having the biggest impact on trap frequencies and trap depth) are:

- The size of the gap between the tips of the two bottom pole pieces
- The transverse alignment of the top compared to the bottom, meaning the pole points meet at a single point (like Fig. 105)
- The size of the vertical gap between the top set of pole pieces and the bottom set
- Flat, defect free surface of the bottom pole pieces (no dents!)

To assemble the trap, I first start by setting the gap size of the bottom pole pieces. This is done by placing shims between the magnet and pole piece base. The shims can be either

insulating (PEEK, Kapton) or conducting (copper), depending on the electrical properties that are desired. The gap size of the top and bottom should be identical, so the top pole piece gap is set at the same time (this is usually an iterative process). An insulating shim can be seen by looking closely at the right pole in the image of Fig. 108 (a).

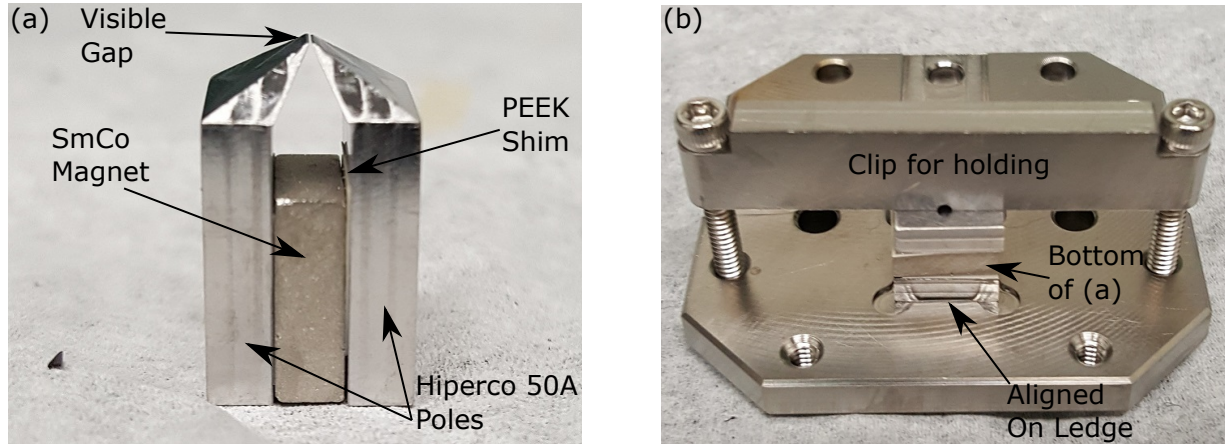


Figure 108: (a) Assembly of bottom pole pieces with shims visible. (b) The bottom poles rest against the ledge in the trap plate.

Next, the transverse alignment of the top and bottom is set. I start by securing the bottom pole pieces in their proper location, and then carefully secure the top pole pieces close to their correct location. For this step, I simply get them close enough such that the intersection point can be seen in a microscope. Since the pole pieces usually have some variance in their widths because of machining (and then shimming for the horizontal gaps), shims must be placed underneath one or both of the top and bottom poles pieces to adjust the height from the backing plate. Usually, the top pole pieces must be electrically isolated from the plate, so insulating film is used. I have found that Kapton films compress less compared to PEEK films, which caused some headache in choosing the correct film thicknesses. Again, this is usually an iterative process.

Once this is determined, the bottom pole pieces are secured into their final location, resting against the ledge on the trap plate (See Fig. 108 (b)). For this assembly, all of the bottom pieces are grounded to the plate.

Next, the top pole pieces must be inserted into their final location (with an electrically

insulating shim between the clip and top pole). This is the most difficult and most dangerous part of the procedure - **extreme caution must be taken** to ensure that the top pole pieces do not slam into the bottom pole pieces - remember, the trap is assembled in a quadrupole fashion, so the poles are naturally going to strongly attract each other. When the pole pieces do slam into one another, the tops become significantly mangled, and dents where the top points hit the bottom are evident. While this does not affect the ability to trap, it has been suspected and is highly likely to cause unwanted and uncontrolled curvature in the trapping potential, especially since particles are biased towards the bottom pole pieces due to gravity.

To avoid this, and also to carefully control the vertical gap distance, a finger is placed through the hole in the trap plate to get the top pole pieces to their rough location. With the finger preventing slamming, the top clip is tightened strongly enough to prevent the pieces from moving, but weakly enough that they can be moved by applying a strong external force. In this way, the pole pieces can be gradually pushed into the proper location.

A final side view of a trap assembly is shown in Fig. 109. The image shows visible separation and alignment of the pole pieces in all important aspects mentioned. In addition, an extra insulating shim is visible in the forefront of the top pole pieces (red Kapton). This extra piece is placed inside the trap channel to help avoid shorting of the top pole pieces to the trap plate.

Finally, the electrical connection to the top poles is made by strongly wrapping a wire underneath the insulating shim and attaching it to a nearby ceramic standoff (see Fig. 35).

D.2.5 Assembly and Trap Frequencies

The assembly of the trap, namely the dimensions of the horizontal gaps and vertical gap, is directly related to the trapping frequencies (and to a less well known extent, the trap depth). The reason the trap in Fig. 107 is displayed is that this particular trap was purposely assembled to create a large vertical and transverse frequency separation ($f_y \approx 96.9$ Hz, $f_x \approx 60.0$ Hz). This can usually be done at the expense of some trapping depth.

By viewing the side of the magnetic field quadrupole diagram Fig. 3 (a) , it can be seen that we can increase the gradient in the vertical direction (by modifying the transverse

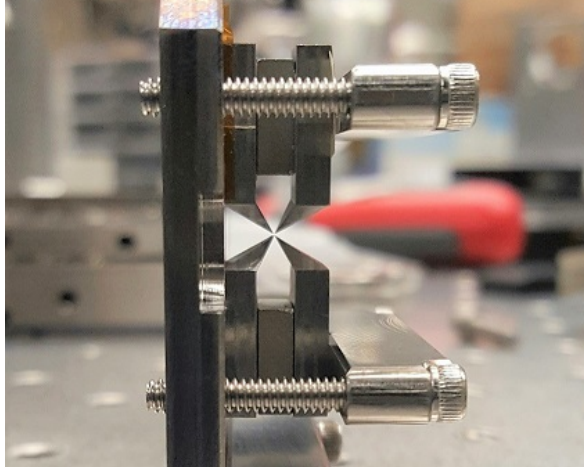



Figure 109: A side view of a finished trap assembly, with correct and visible alignment and separation.


field) by making the horizontal separation of the pole pieces smaller. At the same time, we can decrease the transverse gradient (by modifying the vertical field) by making the vertical separation of the pole pieces larger. In this way, we are creating a large asymmetry in the gradients in each direction, which is equivalent to creating asymmetry in the trapping strength (and thus frequency). However, doing so generally causes an absolute negative shift in all of the frequencies, as all of the gradients decrease sharply by with increased separation between the top and bottom pieces. This analysis is also dependent on the fact that the particle is already biased to a non-zero field region due to gravity.

D.2.6 Hiperc 50A and Magnet Data Sheets



ED FAGAN INC.

Hiperc 50¹ and Hiperc 50A¹ Soft Magnetic Alloys



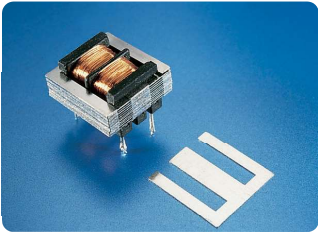
769 Susquehanna Avenue, Franklin Lakes, NJ 07417 • **phone 201.891.4003**
10537 Humboldt Street, Los Alamitos, CA 90720 • **phone 562.431.2568**

DESCRIPTION

An alloy of 49% Cobalt, and 2% Vanadium, balance Iron, Hiperc 50 and Hiperc 50A have the highest magnetic saturation of all soft-magnetic alloys and excels in applications where this attribute is needed. Hiperc 50 maintains its strength after heat treating making it your best choice for applications that experience high forces (e.g. rotating parts).

APPLICATIONS

Special Motors for the Aerospace Industry (e.g. applications where high magnetic saturation and high strength is required with as little weight as possible); Electromagnets for medical applications (e.g. to focus beams for radiation therapy in medical radiology applications); Electrical Generators; Specialty Transformers (e.g. electrical circuits and magnetic circuits where frequencies must be varied); Pole Pieces for Electromagnets; Magnetic Bearings (e.g. applications where rotating parts are levitated); High Magnetic Flux Devices and Instruments.



TYPICAL DC MAGNETIC PROPERTIES - 0.014" STRIP

	Hiperc 50	Hiperc 50A
Saturation Induction - Gauss	24,000	24,000
Maximum Permeability	12,000	15,000
Coercive Force - Oersteds	0.9	0.4
Coercive Force - A/m	72	32

TYPICAL AC MAGNETIC PROPERTIES - 0.014" STRIP

	Hiperc 50	Hiperc 50A
Core Loss W/lb @ 400Hz & 20k G	34	30
B-40 Permeability @ 60Hz	N/A	N/A

N/A = not a typical application value

PHYSICAL PROPERTIES (Hiperc 50 & 50A)

Density	lb/cu in	0.293
Specific Gravity		8.12
Curie Temp	°F	1720
	°C	938
Melting Point	°F	2600
	°C	1427
Electrical Resistivity	micro-ohm-cm	41
	ohm-cir mil/ft	240
Thermal Conductivity	W/cm °C	0.29
	BTU-in/sq. ft-hr-°F	200
Specific Heat	Cal/g-°C	0.10
	BTU/lb-°F	0.10
Thermal Expansion	ppm/°F(75°F to 932°F)	5.6
	ppm/°C(25°C to 500°C)	10.2

CHEMISTRY - maximum % unless noted

	Hiperc 50	Hiperc 50A		Hiperc 50	Hiperc 50A
Iron	Bal	Bal	Silicon	0.15	0.15
Nickel*	0.25	0.25	Vanadium	1.9 nom.	1.9 nom.
Cobalt	49 nom.	49 nom.	Niobium	0.05	na
Chromium	0.15	0.15	Phosphorus	0.015	0.015
Carbon	0.025	0.025	Sulfur	0.010	0.010
Manganese	0.15	0.15			

*Nominal

MECHANICAL PROPERTIES ANNEALED CONDITION

		Hiperc 50	Hiperc 50A
Tensile Strength	ksi	118	104
	MPa	814	717
Yield Strength	ksi	63	53
	MPa	435	365
Elongation	% in 2 in.	9	7
Typical Hardness Anld.	Rockwell Rc	20	20
Modulus of Elasticity	Mpsi	30	30
	kMPa	207	207


FORMS AVAILABLE

Hiperc 50 Strip/Coil	0.004" - 0.020"
Hiperc 50 Plate	0.50" - 5.0"
Hiperc 50A Rod	0.50" - 3.0"

Hiperc 50 & 50A supplied unannealed. If you do not see the size or form you require listed above, please call us. We add new stock material frequently, and may have the size and form you need.

SPECIFICATIONS

ASTM A801 Alloy Type 1




Material Locator

Ed Fagan Inc also specializes in locating exotic materials. So, if you can't locate that hard-to-find material you need... Put EF's material locator service to work for you!

www.Material-Locator.com


1. Hiperc 50 and Hiperc 50A Trademark Carpenter Technology Corp., Reading PA

THE MATERIALS YOU NEED, WHEN YOU NEED THEM



Quality System Certification
DNV-GL
ISO 9001

toll free 800.348.6268
www.edfagan.com
sales@edfagan.com
international sales
+44 (0) 1548 858 770

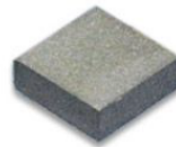


efi
ED FAGAN INC.

1/2017

Figure 110: Hiperc 50A data sheet (provided by Ed Fagan, Inc)

SBM0018 SmCo Block Magnet



[Inquiry](#)

Product ID:	SBM0018
Material:	Sm2Co17
Shape:	Block
Dimension:	3/8" x 3/8" x 1/8" Thickness
Weight(Lbs):	0.02
Grade:	26M
Coating:	No Coating
Magnetization direction:	Through Thickness
Magnetic Face:	3/8" x 3/8"
Max Operating Temp(*C/*F):	300/572

The SBM0018 SmCo Block Magnet is made from high performance grade 26M SmCo, without other protective coating as SmCo magnets have high corrosion resistance. The dimension of this item is 3/8" x 3/8" x 1/8" Thickness, magnetized Through Thickness. The weight of this magnet is 0.02 lbs.

SBM0018 SmCo Block Magnet Safety Tips

Please keep these SmCo magnets away from kids and teenagers, as these magnets may cause severe injury(even death) if been swallowed. Please check our safety guideline before handle these magnets.

Related Applications

No Application!

Figure 111: SmCo data provided at <http://www.stanford-magnets.com/sbm0018-smco-block-magnet.html>

APPENDIX E

SUPPORT SOFTWARE

E.1 PEEK DIAMOND TURNING PROGRAM

```
(This program is for machining the PEEK gasket for homemade glass window UHV sealing.)
(With a radius tool, machine out a peak ring of 20deg)
(Gasket physical parameters:)(Gasket peak position from center 22.5mm)(Gasket thickness 5.0mm)
(Gasket slope angle 20deg)(Gasket approximate depth beneath the slope 2.5mm)
(Tool physical parameters:)(Radius of tool 1.5mm)(Width of tool approximately 4mm)
G01 G18 G40 G90 G71 G94 G97
(Variables)
#100 = 22.5    (X peak position)
#101 = 5.0     (gasket width)
#102 = 20.0    (gasket angle in degrees)
#106 = 4.0     (tool width)
#109 = 2000    (Spindle Speed in RPM)
(internal calculations)
#110 = #100 + #101/2.0 + #106/2.0  (X start position)
#111 = #100 - #101/2.0 - #106/2.0  (X final position)
#112 = #101 + #106                  (X move range)
#116 = ABS[TAN[#102]]
(end internal calculations)
M3S[#150]                (spindle cw)
X30.00 Z20.0 F500        (park position)
G01 X[#110] Z2.00 F200    (move close to start position)
G01 X[#110] Z0.00 F10     (move to start position)
M00                      (pause for surface find)
M26      (spray mist #1)
M27      (spray mist #2)
G01 X[#100] Z[#112*#116/2.0] F0.2 (cutting 1st slope)
G01 X[#111] Z[#112*#116] F10      (move over faster after cutting)
G01 X[#110] F10                  (move over)
G01 X[#100] Z[#112*#116/2.0] F10  (move over faster before cutting 2nd slope)
G01 X[#111] Z0.00 F0.2           (cutting 2nd slope)
G01 Z10.0 F20 (pull clear)
X30.00 Z20.0 F500              (park position)
M29      (spray mist off)
M05      (spindle off)
M30
```

APPENDIX F

PROCEDURES

F.1 LOADING

F.1.1 Loading Setup

F.1.1.1 Horn Setup

1. Connect red wire to red wire on terminal block.
2. Connect black wire to white wire on terminal block.
3. Connect a third wire to the third spot on the terminal block, which currently has a yellow wire that is attached to the horn handle body.
 - The horn is currently grounded to the horn handle by use of a regular (non nylon tipped) set screw.
4. Place around 25-30V onto the HV+ and HV- labeled pins on the horn circuit. It will need about 1.5A for a short amount of time to work correctly.

F.1.1.2 Particle Preparation

1. Line a small plastic container (like the hexagonal ones) with aluminum foil. The aluminum foil is intended to minimize static charge buildup when using a plastic container.
2. Pour a very small amount of material into the container.
 - I usually use a small amount, and remake the container when it runs out.
 - My thought was to prevent the particles from sitting out and accumulating too much dust or moisture.

F.1.1.3 Chamber and Vacuum Preparation

1. It is imperative that all pole pieces are held at the same voltage. Any floating voltage on any pole pieces makes loading incredibly difficult and inconsistent.

- My trap has always been configured with the bottom poles grounded to the plate, and the top two floating (until I short them to the bottoms using an external connection on the feedthru).
2. Have a function generator nearby for checking particle charge.
 3. Make sure that any attached vacuum lines, up to the diaphragm valve, are equilibrated with the room pressure.
 - To do so, I open the vent port on the turbo once I remove the loading nipple (and make sure all valves in between the two are open)
 4. Before loading, it is best to close off as much as the vacuum system as possible, using the valves provided.
 - Even the small conductance from the loading port over to the turbo vent has caused me trouble on occasion.
 - Even wobbly bellows that create pressure fluctuations can blow out the particles.
 5. Make sure the ball valve is pumped out (to rough pumping values) before closing it off.
 - A pocket of air can get trapped inside, which can then cause issues when opening it up later.
 6. Remember that the turbo from the AJA leaves itself VENTED when powered off, so you must manually plug the vent valve.

F.1.1.4 Optics Preparation

1. Move the beam blocker out of the way (I turn the vertical knob that it is currently mounted on).
2. Since the focused illumination beam is short and fat when focused correctly, I move the illumination focusing lens TOWARD the chamber to defocus the beam and illuminate almost the entire Field of View of the objective.
 - When doing this, you will have to adjust the turning mirror directly preceding the focusing lens to illuminate the correct spot. While in theory the beam and particle should be perfectly aligned at 4" from the table and in between two mounting holes, the lack of any DOF for the chamber/particle makes that very difficult.

F.1.2 Loading Procedure

1. Get a large Field of View of the trap region showing on the camera.
2. Make sure the system has equilibrated with room pressure.
3. Make sure at least some part (I prefer at least closing at the Viton valve on the turbo) is closed off.
4. Make sure both the ball valve and the diaphragm valve on the back of the turbo are closed off.
5. Place 0V on the top pole pieces by connecting the function generator output to the top pole pieces feed-through.
 - (Make sure the function generator is ON and set to 0V amplitude, 0V offset).
6. Load particles onto the horn by (mostly) gently pressing down on them in the aluminum lined container.
 - For the 1.54 μm and smaller particles, I like to hear a nice crunch when I push down.
 - You need a very tiny amount of particles. You do not need to cover the entire horn surface.
7. Carefully insert the horn into the loading nipple.

- There is a guide on the trap plate to help you place the tip in the correct location.
 - For dry loading, the tip has to be quite close to the trap, as shown in Fig. 112
 - You should practice this without particles - remove the objective and look into the chamber while you are doing it (be careful of the lasers, of course!).
8. Press the LONG PULSE button on the Arduino (For dry loading, I always use LONG PULSE).
 - For practically every load attempt, you should see SOMETHING on the camera. One press won't always load something, but you should at least see shadows of particles as they drift around or zoom through the trapping region.
 - If you try several times and see nothing, there is probably something wrong!
 9. If there are MANY clumps, blow them out with the rocket blower. It is not worth trying to separate them.
 10. If there are small clumps or several single particles, try knocking out all but one by applying an AC voltage to the top pole pieces.
 - Since each charge-to-mass ratio will be different, many times you can knock excess particles out by driving them out with an electric field.
 - Use the synthesizer with a 1Hz oscillation. Start with small voltages (0.05V) and work your way up until you drive some particles out.
 - Slower oscillations are even more likely to knock out the particles (0.75Hz or 0.5Hz) as they near the bottom pole pieces.
 - In Brad's favorite trap, a voltage up to 10V (which was really 20V, since the function generator expects a 50Ohm load) would be plenty to knock anything out.
 - In tighter traps, higher voltages could be and were needed, so you can use a High Voltage op-amp circuit to drive the particles.
 11. This process generally loads a NEGATIVELY charged particle.
 12. To load a POSITIVE particle, place an experimentally determined NEGATIVE voltage offset on the top pole pieces and repeat the same AC voltage procedure.
 - For Brad, this voltage was usually 1V or less, but there is no right answer.
 - This draws POSITIVE particles upwards in the trap, and pushes negative particles lower.
 - Since the particles are already biased towards the bottom pieces due to gravity, fewer negatively charged particles will be trapped this way.
 - If a day is particularly clumpy, this is a good thing to try, as oppositely-charged particle will have a hard time overcoming this external force in order to stick to each other.
 13. Once you have one particle, nicely align the objective to get a nice image of the particle, and watch it to see if it's a single particle or not.
 - I could usually tell by watching a particle's behavior if it was one or more, but you will need to get a feel of a single particle behavior to do this.
 - Carefully watching the diffraction rings around the particle is also a good check.
 - Spherical, single particles will have very nice, concentric rings when the objective is nicely aligned. As the particle moves, the rings get larger or smaller, but don't change shape.
 - The rings for a multiple-particle or mis-shapen particle will have strange behavior and change shape as the particle orientation changes.
 - With very good focusing, a clear double or triple particle can be seen sometimes.
 14. Once you have a single particle, roughly neutralize using the radiation source at atmospheric pressure.
 - Use a slowly varying (1Hz) AC voltage to drive particle motion. Start with a small voltage (0.5-1V).
 - Increase the voltage to create a reasonably large drive of the particle's amplitude.

- Insert the radiation source into the chamber. I always get the source as close as I physically can to the particle.
 - Monitor the particle motion until no movement is visible, or until you are reasonably satisfied, and increase the voltage (up to 6V output on function generator).
 - The 6V value was used in Brad's favorite trap.
15. To get the absolute best neutralization you can at this step, carefully monitor the driven motion and remove the source at a minimum driven amplitude.
 - Recall, the rough neutralization can both add and remove charge from the particle. You must actively decide when you should remove the source - simply leaving it nearby for a set amount of time will not guarantee best results.
 16. Turn off the AC voltage and any offset.
 17. Short the pole pieces together with a wire on the external feed-through. Do this as a MAKE-BEFORE-BREAK connection.
 - Even neutral particles can be very sensitive to a large voltage transient when disconnecting leads.
 - Always make sure you have a very nice, mechanical connection on each pin. I always pull test to make sure.
 18. Close up the nipple. Viton is generally fine to use for this one, even with baking. It is the only Viton gasket on the chamber.
 - I have used copper and Viton. I don't think the nipple gets nearly as hot as the rest of the chamber, so baking hasn't been an issue yet.
 - With the top-hat mount and at atmospheric pressure, you don't really have to worry about knocking the particle out while doing this. It is very stable.
 19. Open up any valves that you had closed (turbo valve or metal valve, for instance). Do NOT open either of the roughing valves (diaphragm or ball).
 20. Turn on the roughing pump with both roughing valves closed.
 21. Very slowly open the diaphragm valve to pump out the chamber (about 10 minute pump down is generally safe).
 - I am usually even more careful and pump down over 20-30 minutes. It is overly cautious, but I have been burned too many times being impatient, and starting over is quite demoralizing! Be patient.
 - Monitor the pressure on the turbo-side convection gauge. Using the fancy new reader (the reader with a touch screen), I try to pump fast enough the the display changes by ~ 2 Torr per screen update.
 - The pressure will stop dropping as an equilibrium with the half-open valve is reached. When this happens, open the valve up some more.
 - Once you are in the single Torr range, it is generally safe to fully open the diaphragm valve.
 - Let the pressure reach tens of mTorr this way.
 22. Slowly open up the ball valve.
 - This is necessary to correctly provide the backing pressures needed by the turbo.
 - Remember, make sure there is no air pocket in the valve, or you may knock your particle out when a gust of air is let into the chamber!
 23. Rough pump to about 10 mTorr and then:
 24. Turn on the turbo. I never had any issues after reaching this point.

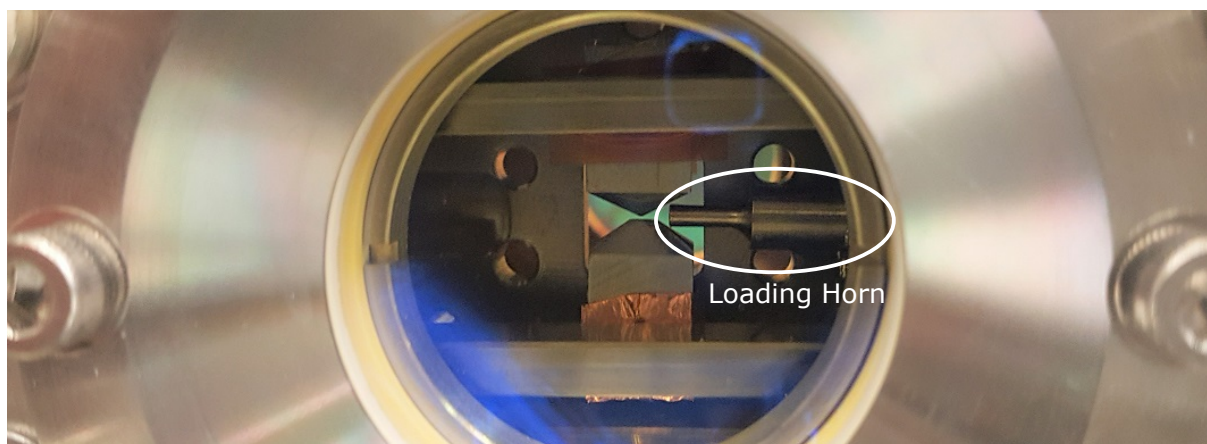


Figure 112: Example of loading horn proximity to trap.

F.1.3 Chamber Baking

To achieve Ultra-High Vacuum temperatures, the system must be baked to relatively high temperatures (at least 125°C) for at least 12 hours (note that this is actually a low temperature bake compared to what is customary in UHV systems).

F.1.3.1 Baking Setup

- The white, fibrous silica heaters work the best, as they can get very hot.
- The silicone heaters are rated to 250C, but I had trouble using them around 130C (they started smoking).
- The silicone heaters need to be very well heat sunk (to the chamber), which can be hard in many places, which may have contributed.
- Wrap as much of the chamber and all metal valves in the heater tape as possible.
- Attach a thermocouple to one of the 1.33" flange ports. I found the best to use is the top flange.
- Certainly, there have been hot spots in my setup. The top thermocouple seems to be the best measure of the temperature.
- A bottom flange usually reads much cooler than the top of the chamber, for instance.
- Attach the thermocouple and tape to a temperature controller.
- Wrap the bellows in its own heater tape. I controlled the bellows heater with a separate variac.

F.1.3.2 Chamber Baking Procedure

1. Load a particle. This procedure starts with the particle loaded and the chamber pumping with a turbo pump. The starting pressure is not important, as long as the turbo is running.
2. Turn on the bellows heater with the variac. With the heater tape I used, I went to a maximum of 80V on this variac.
 - The bellows got pretty hot. It's hard to put a temperature on it since it wasn't a nice, consistent wrap, but it was certainly over 100C in places.
 - It is quite important to also bake out the bellows. A dirty bellows can limit the effectiveness of baking the chamber.
3. Turn the temperature controller on to a high value (150C). I set the value high right away, I do not slowly heat the chamber.
4. Cover the chamber with some silica sheets, for a bit of extra thermal insulation and a quicker heat.
5. The particle will drift up and to the left as it gets hot. The amount of movement is measured as $\sim 60\mu\text{m}$. See Fig. 113.
 - As the particle moves, you must move the illumination to continue watching the particle.
 - I do not move the objective during heat-up and cool-down. The particle will return roughly to its starting location after cooling down.
6. Once you reach temperature, set the controller to said temperature.
 - For instance, I set to 150C first, wait until I reach 130C, then set the temp to 130C. This is faster than letting it slowly reach 130C.
 - I always make sure I reach temperature before leaving for the night.
7. Bake for at least 12 hours at somewhere between 120C-130C.
8. Turn down the variac somewhat ($\sim 60\text{V}$).
9. Set the chamber temperature to 87C.
10. Wait for about one hour at this temperature.
 - This step is to protect the all metal valves. It is probably slightly over-cautious, as the manual suggests doing this if you are actuating above 100C.
11. Turn off the bellows variac.
12. Open up the Ion Pump all metal valve (carefully).
13. Close off the turbo pump Viton valve, and check the the pressure on a pressure gauge roughly matches the ion pump reported pressure.
14. Close off the bellows all metal valve (carefully). THIS PART IS THE MOST DANGEROUS.
15. Turn off the turbo.
16. Once the bellows is cool, disconnected the bellows at the chamber side.
 - I have done this by simply opening the bellows up to atmosphere, and also by letting the turbo spin down. Either works fine.
 - You want to do this step while the chamber is still hot. The pressure is worse when hot, so there is some damping still, and you will surely kick the particle.
17. You can now turn on the fan to help cool the chamber down.
 - It will take at least a few hours for the temperature of the chamber to read room temperature.
 - Even at this point, the inside of the chamber is likely cooling down still. For good data, I wait around 4 hours at the least.

- While you can do feedback cooling if the chamber is still cooling, the particle will certainly drift. The galvo tracking can take care of this, but with the limited size and Gaussian nature of the illumination beam, the calibration of the system will be changing as the particle drifts.
18. Monitor the pressure as the chamber cools, versus the pressure table that I recorded (Bozeman data is most relevant and provided in Section F.1.6. Pressure values are quite consistent run to run, so if the pressure is crappy in one run, there is likely a problem that you need to fix!

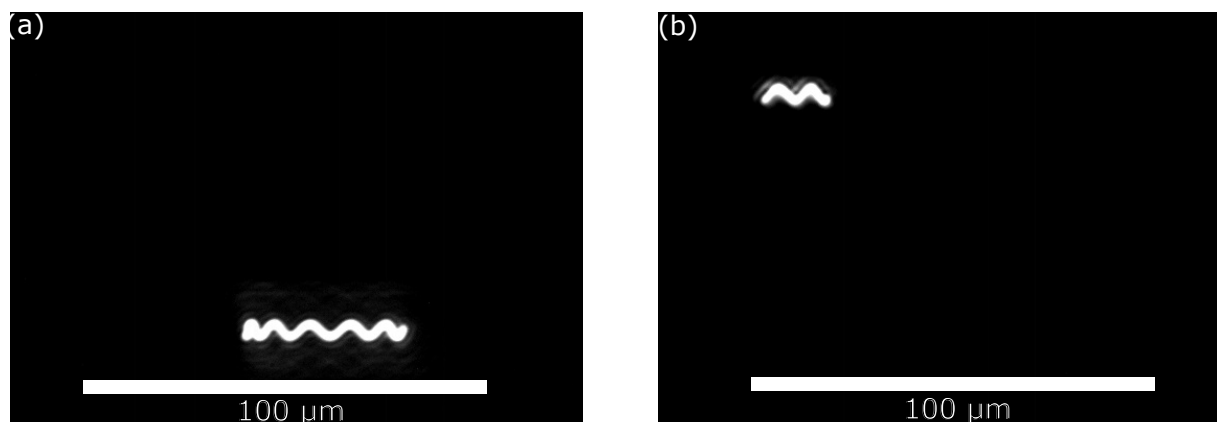


Figure 113: Example of trap expansion as the chamber is baked, showing (a) a cool chamber and (b) a chamber at 130°C. Movement is $\sim 60\mu\text{m}$ vertically, scale bars 100 μm .

F.1.4 Ion Pump Baking

- There are two indications that the Ion Pump needs to be baked out:
 1. The pressure does not read 0.0 when the Ion Pump all metal valve is closed.
 2. The pressure frequently spikes quickly from a low value to a value 10x higher.
- Turn off the ion pump and open it up to the chamber.
- Bake the bellows and the chamber to about 100C each, roughly.
- Remove the magnets from the ion pump. Wrap a third silica heater very well around the entire body of the ion pump.
- Bake it really well using a variac! Again, it's hard to get a good temperature, but I believed to be baking pretty hot (200 C). I checked this with a hand-held thermocouple reader.
- Do this for at least 4 hours. I believe the pump can survive much higher baking when off, so there should be no worry about going hotter.
- Turn off the variac. There is some wiggle room here: while it is still pretty hot, but after it has cooled some, put the magnet back on and turn on the pump.
- The pressure should be somewhat high for a little while (-6's or even in the -5's briefly), but then should stabilize.
- Now, close off the ion pump all metal valve and let it settle down. This can take a while.

F.1.5 PEEK Gasket Tightening

- With the regular PEEK gaskets, I would check the seal tightness every time I cooled down.
 - To "check", I would tighten the windows using a Torque screwdriver as the chamber cooled, leaving the Torque setting at the same value. I usually did this once when quite hot (110), and then again when cooler (80).
 - Again, doing this when very cool was hard, due to lack of damping.
- With the PEEK HT gaskets, I believe the seal was only loose once, after the very first heating cycle.
 - I checked a few more times, but never had any tightening at the same Torque setting.
- Torque setting was nominally 15 or 16 ft-in. The PEEK HT are currently at 18 ft-in, as when I recently had a leak, I had to make sure it was not them.
 - The leak was NOT due to the PEEK, so for as well as I can tell, the PEEK HT seals are quite robust and leak free.

F.1.6 Baking Tables

All baking results from Bozeman are listed in the tables below. The headers refer to the measurements of each type:

- **Temp** is the temperature reported by the thermocouple at to the TOP of the chamber.
- **Ion G** is the Ion Gauge Pressure (Torr).
- **CCG** is the Cold Cathode Gauge Pressure (Torr).
- **Turbo Open** refers to the Viton angle valve being open.
- **Bel. Open** refers to the all metal valve leading to the bellows being open.
- **Ion Open** refers to the all metal valve leading to the ion pump being open.
- **Fan** refers to the fan being used to cool the chamber faster.

Date	Time	Temp	Ion G	Ion Pump	Turbo Open	Bel. Open	Ion Open	Fan
10/10/2017	02:00 PM	20C	4.5E-8		Y	Y	N	N
10/10/2017	04:25 PM	125C	5.0E-7		Y	Y	N	N
10/10/2017	05:45 PM	130C	4.0E-7		Y	Y	N	N
10/11/2017	09:27 AM	130C	2.2E-7		Y	Y	N	N
10/11/2017	11:40 AM	90C	4.5E-8		Y	Y	N	N
10/11/2017	11:41 AM	90C	5.5E-8	6.4E-8	Y	Y	Y	N
10/11/2017	11:42 AM	90C	1.9E-7	1.5E-7	N	Y	Y	N
10/11/2017	12:00 PM	80C		5.0E-8	N	N	Y	N
10/11/2017	01:30 PM	43C		5.0E-9	N	N	Y	N
10/11/2017	03:25 PM	26C		1.0E-9	N	N	Y	N
10/11/2017	05:11 PM	20C		0.4E-9	N	N	Y	N
10/18/2017	??:?? PM	135C (24Hr)	6.0E-7		Y	Y	N	N
10/18/2017	??:?? PM	85C	6.0E-8		N	N	Y	N
10/18/2017	06:07 PM	64C	2.5E-8		N	N	Y	N
10/18/2017	06:55 PM	47.4C	7.7E-9		N	N	Y	N
10/19/2017	06:00 AM	20C	0.2E-9		N	N	Y	N

Table 12: Pressure Table from October 2017 - Bozeman

Date	Time	Temp	CCG	Ion Pump	Turbo Open	Bel. Open	Ion Open	Fan
11/11/2017	10:30 PM	20C		0.0E-9	Y	Y	N	N
11/12/2017	11:50 AM	120C	6.0E-8	0.5E-9	Y	Y	N	N
11/12/2017	12:11 PM	94C	1.7E-8	0.2E-9	Y	Y	N	N
11/12/2017	12:41 PM	85C	1.1E-8	0.2E-9	Y	Y	N	N
11/12/2017	12:42 PM	85C	4.7E-8	1.1E-7	N	Y	Y	N
11/12/2017	12:54 PM	85C		6.4E-8	N	N	Y	N
11/12/2017	01:20 PM	63.5C		3.3E-8	N	N	Y	N
11/12/2017	01:41 PM	55C		2.0E-8	N	N	Y	N
11/12/2017	02:02 PM	48C		1.2E-8	N	N	Y	Y
11/12/2017	02:18 PM	37C		5.0E-9	N	N	Y	Y
11/12/2017	04:34 PM	20.7C		0.7E-9	N	N	Y	Y
11/16/2017	05:49 PM	85C	1.0E-6	0.0E-9	Y	Y	N	N
11/16/2017	06:15 PM	115C	1.0E-6	0.0E-9	Y	Y	N	N
11/17/2017	09:00 AM	115C	5.6E-8	0.5E-9	Y	Y	N	N
11/17/2017	09:45 AM	086C	1.3E-8	0.1E-9	Y	Y	N	N
11/17/2017	10:41 AM	086C	8.0E-9	5.0E-8	Y	Y	Y	N
11/17/2017	10:41 AM	086C	5.0E-8	1.0E-7	N	Y	Y	N
11/17/2017	10:49 AM	086C		7.0E-8	N	N	Y	N
11/17/2017	10:55 AM	080C		5.7E-8	N	N	Y	Y
11/17/2017	11:10 AM	065C		3.0E-8	N	N	Y	Y
11/17/2017	11:30 AM	039C		5.9E-9	N	N	Y	Y
11/17/2017	12:13 PM	025C		1.5E-9	N	N	Y	Y
11/17/2017	01:30 PM	022C		0.7E-9	N	N	Y	Y
11/17/2017	06:30 PM	020C		0.6E-9	N	N	Y	Y
11/18/2017	06:58 PM	111C	8.4E-7	0.0E-9	Y	Y	N	N
11/19/2017	11:35 AM	111C	5.0E-8	0.2E-9	Y	Y	N	N
11/19/2017	11:54 AM	087C	2.3E-8	0.1E-9	Y	Y	N	N
11/19/2017	12:37 PM	085C	1.8E-8	0.1E-9	Y	Y	N	N
11/19/2017	12:38 PM	085C	1.0E-8	6.2E-8	Y	Y	Y	N
11/19/2017	12:38 PM	085C	5.0E-8	1.0E-7	N	Y	Y	N
11/19/2017	12:44 PM	085C		6.8E-8	N	N	Y	Y
11/19/2017	01:01 PM	059C		1.8E-8	N	N	Y	Y
11/19/2017	07:27 PM	021C		0.6E-9	N	N	Y	Y
11/19/2017	10:21 PM	110C	5.4E-7	0.0E-9	Y	Y	N	N
I did not finish		this bake	my	baby	sphere	jumped	out	
11/20/2017	09:36 PM	120C	1.3E-6	0.2E-9	Y	Y	N	N
11/21/2017	09:17 AM	120C	5.5E-8	0.4E-9	Y	Y	N	N
11/21/2017	10:48 AM	085C	2.0E-8	0.2E-9	Y	Y	N	N
11/21/2017	10:48 AM	085C	1.3E-8	1.8E-7	Y	Y	Y	N
11/21/2017	10:48 AM	085C	6.0E-8	2.4E-7	N	Y	Y	N
11/21/2017	10:48 AM	085C		2.0E-7	N	N	Y	N
11/21/2017	11:20 AM	060C		2.0E-7	N	N	Y	N
11/21/2017	12:37 PM	120C	2.0E-7	1.5E-9	Y	Y	N	N
11/21/2017	08:01 PM	120C	5.0E-8	0.3E-9	Y	Y	N	N
11/21/2017	09:16 PM	085C	1.8E-8	0.0E-9	Y	Y	N	N
11/21/2017	09:16 PM	085C	1.1E-8	1.4E-7	Y	Y	Y	N
11/21/2017	09:16 PM	085C		1.6E-7	N	N	Y	N
11/21/2017	10:20 PM	120C	4.7E-8	0.8E-9	Y	Y	N	N
11/22/2017	10:20 AM	120C	5.3E-8	0.5E-9	Y	Y	N	N
11/22/2017	11:20 AM	085C		0.0E-9	Y	Y	N	N
11/22/2017	11:20 AM	085C	8.5E-9	1.4E-7	Y	Y	N	N
11/22/2017	11:20 AM	085C		1.8E-7	N	N	Y	N
11/22/2017	05:17 PM	130C	5.3E-7	0.2E-9	Y	Y	N	N
11/23/2017	10:40 AM	130C	4.2E-8	0.2E-9	Y	Y	N	N
11/23/2017	11:40 AM	085C	8.0E-9	0.0E-9	Y	Y	N	N
11/23/2017	11:40 AM	085C	ERROR	3.5E-8	Y	Y	Y	N
11/23/2017	11:40 AM	085C	3.0E-8	7.3E-8	N	Y	Y	N
11/23/2017	11:40 AM	085C		5.0E-8	N	N	Y	N
11/23/2017	11:59 AM	066C		1.7E-8	N	N	Y	Y
11/23/2017	12:07 PM	056C		9.3E-9	N	N	Y	Y
11/24/2017	10:46 AM	020C		0.4E-9	N	N	Y	Y
11/26/2017	06:30 PM	130C	1.0E-6	0.4E-9	Y	Y	N	N
11/27/2017	09:17 AM	130C	5.3E-8	0.5E-9	Y	Y	N	N
11/27/2017	10:58 AM	085C	1.1E-8	0.1E-9	Y	Y	N	N
11/27/2017	10:58 AM	085C	Error	5.0E-8	Y	Y	Y	N
11/27/2017	10:58 AM	085C	4.5E-8	9.3E-8	N	Y	Y	Y
11/27/2017	10:58 AM	085C		5.5E-8	N	N	Y	Y
11/27/2017	04:46 PM	021C		0.5E-9	N	N	Y	Y
11/28/2017	06:48 PM	130C	1.3E-6	0.3E-9	Y	Y	N	N
11/29/2017	10:10 AM	130C	4.8E-8	0.4E-9	Y	Y	N	N
11/29/2017	11:49 AM	085C		0.1E-9	Y	Y	N	N
11/29/2017	11:49 AM	085C	7.4E-9	5.0E-8	Y	Y	Y	N
11/29/2017	11:55 AM	085C	4.0E-8	9.0E-8	N	Y	Y	N
11/29/2017	12:28 PM	043C		5.0E-9	N	N	Y	Y
11/29/2017	??:?? PM	021C		0.6E-9	N	N	Y	Y
Ion pump fl		uctuating	up to	1.2E-9.				
I decided to		bake ou	t the	pump	bake whol	em	to 200C	

Table 13: Pressure Table from November 2017 - Bozeman

Date	Time	Temp	CCG	Ion Pump	Turbo Open	Bel. Open	Ion Open	Fan
12/02/2017	08:22 PM	130C	6.0E-7	0.2E-9	Y	Y	N	N
12/03/2017	10:33 AM	130C	4.8E-8	0.1E-9	Y	Y	N	N
12/03/2017	11:28 AM	087C	8.6E-9	0.0E-9	Y	Y	N	N
12/03/2017	11:28 AM	087C	ERROR	1.5E-8	Y	Y	Y	N
12/03/2017	11:32 AM	087C	2.7E-8	2.8E-8	N	Y	Y	N
12/03/2017	11:32 AM	087C		2.0E-8	N	N	Y	N
12/03/2017	03:53 PM	021C		0.1E-9	N	N	Y	Y
But it do	es jump	up	to 1E-9 on	occasion	l.			
12/07/2017	10:00 AM	021C		0.1E-9	N	N	Y	N
12/07/2017	05:42 PM	130C	1.0E-6	0.2E-9	Y	Y	N	N
12/08/2017	08:30 AM	130C	4.8E-8	0.2E-9	Y	Y	N	N
12/08/2017	09:59 AM	087C	1.1E-8	0.2E-9	Y	Y	N	N
12/08/2017	09:59 AM	087C	ERROR	3.7E-8	Y	Y	Y	N
12/08/2017	09:59 AM	087C	3.5E-8	6.1E-8	N	Y	Y	N
12/08/2017	09:59 AM	087C	3.5E-8	6.1E-8	N	Y	Y	N
12/08/2017	09:59 AM	087C		4.0E-8	N	N	Y	N
12/08/2017	12:07 PM	022C		0.2E-9	N	N	Y	Y
12/10/2017	05:07 PM	121C	1.1E-6	0.2E-9	Y	Y	N	N
12/11/2017	09:03 AM	121C	3.7E-8	0.2E-9	Y	Y	N	N
12/11/2017	10:16 AM	087C	8.7E-9	4.0E-8	Y	Y	Y	N
12/11/2017	10:16 AM	087C	3.4E-8	6.4E-8	N	Y	Y	N
12/11/2017	10:16 AM	087C		4.6E-8	N	N	Y	N
12/11/2017	02:00 PM	021C		0.2E-9	N	N	Y	Y
12/11/2017	09:00 PM	121C	0.2E-9	7.7E-7	Y	Y	N	N
12/12/2017	08:29 AM	121C	0.4E-9	3.3E-8	Y	Y	N	N
12/12/2017	09:29 AM	087C	0.1E-9	1.3E-8	Y	Y	N	N
12/12/2017	09:45 AM	087C	7.5E-9	4.6E-8	Y	Y	Y	N
12/12/2017	09:45 AM	087C	3.5E-8	7.2E-8	N	Y	Y	N
12/12/2017	09:45 AM	087C		5.0E-8	N	N	Y	N
12/12/2017	04:00 PM	021C		0.3E-9	N	N	Y	N

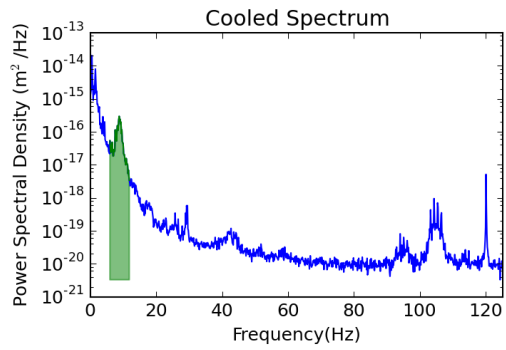
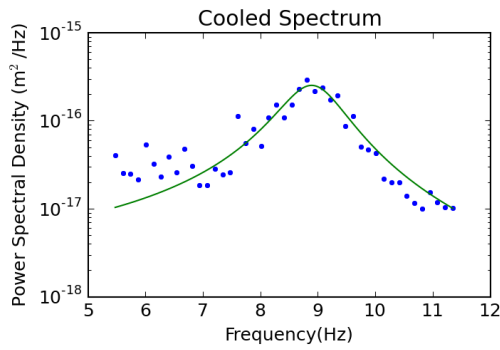
Table 14: Pressure Table from December 2017 - Bozeman

APPENDIX G

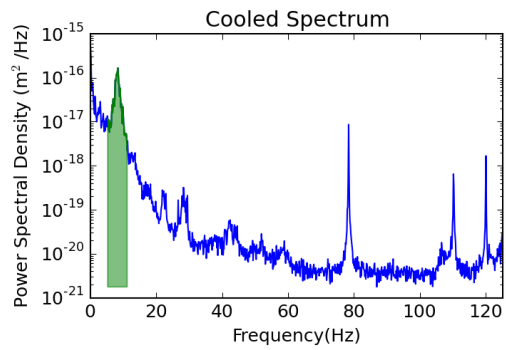
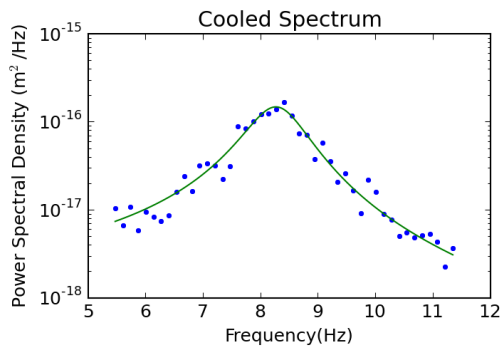
ALL COOLING RESULTS

All cooling results that were obtained with proper detector calibration are displayed in this Appendix. These correspond to the results listed in Tables [7](#), [8](#), and [9](#). Each result has two plots: a fit to the theoretical power spectral density, and a full power spectrum. The power spectrum has a green, shaded segment corresponding to (roughly) the frequency range of interest in the reported temperature.

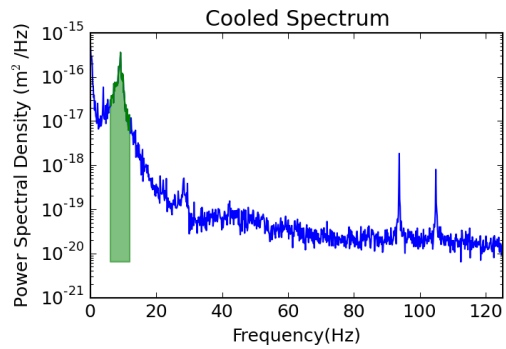
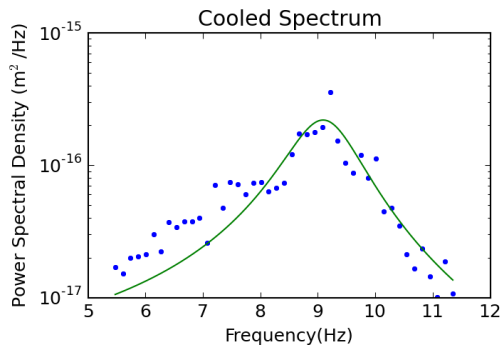
December 12 - Poly



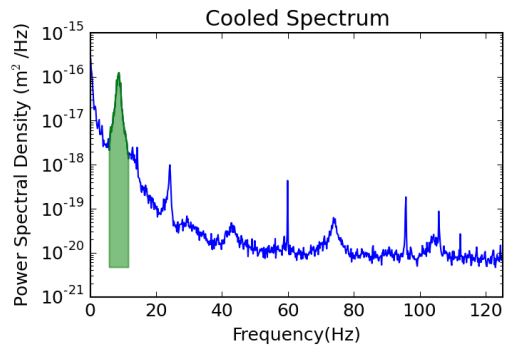
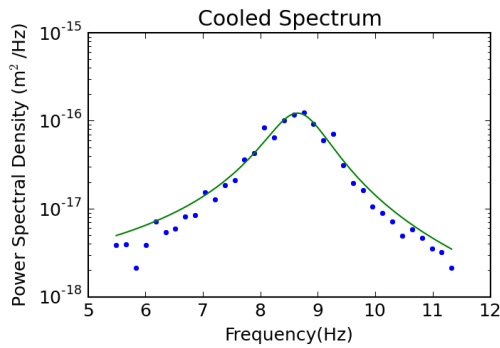
December 10 - Poly



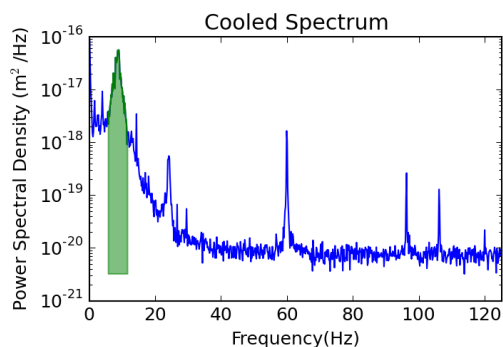
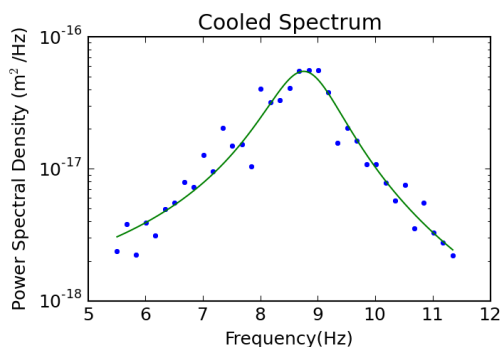
December 07 - Poly? Si



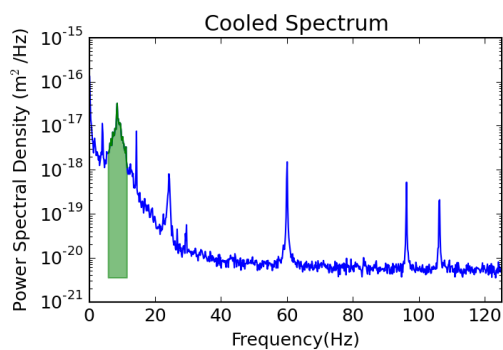
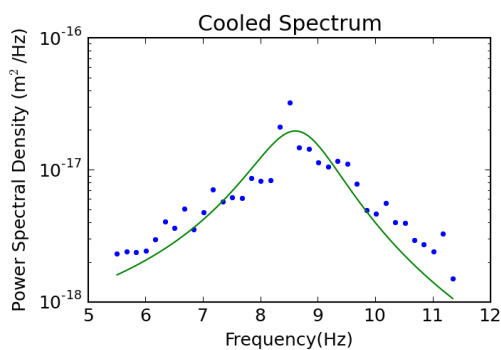
December 02 - Silica 1.54



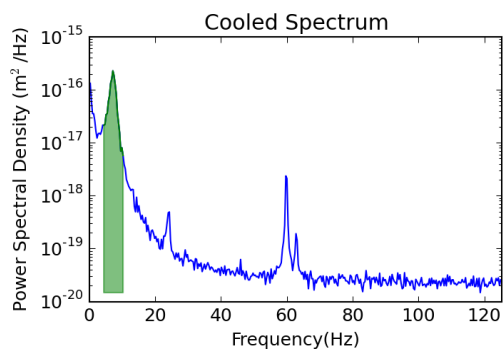
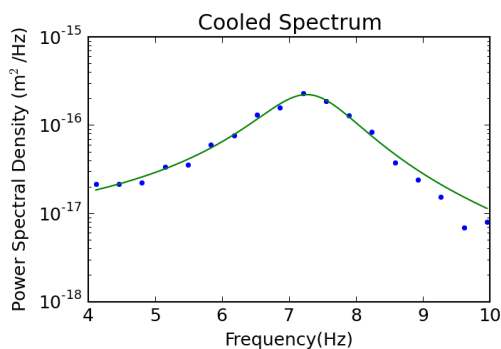
November 26 - 8PM - Silica 1.54



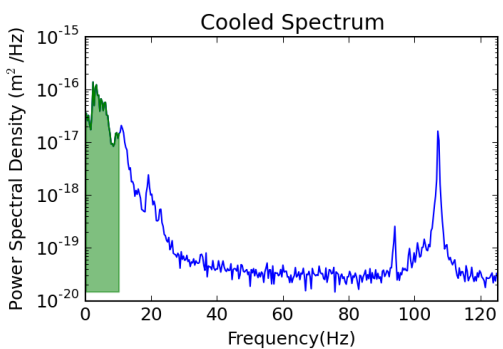
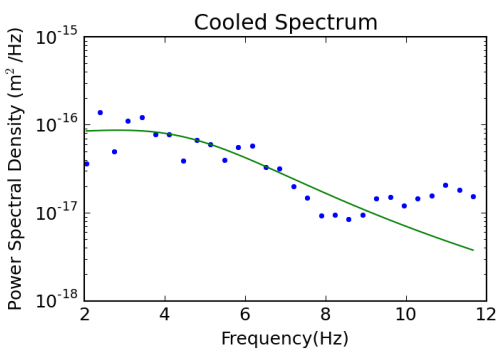
November 26 - MIDNIGHT - Silica 1.54



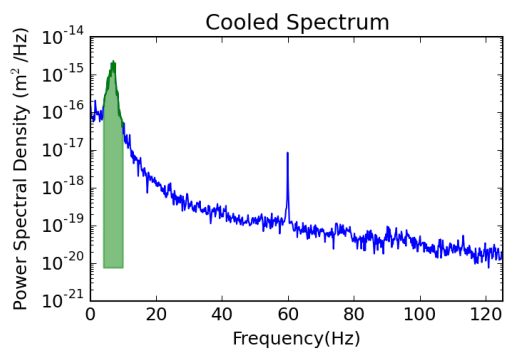
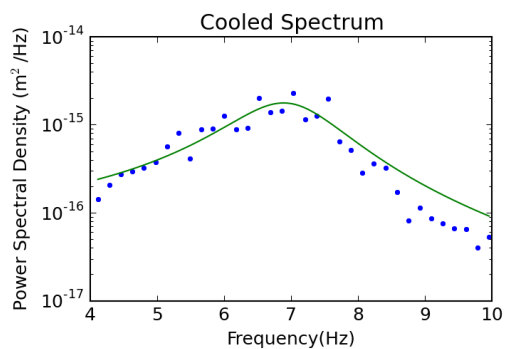
November 18 - Diamond



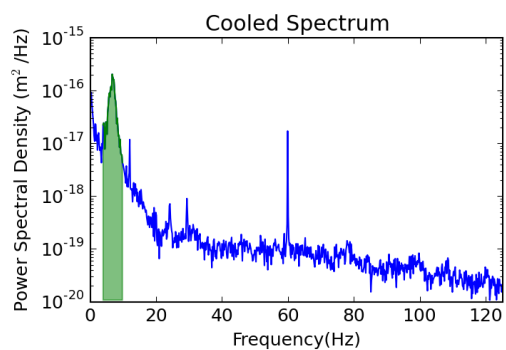
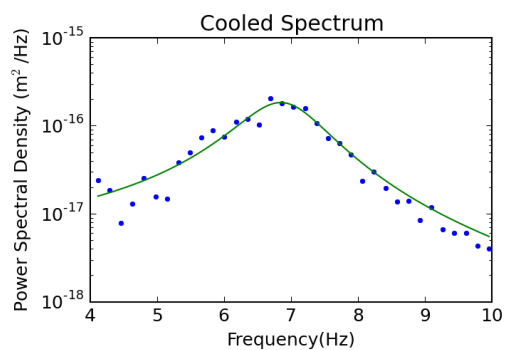
February 01 - Silica 1.54 - PGH



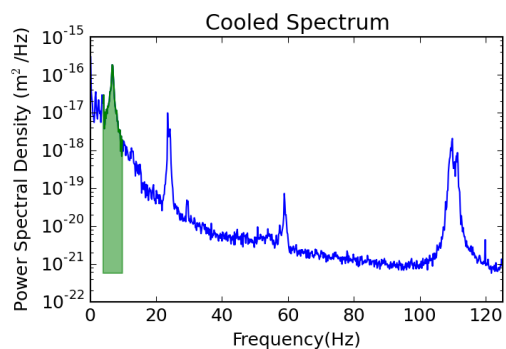
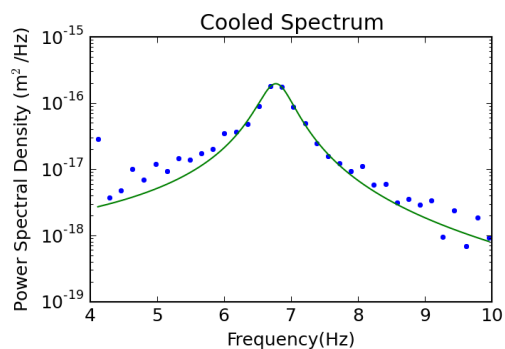
November 10 - E-5 - Silica 7.75



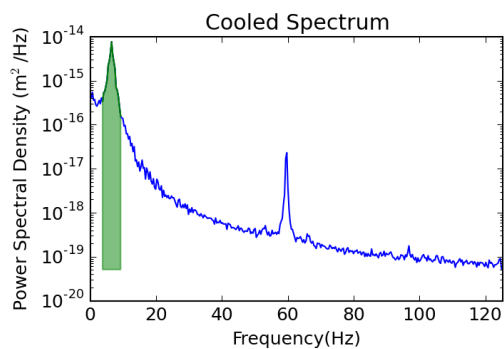
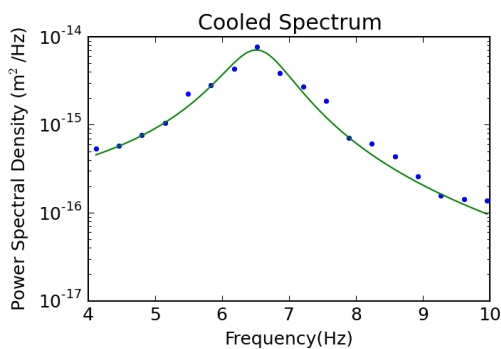
November 10 - E-6 - Silica 7.75



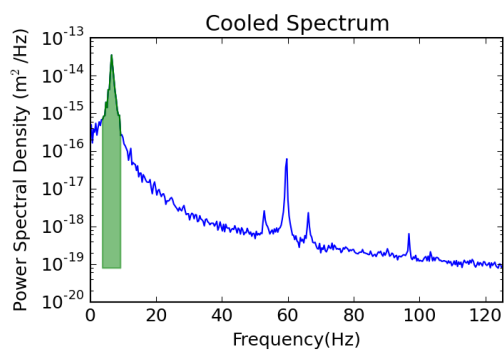
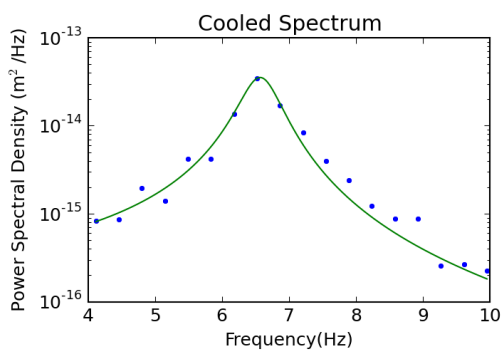
November 10 - E-9 - Silica 7.75



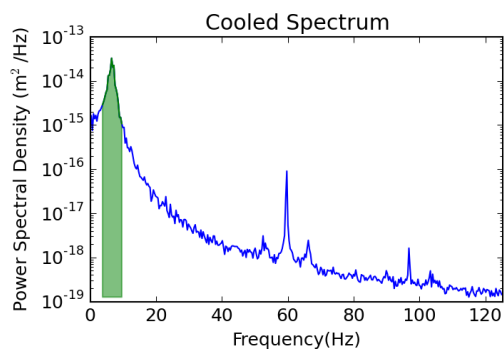
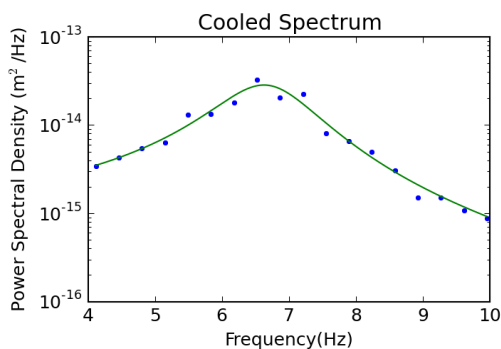
October 15 - 16 - Silica 1.54



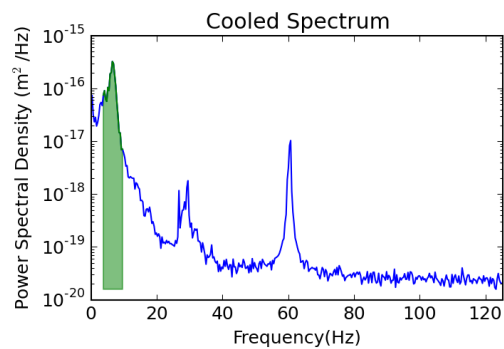
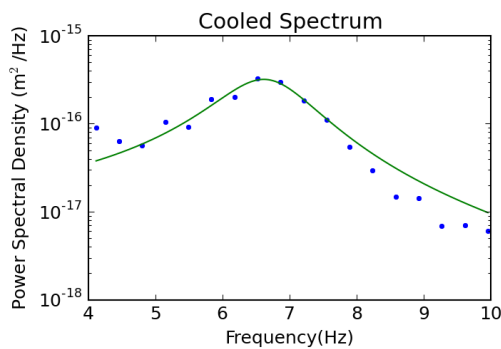
October 15 - 17 - Silica 1.54



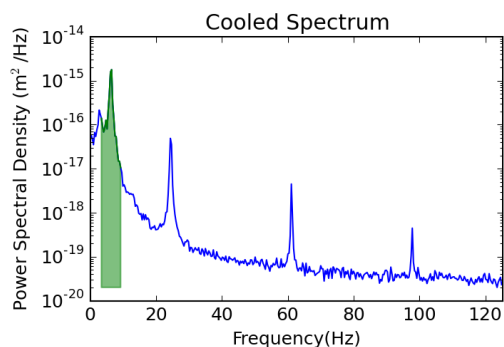
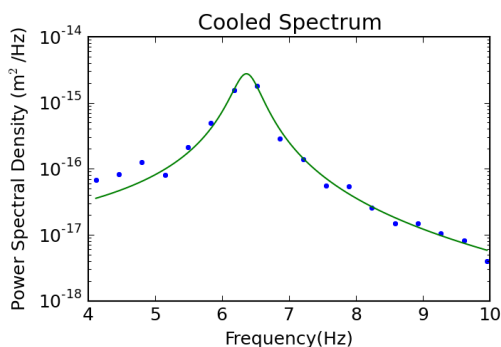
October 15 - 17_2 - Silica 1.54



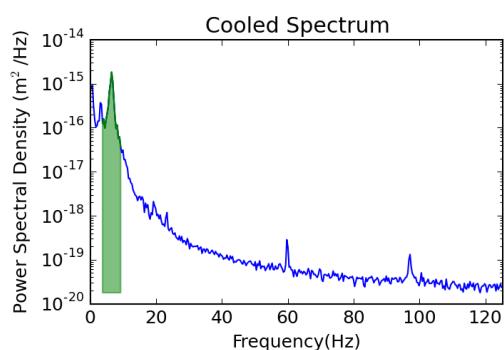
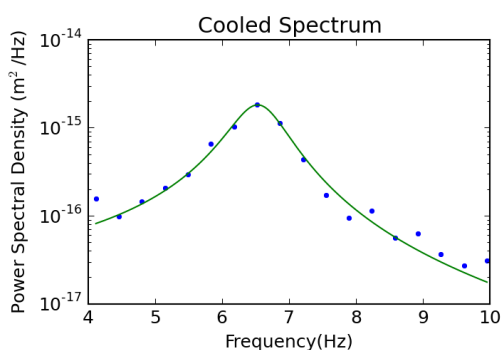
October 15 - Paper - Silica 1.54



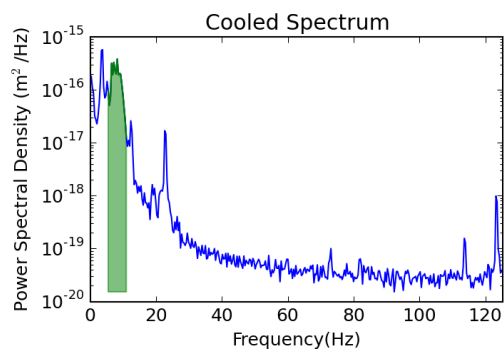
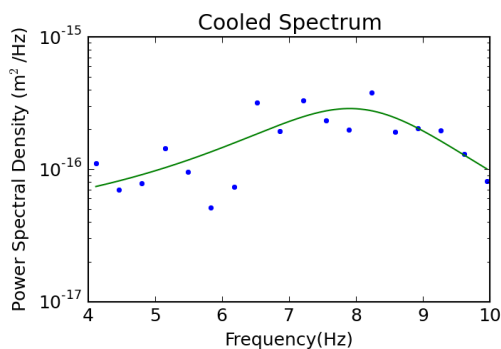
October 09 - 12A - Silica 1.54



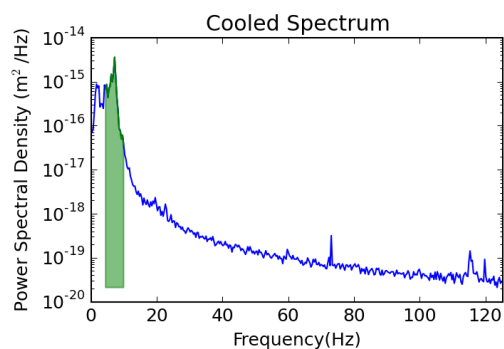
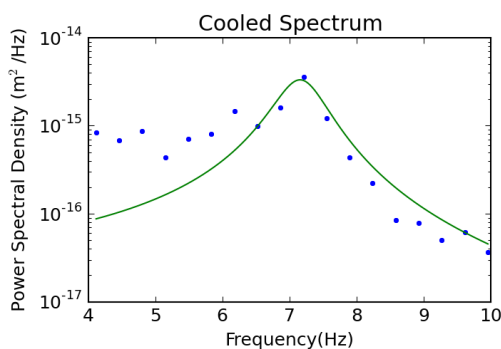
June - 06 - Silica 1.54 - PGH



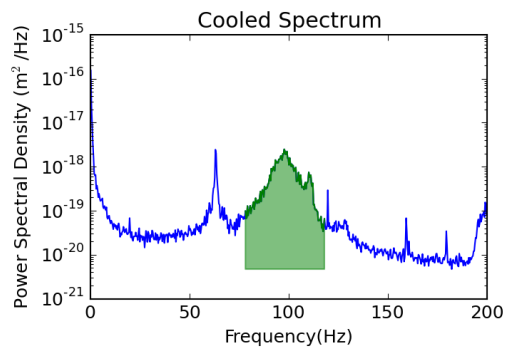
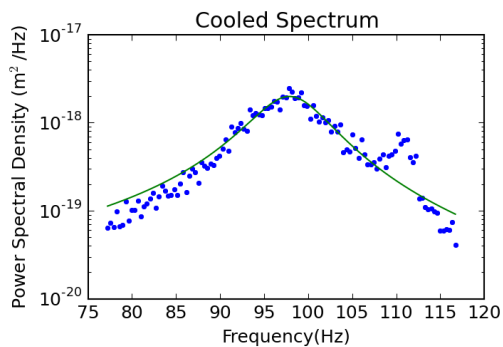
March 15 - Silica 1.54 - PGH



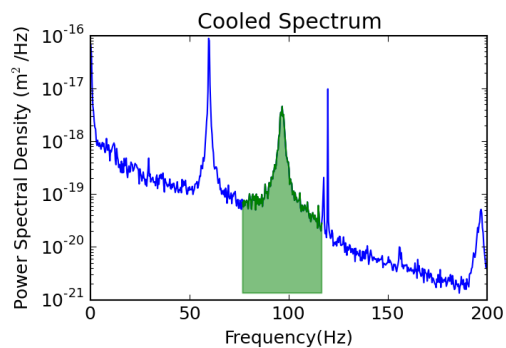
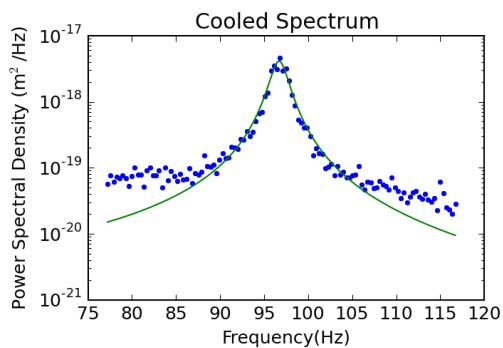
March 08 - Silica 1.54 - PGH



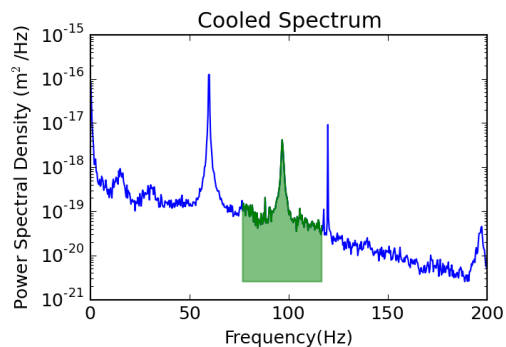
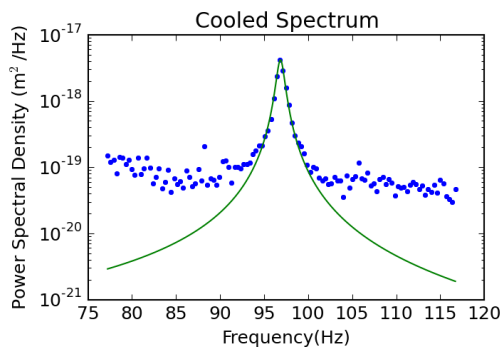
November 18 - Diamond



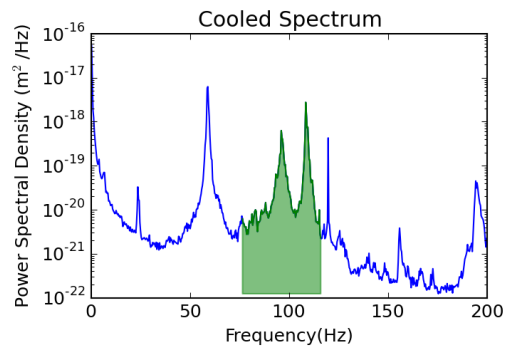
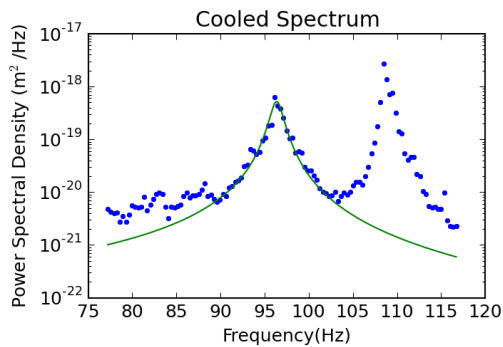
November 10 - Silica 7.75 - E-5



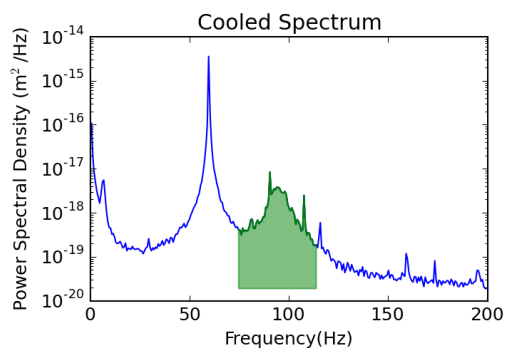
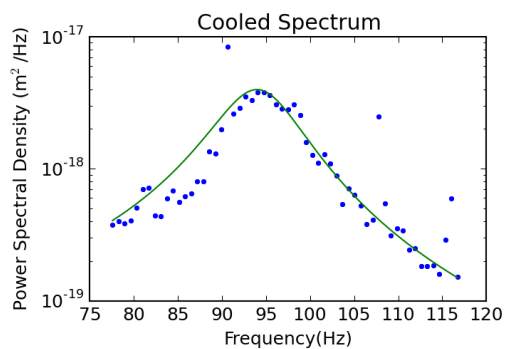
November 10 - Silica 7.75 - E-6



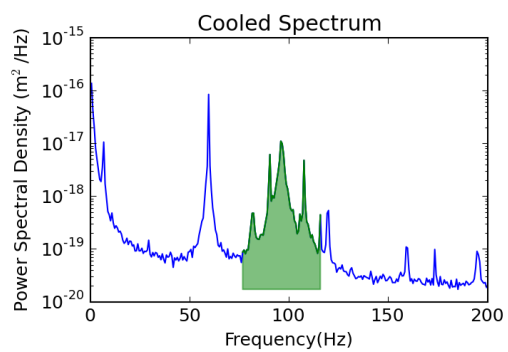
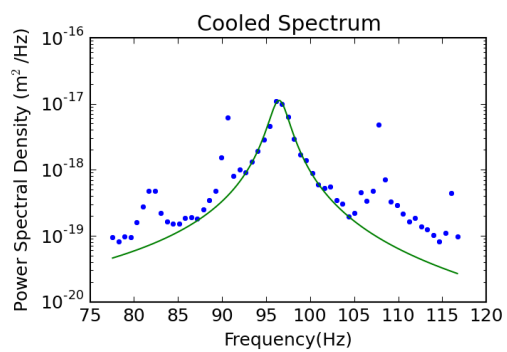
November 10 - Silica 7.75 - E-9



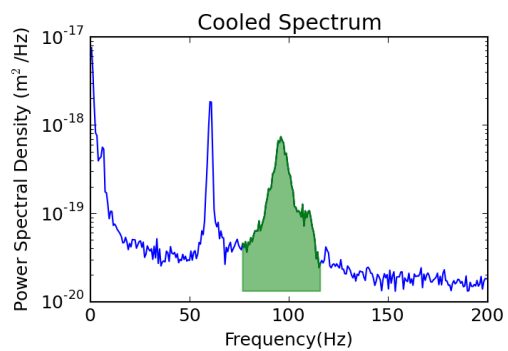
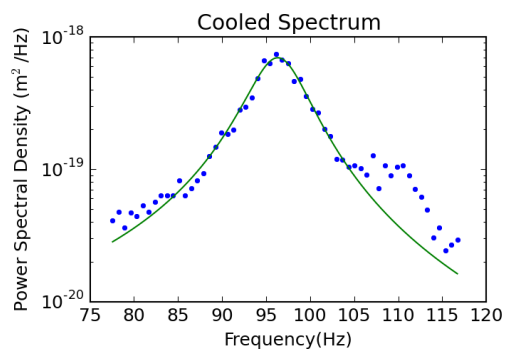
October 15 - 17 - Silica 1.54



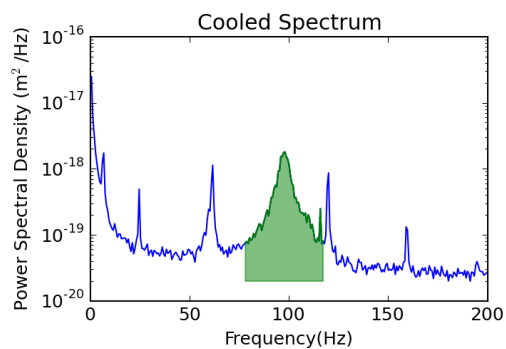
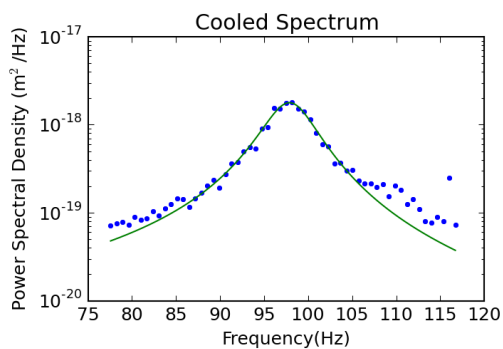
October 15 - 16 - Silica 1.54



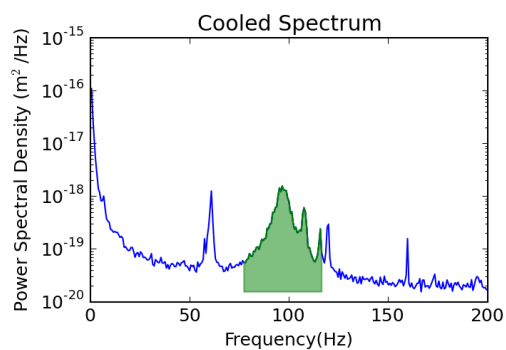
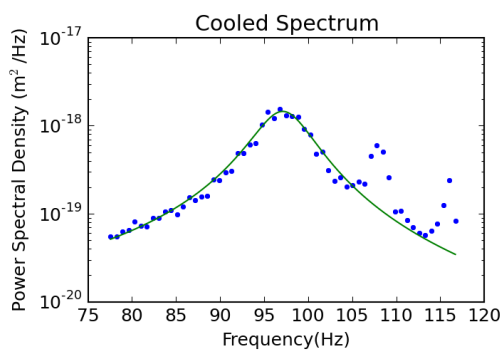
October 15 - Paper - Silica 1.54



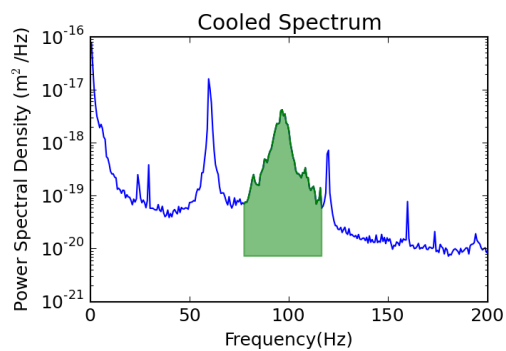
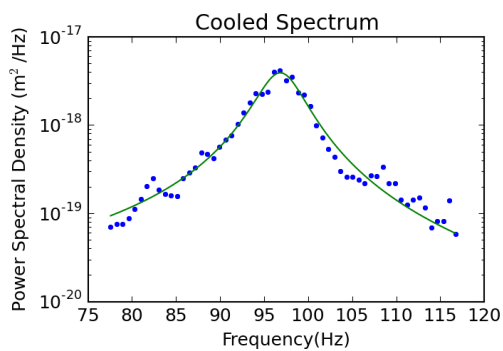
October 9 - 12 - Silica 1.54



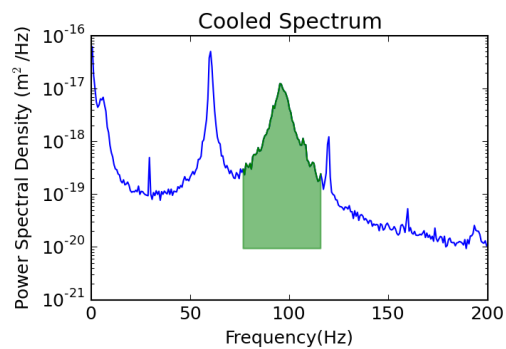
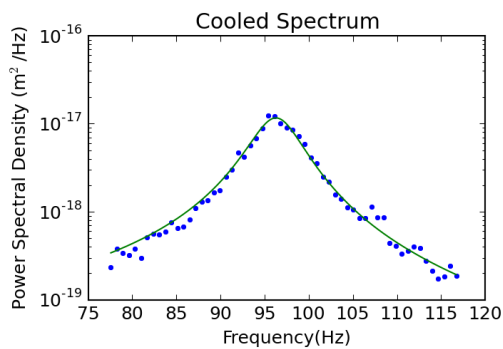
October 9 - 11 - Silica 1.54



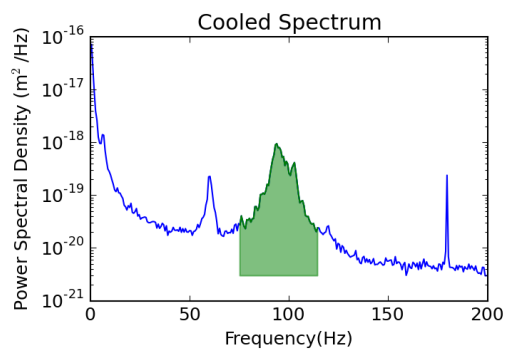
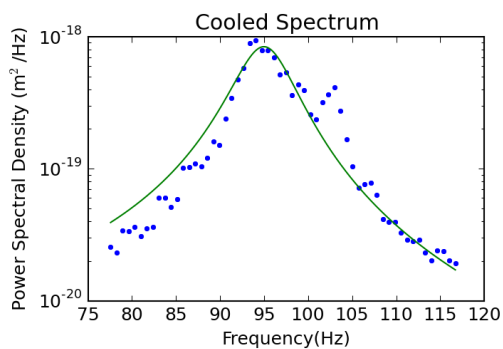
October 9 - 10 - Silica 1.54



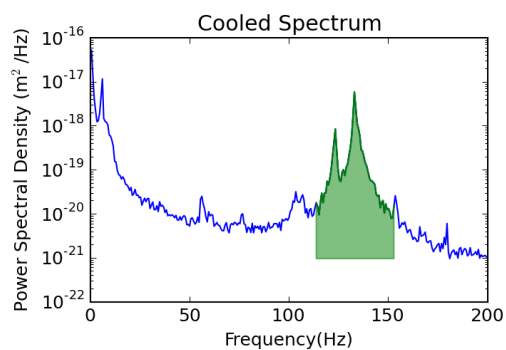
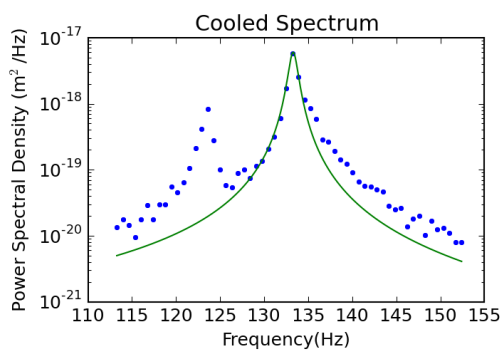
October 9 - 09 - Silica 1.54



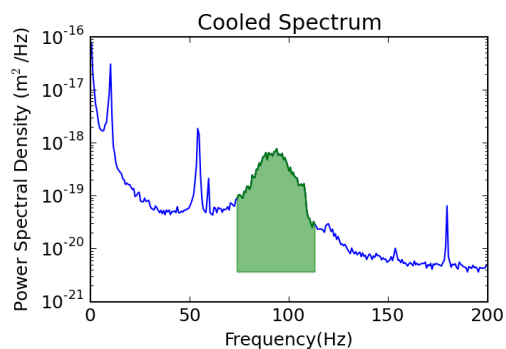
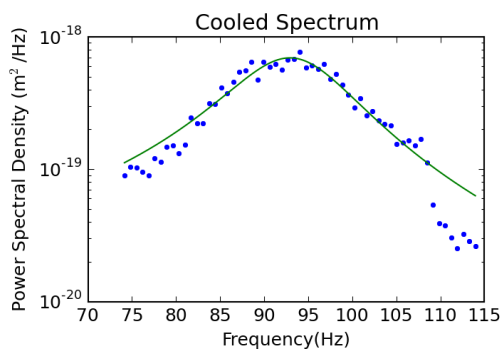
June 06- Silica 1.54 - PGH



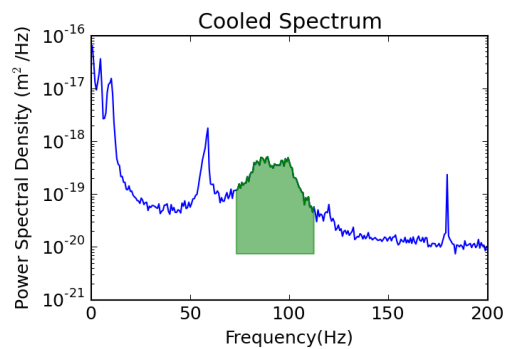
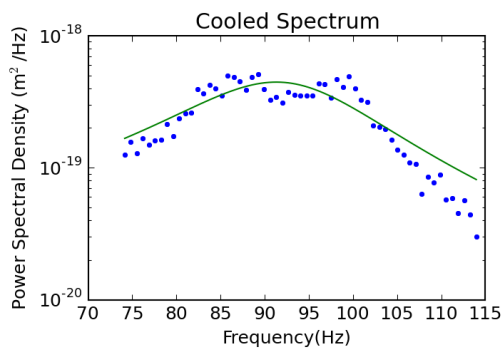
May 25- Silica 1.54 - PGH



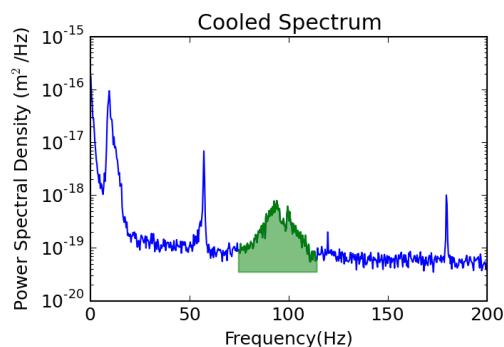
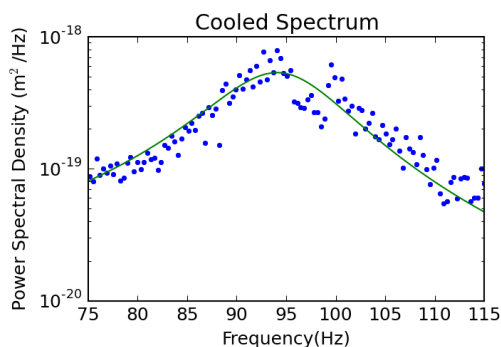
May 17- Silica 1.54 - PGH



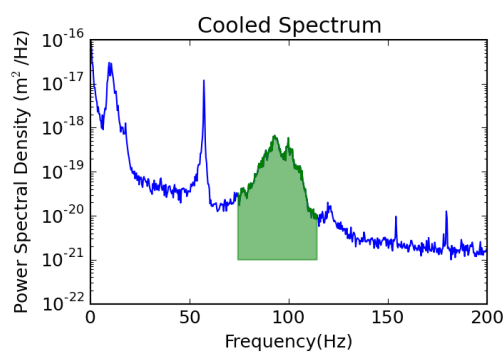
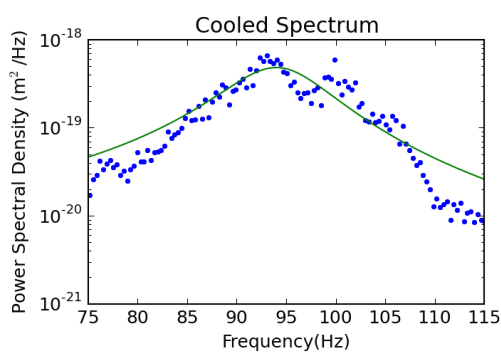
May 16 - Silica 1.54 - PGH



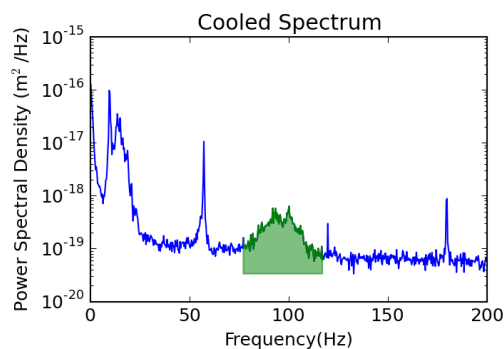
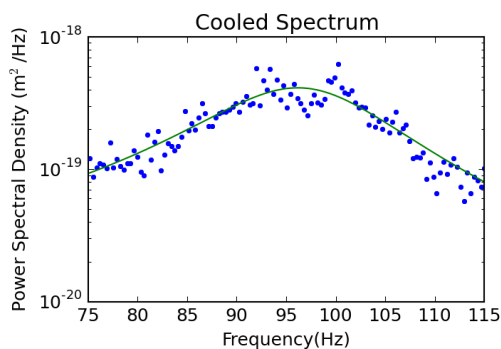
May 22 - Ig - Silica 1.86 - PGH



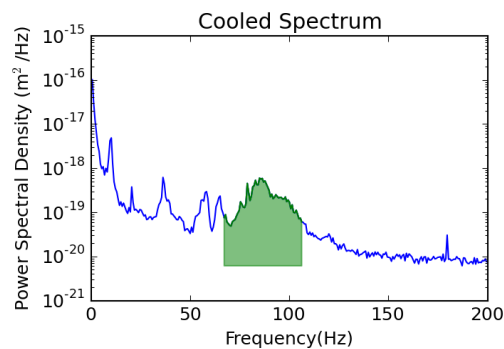
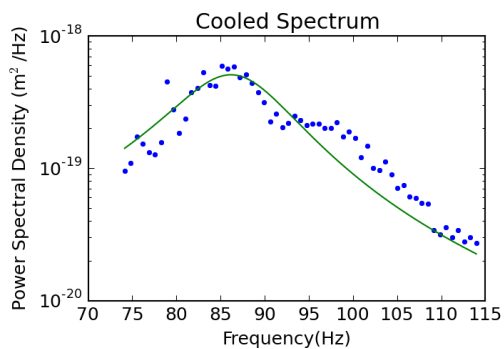
May 22 - Igml - Silica 1.86 - PGH



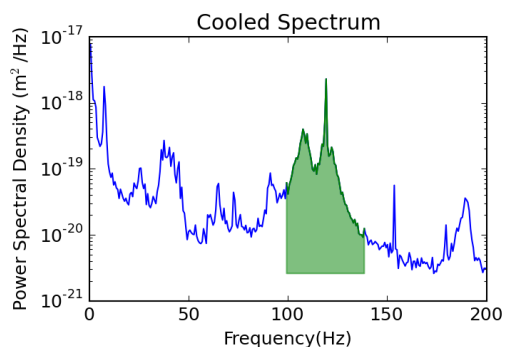
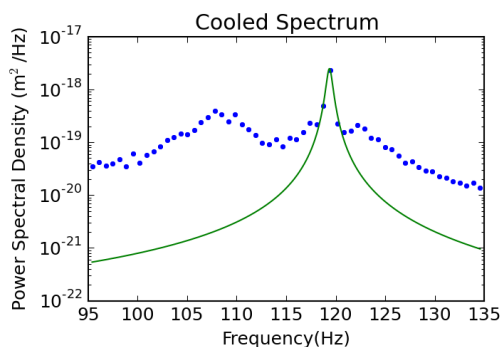
May 22 - Silica 1.86 - PGH



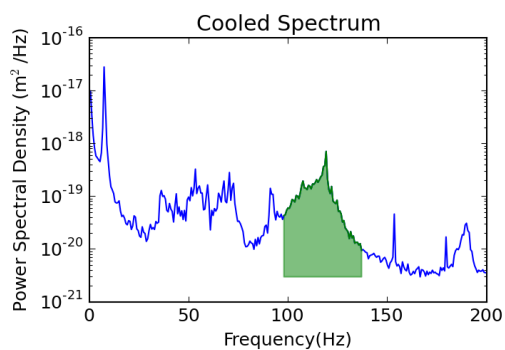
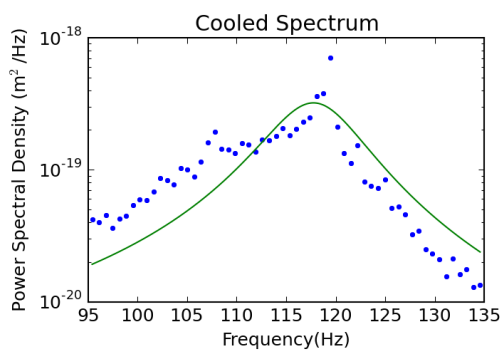
May 11 - Silica 1.54 - PGH



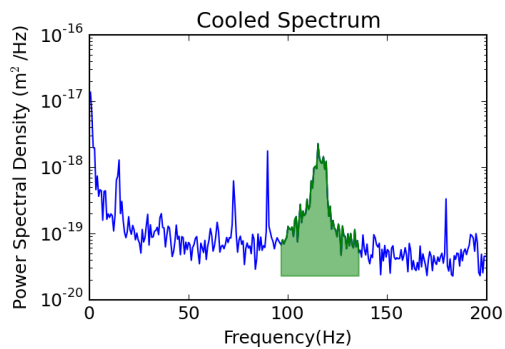
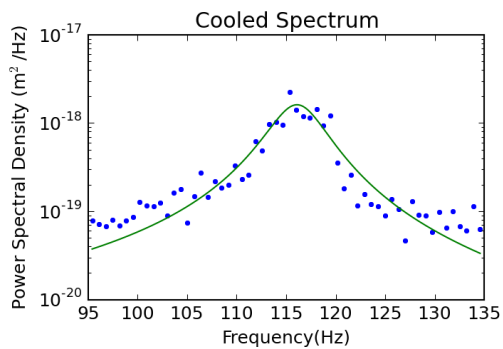
Mar 27 - 43-20 - Silica 1.54 - PGH



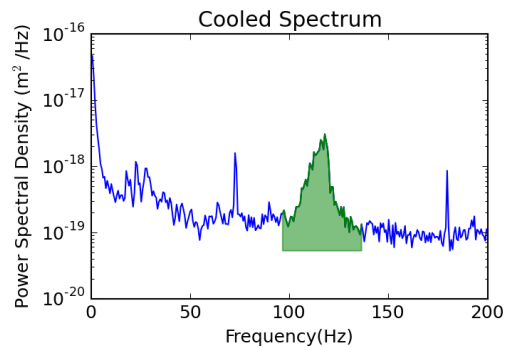
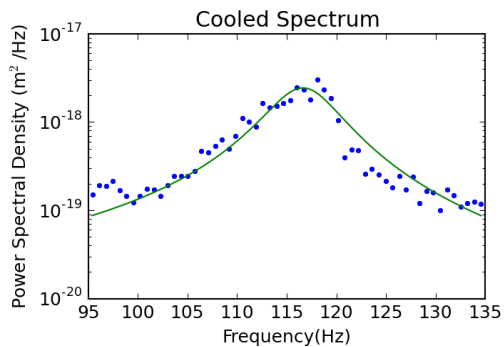
Mar 27 - 43-4 - Silica 1.54 - PGH



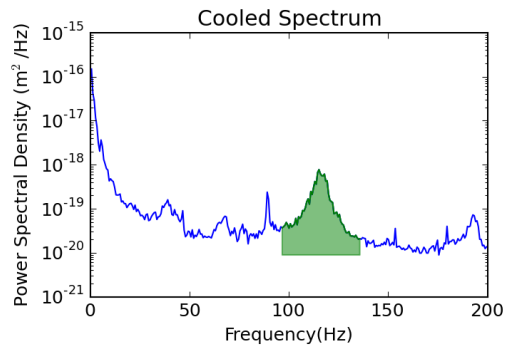
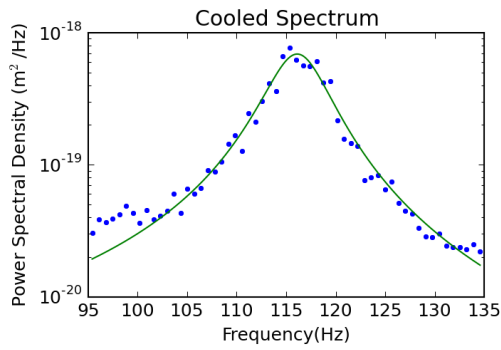
Mar 27 - 35 - Silica 1.54 - PGH



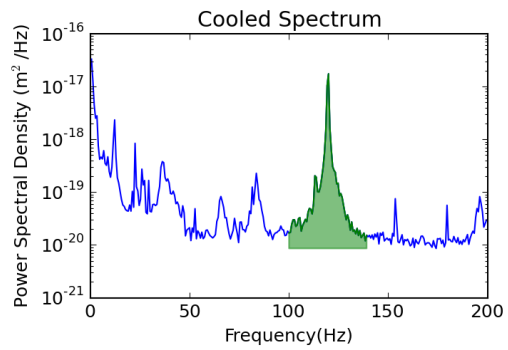
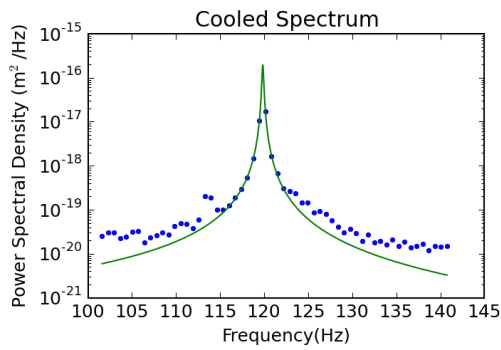
Mar 27 - 28th - Silica 1.54 - PGH



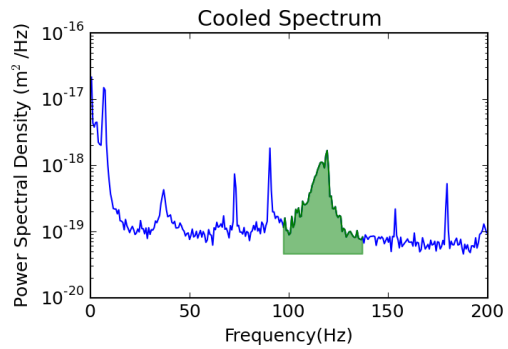
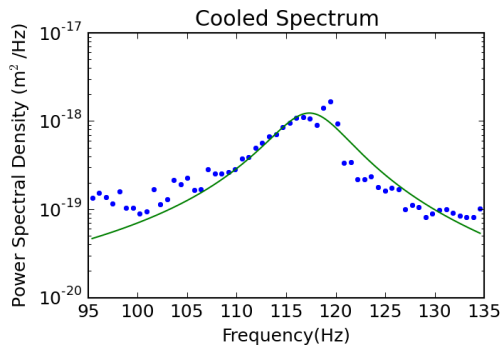
April 20 - Silica 1.54 - PGH



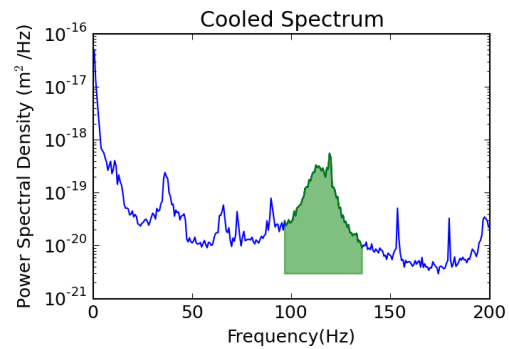
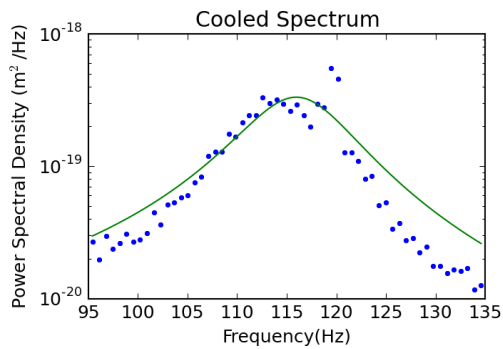
Mar 15 - Silica 7.75 - PGH



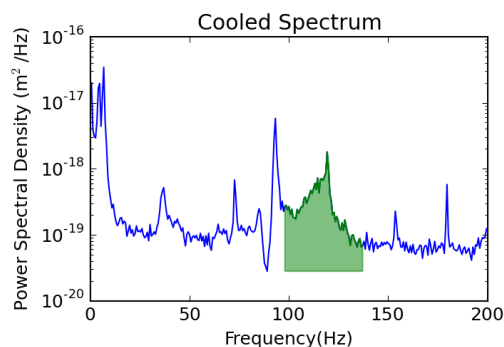
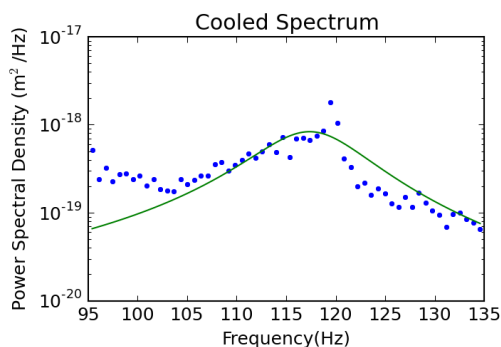
Mar 08 - 13 - Silica 1.54 - PGH



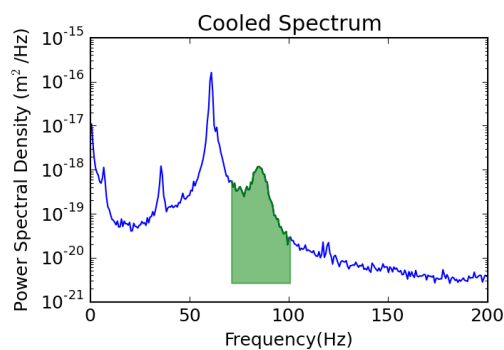
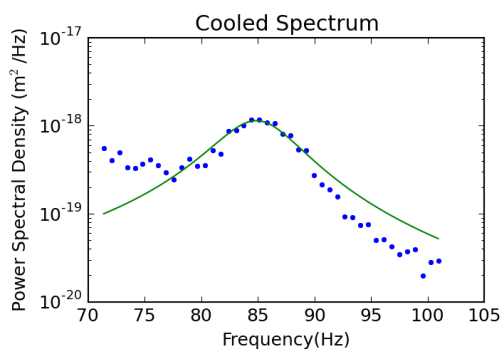
Mar 08 - 10 - Silica 1.54 - PGH



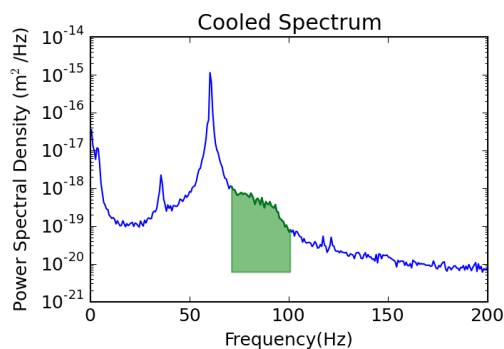
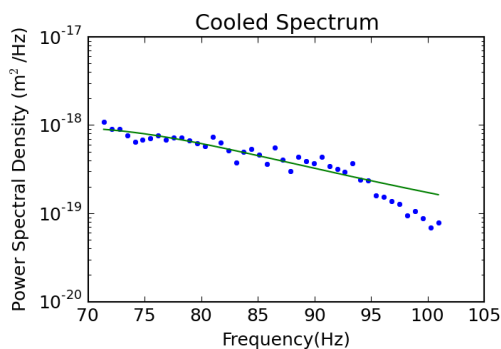
Mar 08 - AntiV - Silica 1.54 - PGH



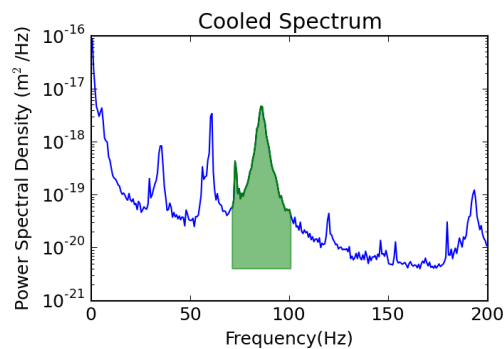
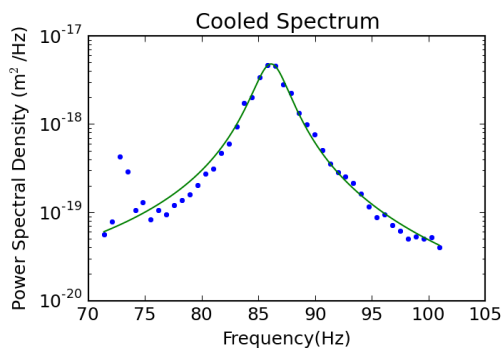
Feb 15 - 16 - Silica 1.54 - PGH



Feb 15 - 17 - Silica 1.54 - PGH



Feb 13 - Silica 1.54 - PGH



BIBLIOGRAPHY

- [1] Paul A. Tipler and Ralph A. Llewellyn. *Modern Physics*. W.H. Freeman and Company, New York, fifth edition edition, 2008.
- [2] Teufel J D, Donner T, Li D, Harlow J W, Allman M S, Cicak K, Sirois A J, Whittaker J D, Lehnert K W, and Simmonds R W. Sideband cooling of micromechanical motion to the quantum ground state. *Nature*, 475:359–363, 2011.
- [3] Chan J, Mayer Alegre T P, Safavi-Naeini A H, Hill J T, Krause A, Groblacher S, Aspelmeyer M, and Painter O. Laser cooling of a nanomechanical oscillator into its quantum ground state. *Nature*, 478:89–92, 2011.
- [4] O’Connell A D et al. Quantum ground state and single-phonon control of a mechanical resonator. *Nature*, 464:697–703, 2010.
- [5] Clark J B, Lecocq F, Simmonds R W, Aumentado J, and Teufel J D. Observation of strong radiation pressure forces from squeezed light on a mechanical oscillator. *Nature Physics*, 12:683–687, 2016.
- [6] Chang D E, Regal C A, Papp S B, Wilson D J, Ye J, Painter O, Kimble H J, and Zoller P. Cavity opto-mechanics using an optically levitated nanosphere. *PNAS*, 107(3):1005–1010, 2009.
- [7] Romero-Isart O, Pflanzner A C, Juan M L, Quidant R, Kiesel N, Aspelmeyer M, and Cirac J I. Optically levitating dielectrics in the quantum regime: Theory and protocols. *Physical Review A*, 83:013803, 2011.
- [8] Bateman J, Nimmrichter S, Hornberger K, and Ulbricht H. Near-field inteferometry of a free-falling nanoparticle from a point-like source. *Nature Communications*, 5:4788, 2014.
- [9] Rashid M, Tufarelli T, Bateman J, Vorosh J, Hempston D, Kim M S, and Ulbricht H. Experimental realization of a thermal squeezed state of levitated optomechanics. *Physical Review Letters*, 117:273601, 2016.
- [10] Jain V, Gieseler J, Moritz C, Dellaho C, Quidant R, and Novotny L. Direct measurement of photon recoil from a levitated nanoparticle. *Physical Review Letters*, 116:243601, 2016.

- [11] Ranjit G, Atherton D P, Stutz J H, Cunningham M, and Geraci A A. Attonewton force detection using microspheres in a dual-beam optical trap in high vacuum. *Physical Review A*, 91:051805(R), 2015.
- [12] Ranjit G, Cunningham M, Casey K, and Geraci A A. Zeptonewton force sensing with nanospheres in an optical lattice. *Physical Review A*, 93:053801, 2016.
- [13] Millen J, Dessuwan T, Barker P, and Anders J. Nanoscale temperature measurements using non-equilibrium brownian dynamics of a levitated nanosphere. *Nature Nanotechnology*, 9:425–429, 2014.
- [14] Kiesel N, Blaser F, Delic U, Grass D, Kaltenbaek R, and Aspelmeyer M. Cavity cooling of an optically levitated submicron particle. *PNAS*, 110(35):1418014185, 2013.
- [15] Goldwater D, Paternostro M, and Barker P F. Testing wave-function-collapse models using parametric heating of a trapped nanosphere. *Physical Review A*, 94:010104(R), 2016.
- [16] Millen J, Fonseca P Z G, Mavrogodatos T, Monteiro T S, and Barker P F. Cavity cooling a single charged levitated nanosphere. *Physical Review Letters*, 114:123602, 2015.
- [17] Fonseca P Z G, Aranas E B, Millen J, Monteiro T S, and Barker P F. Nonlinear dynamics and strong cavity cooling of levitated nanoparticles. *Physical Review Letters*, 117:173602, 2016.
- [18] Gieseler J, Novotny L, and Quidant R. Thermal nonlinearities in a nanomechanical oscillator. *Nature Physics*, 9:806–810, 2013.
- [19] Monteiro F, Ghosh S, Getzels Fine A, and Moore D C. Optical levitation of 10-ng spheres with nano-g acceleration sensitivity. *Physical Review A*, 96:063841, 2017.
- [20] Geraci A A, Papp S B, and Kitching J. Short-range force detection using optically cooled levitated microspheres. *Physical Review Letters*, 105:101101, 2010.
- [21] Moore D C, Rider A D, and Gratta G. Search for millicharged particles using optically levitated microspheres. *Physical Review Letters*, 113:251801, 2014.
- [22] Rider A D, Moore D C, Blakemore C P, Louis M, Lu M, and Gratta G. Search for screened interactions associated with dark energy below the 100 μm length scale. *Physical Review Letters*, 117:101101, 21016.
- [23] Hsu J F. *Cooling the Center-of-Mass Motion of a Diamond Nanocrystal in a Magneto-Gravitational Trap*. PhD thesis, University of Pittsburgh, 2016.
- [24] Jen-Feng Hsu, Peng Ji, Charles W. Lewandowski, and Brian D’Urso. Cooling the motion of diamond nanocrystals in a magneto-gravitational trap in high vacuum. *Scientific Reports*, 6:30125, 2016.

- [25] Simon M D and Geim A K. Diamagnetic levitation: Flying frogs and floating magnets (invited). *Journal of Applied Physics*, 87(9):6200–6204, 2000.
- [26] John David Jackson. *Classical Electrodynamics*. John Wiley & Sons, Inc, Singapore, third edition edition, 1999.
- [27] Cooling the motion of diamond nanocrystals in a magneto-gravitational trap in high vacuum: Supplementary information, <https://www-nature-com.pitt.idm.oclc.org/articles/srep30125#supplementary-information>.
- [28] Pontin A, Bonaldi M, Borrielli A, Cataliotti F S, Marino F, Prodi G A, Serra E, and Marin F. Squeezing a thermal mechanical oscillator by stabilized parametric effect on the optical spring. *Physical Review Letters*, 112:023601, 2014.
- [29] Yang H, Miao H, Lee D-S, Helou B, and Chen Y. Macroscopic quantum mechanics in a classical spacetime. *Physical Review Letters*, 110:170401, 2013.
- [30] GroBardt A, Bateman J, Ulbricht H, and Bassi A. Optomechanical test of the schrodinger-newton equation. *Physical Review D*, 93:096003, 2016.
- [31] Diósi L. Gravity-related wave function collapse: mass density resolution. *Journal of Physics: Conference Series*, 442:012001, 2013.
- [32] Penrose R. Wavefunction collapse as a real gravitational effect. In Fokas A, Grigoryan A, Kibble T, and Zegarlinski B, editors, *Mathematical Physics 2000*, pages 266–282. Imperial College Press, London, 2000.
- [33] Kafri D, Taylor J M, and Milburn G J. A classical channel model for gravitational decoherence. *New Journal of Physics*, 16:065020, 2014.
- [34] Big g redux: Solving the mystery of a perplexing result, <https://www.nist.gov/news-events/news/2016/11/big-g-redux-solving-mystery-perplexing-result>.
- [35] Riley K F, Hobson M P, and Bence S J. *Mathematical Methods for Physics and Engineering*. Cambridge University Press, New York, third edition edition, 2006.
- [36] Scott L. Miller and Donald Childers. *Probability and Random Processes With Applications to Signal Processing and Communications*. Elsevier, 225 Wyman Street, Waltham, MA 02451, second edition edition, 2012.
- [37] Venkatarama Krishnan. *Probability and random processes*. John Wiley & Sones, Inc, Hoboken NJ, second edition edition, 2015.
- [38] King W T. *Open source single molecule force spectroscopy*. PhD thesis, Drexel University, 2013.
- [39] Eric Jones, Travis Oliphant, Pearu Peterson, et al. Scipy: Open source scientific tools for python <http://www.scipy.org>, 2001–.

- [40] Discrete fourier transform (numpy.fft), <https://docs.scipy.org/doc/numpy/reference/routines.fft.html>.
- [41] Epstein P S. On the resistance experienced by spheres in their motion through gases. *Phys. Rev.*, 23:710–732, 1924.
- [42] Karl Jousten. *Handbook of Vacuum Technology*. Wiley-VCH, Boschstr. 12, 69469 Weinheim, Germany, second, completely revised and updated edition edition, 2016.
- [43] Beresnev S A, Chernyak V G, and Fomyagin G A. Motion of a spherical particle in a rarefied gas. part 2. drag and thermal polarization. *J. Fluid Mech.*, 219:405–421, 1990.
- [44] Beresnev S A, Chernyak V G, and Suetin P E. Motion of a spherical particle in a rarefied gas. part 1. a liquid particle in its saturated vapour. *J. Fluid Mech.*, 176:295–310, 1987.
- [45] Gieseler J, Deutsch B, Quidant R, and Novotny L. Subkelving parametric feedback cooling of a laser-trapped nanoparticle. *Physical Review Letters*, 109:103603, 2012.
- [46] Li T, Kheifets S, and Raizen M G. Millikelvin cooling of an optically trapped microsphere in vacuum. *Nature Physics*, 7:527–530, 2011.
- [47] M. Weidemuller et. al L. Ricci. A compact grating-stabilized diode laser system for atomic physics. *Optics Communications*, 117:541–549, 1995.
- [48] Leo Hollberg Carl E. Wiemean. Using diode lasers for atomic physics. *Review of Scientific Instruments*, 62:1, 1990.
- [49] Lewandowski C W. *Untitled - Not Yet Published*. PhD thesis, Motana State University, TBD.
- [50] A. Murari and A. Barzon. Comparison of new peek seals with traditional helicox for ultra high vacuum applications. *Science Direct*, VACUUM 72:327–334, 2004.
- [51] Trackpy v0.3.2 <http://soft-matter.github.io/trackpy/dev/index.html>.
- [52] Frimmer M, Luszcz K, Ferreira S, Jain V, Hebestreit E, and Novotny L. Controlling the net charge on a nanoparticle optically levitated in vacuum. *Physical Review A*, 95:061801, 2017.
- [53] Poggio M, Degen C L, Mamin H J, and Rugar D. Feedback cooling of a cantilever’s fundamental mode below 5mk. *Physical Review Letters*, 99:017201, 2007.
- [54] Eric W Hansen. *Fourier transforms: principles and applications*. John Wiley & Sons, Inc, New Jersey, 2014.
- [55] Johnson J B. Thermal agitation of electricity in conductors. *Physical Review*, 32:97, 1928.

- [56] Zhang B, Zerubia J, and Olivo-Marin J-C. Gaussian approximations of fluorescence microscope point-spread function models. *Applied Optics*, 46(10):1819–1829, 2007.
- [57] Miguel Orszag. *Quantum Optics Including Noise Reduction, Trapped Ions, Quantum Trajectories, and Decoherence*. Springer International Publishing, Switzerland, third edition edition, 2016.
- [58] Direct measurement of photon recoil from a levitated nanoparticle - supplementary information, <http://link.aps.org/supplemental/10.1103/PhysRevLett.116.24360>.
- [59] Blanter Y M and Buttiker M. Shot noise in mesoscopic conductors. *Physics Reports*, 336:1–166, 2000.
- [60] Schottky W. ber spontane stromschwankungen in verschiedenen elektrizittsleitern. *annalen dr physik*, 57:541–567, 1918.
- [61] Fiber optic coupling. <https://www.newport.com/n/fiber-optic-coupling>. Accessed: 2018-02-15.